ELECTRON, PHOTON, AND POSITRON SCATTERING DYNAMICS OF COMPLEX MOLECULAR TARGETS

A Dissertation

by

RALPH J. CAREY

Submitted to the Office of Graduate Studies of
Texas A&M University
in partial fulfillment of the requirements for the degree of

DOCTOR OF PHILOSOPHY

May 2012

Major Subject: Chemistry

ELECTRON, PHOTON, AND POSITRON SCATTERING DYNAMICS OF COMPLEX MOLECULAR TARGETS

A Dissertation

by

RALPH J. CAREY

Submitted to the Office of Graduate Studies of
Texas A&M University
in partial fulfillment of the requirements for the degree of

DOCTOR OF PHILOSOPHY

Approved by:

Chair of Committee, Robert R. Lucchese
Committee Members, John Bevan
Lewis Ford
Michael Hall
Timothy Hughbanks
Head of Department, David Russell

May 2012

Major Subject: Chemistry

ABSTRACT

Electron, Photon, and Positron Scattering Dynamics of
Complex Molecular Targets. (May 2012)
Ralph J. Carey, B.S., Louisiana State University
Chair of Advisory Committee: Dr. Robert R. Lucchese

Electron scattering cross sections have been computed for pyridine and pyrimidine using the static-exchange approximation with model potential to account for dynamic electron correlation. To obtain well-converged orbitals, we have expanded all partial waves to a maximum angular momentum of $l = 60$ for both targets. We have obtained total cross sections for electron scattering energies to 20 eV. Both targets display similar features, namely a dipole-induced increase in the integrated cross section at scattering energies below 5 eV, and peaks corresponding to resonances in b_1, a_2, and b_1 symmetries. These resonances were investigated through a Siegert eigenstate analysis and Breit-Wigner fit of the SECP eigenphase sums. They were also compared to the virtual orbitals obtained from a minimum basis set Hartree-Fock calculation on both targets.

We consider electron scattering resonances from *cis*-diamminedichloroplatinum, $[\mathrm{Pt(NH_3)_2Cl_2}]$, the ligand molecular species $\mathrm{Cl_2}$ ($^1\Sigma_g^+$), and the isolated transition metal center Pt in a nondegenerate atomic state (^1S) at the SECP level of theory. As a rigorous comparison to the single-state, single-configuration SECP level results of these smaller, yet electron dense targets, we have also considered scattering from ground state $\mathrm{Cl_2}$ and Pt in the ^1S and ^3D states in the multichannel configuration-interaction (MCCI) approximation originally developed for photoionization for scattering up to 10 eV.

Photoionization cross sections and angular distributions in the recoil frame (RFPAD) and molecular frame (MFPAD) have been computed for inner-shell C 1s and Cl 2p ionization from the chloroalkanes chloromethane and chloroethane, with ionization leading to a variety of ionic fragment states. We have also computed valence level ionization from the nitro molecule nitromethane CH_3NO_2 leading to the dissociation of the CN bond. All of these calculations were performed in the frozen-core Hartree-Fock approximation. Even at this level of theory, we obtain computed results that compare well to the photoelectron-photoion coincidence measurements.

The fullerene C_{20} is the smallest fullerene predicted to exist, with most relevant structural calculations suggesting the reduction of the icosahedral symmetry into one in which the target species possesses at maximum only a dihedral axis. We have computed positron scattering cross sections for the molecule in two low-symmetry structural isomers C_i and C_2, within the HF approximation. Density functional expressions were used to incorporate important positron-electron interactions within the calculation. We have found similar cross sections and resonance features for both isomers, including a positron scattering resonance whose density is found within the framework of the fullerene cluster.

ACKNOWLEDGMENTS

I acknowledge the financial support of the Robert A. Welch Foundation under Grant A-1020. Technical support from the Texas A&M University Supercomputing Facility and the Laboratory for Molecular Simulation (National Science Foundation Grant CH3-0541587).

I wish to thank my advisor Robert Lucchese, whose guidance and encouragement has allowed me to complete the undertaking of this dissertation. I also thank Prof. Danielle Dowek (Université de Paris-Sud, Orsay) for the hospitality she showed in my visit to her laboratory. I also thank the members of my committee and the members of the Lucchese group for fruitful discussions.

TABLE OF CONTENTS

LIST OF FIGURES

FIGURE Page

FIGURE Page

FIGURE Page

FIGURE Page

LIST OF TABLES

I. INTRODUCTION

Electron, photon, and positron collisions with molecules constitute fundamental processes in physics, with applications in such fields as the material sciences, laser and plasma physics (Christophorou and Olthoff, 2004), and atmospheric chemistry, and, increasingly, biochemistry, in which low-energy electron collisions with DNA have been implicated to initiate mutagenic damage in cells (Whelan and Mason, 2005). For light or particles of sufficient energy several decay channels are possible upon impact with a polyatomic molecule, which are listed for photon collisions in Table 1 and electron collisions in Table 2. Positrons may undergo the unique antimatter reactions of positron annihilation, in which positron and electron collide to release two photons of 511 keV radiation, and positronium (Ps) formation, the bound state of a positron with an electron with threshold energy $E = 6.8$ eV. The collision processes of positrons with polyatomic molecules are given in Table 2.

Through the years, spurred by the increase in supercomputing technology, refinements in code parallelization and the availability of sophisticated electronic structure suites, increasingly refined theoretical methods have been developed to predict the outcomes of scattering phenomena for atoms and polyatomic molecules (Huo, 1995a). These theories employ a variety of means of incorporating the primary dynamics of the scattering process, including target-particle exchange interactions, dynamic correlation, and compound state formation. Multichannel theories have been developed (Burke and Berrington, 1993; Lengsfield and Rescigno, 1991; Lucchese *et al.*, 1986; Takatsuka and McKoy, 1984) to account for inelastic scattering, which leaves the target in an excited rovibrational or electronic state.

This dissertation follows the style of Reviews of Modern Physics.

TABLE 1 Selected photon-induced reaction collision processes (reproduced from Christophorou and Olthoff, 2004).

Process representation	Process description
$h\nu + \mathrm{AX} \rightarrow \mathrm{AX}^*$	Photoabsorption
$h\nu + \mathrm{AX} \rightarrow \mathrm{AX}^+ + e^-$	Photoionization
$h\nu + \mathrm{AX} \rightarrow \mathrm{A} + \mathrm{X}^+ + e^-$	Dissociative photoionization
$h\nu + \mathrm{AX} \rightarrow \mathrm{A} + \mathrm{X}$	Photodissociation
$h\nu + \mathrm{AX}^- \rightarrow \mathrm{AX} + e^-$	Photodetachment
$h\nu + \mathrm{AX}^- \rightarrow \mathrm{A} + \mathrm{X}^-$	Anion photodissociation

TABLE 2 Selected electron- and positron-induced collision processes (reproduced from Kimura *et al.*, 2007).

Process representation	Process description
$e^\pm + \mathrm{AB} \rightarrow e^\pm + \mathrm{AB}$	Elastic scattering
$e^\pm + \mathrm{AB} \rightarrow e^\pm + e^- + \mathrm{AB}^-$	Ionization
$e^- + \mathrm{AB} \rightarrow \mathrm{AB}^-$	Electron attachment
$e^+ + \mathrm{AB} \rightarrow \mathrm{AB}^+$	Positron attachment (not observed)
$e^+ + \mathrm{AB} \rightarrow e^+e^- + \mathrm{AB}^+$	Positronium (Ps) formation
$e^+ + \mathrm{AB} \rightarrow h\nu + \mathrm{AB}^+$	Positron annihilation

A. Overview of scattering theory

In classical scattering (Newton, 1982), the trajectory of the projectile of mass m can be obtained at any time t from the Hamiltonian

$$H = \frac{\mathbf{p}^2}{2m} + V(r), \tag{1}$$

where $V(r)$ is the interaction potential, and

$$\mathbf{p}^2 = p_r^2 + r^{-2}\left[p_\theta^2 + \csc^2\theta\, p_\phi^2\right] = p^2 + r^{-2}J^2 \tag{2}$$

is the canonical momentum vector decomposed in radial coordinates, and J the angular momentum. Using standard Hamilton-Jacobi theory to solve for the classical action variable S and differentiating by the result by angle θ, it results that

$$\theta = J\int_{r=0}^{\infty} dr\, r^{-2}\left[p^2 - 2mV - r^{-2}J\right]^{-1/2}. \tag{3}$$

The deflection angle θ can be obtained from the radial distance of closest approach r_{min} from Eq. 3. It is convenient to define the impact parameter b in terms of the angular momentum and the energy $E = p^2/2m$, or

$$J = pb = \left[2\mu E\right]^{1/2} b, \tag{4}$$

so that

$$\theta(b) = \pi - 2\int_{r_{\text{min}}}^{\infty} dr\, r^{-2}\left[b^{-2}\left(1 - \frac{V}{E}\right) - r^{-2}\right]^{-1/2}. \tag{5}$$

A beam of projectiles with an area $b\,db\,d\theta$ are scattered through a solid angle $d\phi\, d\theta\, \sin\theta$. The differential cross section $\frac{d\sigma}{d\Omega}$, the number of particles per unit time of an incoming particle beam passing through a solid angle of (θ, ϕ), after some cancellations, is given by

$$\frac{d\sigma}{d\Omega} = \frac{b}{\sin\theta}\left|\frac{db}{d\theta}\right|, \tag{6}$$

which completely describes the scattering event.

In nonrelativistic quantum scattering theory, the differential cross section, $\frac{d\sigma}{d\Omega}$, measures the *probability* that a flux of non-interacting particles with well-defined momenta $\mathbf{k}'$ will scatter through a solid angle Ω with resulting momenta $\mathbf{k}$. The quantum differential cross section is given experimentally by

$$\frac{d\sigma}{d\Omega} = |f_{\mathbf{k}'\leftarrow\mathbf{k}}|^2, \tag{7}$$

where $f_{\mathbf{k}'\leftarrow\mathbf{k}}$ is the scattering amplitude. The solutions of the scattering equation are given in terms of stationary states $\psi_{\mathbf{k}}^{+}$ of the scattering (quantum) Hamiltonian $H = H_0 + V$ such that they have the asymptotic form

$$\psi_{\mathbf{k}}^{+}(\mathbf{x}) \xrightarrow[r\to\infty]{} (2\pi)^{-3/2}\left[e^{-i\mathbf{k}\cdot\mathbf{x}} + f_{\mathbf{k}'\leftarrow\mathbf{k}}\frac{e^{ikr}}{r}\right]. \tag{8}$$

The rigorous derivation of $f_{\mathbf{k}'\leftarrow\mathbf{k}}$ of Eq. 7 requires the time-dependent formalism, which concerns the propagation of sharply-defined wave packets in momentum space. A thorough discussion may be found in the reference monograph of Newton (Newton, 1982).

The state vector $|\psi(t)\rangle$ satisfies the time-dependent Schrödinger equation

$$i\frac{d}{dt}\,|\psi(t)\rangle = H\,|\psi(t)\rangle\,, \tag{9}$$

which has the general solution $e^{iHt}\,|\psi\rangle$, where $|\psi\rangle$ represents a stationary state of the Hamiltonian. It may be proved (Taylor, 1972) that every such solution represents the time evolution of some free-particle incoming asymptotic state $e^{-iH_0t}\,|\phi_{\text{in}}\rangle$ at $t \to -\infty$, and that the solution will approach the free-particle motion of some outgoing asymptotic state $e^{-iH_0t}\,|\phi_{\text{out}}\rangle$ at $t \to +\infty$. This important property may be formally represented in terms of isometric, but not unitary, Møller wave operators

$$\Omega_{\pm} \equiv \lim_{t\to\mp\infty} e^{iHt}e^{-iH_0t} \tag{10}$$

such that $|\psi\rangle = \Omega_{+}\,|\phi_{\text{in}}\rangle$ and $|\psi\rangle = \Omega_{-}\,|\phi_{\text{out}}\rangle$ as stated informally. All such scattering states $|\psi\rangle$ are orthogonal to all in- and out-asymptotic free states and to any possible bound states of the scattering Hamiltonian $H = H_0 + V$.

The unitary scattering operator S maps every in-asymptote with every out asymptote as $|\phi_{\text{out}}\rangle = S\,|\phi_{\text{out}}\rangle$. The S-operator is defined in terms of the Møller wave operators

$$S = \Omega_{-}^{\dagger}\Omega_{+}. \tag{11}$$

This is a purely formal result as neither S nor the probability amplitude of incoming states to scattered states are directly observable.

An analytic representation of the S-matrix elements is obtained through the T-matrix (on the energy shell), or

$$\left\langle \mathbf{k}'\left|S\right|\mathbf{k}\right\rangle = \delta(\mathbf{k}'-\mathbf{k}) - 2\pi i\delta(E_{k'}-E)T_{\mathbf{k}'\leftarrow\mathbf{k}}. \tag{12}$$

The on-shell T-operator is related to the scattering amplitude simply as

$$f_{\mathbf{k}'\leftarrow\mathbf{k}} = -(2\pi)^2 T_{\mathbf{k}'\leftarrow\mathbf{k}}. \tag{13}$$

For subsequent discussion, we will concern ourselves with the calculation of the matrix elements of the T-operator, from which all scattering properties may be derived.

The S-operator obeys several invariance principles due to the conservation of the following properties:

1. Linear momentum $D(\mathbf{a}) = e^{-i\mathbf{a}\cdot\mathbf{k}}$. This is a statement that S conserves energy in elastic scattering.

2. Angular momentum $R(\alpha) = e^{-i\alpha\cdot\mathbf{J}}$. This property is especially important, since S commutes both with H_0 and $\mathbf{L}$, it is diagonal in the same set of common (irregular) eigenfunctions $\langle\mathbf{r}|Elm\rangle = (1/2m)^{1/2}\,\pi k\frac{1}{r}\sum_{lm} i^l j_l(kr)Y_{lm}(\hat{r})$. In other words,

$$\left\langle E'l'm'\,|S|\,Elm\right\rangle = \delta(E'-E)\delta_{l'l}\delta_{m'm}s_l, \tag{14}$$

where s_l is the eigenvalue of S. Since S is unitary, it must have an eigenvalue of 1 within an arbitrary phase factor. The eigenvalues of S are therefore

$$s_l = e^{2i\delta_l}, \tag{15}$$

where δ_l is the (real) energy-dependent eigenphase shift. This definition of the eigenphase shift defines its value with (mod π) ambiguity. Furthermore, the symmetry under rotation admits scattering solutions expressible in partial wave lm expansions. In particular, the partial wave expansion of the scattering amplitude is given by

$$f(E,\theta) = \sum_{l=0}(2l+1)f_l(E)P_l(\cos\theta), \tag{16}$$

where

$$f_l(E) = \frac{s_l - 1}{2ik} = \frac{e^{2i\delta_l - 1}}{2ik} = \frac{e^{i\delta_l}\sin\delta_l}{k}. \tag{17}$$

Making use of the definition $d\sigma/d\Omega = |f|^2$ and taking the integral over the solid angle Ω, the partial wave expression for the total cross section is found to be

$$\sigma = \sum_l \sigma_l = \frac{4\pi}{k^2}\sum_l (2l+1)\sin^2\delta_l \tag{18}$$

in terms of only k and the eigenphase shifts δ_l.

3. Parity, such that $P\,|\mathbf{x}\rangle = -\,|\mathbf{x}\rangle$.

4. Time reversal, such that $T\,|\mathbf{x}\rangle = |\mathbf{x}\rangle$ but $T\,|\mathbf{k}\rangle = |-\mathbf{k}\rangle$.

The primary observables of scattering theory will be given within the framework of the more easily calculated time-independent formalism. The following discussion will draw from Taylor, 1972 except where stated otherwise, while rigorous proofs of the time-independent formalism are given in Thirring, 2002. Except where otherwise noted, this discussion describes scattering from atomic centers using atomic units.

The stationary scattering states are most clearly stated in terms the scattering and homogeneous Green operators

$$G(z) = (z - H)^{-1} \tag{19}$$

$$G_0(z) = (z - H_0)^{-1}. \tag{20}$$

The homogeneous Green operator "solves" the free Schrodinger equation

$$\left(\frac{1}{2}\nabla^2 + z\right)\langle \mathbf{x}|G_0(z)|\mathbf{x}'\rangle = \delta(\mathbf{x} - \mathbf{x}'),$$

while the unknown scattering Green operator can be obtained from $G_0(z)$ by the operator identity

$$G(z) = G_0(z) + G_0(z)VG(z). \tag{21}$$

The homogeneous Green operator is diagonal in $|\mathbf{k}\rangle$, such that

$$G_0\,|\mathbf{k}\rangle = \frac{1}{z - H_0}\,|\mathbf{k}\rangle = \frac{1}{z - E_k}\,|\mathbf{k}\rangle\,. \tag{22}$$

The second operator useful in the time-independent theory is the T-operator, defined in terms of Green operators by the relations

$$T(z) = V + VG(z)V \tag{23}$$

$$= V + VG_0(z)T(z). \tag{24}$$

It can be shown (Taylor, 1972) that, in conjunction with analytic representations of the Møller wave operators, that S-operator and the T-operator are related by

$$\langle \mathbf{k}|S|\mathbf{k}'\rangle = \delta(\mathbf{k}' - \mathbf{k}) - 2\pi i\delta(E_{k'} - E_k)\langle \mathbf{k}'|T(E_k + i\varepsilon)|\mathbf{k}\rangle\,. \tag{25}$$

Comparing the matrix elements of the T-operator to the on-shell T-matrix

$$T_{\mathbf{k}'\leftarrow\mathbf{k}} = \left\langle \mathbf{k}' | T(E_k + i\varepsilon) | \mathbf{k} \right\rangle, \tag{26}$$

we can immediately identify the $\langle \mathbf{k}' | T(E_k + i\varepsilon) | \mathbf{k} \rangle$ as the elements of the off-shell T-matrix.

The stationary states are defined

$$|\mathbf{k}\pm\rangle \equiv \Omega_{\pm} \, |\mathbf{k}\rangle, \tag{27}$$

and, by the property of $\Omega_{\pm}$, constitute the solutions of the scattering Schrodinger equation

$$H \, |\mathbf{k}\pm\rangle = E_k \, |\mathbf{k}\pm\rangle. \tag{28}$$

Employing the analytic Møller operators and the homogeneous Green function, the stationary states have the integral solutions

$$|\mathbf{k}\pm\rangle = |\mathbf{k}\rangle + G_0(E_k \pm i\varepsilon) V \, |\mathbf{k}\pm\rangle, \tag{29}$$

the Lippmann-Schwinger equation for $|\mathbf{k}\pm\rangle$. Using the coordinate representation of the Green operator

$$\langle \mathbf{x} | G_0 | \mathbf{x} \rangle = -\frac{m}{2\pi} \frac{\exp\{ik|\mathbf{x}-\mathbf{x}'|\}}{|\mathbf{x}-\mathbf{x}'|} \tag{30}$$

and expanding $|\mathbf{x}-\mathbf{x}'|^{-1}$ in powers of r, the asymptotic form of the scattering solutions are found as

$$\langle \mathbf{x} | \mathbf{k}\pm\rangle \xrightarrow[r\to\infty]{} (2\pi)^{-3/2} \left[e^{i\mathbf{k}\cdot\mathbf{x}} + f_{k\hat{x}\leftarrow\mathbf{k}} \frac{e^{ikr}}{r} \right] \tag{31}$$

as expected. This argument assumes that $V(\mathbf{x})$ tends to zero sufficiently rapidly as $r \to \infty$.

B. Partial-wave time-independent scattering theory

The free radial Schrödinger equation, in atomic units, with eigenfunctions in the form $u(r)/r$, has the form

$$\left[\frac{d^2}{dr^2} - \frac{l(l+1)}{r^2} + k^2 \right] u(r) = 0, \tag{32}$$

where the energy in atomic units is defined $E = k^2/2$. The solutions $u(r)$ regular near the origin are given in terms of the regular Riccati-Bessel functions $j_l(kr)$, which have the asymptotic form $\sim \sin(kr - \pi l/2)$, and the solutions which diverge at the origin are the Riccati-Neumann functions $n_l(kr)$. The solutions $u(r)$ that behave as a plane wave as $r \to \infty$ are the Riccati-Hankel functions $h_l^{\pm}(kr) = n_l(kr) \pm j_l(kr)$, which oscillate as $\sim e^{\pm i(kr-\pi/2)}$. Making use of the coordinate representation of the irregular partial wave basis $\langle \mathbf{x}|Elm\rangle$, the useful partial wave expansion of the plane wave

$$\langle \mathbf{x}|\mathbf{k}\rangle = \frac{4\pi}{kr}\sum_{lm} i^l j_l(kr) Y_{lm}(\hat{r}) Y_{lm}^*(\hat{k}). \tag{33}$$

immediately follows.

When the radial equation contains an interaction potential $V(r)$, the Schrödinger equation becomes

$$\left[\frac{d^2}{dr^2} - \frac{l(l+1)}{r^2} - V(r) + k^2\right] \psi_l(r) = 0, \tag{34}$$

with normalized radial eigenfunctions ψ_l. If the interaction potential decays sufficiently rapidly as $V(r) \to 0$ as $r \to \infty$, then the radial eigenfunctions have an asymptotic form

$$\psi(r) \to j_l(kr) + k f_l(k) h_l^+(kr), \tag{35}$$

where $f_l(k)$ are the partial-wave scattering amplitudes as usual. The asymptotic form of $\psi_l(r)$ may be given in terms of the eigenphase shifts

$$\psi_l(r) \to e^{i\delta_l(k)} \sin\left[kr - \frac{1}{2} l\pi + \delta_l(k)\right], \tag{36}$$

or, equivalently, directly in terms of the eigenvalues of the $\mathbf{S}$ operator s_l such that

$$\psi_l(r) \to \frac{i}{2}\left[h_l^-(kr) - s_l(k) h_l^+(kr)\right], \tag{37}$$

the latter form being particularly useful in the identification of resonant scattering properties.

C. Resonant scattering

Scattering resonances may be described qualitatively as the presence of a metastable bound state at energy E_R with an associated lifetime, in units of energy, Γ. Resonances manifest themselves as sharp peaks in the cross section, with a concomitant rise in the eigenphase sum by π with modulo π ambiguity.

Theoretically, resonances originate as the poles of the S-matrix when the scattering energy E is analytically continued into the complex plane. A branch exists along the positive real energy axis since $E = k^2/2m$ is a double-valued function of the momentum, the canonical variable. Resonances lie in the second (imaginary) sheet of the complex energy plane, whereas true bound states correspond to poles lying on the negative real energy axis. It must be understood that only poles lying near the branch along the positive real energy axis correspond to physically realisable resonant states.

Near an energetically isolated, well-defined resonance, the eigenphase shift consists of a slowly varying background part δ_{bg} and the sharply increasing resonant part δ_{res}, or

$$\delta(E) = \delta_{\text{bg}} + \delta_{\text{res}}. \tag{38}$$

The eigenphase shift of such a resonance is well-described in a Breit-Wigner distribution of a type

$$\delta(E) = \sum_{n=1} a_n (E - E_R)^{n-1} + \arctan\left[\frac{2(E - E_R)}{\Gamma}\right] \tag{39}$$

that allows the resonance parameters to be easily identified from a simple fit of the computed or experimental eigenphase shifts. Qualitatively, the resonant portion of the cross section is given by the Breit-Wigner formula

$$\sigma_l = \sin^2 \delta_l(E) = \frac{(\Gamma/2)^2}{(E - E_R)^2 + (\Gamma/2)^2}, \tag{40}$$

but computed and experimental resonant scattering peaks seldom allow the deployment of this formula.

D. Coulomb scattering

All previous discussion assumed a potential $V(r)$ of the scattering Hamiltonian $H = H_0 + V$ that tends to zero sufficiently rapidly as $r \to \infty$. The Coulomb potential $V(r) = Z_1 e Z_2 e / r$, however, falls very slowly at every radial distance and requires particular treatment. The following discussion is drawn from Baym (Baym, 1973).

The Schrödinger equation for pure Coulomb scattering is

$$\left[-\frac{\hbar^2}{2m}\nabla^2 - \frac{Z_1 Z_2 e^2}{r}\right] f(r) = E f(r) \tag{41}$$

that has exact solutions when transformed into parabolic cylindrical coordinates. If the z axis is coincident with $\mathbf{k}$, then the radial eigenfunctions are given in terms of the confluent hypergeometric function, or

$$f(r) = \Gamma(1+i\gamma)e^{-\pi\gamma/2}e^{ikz}{}_1F_1(-i\gamma, 1, ik(r-z)), \tag{42}$$

where $\gamma = -\frac{1}{a_0 k} = -\frac{mZ_1Z_2}{k}$ is the unitless strength parameter and a_0 the Bohr radius. The confluent hypergeometric function ${}_1F_1(a,b,x)$ has the power series expansion for small values of x

$$= 1 + \frac{ax}{b\cdot 1} + \frac{a(a+1)x^2}{b(b+1)\cdot 1\cdot 2} + \ldots$$

and the asymptotic expansion as $ix \to \infty$

$$\frac{e^{\frac{\pi}{2}\gamma}}{\Gamma(1+i\gamma)}\left[e^{i\gamma\log(ix)}\left(1 - \frac{\gamma^2}{x} + \ldots\right) + \frac{\Gamma(1+i\gamma)}{\Gamma(-i\gamma)}\frac{e^x}{x}e^{-i\gamma\log(-ix)}\right].$$

The Coulomb eigenfunctions have the partial wave expansion

$$f(r) = \frac{4\pi}{kr}\sum_{lm} i^l e^{i\eta_l} F_l(\gamma, kr) Y^*_{lm}(\hat{k}) Y_{lm}(\hat{r}), \tag{43}$$

where $F_l(\gamma, kr)$ represents the Coulomb function, which has the asymptotic value

$$\sin\left[kr - \gamma\ln 2kr - \frac{\pi l}{2} + \eta_l\right] \tag{44}$$

and

$$\eta_l = \arg\left[\Gamma(l+1+i\gamma)\right] \tag{45}$$

defines the Coulomb eigenphase shift.

The Coulomb S-matrix eigenvalues are exactly solvable, giving

$$e^{2i\eta_l} = \frac{\Gamma(l+1+i\gamma)}{\Gamma(l+1-i\gamma)}. \tag{46}$$

As $1/\Gamma(z)$ is analytic for all complex arguments z (the Gamma function has no roots for any z) and has simple poles at $z = 0, -1, -2, \ldots$, $\mathbf{S}$ has poles at every value for which $l+$

$1+i\gamma = 0, -1, -2, \ldots$, or $k = i/na_0$, where $n = l+1, l+2, \ldots$. For an attractive Coulomb potential, this implies

$$E = \frac{\hbar^2 k^2}{2m} = -\frac{me^4}{2\hbar^2 n^2},$$

the bound states of the nonrelativistic hydrogenic atom.

In the Lippmann-Schwinger formulation of pure Coulomb scattering, the necessary radial Green function is stated for reference (Newton, 1982)

$$\begin{aligned} & G^{+}(r,r') = i(-1)^l (4k^2 rr')^{l+1} e^{ik(\mathbf{r}+\mathbf{r}')} \frac{\Gamma(l+1+i\gamma)}{2k(2l+1)!} \\ & \times {}_1F_1(l+1+i\gamma, 2l+2, -2ikr_<) \\ & \times \Phi(l+1_i\gamma, 2l+2, -2ikr_>), \end{aligned} \tag{47}$$

where $\Phi(a,b,x)$ are the irregular confluent hypergeometric functions.

E. Variational principles for elastic scattering

The Schwinger variational method (Lucchese *et al.*, 1986) is a technique to render the T-matrix stationary with respect to small fluctuations of approximate expressions of the stationary scattering states $\psi^{\pm}$ using the Lippmann-Schwinger integral definitions. The derivation is straightforward: the T-matrix is defined

$$T = \begin{cases} \langle \phi \,| V |\, \psi^{+} \rangle \\ \langle \psi^{-} \,| V |\, \phi \rangle, \end{cases} \tag{48}$$

where ϕ are the solutions of the homogenous Hamiltonian H^0. Employing the Lippmann-Schwinger equation for $|\phi\rangle = |\psi^{+}\rangle - G_0^{+} V\,|\psi^{+}\rangle$, we arrive at the functional

$$\tilde{T} = \left\langle \phi \,| V |\, \psi^{+} \right\rangle + \left\langle \psi^{-} \,| V |\, \phi \right\rangle - \left\langle \psi^{-} \left| V - V G_0^{+} V \right| \psi^{+} \right\rangle, \tag{49}$$

which we will show is stationary with respect to first-order fluctuations in $\psi^{\pm}$. Accordingly,

$$\begin{aligned} \delta\tilde{T} &= \left[\langle\phi| + \left\langle \psi^{-}\right| V G_0^{-} - \left\langle \psi^{-}\right|\right] V \,|\delta\psi^{+}\rangle \\ &\quad + \left\langle \delta\psi^{-}\right| V \left[|\phi\rangle + G_0^{+} V\,|\psi^{+}\rangle - |\psi^{+}\rangle\right] \\ &= 0, \end{aligned}$$

where we have freely made use of several substitutions of $\psi^{\pm}$ based on the Lippmann-Schwinger equation and its Hermitian conjugate. Let $|\psi^{+}\rangle = \sum_i c_i\,|\chi_i\rangle$ and $\langle\psi^{-}\,| = \sum_j c_j^{*}\,\langle\chi_j\,|$ be basis-set expansions in χ of $\psi^{\pm}$. Inserting these definitions into the stationary T-matrix expression of Eq. 48 and treating the expansion coefficients as Lagrange multipliers $\partial\tilde{T}/\partial c_i = 0$ and $\partial\tilde{T}/\partial c_j^{*} = 0$, we arrive at the normalization-independent stationary T-matrix

$$T = \sum_i \frac{\langle\phi\,|V|\,\chi_i\rangle\,\langle\chi_i\,|V|\,\phi\rangle}{\langle\chi_i\,|V - VG_0^{+}V|\,\chi_i\rangle} \tag{50}$$

that we use as the basis for numerical computation of the transition amplitudes.

The normalization independent general transition matrix elements $\tilde{M}$ comparable to the form of Eq. 50 is given as

$$\tilde{M} = \sum_{ij} \frac{\langle R|u_i\rangle\,\langle v_j|S\rangle}{\langle v_i\,|1-K|\,u_j\rangle}, \tag{51}$$

where R and S satisfy Lippmann-Schwinger expressions

$$(1-K)\,|\psi\rangle = |S\rangle \tag{52}$$

$$\langle\chi|\,(1-K) = \langle R| \tag{53}$$

for solutions ψ and χ expanded in basis sets $|\psi\rangle = \sum_i a_i\,|u_i\rangle$ and $\langle\chi| = \sum_j b_j\,\langle v_j|$ for a given kernel K. The normalized expression $\tilde{M} = M_0$ serves as the first-order approximation to the general expression

$$M_c = M_0 - M_{\mathrm{err}} \tag{54}$$

that is solve by iterative techniques. Specifically, the error term has the Born series expansion

$$M_{\mathrm{err}} = \sum_{m=0} \langle\chi_0\,|(1-X)\,[(K+KTK)\,(1-X)]^{m}|\,\psi_0\rangle \tag{55}$$

where the kernel

$$K = G_0^{+}V \tag{56}$$

is the Green function and the interaction potential,

$$T_{ij} = \sum_{ij} \frac{|u_i\rangle\,\langle v_j|}{\langle v_i\,|1-K|\,u_j\rangle} \tag{57}$$

is the transition operator, and

$$X_{ij} = \sum_{ij} \frac{|u_i\rangle \langle v_j|}{\langle v_i | u_j \rangle} \tag{58}$$

is the overlap matrix between the basis set elements. The error estimate is computed through the $[N/N]$ Padé approximant correction of the form

$$M_N^{\mathrm{P}} = M_0 + \sum_{ij} \frac{\langle \chi_0 | 1 - X | u_i \rangle \langle v_j | 1 - X | \psi_0 \rangle}{\langle v_i | (1 - X) [1 - (K + KTK)(1 - X)] | u_i \rangle} \tag{59}$$

that greatly enhances the convergence of the iterations. Variational expressions of transition amplitudes other than the T-matrix are also available from generalized derivations of Eq. 51 (Lucchese *et al.*, 1986). In particular, variational expressions for the transition matrix elements of the dipole operator μ may be derived in a similar manner.

F. Variational solutions of the bound Schrödinger equation

One means of reducing a multielectron problem is to employ various approximation methods the describe the initial state as a product of one-electron functions. The Hartree-Fock equations are the variational solutions that minimize the energy of the Schrödinger equation in which the initial wave function is a configuration state function (CSF) composed of a single determinant of one-electron functions. Let

$$\Psi = \left| \chi_1 \chi_2 \ldots \chi_i \chi_j \ldots \chi_N \right| \tag{60}$$

represent the N-electron single-determinant wave function composed of an antisymmetrized product of one-electron spin orbitals

$$\chi_i = \begin{cases} \phi_i \alpha \\ \phi_i \beta \end{cases} \tag{61}$$

composed of spatial orbitals ϕ and spin functions α and β. The Hartree-Fock equations are based on the variational principle that the Hartree-Fock orbitals are those that render the functional

$$\langle \delta\Psi | H - E | \Psi \rangle = 0 \tag{62}$$

stationary, where

$$H = \sum_{i}^{N} h_i + \sum_{ij}^{N} \frac{1}{|r_i - r_j|} \tag{63}$$

is the electronic molecular Hamiltonian with one-electron operator

$$h_i = -\frac{1}{2}\nabla_i^2 - \sum_{\gamma=1}^{M} \frac{Z_\gamma}{|r_i - R_\gamma|}, \tag{64}$$

and

$$\delta\Psi_i = |\chi_1\chi_2 \ldots \delta\phi_i\chi_j \ldots \chi_N| \tag{65}$$

represents the variation over the i^{th} spin orbital. Taking the variation over all N spin orbitals and making use of the Slater-Condon rules for matrix elements over one- and two-electron operators, the resulting stationary expression for the i^{th} spin orbital of spatial coordinate r_1 is

$$\left[h_i(r_1) + \sum_{j=1}^{N} J_j(r_1) - K_j(r_1) \right] \chi_i(r_1) = \varepsilon_i \chi_i(r_1), \tag{66}$$

where J_i and K_i are the usual Coulomb and exchange operators and ε_i the energy of the i^{th} spin orbital. Multiplying on the left by α^* and integrating over the spin coordinate results in the Hartree-Fock equations

$$\left[h_a(r_1) + \sum_{b=1}^{n_{\text{occ}}} 2J_b(r_1) - K_b(r_1) \right] \phi_a(r_1) = \varepsilon_a \phi_a(r_1), \tag{67}$$

where

$$H_a^{\text{HF}} = h_a + \sum_{b=1}^{n_{\text{occ}}} 2J_b(r_1) - K_b(r_1) \tag{68}$$

is the one-electron Hartree-Fock operator of the a^{th} occupied orbital.

G. Variational solutions of the continuum Schrödinger equation

Most scattering calculations involving molecules employ two fundamental approximations about the nature of the interaction event that greatly simplify the resulting equations (Gianturco and Jain, 1986; Lane, 1980). The first is the *Born-Oppenheimer approximation*, which, as in the case in molecular structure theory, assumes that the complete Hamiltonian is separable in terms of a sum of electronic and nuclear coordinates. The eigenfunctions are then a product of a nuclear wave function that may be solved classically and an electronic wave function that depends only parametrically on the positions of the nuclei. The starting point for most calculations, therefore, makes use of the continuum three-dimensional Schrödinger equation, in atomic units,

$$(H_n + H_M - E)\Psi = 0, \tag{69}$$

where

$$H_n = \sum_{i=1}^{n} -\frac{1}{2}\nabla_i^2 - \sum_{\alpha}^{M} \frac{Z_\alpha}{|r_i - R_\alpha|} + \sum_{i<j}^{n} \frac{1}{|r_i - r_j|} \tag{70}$$

is the Hamiltonian of the n occupied orbitals, and

$$H_M = -\sum_{\alpha=1}^{M} \frac{1}{2M_\alpha}\nabla_\alpha^2 + \sum_{\alpha<\beta}^{M} \frac{Z_\alpha Z_\beta}{|R_\alpha - R_\beta|} \tag{71}$$

the Hamiltonian of the M nuclei. The other fundamental approximation in molecular scattering is the *fixed-nuclei approximation*, which states that the nuclear coordinates remain fixed during the scattering event and reduces the scattering equation only to the product of the continuum wave function with the bound electrons of target. Thus, only the electronic Hamiltonian need be considered for the electron-molecule system.

Within these approximations, the continuum Hartree-Fock equations can be constructed in much the same manner as for the bound state. Let

$$\Psi_k = |\phi_1\alpha\phi_1\beta\ldots\phi_n\alpha\phi_n\beta\phi_k\alpha| \tag{72}$$

be the single determinant wave function of the $N+1$ electron target with continuum (spatial) orbital ϕ_k. The stationary condition of the Schrödinger equation is simply

$$\langle\delta\Psi_k|H - E|\Psi_k\rangle = 0, \tag{73}$$

where H has the same form as Eq. 70. In general, neither ϕ_k nor the variation $\delta\phi_k$ are orthogonal to the ϕ_n occupied orbitals or to each other. Orthogonality of the continuum orbital to all bound orbitals is enforced through the use of the projection operator

$$P + \sum_{i=1}^{n_{\text{occ}}} |\phi_i\rangle\langle\phi_i| = 1 \tag{74}$$

such that

$$|P\phi_k\rangle + \sum_{i=1}^{n_{\text{occ}}} |\phi_i\rangle \langle\phi_i|\phi_k\rangle \tag{75}$$

$$\langle P\phi_k| + \sum_{i=1}^{n_{\text{occ}}} \langle\phi_k|\phi_i\rangle \langle\phi_i| \, , \tag{76}$$

and similarly for $\delta\phi_k$. Taking the variation $\delta\Psi_k$ over all possible orbitals ϕ_k and making use of Slater-Condon rules as mentioned previously results in the *static-exchange approximation* (SE) of the continuum orbital

$$\left\langle P\delta\phi_k \left| H^{\text{HF}} - (E - E^{\text{HF}}) \right| P\phi_k \right\rangle = 0, \tag{77}$$

where E^{HF} is the SCF energy of the Hartree-Fock wave function.

As a single-channel method, the SE approximation notably lacks an adequate description of inelastic processes or the response of the target orbitals in the presence of the continuum electron. Consequently, the approach that we have taken uses optical potentials that are appended to the form V_{SE} of Eq. 77 (Klonover and Kaldor, 1978; Padial and Norcross, 1984) to incorporate target polarization. Historically, model potentials have approximated the computationally difficult nonlocal exchange interaction of Eq. 77 (Gianturco *et al.*, 1987; Hara, 1967). With the improvements in computing technology, these model exchange potentials have in the strict sense of reducing the complexity of the scattering equations become obsolete; however, they retain value particularly in the calculation of one-electron resonances in a Siegert eigenstate formalism, as discussed in Lucchese and Gianturco, 1996.

In the current implementation of the scattering calculation, we make use of an optical potential that smoothly joins DFT expressions for the dynamic electron (Perdew and Zunger, 1981) or positron (Boroński and Nieminen, 1986) correlation with the target electron density with the asymptotic $\sim \alpha/2r^4$ static polarizability derived from second-order perturbation theory. Because the two interactions generally do not intersect at any radial distance from the center of expansion r, the two functions are smoothly joined at a radial distance r_{match}. We will detail the use of this approximation in the upcoming sections.

H. Numerical solutions of the scattering equations

Numerous numerical solution methods have been developed to solve the close-coupling scattering equations as presented in Eq. 77. For all current projects, we employ the single-center expansion method (Gianturco and Jain, 1986), which expands all three-dimensional functions $F(\mathbf{r})$ in terms of symmetry-adapted angular functions and radial functions represented on a numerical grid. The expansion takes the form

$$F^{p\mu}(\mathbf{r}) = \sum_{lh}(1/r)f_{lh}^{p\mu}(r)X_{lh}^{p\mu}(\theta,\phi), \tag{78}$$

where lh are the symmetry-adapted lm, and $p\mu$ label the components of the irreducible representation (IR) of the expanded function. The angular functions $X_{lh}^{p\mu}$ are linear combinations of the spherical harmonics that transform as the $p\mu$ IR of the point group of the target. Once the wave functions of the target orbitals and the continuum electron have been expanded by Eq. 78, the three-dimensional scattering equation Eq. 77 reduces to a radial equation

$$\left[\frac{1}{2}\frac{d^2}{dr^2} + (E - \varepsilon_\alpha)\right]\psi_{lh\alpha}(r) = \sum_{l'h'\beta}\int_0^\infty dr' V_{lh\alpha,l'h'\beta}(r',r)\psi_{l'h'\beta}(r'). \tag{79}$$

Within the state-exchange approximation, the close-coupling expansion on the right side of Eq. 79 is truncated to a single state $\beta = 1$ and the interaction potential $V_{lh\alpha,l'h'\beta}(r,r')$ reduces to that of Eq. 77 and any optional optical potentials. The scattering equations transformed into the Lippmann-Schwinger integral formulation are solved by means of the iterative Schwinger variational technique with Padé approximant corrections described briefly in Sec. I.G and in detail in (Lucchese *et al.*, 1982).

I. Other scattering methods

In addition to the solution methods detailed in the rest of the report, other center expansion methods are currently under development. Here, we shall survey those methods that have been particularly useful in obtaining scattering and photoionization properties for polyatomic molecules.

1. R-Matrix Methods: The *R*-matrix methods (Burke and Berrington, 1993; Tennyson, 2010) have at their basis the division of the configuration space about the target into an inner region, which contains the $N+1$ wave function of the target and continuum electron, and an outer region containing only the wave function of the propagating electron. Within the inner region $r < b$ where exchange effects are important, the scattering Hamiltonian is diagonalized in the basis of the $N+1$ electron configuration interaction wave function. In the asymptotic region $r > a$, the scattering wave function perturbation theory. At a matching radial distance $r = a$ the radial continuum wave function and its first derivative are linked by the matrix R, from which all properties of the scattering event may be derived. The *R*-matrix methods constitute perhaps the most rigorous of the current scattering theories as it contains no optical models and provide a benchmark on calculations performed with a less formal theoretical framework.

2. Variational Methods: These methods derive from formulations of the nonrelativistic scattering equations given in either the integral or differential form that are stationary with respect to small perturbations in the given trial wave function. This allows scattering properties derived from the variational expression to be independent of the normalization of the approximate wave function (Newton, 1982). Two noteworthy variational formulations of the scattering equations include the Schwinger variational method (Lucchese *et al.*, 1986) and the related complex Kohn variational method (Lengsfield and Rescigno, 1991).

   The Schwinger variational expressions have been derived in Sec. I.E and form the basis for the numerical solution of the molecular Schrödinger equation that we use in all subsequent projects. The complex Kohn variational method solves for T-matrix elements through an alternative stationary expression

$$T = -2\left[\int dr' f_l L f_l - \mathbf{s}\mathbf{M}^{-1}\mathbf{s}\right], \tag{80}$$

in which f_l and g_l are the regular and irregular asymptotic radial solutions of a trial wave function of the form

$$u_l = f_l(r) + \lambda g_l(r) + \sum_i^n c_i \phi_i, \tag{81}$$

ϕ_i are a set of square integrable (L^2) scattering basis functions, and L is the partial wave radial Schrödinger equation. The variational parameters of Eq. 80 are minimized to compute the T-matrix elements. Both methods lend themselves readily to multichannel adaptation (Huo, 1995b; Rescigno *et al.*, 1995b) and admit accurate computation of electron scattering and photoionization observables from complex molecular targets.

J. Molecular photoionization

In photoionization, the scattering properties are obtained from the transition matrix elements $I_{fi\hat{k}}$ that are derived from first-order time-dependent perturbation theory

$$I = \left\langle \Psi_i \left| \sum_{j=1}^{N} \exp\left(i\frac{\omega}{c}\hat{s}\cdot\mathbf{r}_j\right)\hat{n}\cdot\nabla_{r_j} \right| \Psi_{f\hat{k}}^{(-)} \right\rangle, \tag{82}$$

where Ψ_i is the initial state and $\Psi_{f\{k}^{(-)}$ the final state consisting of the ionized target and photoelectron with asymptotic momentum $\hat{k}$. The transition operator

$$\sum_{j=1}^{N} \exp\left(-i\frac{\omega}{c}\hat{s}\cdot\mathbf{r}_j\right)\hat{n}\cdot\nabla_{r_j} \tag{83}$$

is easily derived from the quantized Hamiltonian of the nonrelativistic electromagnetic field $H = \frac{1}{2m}\left[\frac{\hbar}{i}\nabla + \frac{e}{c}\mathbf{A}\right]^2 - e\phi$, where $\mathbf{A}$ and ϕ are the vector and scalar field potentials as usual. For photons of low kinetic energy, the exponential term may be expanded in the series

$$\exp\left(-i\frac{\omega}{c}\hat{s}\cdot\mathbf{r}\right) = 1 - \frac{\omega}{c}\hat{s}\cdot\mathbf{r} + \ldots \tag{84}$$

If only the first term of the expansion is retained, then the transition matrix elements are computed within the *dipole approximation*

$$I_{if}^{\mathrm{V}} = k^{1/2}\left\langle \Psi_i \left| \sum_j \hat{n}\cdot\nabla_{r_j} \right| \Psi_{fk}^{(-)} \right\rangle. \tag{85}$$

In Eq. 85 the transition matrix elements are distinguished with respect to the gauge, *viz.* representation of the dipole operator, which in this case is the velocity gauge. The fully equivalent length gauge is given by simply

$$I_{if}^{\mathrm{L}} = \frac{k^{1/2}}{E} \left\langle \Psi_i \middle| \sum_j \hat{n} \cdot \mathbf{r}_j \middle| \Psi_{f,\hat{k}}^{(-)} \right\rangle. \tag{86}$$

The differential cross section for photoionization are then given in either gauge as

$$\frac{d\sigma^{\mathrm{L,V}}}{d\Omega} = \frac{4\pi^2}{cE} \left| T_{if}^{\mathrm{L,V}} \right|^2. \tag{87}$$

One particular gauge, the so-called mixed gauge

$$\frac{d\sigma^{\mathrm{M}}}{d\Omega} = \frac{4\pi^2}{cE} \Re \left[\left| T_{if}^{\mathrm{M}} \right|^* T_{if}^{\mathrm{V}} \right], \tag{88}$$

is especially useful in that Eq. 88 satisfies the Thomas-Reiche-Kuhn sum rule, which relates the total number of electrons of the target with the sum over the oscillator strengths of the bound electrons and the integral over continuum oscillator strengths

$$N = \int_{E_0}^{\infty} \frac{df_{if}}{dE} dE + \sum_k f_{ik}, \tag{89}$$

where the oscillator strength is defined in terms of the photoionization cross section

$$\frac{df_{if}}{dE} = \frac{c}{2\pi^2} \sigma_{if}. \tag{90}$$

K. Photoelectron angular distributions

Early experimental angular distributions did not resolve the orientation of the target molecule with respect to the direction of the light at the moment of photoionization (Dill, 1976). Consequently, the measured angular distribution measured partially integrated cross sections over the unobserved coordinate. The integrated target angular distributions (ITAD) measured the photoelectron angular distribution $\theta_{\mathbf{k}}$ with respect to the light polarization vector over all orientations of the molecule

$$\frac{d\sigma}{d\Omega} = \frac{\sigma}{4\pi} \left[1 + \beta_{\mathbf{k}} P_2 \left(\cos\theta_{\mathbf{k}} \right) \right], \tag{91}$$

where the asymmetry parameter $\beta_{\mathbf{k}}$ can be expressed algebraically in terms of the transition matrix elements (in partial wave components) (Natalense and Lucchese, 1999)

$$\begin{aligned}\beta_{\mathbf{k}} = \frac{3}{5}\frac{1}{\left|I_{lm\mu}\right|^2} & \sum_{lm\mu,l'm'\mu',M} (-1)^{m-\mu'} \left[(2l+1)(2l'+1)\right]^{\frac{1}{2}} \\ & \times I_{lm\mu} I^*_{l'm'\mu'} \\ & \times \langle 1100|20\rangle \left\langle ll'00\right\rangle \\ & \times \left\langle 11-\mu\mu'|2M\right\rangle \left\langle ll'-mm'|2-M\right\rangle . \end{aligned} \tag{92}$$

The asymmetry parameter bears a range $-1 \leq \beta_{\mathbf{k}} \leq 2$, in which a value $\beta_{\mathbf{k}} = 2$ implies ionization with the continuum electron aligned parallel with respect to the light polarization and $\beta_{\mathbf{k}} = -1$ a perpendicular transition. The integrated detector angular distribution (IDAD), which measures a fixed angle $\theta_{\mathbf{n}}$ between the orientation of the target and the light polarization over all directions of the photoelectron. In this case the angular distributions take a similar form as the ITAD (Wallace and Dill, 1978a),

$$\frac{d\sigma}{d\Omega} = \frac{\sigma}{4\pi}\left[1 + \beta_{\mathbf{n}} P_2(\cos\theta_{\mathbf{n}})\right], \tag{93}$$

where $-1 \leq \beta_{\mathbf{n}} \leq 2$, a value $\beta_{\mathbf{n}} = 2$ corresponds to excitations with the dipole operator parallel to the molecular axis and $\beta_{\mathbf{n}} = -1$ excitations in the perpendicular direction.

The most general description of photoelectron angular distributions relates the direction of photoelectron momentum (θ_k, ϕ_k) with the light polarization (θ_n, ϕ_n) at the moment of photon impact (Dill *et al.*, 1976). These angular distributions can be analyzed in a spherical harmonic expansion (Lucchese, 2004)

$$\frac{d\sigma}{d\Omega} = \sum_{L'} \sum_{M'=-L'}^{L} \sum_{L=0}^{2} \sum_{M=-L}^{L} A_{L'M',LM} Y_{L'M'}(\hat{k}) Y^*_{LMN}(\hat{n}), \tag{94}$$

where the expansion coefficients $A_{L'M',LM}$ involve a product squared of the dipole transition elements

$$\begin{aligned} A_{L'M',LM} = \frac{4\pi^2}{cE} & \sum_{lm\mu,l'm'\mu'} I_{lm\mu} I^*_{l'm'\mu'} (-1)^{m+\mu'} \\ & \left[\frac{(2l+1)(2l'+1)}{(2L+1)(2L'+1)}\right]^{1/2} \\ & \times \left\langle ll'00|L'0\right\rangle \left\langle ll',-mm'|L'M'\right\rangle \\ & \times \langle 1100|L0\rangle \langle 11,\mu,-\mu|LM\rangle . \end{aligned} \tag{95}$$

The total photoionization cross section is then simply the modulus square of the dipole transition elements

$$\sigma = \frac{4\pi^2}{3cE} \sum_{lm\mu} \left| I_{lm\mu} \right|^2 . \tag{96}$$

In a photodissociation coincidence experiment, the momentum vectors of the ionic fragment and the photoelectron with respect to the light polarization are measured in coincidence, allowing the prediction of the molecular-frame angular distribution (MFPAD) (Dill, 1976). For polyatomic molecules, the absolute orientation of the molecule with respect to the recoil vector is not known and only the recoil momentum can be detected. If we assume that the lifetime of the cation is sufficiently short with respect to its rotatational period, then the recoil axis and the molecular axis are coincident in the *axial recoil approximation*. In this case, the coincidence experiment measures the recoil-frame angular distribution (RFPAD), which has the form (Lucchese, 2004)

$$\begin{aligned} I(\theta_k, \phi_k, \theta_n, \phi_n) &= F_{00}(\theta_k) + F_{20}(\theta_k) P_{20}(\cos\theta_n) \\ &+ F_{21}(\theta_k) P_{21}(\cos\theta_n) \cos(\phi_k - \phi_n) \\ &+ F_{22}(\theta_n) P_{22}(\cos\theta_n) \cos\left[2(\phi_k - \phi_n)\right], \end{aligned} \tag{97}$$

where the F_{LN} functions are defined in expansions of associated Legendre polynomials in the given reference.

L. Variational solution of the photoionization equation

As in the case of elastic electron scattering described Sec. I.G, in photoionization the adiabatic approximation is used to separate of the initial and final states in terms of target and continuum wave functions that depend on the electron coordinates and parametrically on the nuclear coordinates. The target and continuum orbitals may be represented by a number of different levels of theory (Lucchese, 2002); for the photoionization computations of the present report, the initial orbitals are represented at the closed-shell Hartree-Fock (single-determinant) level, and the ionized $N-1$-electron target + continuum electron state is represented by the wave function

$$\Psi_k = \frac{1}{2}^{1/2} \left[|\phi_1 \alpha \phi_2 \beta \ldots \phi_n \alpha \phi_k \beta| + |\phi_1 \alpha \phi_2 \beta \ldots \phi_n \beta \phi_k \alpha| \right], \tag{98}$$

in which the continuum electron has been ionized from the n^{th} occupied orbital. The stationary condition of the Schrödinger equation for the continuum orbital is given by

$$\langle \delta \Psi_k | H - E | \Psi_k \rangle = 0. \tag{99}$$

Unlike the case for electron scattering, the orthogonality of the continuum orbital ϕ_k to the closed-shell ϕ_n orbitals may not be assumed, since ϕ_k is an eigenfunction of the continuum Coulomb Hamiltonian, with a free-particle partial wave expansion

$$\phi_k(\mathbf{r}) = \sum_{lm} \frac{1}{r} F_l(\gamma, kr) Y_{lm}(\hat{r}) \tag{100}$$

where $F_l(\gamma, kr)$ are the regular Coulomb functions. Inserting Eq. 98 into 99, making use of the projection operators Eq. 74 and 76, and taking variations over all ϕ_k and $P\phi_k$, after some algebra, we arrive at the Hartree-Fock equations of the continuum orbital and its projection

$$\begin{aligned} 0 =& \langle P \delta \phi_k | \bar{H} - \bar{E} | P \phi_k \rangle \\ &+ 2 \langle \delta \phi_k | \phi_n \rangle \langle \phi_n | \bar{H} - K_n - \bar{E} | \phi_n \rangle \langle \phi_n | \phi_k \rangle \\ &+ 2 \langle \delta \phi_k | \phi_n \rangle \langle \phi_n | \bar{H} - K_n | P \phi_k \rangle \\ &+ 2 \langle P \delta \phi_k | \bar{H} - K_n | \phi_n \rangle \langle \phi_n | \phi_k \rangle, \end{aligned} \tag{101}$$

where

$$\bar{H} = \sum_i h_i + \sum_{j=1}^{n-1} 2J_j - K_j + J_n + K_n \tag{102}$$

is the frozen-core Hartree-Fock (FCHF) Hamiltonian and

$$\bar{E} = E - (E^{\text{HF}} - \varepsilon_n) \tag{103}$$

the FCHF energy. Since the target orbitals are not assumed to have relaxed after the collision, ϕ_n remains an eigenfunction of H^{HF}; thus, Eq. 101 is simplified to

$$0 = \langle P \delta \phi_k | \bar{H} - \bar{E} | P \phi_k \rangle + 2(\varepsilon_n - \bar{E}) \langle \delta \phi_k | \phi_n \rangle \langle \phi_n | \phi_k \rangle, \tag{104}$$

which can be further approximated still by assuming that $P\delta\phi_k$ is orthogonal to the orbital from which it is ionized. In this case, we result in the frozen-core Hartree-Fock approximation

$$0 = \langle P\delta\phi_k | \bar{H} - \bar{E} | P\phi_k \rangle , \tag{105}$$

which is distinguished from the variational solutions of the static exchange operator by the form of the continuum wave function and the presence of extra repulsion operators in the effective Hamiltonian.

The Lippmann-Schwinger equation that enforces the orthogonality of the continuum electron to all bound orbitals can be constructed from a suitable pseudopotential that recovers the differential equation for ϕ_k in the form given in Eq. 101, namely

$$(1-Q)L(1-Q)\,|\phi_k\rangle = 0, \tag{106}$$

where

$$Q = 1 - P = \sum_{i=1}^{n_{\mathrm{occ}}} |\phi_i\rangle\,\langle\phi_i| \tag{107}$$

and

$$L = -\frac{1}{2}\nabla^2 + V - \bar{E}. \tag{108}$$

The Lippmann-Schwinger equation is

$$|\phi_k^-\rangle = |\phi_k^0\rangle + G_0^- V_Q\,|\phi_k\rangle , \tag{109}$$

where ϕ_k^0 is the free-particle Coulomb eigenfunction, G_0^- the free-particle Coulomb Green function for an outgoing plane wave, and

$$V_Q = V - LQ - QL + QLQ \tag{110}$$

the Phillips-Kleinman pseudopotential.

As a single-configuration method, the FCHF approximation is unsuited to describe scattering from multiconfigurational initial or target states. Furthermore, the FCHF approximation neglects important effects such as polarization of the target molecule by the photoelectron or the opening of closed channels through dipole forbidden excitations.

Multichannel effects may be taken into account through close-coupling expansion of the final ion pseudostates, either by retaining the Hartree-Fock description of the initial state and frozen-core representations of each ion state (multichannel Hartree-Fock (Basden and Lucchese, 1988)), or through a multireference configuration-interaction expansion of the target orbitals and complete active space SCF (CASSCF) descriptions of the resulting ion states (multichannel CI (Stratmann and Lucchese, 1995)). An alternative method that we employ in Cl 1s and Cl 2p photoionization of C_2H_5Cl and the full valence photoionization of CH_3NO_2 to recover correlation and polarization lies in the incorporation of a local, energy-dependent optical potential (Perdew and Zunger, 1981) of the form described in Sec. I.G to the FCHF equations. As the a one-electron method, the FCHF approximation cannot recover essentially two-electron processes such as the relaxation of the ion state.

M. Overview of current projects

1. Electron scattering of pyridine and pyrimidine

Low-energy collisions of electrons with gas- and condensed-phase biomolecules have been an intense focus of experimental research for some time (Sanche, 2005). The computational treatment of scattering from biomolecules entails difficulties on account of the low structural symmetry and large number of target electrons. Consequently, tractable analogues (Bouchiha *et al.*, 2006; De Oliveira *et al.*, 2010; Khakoo *et al.*, 2010; Winstead and McKoy, 2007a) have been sought to recover the scattering dynamics of the larger biomolecules at the fraction of computational cost. To this end, we have computed integrated total and partial elastic scattering cross sections of low-energy (0.5-20 eV) electrons from *N*-heterocyclic aromatic hydrocarbons pyridine and pyrimidine as computationally tractable analogues of the the nucleotide bases. In particular, pyridine comprises the active site of nicotinamide adenine dinucleotide (NAD) and pyrimidine the DNA nucleotide bases thymine and cytosine, and the RNA base uracil.

2. *Low-energy electron scattering resonance dynamics of cis-diamminedichloroplatinum*

The platinum-based inorganic complex known under the clinical trial name as cisplatin (*cis*-diamminedichloroplatinum(II)), $[\mathrm{Pt(NH_3)_2Cl_2}]$ (CDDP) has been used in chemotherapeutic treatment of genitourinary and small tissue-lung cancers since its fortuitous discovery nearly fifty years ago (Rosenberg *et al.*, 1965, 1969). On account of its well-investigated toxicity and cellular resistance (Giaccone, 2000; Judson and Kelland, 2000; Kelland, 2000), second-generation platinum-based complexes have been developed. Unfortunately, only a few of these compounds have found therapeutic use, mostly against the same array of tumors as the parent compound (Lebwohl and Canetta, 1998). While the exact mechanism for the cellular activation of cisplatin remains under investigation, it is assumed (Jamieson and Lippard, 1999) that cisplatin enters the cell through passive diffusion, loses one or both chlorine atoms through hydrolysis, then binds with the nitrogen of adenine or guanine forming an adduct that induces cytolysis. The cytogenic properties of cisplatin is greatly enhanced when chemotherapy is combined with radiation therapy (Howe *et al.*, 2001). This property is believed to be due to the generation of low energy electrons from the radiation that subsequently cause DNA strand cleavage directly, or otherwise interact with the cisplatin to form temporary negative ions that increase its binding ability (Zheng *et al.*, 2008). One group has proposed a novel means of (gas-phase) cisplatin activation through collision with a low-energy electron (Kopyra *et al.*, 2009) that causes the molecule to lose both chlorine ligands in the reaction. We have obtained the electron attachment dynamics of gas-phase CDDP using a model potential and find that the resonant energy is in qualitative agreement with electron binding energy found in Kopyra *et al.*, 2009.

3. *Application of the multichannel Schwinger variational method to electron scattering from* $\mathrm{Cl_2}$ *and* Pt

One question that arises in electron scattering from the cisplatin molecule is this: to what extent does the CDDP scattering cross section stem from the platinum atom alone within an inhomogeneous molecular field induced by the ligand species? Because the Pt atom is found in a ^3D ground state, and possesses manifold low-energy excited states (Smirnov, 2004), the relevant scattering properties of the ground state species may not be reasonably derived within the single-determinant based static-exchange approximation. Accordingly, the multichannel complete active space configuration-interaction (MCCI) method of Stratmann and Lucchese (Stratmann and Lucchese, 1995) has been adapted for electron scattering and applied for low energy scattering from the constituent moieties of the CDDP molecule Cl_2 and platinum atom. This method provides a theoretically sound means of recovering multichannel scattering effects and correlation due to the mixing of the scattering channels. The results of this preliminary investigation, however, show that further modification will be necessary to include the important polarization interaction that is poorly recovered in close-coupling based scattering methods (Rescigno *et al.*, 1995a).

4. Photoionization of CH_3Cl *and* C_2H_5Cl*: Molecular frame angular distributions near the* C 1s *and* Cl 2p *ionization thresholds*

Numerous measured photoelectron and total photoabsorption cross sections of CH_3Cl have been available for some time for photon impact with the chloroalkanes (Hitchcock and Mancini, 1994). More recently, valence shell photoionization cross sections and MF-PADs have been computed using the semiempirical continuum multiscattering (CMS) $X\alpha$ method (Downie and Powis, 1999a,b; Hikosaka *et al.*, 2001; Powis, 1997). By contrast, photoelectron and photoabsorption spectra of C_2H_5Cl are comparatively scarce (Fan and Leung, 2002), and, to the best of our knowledge, no photoionization cross sections or photoelectron angular distributions have been published for this species. We have calculated integrated and molecular frame photoionization differential cross sections between 0.5 eV and 5.0 eV above the C 1s and Cl 2p ionization thresholds of the organohalides CH_3Cl (Lucchese *et al.*, 2009) and C_2H_5Cl within the FCHF approximation. Comparison with unpublished experiment (Elkharrat, 2009) shows that the theory recovers the angular distributions of photoelectrons ejected in the primary C-Cl fragmentation channel well.

5. Valence photoionization of nitromethane, CH_3NO_2

The electronic spectrum of the smallest nitroalkane, nitromethane, have been investigated extensively (Kilic *et al.*, 1997), yet there have been no known experimental or computational angular distributions published for this molecule. Initial recoil frame angular distributions have been recorded by Vredenborg *et al.* (Vredenborg *et al.*, 2011), and indicates that photoelectron intensity is directed preferentially towards the CH_3 moiety after the primary C-N bond dissociation. We have computed valence-shell photoionization cross sections for nitromethane for photoelectron energies up to 20 eV above the respective ionization thresholds and computed RFPADs for photoelectrons of kinetic energy 0.5 eV and 5.0 eV. Our calculations show a similar propensity for electron intensity along the C-N bond from a higher-valence molecular orbital than that proposed in Vredenborg *et al.*, 2011.

6. Positron scattering from C_{20}

Fullerenes, an allotrope of carbon consisting of a closed hollow network of carbon atoms, have generated intense experimental interest ever since the fortuitous discovery by Kroto and collaborators over thirty years ago (Kroto *et al.*, 1985). Relevant previous computational research includes determining the minimum energy geometries of the smaller ($N < 60$) fullerenes, including the smallest proposed fullerene, C_{20}, that is presumed to exist (Kroto, 1987). Another interest in fullerene physics lies in the interaction of fullerenes with low-energy electrons and positrons (Gianturco *et al.*, 1998). To this end, we have computed total and partial integrated cross sections for low-energy positron scattering by C_{20} in two low-symmetry structural isomers. We also locate hypothetical positron resonances, particularly those whose probability densities are located within the carbon framework.

II. ELASTIC SCATTERING CROSS SECTIONS AND ONE-ELECTRON RESONANCES OF PYRIDINE AND PYRIMIDINE

A. Introduction

Perhaps the most remarkable feature of low-energy scattering phenomena is the resonance, which manifests itself by the presence of large variations in the scattering cross section (Taylor, 1972). Qualitatively, resonant scattering may be described as the creation of a nearly-bound state of the impinging electron within the target-projectile system, with a resonance energy E_R and width Γ, which is inversely proportional to the lifetime of the resonant state. Differing formation and decay processes lead to the characterization of resonances as shape resonances, Feshbach resonances, or core excitation resonances of the neutral target (Schulz, 1973a). Resonance identification and classification in electron scattering from molecular targets has long been an established area of experimental and theoretical study and has been the subject of a number of comprehensive reviews (Gianturco and Jain, 1986; Lane, 1980; Schulz, 1973b).

In the present study of electron molecule interactions we will only consider elastic collisions with gas-phase targets. Additionally, we make several assumptions about the system to further reduce computational difficulty. Among the most vital of these is the fixed-nuclei approximation, which assumes that electronic and nuclear motion are decoupled during the scattering event. Another approximation widely used in scattering theory treats the correlation of the wave function of the bound electrons in the presence of the continuum electron through selection of virtual orbitals that capture relevant excitations of the temporary anionic state (Winstead *et al.*, 2005) or through various one-electron model potentials (Gianturco *et al.*, 1987; Klonover and Kaldor, 1977). In the latter approach used here, a single-particle description of electron correlation and polarization cannot account for all of the features of experimental (quasi)elastic cross sections or, particularly, the enhancement or diminution of elastic shape resonances that mix with inelastic channels.

This issue has become significant in recent theoretical investigations of resonance formation in low-energy electron scattering from the pyrimidine nucleotide bases (Winstead *et al.*, 2007). Burrow (Burrow, 2005) has argued that the assignments of the π^* resonances in a 2004 computational study by Gianturco and Lucchese (Gianturco and Lucchese, 2004) on the resonant precursors to the dissociation of uracil must be empirically shifted to yield quantitative results. Similarly, in a comment by Winstead and McKoy (Winstead and McKoy, 2008) on resonant scattering from uracil by Gianturco and collaborators (Gianturco *et al.*, 2008), they suggest that the large ($\sim$ 3 D) dipole moment of uracil may have introduced a numerical artifact that impeded correct assignment of uracil π^* resonances. To consider wider applicability of the one-electron model potentials we consider here other smaller but nontrivial analogues to these complex targets.

For this purpose, we investigate the shape resonances of the azabenzenes pyridine and pyrimidine. Azabenzenes are a class of 6-membered heterocyclic aromatic molecules in which one or more N moieties replace the CH fragments within the carbon ring. Pyridine (C_5H_5N) is the simplest azabenzene; pyrimidine (1,3-diazine, $C_4H_4N_2$) comprises one of the three diazabenzenes. These molecules play a large role in chemistry and molecular physics – pyridine is the active site of the electron transporter nicotinamide adenine dinucleotide (NAD) (Boese and Martin, 2004) and serves as a substrate in surface science owing to its well-investigated enhanced Raman scattering on etched metal surfaces (Chang and Furtak, 1982); pyrimidine, the backbone for the nucleotides thymine, cytosine, and uracil, forms the basis of modern drug synthesis (Boese and Martin, 2004). Because of the small size and relatively high ground electronic state symmetry of C_{2v}, the azabenzene series can be regarded as computationally tractable analogues of their larger and less symmetrical biological counterparts. At the same time, they stand as worthwhile molecular targets in their own right, since the inclusion of one or more perturbing nitrogen atoms admits a systematic study of the reduction of symmetry in scattering of the 6-membered aromatic hydrocarbons from benzene (D_{6h}) through lower-symmetry $1,\ldots,4-N$ heterocycles to the planar (C_s) or nonsymmetrical (C_1) nucleotides of current experimental interest (Sanche, 2005).

The approach we consider for the present report has been undertaken in the investigation of tetrahydrofuran (C_4H_8O, THF), which has been treated as an analogue to the deoxyribose monophosphate backbone of DNA and the furanose sugars of other nucleotide bases in low energy integral (Mozejko *et al.*, 2006; Zecca *et al.*, 2005) and differential (Allan, 2007; Colyer *et al.*, 2007; Dampc *et al.*, 2007) electron scattering experiments. In contrast to the present investigation, a number of theoretical results using a variety of high-level computational methods have been produced for THF. Bouchiha *et al.* computed elastic and inelastic (electronic excitation) scattering cross sections for THF using the *R*-matrix method (Bouchiha *et al.*, 2006). Trevisan *et al.* (Trevisan *et al.*, 2006) computed elastic differential and momentum transfer cross sections by the complex Kohn variational method. Using the *R*-matrix method, Tonzani and Greene (Tonzani and Greene, 2006a) calculated THF and phosphoric acid cross sections as approximants for the DNA backbone monomers. Their results were also compared to the hydrocarbon parent molecule cyclopentane. Winstead and McKoy (Winstead and Mckoy, 2006) compared THF to the biologically relevant species deoxyribose and deoxyribose monophosphate using the Schwinger multichannel method. In general, these theoretical investigations have been successful in describing gas-phase THF elastic scattering phenomena above 1 eV (Allan, 2007). Recently, Khakoo *et al.* (Khakoo *et al.*, 2010) have reported experimental and theoretical differential cross sections at low scattering energies for the unsaturated five-membered heterocycle furan (C_4H_4O).

The earliest relevant experimental study yielding the resonance energies of the series of azabenzenes is that of Huebner *et al.* (Huebner *et al.*, 1968), who attributed the doublet resonances of pyridine to the splitting of the lowest-energy degenerate orbital of benzene. This was followed by the threshold electron spectrometric study of Pisanias *et al.* (Pisanias *et al.*, 1973) and the vibrationally-resolved differential electron transmission experiment of Nenner and Schulz (Nenner and Schulz, 1975) on the series of azines, and the electron transmission study on pyridine and the diazines by Mathur and Hasted (Mathur and Hasted, 1976). Pisanias *et al.* find pyridine resonance energies of 0.84 and 1.30 eV, and pyrimidine resonances of 0.8 and 1.9 eV. For pyridine, Nenner and Schulz characterize three resonances by symmetry, namely, a sharp $^2B_1$ resonance at 0.62 eV, a $^2A_2$ resonance at 1.2 eV, and the third a broad, vibrationally unresolved $^2B_1$ resonance at 4.58 eV. The two lowest-energy resonances confirm the hypothesis provided by Huebner *et al.* that these resonances of pyrimidine stem from capture into the doubly-degenerate e_{2u} orbital of benzene split by the nitrogen atom, leaving one state unperturbed and the other lowered in energy. Nenner and Schulz predict that the third resonance results from the mixture of a simple $^2B_1$ shape resonance with a core-excited resonance of the same symmetry of the neutral, analogous in formation to that of the $^2B_{2g}$ resonance of benzene which they locate at 4.85 eV. For pyrimidine, Nenner and Schulz similarly identify three resonances: a very low-energy 0.25 eV $^2A_2$, a broader 0.77 eV $^2B_1$, and a vibrationally structureless 4.24 eV $^2B_1$, the latter being formed through similar means of electron capture as the equivalent resonance in pyridine. Mathur and Hasted discovered two broad high-energy resonances in pyridine at 7.27 eV and 7.86 eV in addition to those already characterized by the older studies. Unfortunately, Mathur and Hasted neither label the symmetries of these resonances nor provide possible mechanisms of formation.

The primary experimental interest in the azabenzenes, however, has been in the spectroscopic determination of the energies and states of electronic transitions. Experimental ground and excited electronic state properties of the series of aromatic azabenzenes and azanapthalenes have been catalogued in a comprehensive review of Innes *et al.* (Innes *et al.*, 1988). To the best of our knowledge, there have been no published integral or differential electron scattering cross sections for pyridine in the gas phase. Very recently, experimental quasielastic positron scattering cross sections have become available for gas-phase pyrimidine (Zecca *et al.*, 2010), with electron scattering total cross sections derived from the positron cross section using the independent atom model (IAM). We shall compare our computed results with the semiempirical pyrimidine results of Zecca *et al.*, 2010 and the elastic scattering measurements from the parent benzene (Cho *et al.*, 2001; Makochekanwa *et al.*, 2003b; Mozejko *et al.*, 1996; Sueoka, 1988), which has been studied over a broad range of electron collision energies.

Theoretical treatment of electron scattering from pyridine, pyrimidine, and the other azabenzenes is similarly scarce. In addition to Zecca *et al.*, 2010, we are aware of a semiempirical scattering study considering valence photoelectron distributions and asymmetry parameters calculated for 5- and 6-membered heterocycles by the continuum multiscattering $X\alpha$ method (Suzuki and Suzuki, 2008). As with experimental interest, most computations have focused on determining vibrational and electronic spectroscopic properties by various quantum chemical methods. Electronic spectra have been computed by high-level theory, including multireference configuration interaction studies on pyridine (Walker *et al.*, 1990) and pyrimidine (Palmer *et al.*, 1990), complete active space SCF computations on the azide series (Fulscher *et al.*, 1992), and a very recently published series of computational benchmarks on aliphatic hydrocarbons, aromatic heterocycles, and the nucleobases using coupled cluster methods (Schreiber *et al.*, 2008).

Ab initio integral and differential cross sections have been published for benzene (Bettega *et al.*, 2000; Gianturco and Lucchese, 1998, 2000). Additionally, Winstead and McKoy have performed sophisticated Schwinger multichannel calculations on the related diazene pyrazine (Winstead and McKoy, 2007b; Winstead *et al.*, 2007). In the pyrazine study, Winstead and McKoy consider the limitations of single-electron scattering methods to predict resonance energies due to resonant channel coupling between simple shape resonances and possible two-electron resonances. In particular, in their investigation of the pyrazine $^2B_{2g}$ resonance, which Nenner and Schulz (Nenner and Schulz, 1975) suspected form in the same manner as the benzene resonance of the same symmetry, Winstead and McKoy find that neglect of triplet excitations of the target wave function resulted in a substantial difference between their computed result and experiment (Nenner and Schulz, 1975). This has great implications for the present study, since, as mentioned previously, the $^2B_1$ resonances of pyridine and pyrimidine are predicted to decay through a similar mechanism.

The content of this paper is as follows. In Sec. II.B we report computational details and discuss our scattering results for pyridine and pyrimidine. Conclusions are summarized in Sec. II.G.

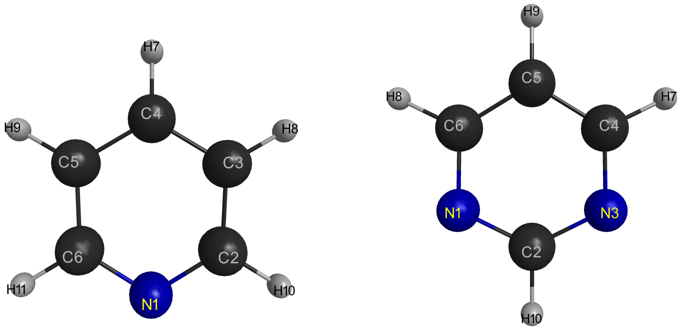

FIG. 1 Molecular structures of pyridine, top, and pyrimidine, bottom, displayed in standard orientation.

B. Computational results

All scattering calculations were performed using the EPOLYSCAT scattering code suite developed by Lucchese and collaborators (Gianturco *et al.*, 1994; Natalense and Lucchese, 1999), in which a single-center expansion (SCE) of continuum electron and target wave functions reduces the continuum nonrelativistic Schrödinger equation into a set of linear differential or integral equations that are solved numerically. Details may be found in the given references.

For the current scattering calculations we make use of two model potentials termed SECP, the static-exchange with correlation-polarization (V_{SECP}), and ASMECP, the adiabatic static-model-exchange with correlation-polarization (V_{ASMECP}). The V_{SECP} combines the Hartree-Fock type static exchange potential involving the Coulomb and exchange operators with V_{CP}, a model potential that smoothly joins the long-range dipole polarization interaction with short-range electron correlation terms derived from density functional theory (Perdew and Zunger, 1981). This potential thereby provides a description of the primary interactions involved in the scattering process. The so-called adiabatic potential combines V_{CP} with the static interaction and an energy-dependent local model exchange term (Hara, 1967) that allows the scattering equations to be written in a form that admits solutions in terms of Siegert states (Tolstikhin *et al.*, 1998) with complex eigenvalues corresponding to resonance energies and lifetimes.

TABLE 3 Comparison of SCF diagonal elements of the polarizability tensor $\alpha_{\alpha\beta}$ (in au), and SCF and experimental isotropic polarizabilities $\bar{\alpha}$ (in au) and dipole moments μ (in debye) of pyridine and pyrimidine.

	α_{xx}	α_{yy}	α_{zz}	$\bar{\alpha}^{SCF}$	$\bar{\alpha}^{Exp.}$		μ^{SCF}	$\mu^{Exp.}$
Pyridine	40.97	74.47	70.19	61.87	64.1[a]	60.93[b]	2.382	2.215[c]
Pyrimidine	36.97	65.52	67.87	56.77			2.385	2.334[d]

[a] Calaminici *et al.*, 2000
[b] Tixier *et al.*, 2002
[c] Sorensen *et al.*, 1974
[d] Blackman *et al.*, 1970

The Hartree-Fock target wave functions were obtained from an expansion in cartesian gaussian functions using the augmented correlation-consisted valence triple zeta (aug-cc-pVTZ) basis set within the GAUSSIAN03 (Frisch *et al.*, 2004) molecular structure suite. The geometries of both targets were constrained to their reference experimental values (Fernholt and Romming, 1978; Huber and Herzberg, 1979) in C_{2v} symmetry. This yielded converged SCF energies of $E^{SCF}_{\text{pyridine}} = -246.779580$ hartree and $E^{SCF}_{\text{pyrimidine}} = -262.781073$ hartree. In Fig. 1 (Bode and Gordon, 1998), we present the atomic numbering scheme of the two molecules in their respective standard orientations, which is used for all figures in the present study.

The maximum angular momentum l used in the partial wave expansion of the target orbitals and continuum electron wave function at the SECP and ASMECP levels for both molecular targets was $l_{\max} = 60$. This resulted in occupied orbitals normalized to better than 0.998 for both pyridine and pyrimidine. We treated the asymptotic polarizability needed for the correlation potential V_{CP} by using the diagonal elements of the polarizability tensor $\alpha_{\alpha\beta}$ centered on the target center-of-mass, as obtained from Frisch *et al.*, 2004. As seen in Table 3, the computed pyridine isotropic polarizability compares well to experimental values. Unfortunately, we were not able to locate a published experimental polarizability for pyrimidine.

Both molecular targets possess substantial dipole moments, as given in Table 3. Two immediate consequences of this include the well-known divergence of the differential cross sections at low scattering angles for molecules computed within the FN approximation (Rescigno and Schneider, 1992) and the question of the sufficiency of the dipole of either pyridine or pyrimidine to form a diffuse anionic state. We have computed electron differential cross sections for both targets using the SECP method neglecting dipole scattering, and corrected for the permanent dipole moment by employing a Born closure procedure, and present the results elsewhere in this paper (Sec. II.F). On the possibility of dipole bound anion formation in pyridine and pyrimidine, we make make the following arguments that these are not relevant processes at low energy for either molecule. Although both dipole moments are greater than the minimum binding threshold of 1.6 D predicted by the Born approximation for an electron interacting with a stationary dipole, and lies near the threshold of 2.5 D needed to bind an electron to a rotating dipole (Garrett, 1971), we suspect that neither pyridine nor pyrimidine form anionic states in this manner. In their study of the binding energies of electrons to the dipole moments of the series of aldehydes, ketones, and cyanides, Desfrançois *et al.* found pivaldehyde (2,2-dimethylpropanal, $(CH_3)_3CCOH$) to be the species with the lowest $\mu = 2.66$ D that resulted in an anionic state with a binding energy greater than 0.1 meV. (Desfrancois *et al.*, 1994). Pyridine has not been observed to form dipole-bound anions in the gas-phase for homogeneous molecular clusters $[\mathrm{Py}]_n^-$ for which $n \leq 3$ (Han *et al.*, 1998, 1999). A similar null result was confirmed for pyrimidine in solution (Chen and Holroyd, 1996); however, doubt has been raised on the stability of dipole-bound anions in the condensed phase (Sevilla *et al.*, 1994). Furthermore, because both species have negative ($E_{\mathrm{A}}^{\mathrm{pyridine}} = -0.62$ eV) or near zero ($E_{\mathrm{A}}^{\mathrm{pyrimidine}} \geq 0$ eV) electron affinities (Nenner and Schulz, 1975), the valence anionic species are not thermodynamically favored in the gas phase. Consequently, both species in the gas phase are expected to lack the covalent or dipole-bound anionic states of the pyrimidine nucleotide bases uracil and thymine (Hendricks *et al.*, 1998) that have resulted in numerical artifacts observed in calculation of their electronic scattering spectra (Gianturco *et al.*, 2008; Winstead and McKoy, 2008). We must add, however, that we cannot

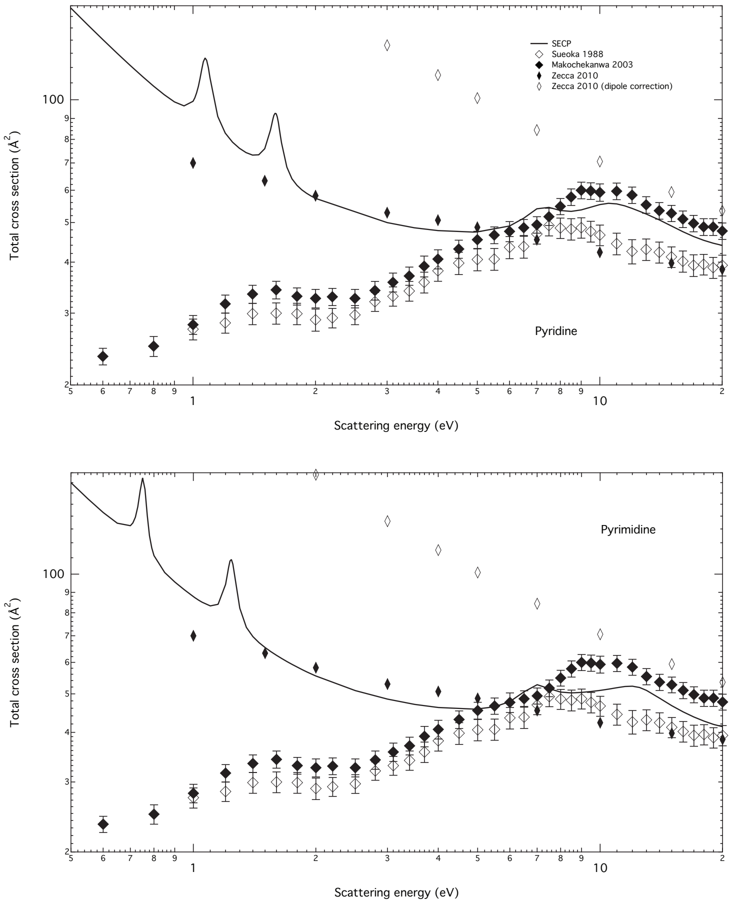

FIG. 2 Computed integral elastic cross section using the SECP potential compared to measured elastic scattering cross sections from benzene (C_6H_6) [Sueoka, 1988 (empty diamonds), Makochekanwa *et al.*, 2003b (filled diamonds)] and semiempirical cross sections of pyrimidine [Zecca *et al.*, 2010] including dipole correction (empty lozenges) and no correction (filled lozenges). The upper panel displays pyridine and the lower panel pyrimidine.

make a direct comparison in the electron scattering spectra of pyridine and uracil since the presence of the two keto groups in uracil introduces σ^* levels that are not present in pyrimidine.

C. Total cross sections

In Fig. 2 we compare computed (rotationally summed) elastic total cross section of pyridine (upper panel) and pyrimidine (lower panel) uncorrected for dipole scattering to the representative (quasi)elastic benzene measurements of Sueoka (Sueoka, 1988) (empty diamonds) and Makochekanwa *et al.* (filled diamonds) (Makochekanwa *et al.*, 2003b). The pyrimidine IAM electron scattering calculations of Zecca *et al.* (Zecca *et al.*, 2010) neglecting dipole scattering (filled lozenges) and including the first rotational excitation (empty lozenges) are compared to both target molecules.

The most prominent feature of our computed cross section is the strong dipole-induced increase at collision energies below 5 eV. This phenomenon has not only been observed in experimental and computed cross sections of molecules with substantial dipole moments, such as water (Itikawa and Mason, 2005), it has also been noted in benzene itself (Gulley *et al.*, 1998b). Although benzene is nonpolar, by virtue of suspected quadrupole (Bettega *et al.*, 2000) or virtual state scattering (Kimura *et al.*, 2004), its elastic cross section increases by a similar magnitude at collision energies lower than those reported in Fig. 2. In spite of this enhanced scattering cross section, two well-defined peaks near 1.0 and 1.5 eV may nevertheless be distinguished from the background; however, it is doubtful that these peaks may be seen in cross sections of vibrationally unresolved experiment. The similarly sharp peak near the benzene 1.1 eV $^2E_{2u}$ resonance, clearly suggested by theories employing the FN approximation (see Figs. 1 of Gianturco and Lucchese, 1998 and Bettega *et al.*, 2000), has not been detected in any experimental cross section to date. The pyrimidine cross section of Zecca *et al.* (Zecca *et al.*, 2010) displayed in Fig. 2 likewise does not indicate features of resonant scattering, although this may be due to the fact that their cross section was derived from quasielastic integrated positron scattering measurements, for which resonant scattering phenomena in molecules have not been observed (Surko *et al.*, 2005). Computing a weighted average of cross sections at the modified nuclear coordinates of each vibrational state may render more accurate results. In both targets, two broader peaks with maximum cross sections of about 50 Å^2 may also be seen at collision energies near 7 eV and 11 eV. In general, at scattering energies lower than 5

TABLE 4 Extended Hückel theory relative energy levels of the π^* orbitals of pyridine and pyrimidine expressed as a fraction of the benzene π^* orbital energies $e_{2u} = -0.30522$ au and $b_{2g} = -0.17473$ au.

Orbital Symmetry	Relative Energy	Orbital Symmetry	Relative Energy	Orbital Symmetry	Relative Energy
Benzene		Pyridine		Pyrimidine	
e_{2u}	1.000	b_1	1.032	a_2	1.037
		a_2	0.996	b_1	1.016
b_{2g}	1.000	b_1	1.016	b_1	1.036

eV, our cross sections compare in magnitude to uncorrected results of Zecca *et al* (Zecca *et al.*, 2010), and for scattering energies greater than 5 eV, our integrated cross section lies within the lower bounds of the experimental error of the forward-scattering corrected results of Makochekanwa *et al.* (Makochekanwa *et al.*, 2003b). Our SECP cross sections reproduce the major features of the benzene cross sections beyond the resonance scattering region, an expected result given the similarity of the two molecules and the decreasing importance of electron correlation at higher collision energies.

D. Computed π^* resonances

Before beginning a detailed discussion on the computed resonance properties, we wanted to determine the extent to which the relative ordering of the π^* resonances of pyridine and pyrimidine could be explained *solely* by the perturbing influence of the nitrogen atom on the benzene π system. To that end, we performed an extended Hückel calculation using the Hoffmann parameterization (Frisch *et al.*, 2004; Hoffmann, 1964) of pyridine and pyrimidine to obtain relative energy levels the π^* orbitals with respect to benzene. We found the relative energy levels of the unoccupied orbitals of pyridine and pyrimidine perturbed to an extent similar to to resonances found by experiment (Mathur and Hasted, 1976; Nenner and Schulz, 1975). The results are presented in Table 4. Admittedly, a semiempirical method such as the Hückel approximation should, by construction, give results close to experiment, but the qualitative agreement between the degree of perturbation of the π^* resonance energies and the Hückel virtual orbitals suggests that the mechanism

TABLE 5 Virtual MBS-SCF molecular orbitals of the ground electronic state of pyridine and pyrimidine corresponding to resonant states. Orbital energies are in eV.

MO	Symmetry	E^{SCF}	MO	Symmetry	E^{SCF}
	Pyridine			Pyrimidine	
22	b_1	6.56	22	a_2	5.99
23	a_2	6.82	23	b_1	6.16
24	b_1	13.10	24	b_1	12.49
26	b_2	17.33	26	a_1	17.27
27	a_1	18.48	27	b_2	17.94

of the π^* resonance formation of all three species result primarily from electron capture into virtual orbitals whose energies reflect the degree of perturbation brought about by the heteroatom. Notably, the extended Hückel method correctly orders the symmetry of the virtual orbitals of all three species. However, the resulting Hückel wave functions are crude and better orbitals computed at a similarly low cost can be obtained from a minimal basis set Hartee-Fock (MBS-SCF) calculation. The energies resulting from the current calculation are listed in Table 5. We mention that none of the following resonance energies or widths have been obtained from an empirical function of the MBS virtual orbital energy to bond length, such as that detailed in Chen and Gallup (Chen and Gallup, 1990). Instead, we make use of a minimum basis set Hartree-Fock calculation to generate a set of valence-type virtual orbitals whose energies can be understood to approximate the zeroth-order state of a quasibound electron and whose wave function can used to characterize scattering resonances of the appropriate symmetry type (Sheehy *et al.*, 1989).

In Figs. 3 and 4 we present by IR the computed partial integrated cross sections (filled line) in Å^2 and the corresponding eigenphase sums (dashed line) of pyridine and pyrimidine, respectively. By fitting the collision energies (in eV) to the eigenphase sums $\delta(E)$ as determined by the SECP calculation to a Breit-Wigner form

$$\delta(E) = a + b\,(E - E_R) + c\,(E - E_R)^2 + \arctan\left[\frac{2\,(E - E_R)}{\Gamma}\right] \tag{111}$$

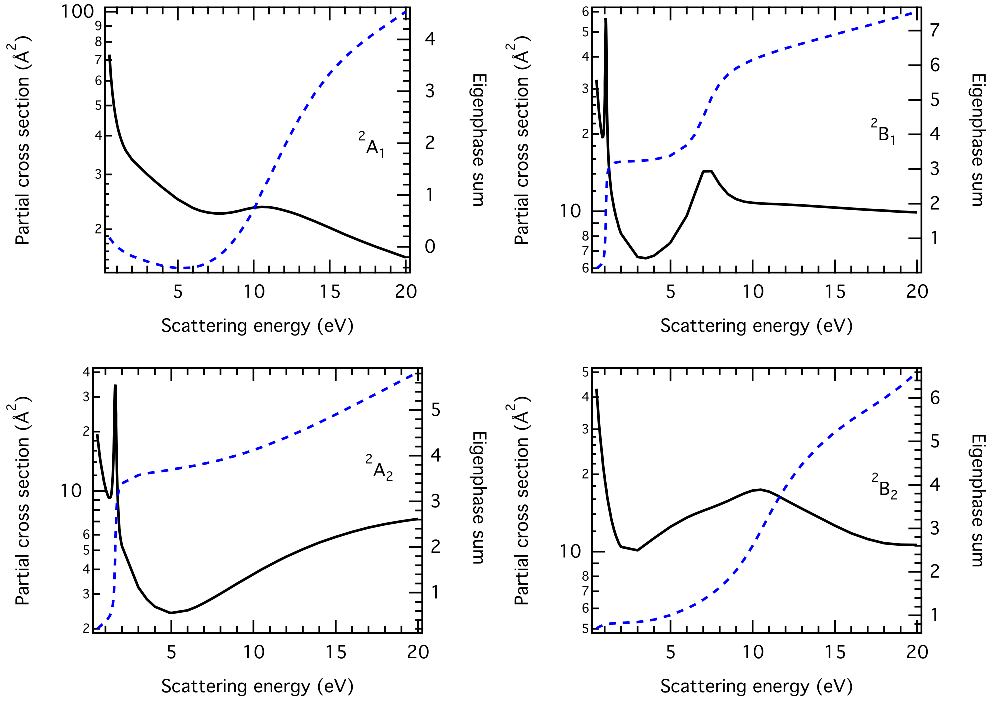

FIG. 3 Computed partial cross sections in Å^2 (filled line) and eigenphase sums (dashed line) of pyridine using the SECP potential

we are able to extract the resonance parameters obtained by the more rigorous of our two model potentials. We list the energies and widths (in eV) of resonances located by our fit in Table 6. We identify five pyridine and pyrimidine resonances, the two lowest in energy have been attributed to temporary electron capture into the π^* orbitals resulting from the lifting of the degeneracy by the N atom of the degenerate e_{2u} orbital of benzene, as stated in Sec. II.A (Huebner *et al.*, 1968; Nenner and Schulz, 1975; Pisanias *et al.*, 1973) and elsewhere. For pyridine, the lowest-energy $^2B_2$ resonance of 1.07 eV lies within 0.5 eV of the experimental value of 0.62 eV (Nenner and Schulz, 1975), while the somewhat broader $^2A_2$ resonance of 1.6 eV also lies within 0.5 eV of the experimental 1.2 eV $^2A_2$ pyridine resonance (Nenner and Schulz, 1975). The pyrimidine resonances 0.75 eV $^2A_2$ and 1.24 eV $^2B_1$ also lie within 0.5 eV of their experimental values of $\sim$ 0.25 eV and 0.77 eV (Nenner and Schulz, 1975). The positions and narrow widths, suggestive of long

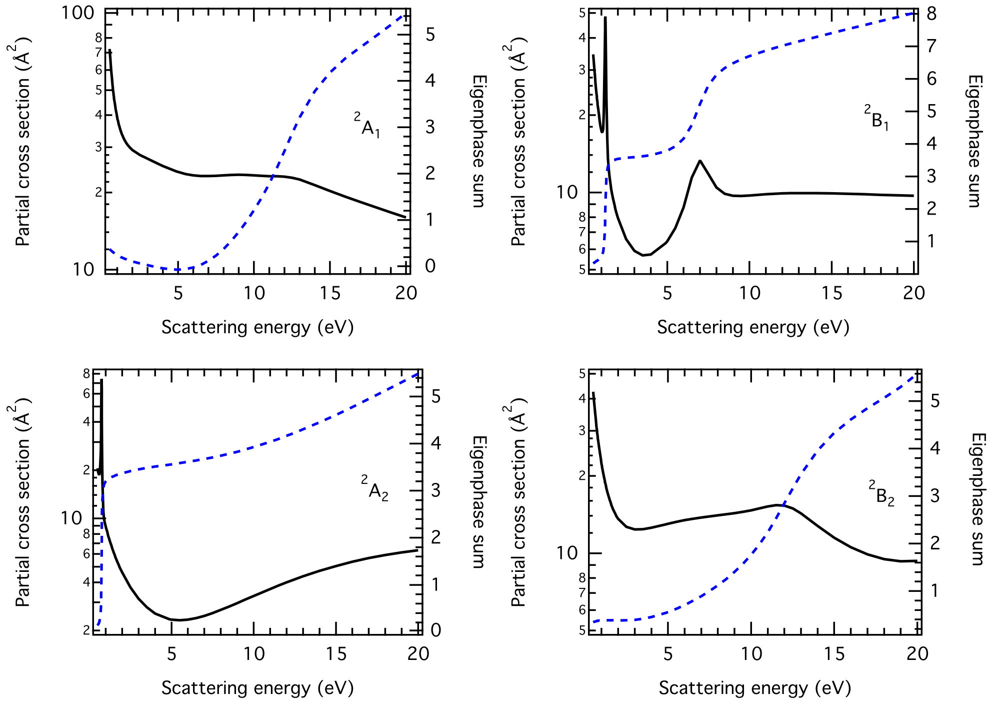

FIG. 4 The same as Fig. 3 for pyrimidine.

lifetimes, for these resonances, are in excellent agreement with experiment, in view of the level of approximation used in their computation.

The third π^* resonances found from the SECP potential, namely the 7.3 eV resonance and the pyrimidine 6.9 eV both in B_1 symmetry, corresponds to the experimental $^2B_1$ resonance of 4.6 eV (Mathur and Hasted, 1976; Nenner and Schulz, 1975) and the benzene $^2B_{2g}$ resonance measured between 4.5 and 4.8 eV (Cho *et al.*, 2001; Kimura *et al.*, 2004; Nenner and Schulz, 1975). The reason for the relatively poor agreement between our results and experiment lies in the suspected multiconfigurational description of this resonance. Nenner and Schulz (Nenner and Schulz, 1975) have proposed for the equivalent benzene resonance that it is best described as a mixture between a shape resonance of configuration $\ldots(e_{1g})^4(b_{2g})^1\ ^2B_{2g}$ and a core excited resonance resulting from temporary electron capture into an excited state of the neutral with a configuration $\ldots(e_{1g})^3(e_{2u})^1$. The proposed configuration of the temporary anion $\ldots(e_{1g})^4(e_{2u})^1$ results in several states $(^2E_{1g}, {}^4E_{1g}, {}^2B_{1g}, {}^2B_{2g})$, one of which possesses the correct symmetry and spin as the shape resonance. In their SMC calculation of the three lowest-energy resonances of the related heterocycle pyrazine (1,4-diazabenzene, ground state symmetry D_{2h}), Winstead and McKoy (Winstead *et al.*, 2007) account for the configuration mixing of the pyrazine $^2B_{2g}$ resonance by incorporating thirty modified virtual orbitals that include singlet- and triplet-coupled excitation from the six outermost valence orbitals as polarization orbitals of the one electron basis set. This was found to produce the best ($\sim$ 4.4 eV) agreement with experiment (4.10 eV) (Nenner and Schulz, 1975), compared to wave functions that included various modified virtual orbitals resulting only from singlet-coupled excitations as polarization orbitals. However, as Winstead and McKoy note, the use of such a mixed configuration wave function overdescribes doubles excitations of the temporary anionic state in comparison to the neutral and thus cannot be used as a general means to produce total scattering cross sections. In our current numerical experiment, in which we account for the distortion of the target orbitals described by a single electronic configuration in the presence of the continuum electron through a model potential, we are not able to include such effects.

In addition to fitting the SECP eigenphase sums to a Breit-Wigner equation, we have also determined resonance parameters from the search over the unphysical sheet of the complex energy plane for poles of the S-matrix. The S-matrix elements were obtained from a fit to the correct asymptotic scattering conditions of the continuum wave functions resulting from the SCE scattering equations diagonalized with the ASMECP potential. To rule out short-lived, background, or otherwise spurious resonances, we have limited our search to include poles that lie reasonably close to the positive real energy axis, *viz.*, with a maximum imaginary width Γ of 8.0 eV. Even after this truncation, the ASMECP nonetheless predicts a number of resonances neither observed in available experiment nor extracted from the SECP eigenphase sums. Although we will limit our discussion of ASMECP π^* resonances only to those of the narrowest-width lying near experimentally-observed energies, we list these energies in Table 7 for the sake of completeness. Interestingly, we do not predict an array of high-energy resonances for pyridine or pyrimidine as seen the Gianturco and Lucchese study of benzene (Gianturco and Lucchese, 1998), even after

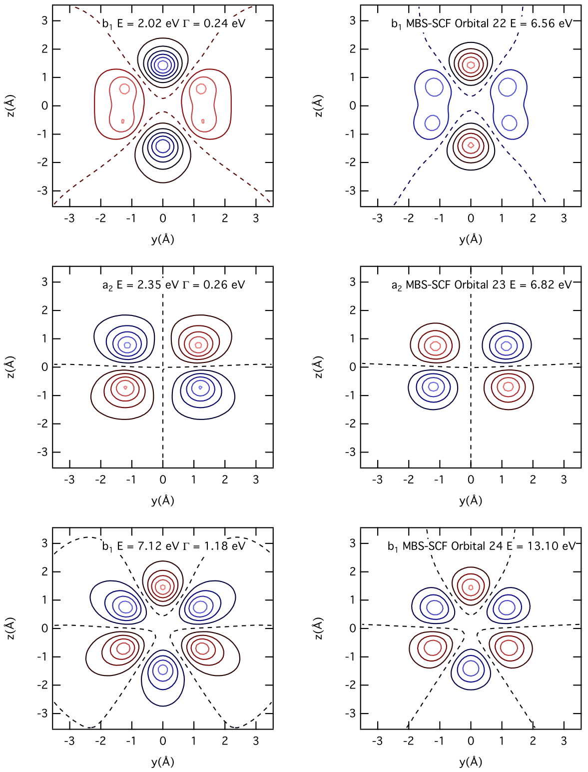

FIG. 5 Left hand column: Contour plots of the real part of the π^* continuum wave functions computed using the ASMECP potential of electrons scattering from pyridine. The IR, energy (in eV), and width (in eV) are also reported. Right hand column: Two-dimensional contour plots of the corresponding virtual orbitals computed from a MBS-SCF optimization of the ground state target. Each contour is separated by 0.05 Å with nodes represented as dashed lines. All plots lie in a plane 0.5 Å above the target.

limiting the resonance search to 20 eV. Since V_{ASMECP} is by construction an approximate, entirely local, potential, some discrepancy is to be expected between the results shown in Table 7 and those from V_{SECP} in Table 6. Nevertheless, for the ASMECP resonances of pyridine at $^2B_1$ 2.0 eV and 2.4 $^2A_2$, and those of pyrimidine at 1.6 $^2A_2$ and 2.0 $^2B_1$, the results lie within $\sim$ 1.5 eV of the experimental values referred to in Sec. II.A.

In Figs. 5 and 6, contour plots of the real parts of the scattering wave function are compared to the virtual orbitals of the same symmetry obtained from a MBS-SCF optimization of the targets at their experimental geometry (Werner *et al.*, 2006). In all figures, the tar-

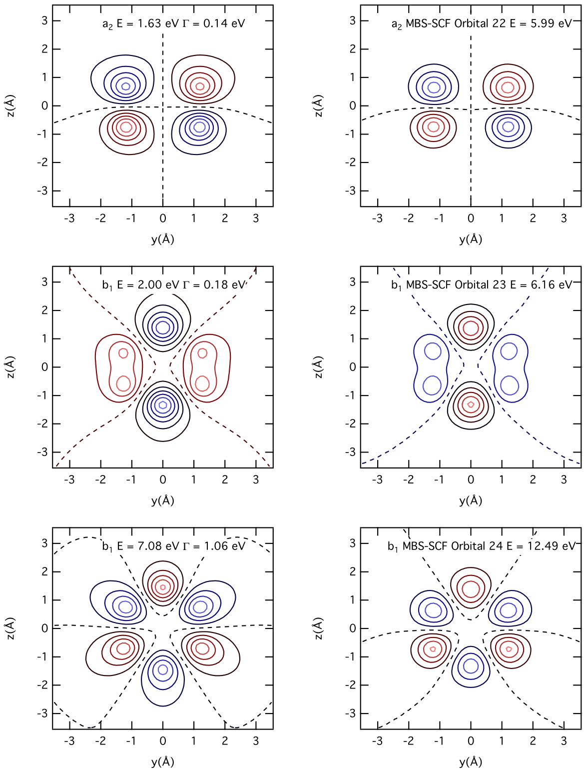

FIG. 6 The same as in Fig. 5 for pyrimidine.

gets lie in their standard orientations as in Fig. 1, with the center of mass located at the origin. All π^* contours in Fig. 5 and 6 are displayed 0.5 Å above the *yz* molecular plane, which possesses the node of the resonance wave function. For both species, the three lowest-energy virtual orbitals correctly predict the symmetry and the ordering of the resonant states; their energies are, as expected, higher than those obtained from the ASMECP calculation, due in part to a lack of polarizing functions to describe the significantly delocalized continuum electron. For pyridine (Fig. 5), examining the nodal structure of the MBS orbitals and invoking the π orbital species notation given in Innes *et al.*, 1988, in which the nodes passing through atoms of the ring plane are denoted ‘a’ and those through bonds ‘b’, we can clearly characterize the lowest-energy $^2B_1$ resonance as temporary entrapment of the continuum electron into a π^*_{bb} orbital, which a natural bond orbital analysis on the MBS virtual orbital (Carpenter and Weinhold, 1988; Frisch *et al.*, 2004) indicates to be centered over the N1-C2 resonant antibond. Similarly, the $^2A_2$ resonance is a π^*_{ab}

TABLE 6 Energies E_R and widths Γ in eV of pyridine and pyrimidine resonances obtained by fit of SECP eigenphase sums to Eq. 111.

Symmetry	E_R^{SECP}	Γ^{SECP}	Symmetry	E_R^{SECP}	Γ^{SECP}
	Pyridine			Pyrimidine	
b_1	1.07	0.09	a_2	0.75	0.04
a_2	1.60	0.13	b_1	1.24	0.08
b_1	7.30	1.77	b_1	6.88	1.51
b_2	10.56	3.25	a_1	11.58	3.67
a_1	11.47	4.65	b_2	11.66	4.10

resonance resulting from capture over a C5-C6 antibond (i.e., near the N atom), and the second $^2B_1$ resonance is a π^*_{bbb} orbital centered over the higher-energy C3-C4 antibond. Likewise, for pyrimidine (Fig. 6), the clear nodal structure of the π^* resonance wave functions admits their facile classification in terms of temporary capture into virtual orbitals, *viz.*, the $^2A_2$ resonance stems from capture into a π^*_{ab} orbital, the first of the two $^2B_1$ resonances a π^*_{bb} orbital, and the second a π^*_{bbb} virtual orbital. Natural bond orbital analysis of the MBS virtual orbitals indicates that these π^* orbitals have predominant N1-C2, N3-C4, and C5-H6 antibonding character, respectively.

E. Computed σ^* resonances

For both targets, the σ^* resonances obtained from the Breit-Wigner fit of the SECP eigenphase sums have energies around 11 eV and spatial symmetries of A_1 or B_2. Due to their broad widths, precise resonance energies were difficult to determine, so the energies in Table 6 represent best estimates. We propose that the $^2A_1$ and $^2B_2$ resonances we find in pyridine and pyrimidine result, in part, from temporary electron capture into the orbitals resulting from the N-induced split of the doubly degenerate e_{1u} virtual orbital of benzene (Allan, 1989; Gulley and Buckman, 1999) to the reduced symmetry ($D_{6h} \to C_{2v}$) a_1 and b_2 orbitals of the azabenzenes. These resonances may correspond to the 7.27 and 7.86

eV resonances seen in the transmission electron spectroscopic study of gas-phase pyridine (Mathur and Hasted, 1976) and to the broad 6-7 eV peak seen in the vibrational energy loss spectrum of condensed-phase pyrimidine (Levesque *et al.*, 2005). Both of these experimental features bear resemblance to the $^2E_{1u}$ shape resonance of gas-phase benzene near 8.5 eV (Gulley and Buckman, 1999). This benzene resonance was computed to have an energy 10.07 eV and width 4.15 eV by the SECP results of Gianturco and Lucchese (Gianturco and Lucchese, 1998), whereas the SEP results of Bettega *et al.* (Bettega *et al.*, 2000) did not find a resonance in this symmetry at this energy. Why this resonance should appear at a lower energy and width in the calculated benzene results of Gianturco and Lucchese than in either of the azabenzenes, whose resonance energies should be lowered by the nitrogen atom, is not clear. We draw only a tentative conclusion from our SECP results since our implementation of the Breit-Wigner form does not admit multiple scattering resonances, and, doubtless, other means of temporary electron capture besides simple shape resonance formation may occur at these collision energies. More experimental data are needed to determine the extent to which various inelastic channels not taken into account by our single-particle, FN treatment of the target nuclei occur with its formation.

The σ^* resonance energies, widths, and pole orders found by analytic search of the S-matrix poles are presented in Table 7. These resonances are characterized by widths broader than the uncharacterized π^* resonances of Table 6 and energies approximately 1.5 eV greater than those obtained from the SECP fit. In Figs. 7 and 8 we compare contours of the real parts of the resonance wave functions with the smallest width with the corresponding MBS-SCF virtual orbitals. In particular, the benzene MBS-SCF e_{1u} orbital with energy $E = 17.67$ eV is found in pyridine to split into a b_2 orbital with energy $E = 17.33$ eV and an a_1 orbital of energy $E = 18.48$ eV. In pyrimidine, the resulting orbital symmetries are reversed, so that the a_1 orbital at $E = 17.27$ eV is lower in energy than the b_2 at $E = 17.94$ eV. In contrast to the π^* resonances discussed in Sec. II.D, these σ^* MBS virtual orbitals do not resemble the σ^* resonant wave functions computed using V_{ASMECP}. The absence of a qualitative correspondence between the MBS virtual orbital and the resonance wave function has been noted in the computed ASMECP 12.25 $^2E_{1u}$ resonance wave

TABLE 7 Computed energies E_R and widths Γ (in eV) of pyridine and pyrimidine resonances located by search of the complex energy plane. All poles with imaginary energy less than 8 eV are shown. The multiplicity of poles with a pole order greater than one is also listed.

Symmetry	E_R^{ASMECP}	Γ^{ASMECP}	Pole Order	Symmetry	E_R^{ASMECP}	Γ^{ASMECP}	Pole Order
	Pyridine				Pyrimidine		
b_1	1.40	4.96		b_1	0.49	3.09	
b_1	2.02	0.24		b_1	1.41	5.14	
a_2	2.35	0.26		a_2	1.63	0.14	
b_1	7.12	1.18		b_1	2.00	0.18	
a_1	11.84	6.84	4	b_1	2.47	7.11	
b_2	12.09	4.35		b_1	7.08	1.06	
a_1	12.99	6.00	3	a_1	10.24	6.67	
				a_1	12.32	6.85	
				b_2	13.08	6.32	4
				a_1	13.22	2.99	
				b_2	13.47	3.99	2

function of benzene (Gianturco and Lucchese, 1998), in which contributions from the H atoms are absent from the MBS virtual orbital. The ${}^2B_2$ resonances of both species have real wave functions that are roughly analogous to the MBS b_2 virtual orbital counterparts. Some antibonding σ^* character may be detected in ${}^2B_2$ resonance wave functions, which is compared to MBS orbital 26 of pyridine and MBS orbital 27 of pyrimidine. Natural bond orbital analysis of the respective b_2 MBS virtual orbitals indicates these are antibonding CH sp^2 orbitals, the features of which are evident only in part for the real ${}^2B_1$ scattering wave functions. By contrast, the MBS-SCF a_1 orbitals of pyridine and pyrimidine bear only a slight resemblance to either ASMECP ${}^2A_1$ resonance wave function and demonstrates the extent to which neither of the broad ${}^2A_1$ resonances may be described as

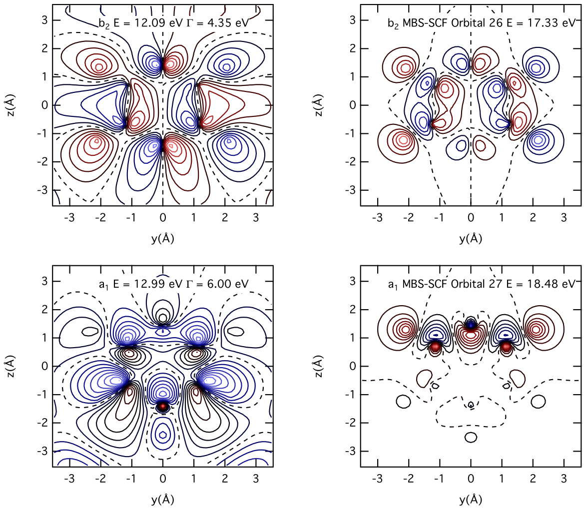

FIG. 7 Left hand column: Contour plots of the real parts of the σ^* continuum wave functions computed using the ASMECP potential of electrons scattering from pyridine. The IR, energy (in eV), and width (in eV) are also reported. Right hand column: Two-dimensional contour plots of the corresponding virtual orbitals computed from a MBS-SCF optimization of the ground state target. Each contour is separated by 0.05 Å with nodes represented as dashed lines.

simple electron capture into an unoccupied molecular orbital. The $^2A_1$ resonances are true scattering states, with no correlation to capture within any canonical virtual orbital.

In their computational electron scattering study of benzene, Gianturco and Lucchese (Gianturco and Lucchese, 1998) find a broad, high-energy $^2A_{2g}$ resonance resulting from trapping within the a_{2g} unoccupied orbital, which has an MBS-SCF energy of 29.48 eV. This resonance has an energy $E_R^{\text{SECP}} = 21.1$ eV and width $\Gamma^{\text{SECP}} = 7.0$ eV using SECP results, and $E_R^{\text{ASMECP}} = 21.5$ eV and a narrower width $\Gamma^{\text{ASMECP}} = 4.8$ eV using the approximate ASMECP results. Similarly, Bettega *et al.* (Bettega *et al.*, 2000) locate the same resonance at 22 eV using the SEP results from their SMC calculation. In pyridine and pyrimidine, the equivalent b_2 virtual orbitals have MBS-SCF energies of, respectively, 29.26 eV and 28.95 eV, as listed in Table 5. Since unscaled MBS orbital energies represent an approximate upper bound to the resonance energy, we must extend our search to scattering energies to 30 eV to locate these $^2B_2$ resonances. Within the scope of the present calculation, we find no evidence for the symmetry-allowed $^2B_2$ resonance in either

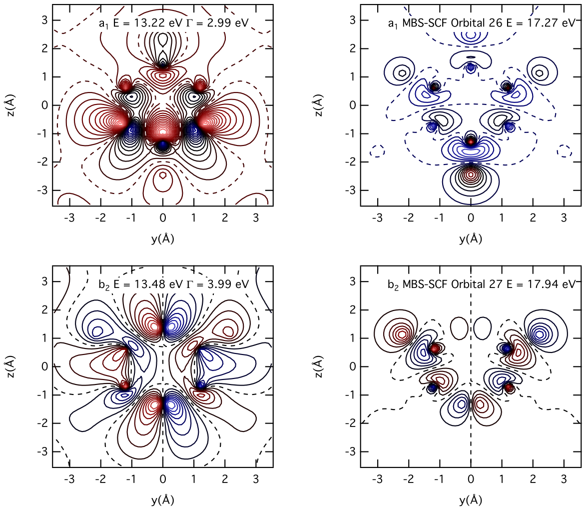

FIG. 8 The same as in Fig. 7 for pyrimidine.

species. Neither b_2 SECP eigenphase sum shown in Figs. 3 and 4 display the typical feature of a scattering resonance, namely, an increase in the eigenphase sum by $\pi \pmod{\pi}$. Likewise, our analytic search of S-matrix poles produced by the ASMECP potential does not find resonances at an energy near those of the benzene $^2A_{2g}$ resonances.

F. Differential cross sections

Within the fixed-nuclei approximation, the differential cross section for scattering into a given polar angle θ can be expressed as an expansion in terms of Legendre polynomials

$$\frac{d\sigma}{d\Omega} = \sum_L A_L P_L(\cos\theta) \tag{112}$$

where the expansion coefficients A_L constitute a unitary transformation of the scattering T-matrix elements that involve sums over the set of initial and final angular momenta $l'l$. In the presence of a long-range potential such as a permanent electric dipole moment, a large number of $l'l$ channels of the T-matrix must be evaluated to overcome the slow convergence of the series expansion over the A_L coefficients in Eq 112. In this case the convergence over L of the differential cross section can be greatly enhanced through first-order perturbation theory, such as the Born approximation, since the higher-order angular momenta $l'l$ of the T-matrix are dominated by the dipole interaction (Rescigno and Schneider, 1992). One common method of incorporating the Born approximation lies through use of a Born closure formula of the form (Itikawa and Mason, 2005)

$$\frac{d\sigma}{d\Omega} = q^B + \sum_L \left(A_L - A_L^B\right) P_L(\cos\theta), \tag{113}$$

where A_L and A_L^B are the close-coupling and Born approximation correction expansion coefficients, and

$$q^B = \sum_{j'\tau'} q_{\text{rot}}^b \left(j'\tau' \leftarrow j\tau\right) \tag{114}$$

is the analytic Born differential cross section of the target undergoing a dipole or higher-order transition from rotational state $j\tau$ to $j'\tau'$.

An equivalent form of Eq. 113 that we employ in the current calculation is that derived by Sanna and Gianturco (Gianturco *et al.*, 1998), as follows:

$$\frac{d\sigma}{d\Omega}(j'\nu' \leftarrow j\nu) = \frac{d\sigma}{d\Omega}^{\text{FBA}}(j'\nu' \leftarrow j\nu) + \Delta\frac{d\sigma}{d\Omega}(j'\nu' \leftarrow j\nu), \tag{115}$$

where

$$\begin{aligned}\Delta\frac{d\sigma}{d\Omega}(j'\nu' \leftarrow j\nu) = \frac{1}{4k_{j\nu}^2}\sum_L &\left[A_L(j'\nu' \leftarrow j\nu) - A_L^B(j'\nu' \leftarrow j\nu)\right] \\ &\times P_L(\cos\theta)\end{aligned} \tag{116}$$

In Eq. 115, $d\sigma^{\text{FBA}/d\Omega}(j'\nu' \leftarrow j\nu)$ comprises the analytic Born approximation resulting from a given rotational transition, and $\Delta d\sigma/d\Omega(j'\nu' \leftarrow j\nu)$ of Eq. 116 the contribution of the close-coupling expansion corrected by the removal of dipole scattering components computed within the unitarized Born formulation of the T-matrix as constructed from the FBA K-matrix elements. The advantage of Eq. 115 lies in the fact that the series over L now terminates at a given value $L_{\max}$. Expressions for the A_L and A_L^B expansion coefficients and the unitarized Born T-matrix may be found in the given reference and Sanna and Gianturco, 1998.

Born-corrected differential cross sections (BDCS) were generated using the POLYDCS utility of Sanna and Gianturco (Sanna and Gianturco, 1998), which was subsequently modified to admit calculation of the rotational states of asymmetric rotors. In dipole scattering, the only allowed transition from the rotational ground state is $j'_1 \leftarrow j_0$; thus, differential cross sections of the two lowest $j' \leftarrow j$ rotational transitions are considered, namely the elastic $j'_0 \leftarrow j_0$ and the dipole $j'_1 \leftarrow j_0$, averaging over the initial τ states and summing over the final τ' states. We also compute dipole corrected cross section less rigorously through addition of the DCS generated by EPOLYSCAT to the dipole cross section computed from analytic Born expression of Eq. 114 alone that we term corrected DCS. For both target molecules, the initial rotationally elastic T-matrix elements were obtained from previous SECP calculations. The maximum angular momentum in the analytic Born K-matrices is $l^B_{\max} = 64$ and in the $P_L(\cos\theta)$ close-coupling and unitarized Born expansions is $L^B_{\max} = 24$.

Differential cross sections computed near the respective SECP resonant scattering energies are presented for pyridine (Fig. 9) and pyrimidine (Fig. 10) with no dipole correction (DCS) and corrected for dipole scattering using the analytic Born expression of Eq. **??** (corrected DCS). All cross sections are compared to the benzene DCS of Cho *et al.* (Cho *et al.*, 2001) (filled diamonds) measured at resonant scattering energies, namely the $^2E_{2u}$ resonance at 1.1 eV, the $^2B_{2g}$ resonance at 4.9 eV, and the $^2E_{1u}$ resonance at 8.5 eV.

The computed SECP differential cross sections for both species are nearly identical, in both shape and magnitude, at comparable resonant scattering energies. As can be expected, each DCS is dominated by large forward scattering contributions, but backward scattering contributions remain small among all computed cross sections. Additionally, little difference is seen among the pyridine and pyrimidine DCS computed at nearly degenerate $^2A_2$ and $^2B_1$ resonance energies. The oscillations evident in the lowest energy SECP differential cross sections arise from the pathological treatment of the permanent dipole in the FN approximation and not as a consequence of resonant scattering, since these features vanish when dipole scattering is taken into account, as verified in the corresponding corrected DCS profiles. As seen in Figs. 9 and 10, the oscillations diminish at higher electron scattering energies. At collision energies greater than 5 eV the influence of the dipole moment on the DCS decreases to the extent that both the uncorrected SECP DCS and the corrected DCS computed at the second respective $^2B_1$ resonance energies of pyridine (7.3 eV) and pyrimidine (6.9 eV) compare in magnitude, if not in profile, to the

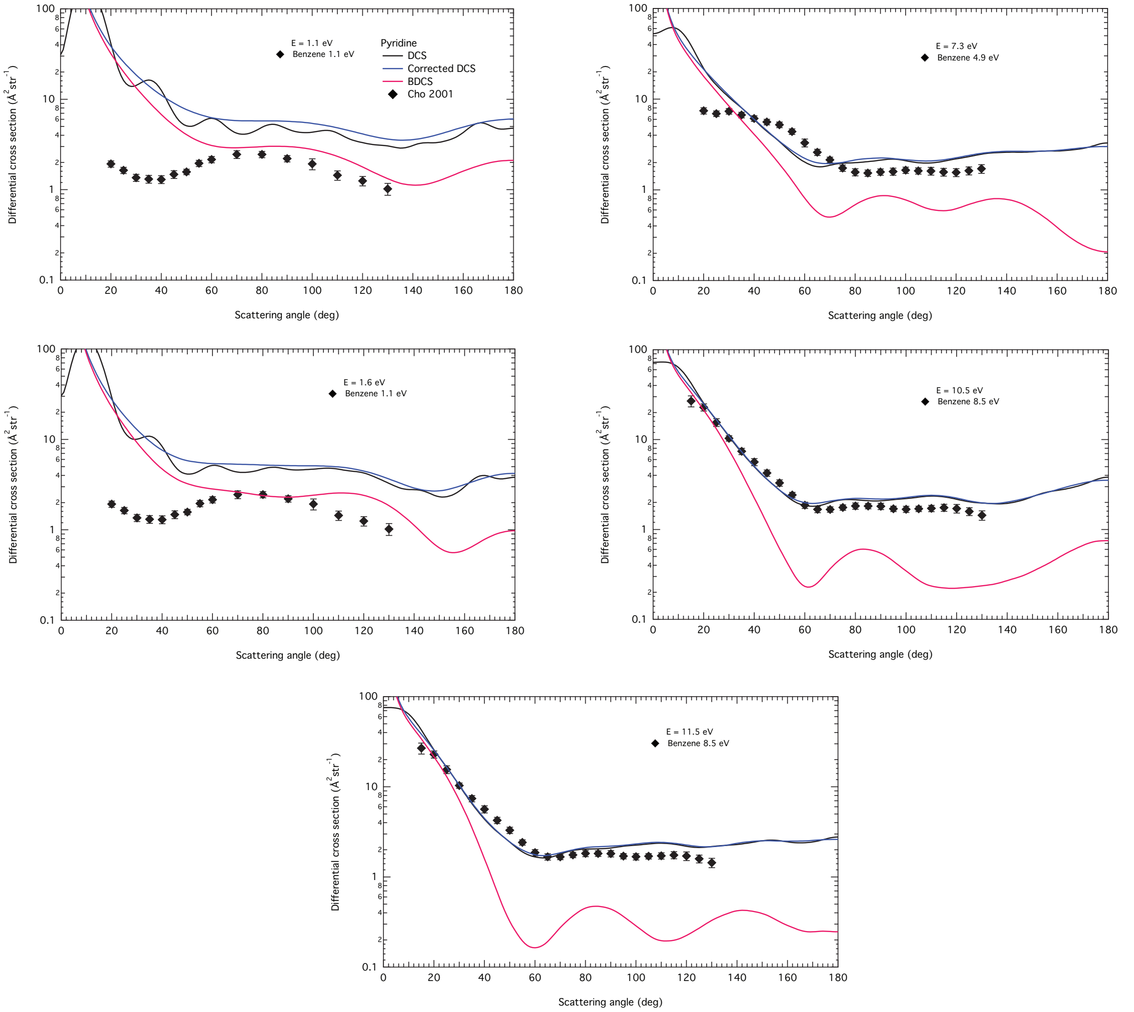

FIG. 9 Computed SECP differential cross sections with no Born dipole correction (DCS), including analytic Born expressions for the dipole moment (corrected DCS), and with the Born closure procedure (BDCS) for pyridine at the SECP resonant scattering energies. The experimental results for benzene are taken from Cho *et al.* [Cho *et al.*, 2001 (filled diamonds)]

DCS measured at the $^2B_{2g}$ core-excited resonance of benzene. Lastly, we note the excellent agreement between the pyridine 10.5 eV and 11.5 eV and pyrimidine 11.5 eV SECP DCS with the measured benzene DCS of 8.5 eV at all but the most forward scattering angles.

As is evident, for polar molecules, the Born-closure treatment is necessary for qualitative treatment of the differential cross sections at the lowest scattering energies in the

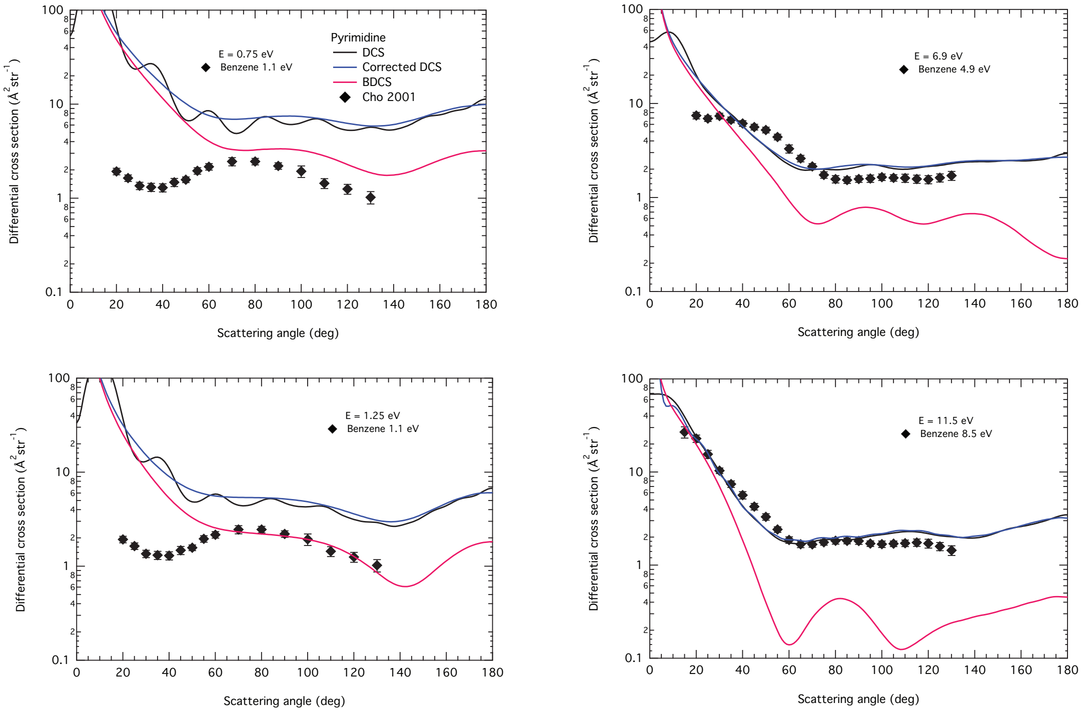

FIG. 10 The same as in Fig. 9 for pyrimidine.

forward direction, as seen in the 1.1 eV and 1.6 eV BDCS of pyridine in Fig. 9 and the 0.75 eV and 1.25 eV BDCS of pyrimidine in Fig. 10. Accordingly, we have employed a simplified Born correction model that recovers the sharply increasing magnitude at zero scattering angle and eliminates the numerical instability of the uncorrected SECP values at mid and higher scattering angles. This treatment is approximate because it excludes non-dipole $j_1 \leftarrow j_0$ contributions. The exact Born closure procedure of Eq. 113, however, has been found to yield unphysical negative cross sections if the partial-wave expansion of the rotationally inelastic scattering amplitudes do not converge, particularly at higher scattering angles (Rescigno and Schneider, 1992). In the current calculations generated by POLYDCS that make use of the closure procedure stated in Eq. 115, negative differential cross sections were identified in the $j_1' \leftarrow j_0$ rotational transition close-coupling and unitarized Born cross sections at every computed energy for scattering angles greater than 40°. The numerical instabilities of the unconverged inelastic partial cross sections, however, did not result in pathological behaviour of the BDCS, as shown in Figs. 9 and 10. The truncation of the close-coupling expansion at $L = 24$ of Eq. 115 results in an underestimation of the cross section due to non-dipole scattering. At angles greater than $\theta = 60^\circ$ and electron energies greater than 5 eV, the BDCS cross sections of both targets lie one order of magnitude below both the computed SECP DCS and the measured benzene DCS of Cho *et al.*. The Born closure formula given in the form of Eq. 115 relies too strongly upon the Born approximation, which is increasingly invalid at higher scattering angles for these complex targets.

G. Conclusion

We have investigated the resonance energies and widths of the azabenzenes pyridine and pyrimidine using a SCE treatment of the molecular and continuum electrons. The total cross sections computed by the SECP potential are similar to the experimental elastic benzene cross section at collision energies greater than 10 eV, where correlation between the scattering and bound electron wave functions is less critical. At low collision energies, both targets display peaks indicating resonant scattering superimposed upon an increased background typical of species with dipole moments. The differential cross sections computed with no explicit correction for the dipole moment, and with two model Born closure procedures, display little significant difference between species and approximate the measured benzene DCS at higher scattering energies. We identified five resonances for pyridine and pyrimidine from features of the SECP partial cross sections and have obtained resonance parameters using a simple fit of the energies to the computed eigenphase sums. We have also identified resonances through an analytic search of the poles of the *S*-matrix as obtained from solving the scattering equations with the ASMECP potential. While the resonance energies are not in as good agreement with experiment as the SECP, the entirely-local model potential used to obtain the *S*-matrix elements allows resonant wave functions to be computed, admitting qualitative classification of scattering resonances through comparison with virtual molecular orbitals computed from a MBS-SCF optimization of the target. While the process of electron entrapment by angular momentum barriers corresponding to these virtual orbitals is adequate to describe the the formation of the lowest-energy π^* and σ^* resonances, some extension of our method will be needed to account for resonances formed through inelastic or multi-electron mechanisms.

III. ELECTRON SCATTERING FROM GAS PHASE CIS-DIAMMINEDICHLOROPLATINUM(II): QUANTUM ANALYSIS OF RESONANCE DYNAMICS

A. Introduction

The interaction of low-energy electrons with molecules of biological importance has received considerable interest through the years ever since the discovery that the formation of temporary negative ion causes the dissociation of isolated strands of nucleotide bases (Boudaiffa *et al.*, 2000). Increasingly sophisticated theoretical methods have been developed to treat the interaction of the electron with large, low-symmetry, electron-dense target species such as biomolecules. These models have been shown to recover with some quantitative accuracy the primary resonant features of the scattering event as it relates to scattering from representative targets such as gas-phase uracil (Dora *et al.*, 2009; Gianturco *et al.*, 2008, 2009; Tonzani and Greene, 2006b; Winstead and McKoy, 2006c). Along these lines, researchers have also investigated the role of vibration and nuclear rearrangement in the dissipation of the excess energy imparted to the target by the continuum electron. The necessity of treating the scattering problem within multiple, coupled set of degrees of freedom involving nuclear and electronic coordinates, however, is clearly a crucial stumbling block for this research. One way of simplifying this issue is to consider the scattering phenomena resulting from nuclear motion constrained only to one-dimensional degrees of freedom, as is naturally the case in the dissociative attachment of diatomic and linear triatomic molecules, or in assuming that only a few symmetry-preserving vibrations of the polyatomic species are excited by the kinetic energy of the electron (Allan, 1989). The latter mechanism also serves as a means of stabilizing the resonant state, as the vibrational energy of resonant attachment may be quenched through distribution into “inactive” vibrational modes (Thoss and Domcke, 1998).

Additionally, it is known that radiotherapy, which combines the use of ionizing radiation with the inclusion of cytotoxic agents within the tumor cells, has been developed as a complementary treatment to more traditional chemotherapy (Howe *et al.*, 2001). Four decades ago it was shown that the substitution of thymidine nucleoside (thymine nucleobase bound to a sugar moiety) within the genetic sequence of cellular DNA by its halogenated analogues, did not change the normal gene expression in non-irradiated cells but increased the sensitivity of those cells to X-rays by a factor of 4 (Zamenhof *et al.*, 1958). In spite of the fact that the molecular mechanism was not unravelled, it was nevertheless proposed that halogen-modified nucleic acids could also show sensitization to radiation damage (Szybalski, 1974) and that the enhanced genotoxic effects could be attributed to the action of hydrated electrons (Sevilla *et al.*, 1974). The more recent observations that low-energy electrons, as mentioned, could induce strand-breaking effects in nucleobases (Huels *et al.*, 2003) has led to more detailed analysis of the molecular response of halogenated nucleobases (e.g. bromouracil, BrU) or of bases paired with adenine in the gas phase and the production of the anion Br^-, as the outcomes of dissociative electron attachment (DEA) paths activated by environmental electrons (Li *et al.*, 2003). The connection between production of halogenic anions and the radiosensitization of haloderivatives by attachment of Br, Cl and I has been further confirmed by recent studies that have revealed production of both halogenic anions and of residual-basis anions (Li *et al.*, 2002). Along similar lines, it was also found that ultrafast electron-transfer from transient anions of deoxyribonucleotides consisting of one of the four DNA basis coupled to the sugar-phosphate groups in water (dXMP with X= A, C, G, or T) to halogenated radiosensitizers like bromodeoxyuridine (BrdU) and iododeoxyuridine (IdU) is a very efficient process (Wang *et al.*, 2009). Such ultrashort, time-resolved electron-transfer experiments were also carried out with cisplatin, widely used as a chemotherapeutic anticancer agent.

In the present work we therefore consider the electron scattering and resonance properties of the biologically relevant inorganic molecular complex cisplatin (*cis*-diamminedichloroplatinum(II), $[\mathrm{Pt(NH_3)_2Cl_2}]$, hereafter referred to as CDDP. This molecule has received intense clinical and biophysical investigation ever since the fortuitous discovery of its anti-cell division properties decades ago (Rosenberg *et al.*, 1965, 1969). One open question lies in the manner in which the chlorine atoms are lost from cisplatin within living cells, since X-ray crystal structures and NMR spectra of CDDP and nuclei acid oligomers indicate that cisplatin is activated only upon the loss of one or both chlorine atoms within the cell (Jamieson and Lippard, 1999; Jung and Lippard, 2007). On account of its importance as an antitumor agent in human and animal subjects, reaction dynamics of gas-phase CDDP have generated research motivated towards the deeper understanding of the role low-energy electrons play in the the biological activation of this species. Recently, Kopyra *et al.* (Kopyra *et al.*, 2009) have proposed an alternative mechanisms in which the loss of both Cl atoms occurs through collision with a single low-energy electron through two competing reactions

$$\begin{aligned} &(\text{Major}) \;\; e^- + [\text{Pt(NH}_3)_2\text{Cl}_2] \;\rightarrow\; [\text{Pt(NH}_3)_2]^- + \text{Cl}_2 \\ &(\text{Minor}) \;\; e^- + [\text{Pt(NH}_3)_2\text{Cl}_2] \;\rightarrow\; [\text{Pt(NH}_3)_2] + \text{Cl}_2^- . \end{aligned}$$

From energy balance considerations, the first reaction is favored because of the more intense ion yield. From the bond fragmentation energy of PtCl, the Cl_2 bond dissociation energy (Leroy and Bernstein, 1971) $D_0 = 19997.2\ \text{cm}^{-1} = 2.48$ eV, and the electron affinity of molecular chlorine (Chupka *et al.*, 1971) $E_\text{A} = 2.38$ eV, they calculate an electron affinity of the dechlorinated species *cis*-diammineplatinum (CDP) $E_\text{A} \geq 2.9$ eV. The competing reaction involving the dissociation of the two amine ligands was not considered to be thermodynamically favored because of the lack of a measurable electron affinity in gas-phase NH_3. Furthermore, Kopyra and coworkers propose that this reaction does not proceed through any radical intermediate.

We investigate the one-electron scattering properties of CDDP and its derivatives within the single-center expansion technique (Gianturco and Jain, 1986) and we compare the electron attachment energies of CDDP which we found as resonances with the energy considerations reported by Kopyra *et al.* (Kopyra *et al.*, 2009), which we shall discuss in further detail.

The platinum atom constitutes not only the first transition metal target but also the largest atomic center ($Z = 78$) we have treated using *ab initio* scattering methods; moreover, we are not aware of any *ab initio* or DFT electron scattering study to date involving cisplatin or its dechlorinated derivatives. Very recently, Msezane and coworkers (Felfli *et al.*, 2010; Msezane *et al.*, 2008) have computed low energy cross sections and resonance energies for neutral and excited Au and Pt atoms using the Mulholland formula with complex angular momenta analysis. Electron scattering calculations from 5*d* block atoms well described within a single electronic configuration, such as Hg, with a ground state configuration $(6s)^2\ {}^1S$ (Burrow *et al.*, 1998; Fursa *et al.*, 2003; Zatsarinny and Bartschat, 2009), or possessing a minimal number of active electrons, such as Pb (Tosic *et al.*, 2008; Wijesundera *et al.*, 1992), are well represented in the literature. By contrast, molecular dynamics calculations involving transition metal complexes either in the gas phase, or through the incorporation of solvent effects with various model interactions, have long made use of density functional theory (DFT) (Dedieu, 2000; Fortunelli, 1999; Zhang *et al.*, 2001)for modeling the relevant interactions. The chief aim of our study is to provide a computationally realistic treatment of the electron attachment mechanism for CDDP to unravel the possible elementary mechanism that presides over its macroscopic role as a radiosensitizing compound. This work is organized as follows: In Sec. III.B we present details of the geometry optimization of CDDP and the convergence parameters of the scattering calculations. In Sec. III.C we discuss the results of the current calculation, i.e. computed integral cross sections and possible low-energy resonant states, respectively. In Sec. III.D we present future areas of investigations.

B. Computational details

1. Geometry optimization of CDDP

Preliminary geometry optimizations and frequency analysis using the GAUSSIAN03 code suite (Frisch *et al.*, 2004) were conducted using the Becke three parameter exchange functional (Becke, 1993a,b) and the Lee-Yang-Parr correlation functional (Lee *et al.*, 1988) (GAUSSIAN03 keyword: B3LYP) from a variety of initial nuclear coordinates. Treatment of the Pt atom consisted of two standard relativistic effective core potential (ECP): the Stuttgart-Dresden ECP (GAUSSIAN03 keyword: SDD) which uses the MWB-60 pseudopotential (Andrae *et al.*, 1990), and the Los Alamos ECP (GAUSSIAN03 keyword: LANL2DZ) using the Hay and Wadt relativistic pseudopotential (Hay and Wadt,

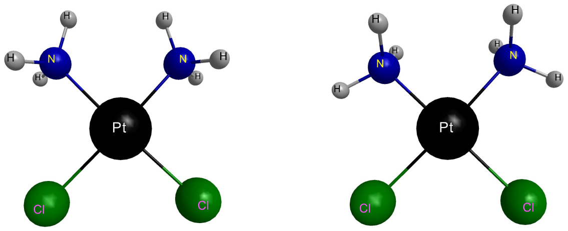

FIG. 11 The experimental crystal structures of *cis*-diamminedichloroplatinum(II) in two stereoisomers of the amine group. The isomer on the right is found by DFT optimization to be the global minimum structure. Both structures were created with the MACMOLPLOT utility of Bode and Gordon, 1998.

1985). The remaining atoms were described via the Dunning-Huzinaga double zeta basis set (GAUSSIAN03 keyword: D95), with one *d* and *p* polarizing function placed on the heavy atoms and the hydrogens, respectively.

The generally accepted molecular structure of CDDP has been obtained from X-ray crystal structure of the CDDP dimer, which possesses triclinic symmetry (Milburn and Truter, 1966). Consequently, the dimers not only have unequal PtCl and PtN bond lengths, but also the ligands do not lie on a single molecular plane. In order to improve the convergence of our geometry optimizations through the use of symmetrized nuclear coordinates, we have considered two structures, one retaining the experimental bond lengths and parameters as given in Table 8 but possessing a molecular plane C_s, and the other from a synthetic C_{2v} geometry, the Pt, N, and Cl atoms fixed on a plane, bond angles between ligands initialized to 90° and the *r*PtCl and *r*PtN bond lengths set to their respective average crystallographic distances given in Milburn and Truter, 1966. Because the orientation of the hydrogen atoms of the amine groups with respect to the molecular plane is not apparent from the crystal structure, we have considered two orientations, as shown in Fig. 11. The amine hydrogens in both views were initially fixed to tetrahedral bond lengths (1.008 Å) and angles (109.0°). Subsequent frequency analysis on the C_s and C_{2v} optimized ge-

TABLE 8 Geometry parameters of *cis*-diamminedichloroplatinum(II) from the X-ray crystallographic data of Milburn *et al.* (Milburn and Truter, 1966). Bond lengths *r*XY in Angstrom and bond angles *a*XYZ in degrees.

Geometry parameter	Parameter
*r*PtCl1	2.328
*r*PtCl2	2.333
*r*PtN1	1.95
*r*PtN2	2.05
*r*NH	1.087
*a*ClPtCl	91.09
*a*ClPtN1	88.5
*a*ClPtN2	92.0
*a*PtNH	109.0

ometries indicates that the amine structure in the right panel of Fig. 11 is a true minimum of the potential energy surface, whereas the other orientation yields a second order saddle point, with two negative frequencies stemming from out-of-plane amine wagging motions.

After concluding the major portion of the DFT optimizations, we have encountered a paper (Wysokinski and Michalska, 2001) that suggests that common exchange functionals including the Becke three parameter functional are inappropriate to calculate structural properties of platinum complexes. The authors suggest to use instead the Perdew-Wang (PW) (Perdew *et al.*, 1992; Perdew and Wang, 1992) exchange functional as an alternative. Accordingly, we have performed geometry optimizations (Frisch *et al.*, 2004) using the GAUSSIAN03 internally-modified Perdew-Wang density functional (Adamo and Barone, 1998) (keyword: mPW1PW91, hereafter abbreviated mPW), selecting the SDD effective core potential of Pt atom and retaining the D95(d,p) basis set for the ligands, as this level of theory was found to produce relatively better converged optimizations than the B3LYP functional. We selected the C_{2v} optimized structure to retain the greatest number of sym-

TABLE 9 Optimized internal coordinates of CDDP in C_{2v} symmetry using the mPW density functional and the Stuttgart-Dresden (SDD) Pt ECP. The ligand atoms are described with the D95(d,p) basis set. Bond lengths *r*XY in Angstrom and bond angles *a*XYZ in degrees. DFT energies *E* and gradients RMS values in au.

Geometry parameter	mPW/D95(d,p)[SDD]
*r*PtCl	2.31250
*r*PtN	2.08595
*r*NH	1.02592
*r*NH	1.01713
*a*ClPtCl	95.36476
*a*NPtN	98.37213
*a*ClPtN	83.13156
E	−1153.05169010
RMS	0.00005243

metry elements to reduce the computational effort for subsequent calculations. Internal coordinates of CDDP after optimization with the PW functional and the SDD ECP are presented in Table 9, and the Cartesian coordinates are given in Table 10.

2. *Convergence parameters*

The scattering calculations on CDDP were performed using the EPOLYSCAT (Gianturco *et al.*, 1994; Natalense and Lucchese, 1999) code suite of Lucchese and collaborators, which employs a single-center expansion (SCE) of the bound and continuum electron wave functions to reduce the non-relativistic Schrödinger equation into a series of one-dimensional angular and radial equations that are solved using the Schwinger variational method with Padé approximant corrections. The interaction potential between the continuum electron and the bound electrons of the targets is represented by one of two optical potentials: the exact static-exchange potential resulting from the solution of the nonrela-

TABLE 10 Cartesian coordinates (in Å) of the mPW/D95(d,p)[SDD] optimized geometry in C_{2v} symmetry of CDDP in standard orientation.

Center	Cartesian coordinate		
Pt	0.000000	0.000000	0.185928
Cl	0.000000	1.709584	−1.370635
Cl	0.000000	−1.709584	−1.370635
N	0.000000	1.578726	1.549318
N	0.000000	−1.578726	1.549318
H	0.000000	2.394580	0.927310
H	0.000000	−2.394580	0.927310
H	−0.827603	1.628158	2.138540
H	0.827603	−1.628158	2.138540
H	0.827603	1.628158	2.138540
H	−0.827603	−1.628158	2.138540

tivistic scattering equation within the Hartree-Fock approximation including DFT expressions of Perdew and Zunger (Perdew and Zunger, 1981) for electron correlation (SECP); and an entirely local Hara exchange (Hara, 1967) and Perdew-Zunger model interaction potential (ASMECP) that admits solutions in terms of Siegert eigenstates (Tolstikhin *et al.*, 1997) and which is especially useful in one-electron resonance analysis. Details of the computational method may be found in the given references. However, the current implementation of the scattering code treats only gas phase scattering and does not admit the use of ECPs. Therefore, we must consider an all-electron basis set for the Pt atom, selecting, for this purpose, the scalar relativistic, generally-contracted polarized valence triple zeta (VTZP) basis set developed by Noro and collaborators (Koga *et al.*, 2000; Osanai *et al.*, 2004). For the Cl and N atoms, we likewise considered polarized relativistic valence triple zeta basis sets (Koga *et al.*, 2000; Noro *et al.*, 1997; Sekiya *et al.*, 1998), while the H atom

TABLE 11 Spherical gaussian basis set contraction scheme used for the transition metal center and ligand atoms of CDDP.

Center	*s*	*p*	*d*	*f*
Pt	25,25,25,25,25,25,1	20,20,20,20,4	14,14,14,11,3	11,5
Cl	14,14,14,1,1	9,9,1,1	3,1	2
N	10,10,1,1	5,1,1,1	2,1	1
H	4,1,1	2,1	2	

was treated using a nonrelativistic VTZP basis set (Noro *et al.*, 2003). In Table 11 we list the basis set contractions for each of the atomic centers of CDDP.

These basis sets have been optimized for use in valence-correlated post-Hartree Fock and MCSCF calculations, incorporating scalar relativistic effects through the third-order Douglas-Kroll-Hess (DKH3) Hamiltonian (Douglas and Kroll, 1974; Wolf *et al.*, 2002). Consequently, we collectively denote this basis sets of the Pt, Cl, and N atoms DKH3-VTZP, and of the H atom VTZP. All basis sets were obtained from the database currently maintained in Noro *et al.*, 2012. The spherical gaussian exponents and contraction coefficients of the selected basis sets may be found in the database and in the given references.

The C_{2v} CDDP target orbitals were obtained at the Hartree-Fock level including scalar DKH3 relativistic corrections using the MOLPRO2006 code suite (Werner *et al.*, 2006). Electron correlation energy was approximated by full-core, second-order Møller-Plesset (FMP2) perturbation theory, which will introduce error as the basis sets were optimized to be used only for valence-electron correlation, as stated previously. We make use of the mPW/D95(d,p)[SDD] geometry in the coordinates of Table 10 in all subsequent scattering calculations.

In the single-center expansion of the CDDP and continuum orbitals, all partial waves up to $l_{\max} = 80$ were retained. At this level of expansion, with the exception of the Cl 1s $(2b_2)^2$ and $(5a_1)^2$ orbitals, which were normalized only to 0.884, the remaining sixty-four target molecular orbitals of CDDP were normalized to 0.980 or better. The maximum l

in the asymptotic scattering region is $l_{\text{max}}^{\text{asymp}} = 17$. The maximum distance of the radial grid was $r_{\text{max}} = 9.76623$ Å . We include polarization by placing the diagonal terms of the dipole polarizability tensor $\alpha_{\alpha\beta}$ calculated at the FMP2 level, namely $\alpha_{\text{xx}} = 54.627841$ au, $\alpha_{\text{yy}} = 104.192194$ au, and $\alpha_{\text{zz}} = 95.987186$ au, at the target center of mass. The radial distance at which the DFT correlation potential was matched to the asymptotic polarizability was $r_m = 3.21204$ Å . The maximum l in the partial wave expansion of the T-matrix solutions was $l_{\text{Tmax}}^{\text{SECP}} = 5$ as computed by SECP and $l_{\text{Tmax}}^{\text{ASMECP}} = 15$ using the entirely local ASMECP potential. Because CDDP is polar, with a computed dipole moment $\mu^{\text{MP2}} = 11.7844$ D, the rotationally-summed total cross section obtained within the fixed-nuclei approximation diverges at low scattering energies (Rescigno and Lengsfield, 1992). The present calculations yielded unstable integrations below an electron scattering energy of 0.5 eV; therefore, our method may not locate CDDP resonances or bound states resulting from electron scattering below this energy.

C. Computational results

1. Preliminary cross sections for the isolated Pt atom

To gauge the extent to which the total cross section of CDDP depends on solely the Pt atom, we have computed integrated cross sections for isolated transition metal center. To the best of our knowledge, there have been no experimental cross sections generated for the Pt atom in the gas phase.

The Pt atom has a seven-fold degenerate electronic ground state configuration $(5d^9 6s)^3D_3$, with low-lying $^1D_2$ and $(5d^8 6s^2)$ $^3F_4$ states approximately 0.1 eV higher in energy. The lowest-energy $l = 0$ state, with a configuration $(5d^{10})$ $^1S_0$, is 0.76 eV above the ground state (Hotop and Lineberger, 1973). The anion Pt$^-$ has a ground state configuration $(5d^9 6s^2)$ $^2D_{5/2}$, with a measured adiabatic electron affinity of $E_{\text{A}} = 2.13$ eV, and two excited states, a 1.21 eV $(5d^9 6s^2)$ $^2D_{3/2}$ state and a 1.28 eV $(5d^{10} 6s^1)$ $^2S_{1/2}$ anionic state that was predicted to exist by multiconfigurational Dirac-Fock structure calculations but was not observed experimentally (Bilodeau *et al.*, 1999) until quite recently (Andersson *et al.*, 2009).

To circumvent the difficulties that arise in treating a degenerate open-shell molecule within the static-exchange approximation, we have calculated cross sections for Pt atom in the excited $(5d^{10})\ ^1S$ state using the EPOLYSCAT code. We briefly detail the computational method as follows: the SCF orbitals were obtained from the MOLPRO2006 code suite using the Pt DKH3-VTZP basis set augmented with $[1s1p1d1f]$ diffuse functions as given in Noro *et al.*, 2012 which we henceforth denote as aug-DKH3-VTZP. We find a singlet state SCF energy of -18414.48920502 au and an FMP2 energy of -18415.00593488 au, both of which are below the ^3D SCF energy of -18411.40349587 au reported for this basis set.

The orbitals of the atomic center are given in the Abelian D_{2h} point group from the SCF MOLPRO2006 output. However, for the current calculations in EPOLYSCAT, we construct the atom in an icosahedral symmetry (I_h), since, for reference (Kettle and Smith, 1967), the irreducible representations of I_h uniquely span the lowest $l \leq 2$ atomic orbital symmetry, namely, $s \rightarrow a_g$, $p \rightarrow t_{1u}$, and $d \rightarrow h_g$. All higher-order angular momenta, *e.g.* $f \rightarrow t_{2u} + g_u$, span multiple irreducible representations of the icosahedral point group. Accordingly, we generate SECP electron scattering cross sections from Pt in the singlet state ^1A_g, momentarily neglecting the more complex treatment necessary to treat electron scattering from the ground triplet state ^3H_g. For ease of discussion, we shall employ atomic symmetry when presenting SECP and model results for Pt atom. In the single-center expansion of the continuum orbital and the bound Pt orbitals, partial waves were expanded to a maximum angular momentum of $l_{\text{max}}^{\text{Pt}} = 16$ for targets in the singlet state. Truncation of the SCE at this value resulted in all Pt orbitals normalized to unity. Orthogonality conditions of the static-exchange operator were enforced for the continuum electron to the bound target orbitals under varying constraints: the continuum orbital was orthogonalized to all bound orbitals, for all but the degenerate $5d$ orbitals, and all but the inner- and outer valence $5s$, $5p$, $4f$, and $5d$ orbitals of the ^1S state wave function. We have treated polarization through placing the computed singlet FMP2 isotropic polarizability $\bar{\alpha} = 30.730518$

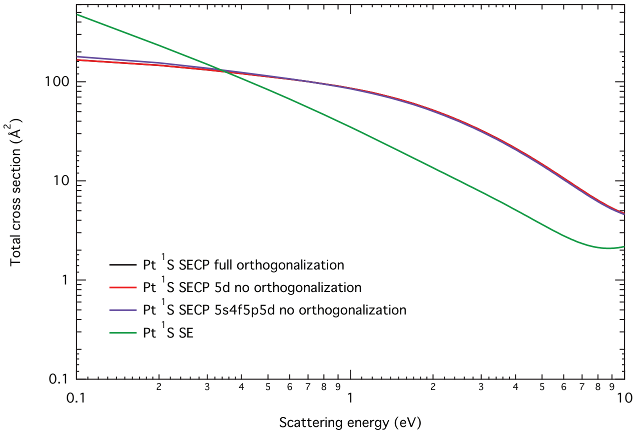

FIG. 12 Computed SECP integrated cross sections for electron scattering from Pt atom in the ^1S state comparing three levels of continuum orthogonalization. Scattering energies are in eV and cross sections in $\mathring{A}^2$.

au on the Pt center. The matching radius of the static polarizability to the model DFT correlation potential was $r_{\mathrm{match}} = 2.939747$ Å .

To the best of our knowledge, the only electron scattering spectra available for the platinum atom are the computational studies of Msezane and collaborators (Felfli *et al.*, 2010; Msezane *et al.*, 2008), as stated in the Introduction, who have reported total cross sections and resonant scattering states for Pt and Au using a Regge pole method and a semiempirical Thomas-Fermi interaction potential. Msezane and collaborators find three resonances for Pt, with complex angular momentum and energy $L = 1$ (0.14 eV), $L = 3$ (1.12 eV), and $L = 5$ (2.2 eV), the last predicted to correspond to the Pt anionic bound state. The computed total cross section in Msezane *et al.*, 2008 exhibits two peaks below 2.5 eV at the resonant energies superimposed upon a background decaying from a maximum (≥ 1500 au $= 420$ $\mathring{A}^2$) at threshold.

In Fig. 12, we present the ^1S SECP integral cross sections at three levels approximation of the static-exchange interaction potential, as mentioned previously. With the exception of the lowest scattering energies in the ^2S symmetry, these orthogonality conditions do not result in major differences in either the total or the partial cross sections shown in Fig 13. Unlike the total cross section presented in Fig. 4 of Msezane *et al.*, 2008, the ^1S SECP total

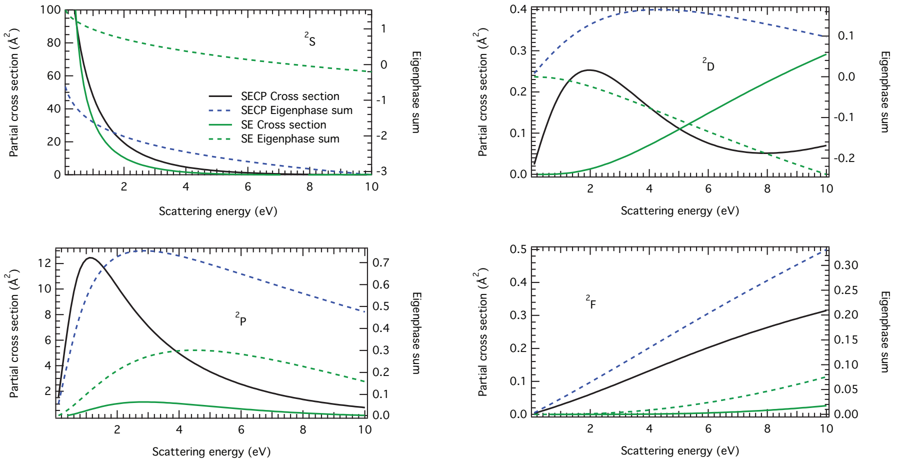

FIG. 13 Computed SECP integrated partial cross sections for electron scattering from Pt atom in the ^1S state. The continuum electron is orthogonalized to all bound orbitals. Scattering energies are in eV and cross sections in Å^2.

TABLE 12 Selected roots (complex zeros of the inverse S-matrix) of the Siegert eigenstates of the ASMECP potential for Pt atom in ^1S symmetry. Real energies E_R and widths Γ are in eV. The continuum electron is orthogonalized to all bound orbitals.

Root	E_R	Γ
	^2P	
1	0.892328	2.477358
2	1.896298	3.825192
3	3.327269	5.273708
4	5.158943	6.760866
	^2D	
1	0.528934	2.215096
2	1.518571	3.451642
3	2.852494	4.783052
4	4.540321	6.180572

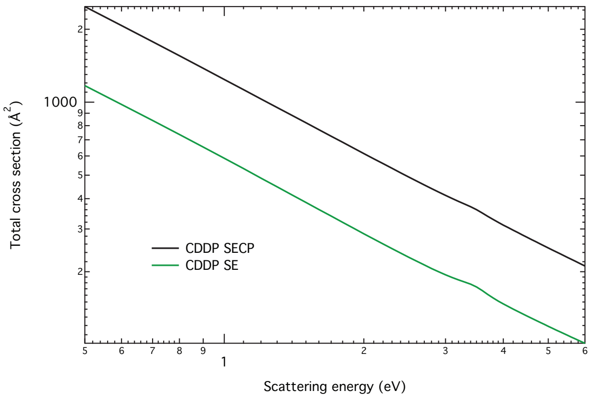

FIG. 14 Computed SECP integrated cross sections for electron scattering from *cis*-diamminedichloroplatinum(II). Scattering energies are in eV and cross sections in Å^2.

cross sections display a monotonic decay at increasing scattering energies. Incidentally, the SECP total cross sections computed at all levels of orthogonalization are uniformly lower in magnitude than those calculated in Msezane *et al.*, 2008.

In Fig. 13 SECP partial cross sections (solid lines) and eigenphase sums (dashed lines) in ^2S, ^2P, ^2D, and ^2F symmetries are displayed. We see that the ^2S partial cross section provides the dominant intensity to the total cross section, whereas the ^2D and ^2F cross sections are small at all scattering energies, with cross sections below $\sigma = 0.5$ Å^2. The ^2P partial cross section, however, displays a maximum $\sigma = 12$ Å^2 near 1.0 eV electron energy, with the corresponding eigenphase sum rising to $\delta_E = \pi/4$ near 2.8 eV. Accordingly, we isolate the complex zeroes E_R and Γ of the inverse S-matrix for scattering in ^2P symmetry using the ASMECP potential as detailed previously and present the results in Table 12. The different levels of orthogonalization were not found to shift appreciably the real or imaginary energies of the complex pole search, which are significantly larger (implying shorter-lived resonances) than those identified in the complex angular momentum analysis of Msezane *et al.*, 2008.

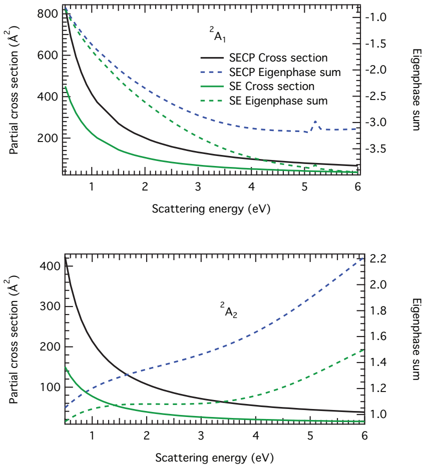

FIG. 15 Computed SECP partial cross sections for electron scattering from *cis*-diamminedichloroplatinum(II). Scattering energies are in eV and cross sections in Å^2.

2. *Total and partial cross sections of CDDP*

In Fig. 14 we present the integral elastic cross section for electron collision with *cis*-diamminedichloroplatinum(II) in its ground electronic state and in the optimized C_{2v} mPW/D95(d,p)[SDD] geometry given in Column II of Table 9. The computed cross section, ten times the magnitude of the isolated ^1S Pt atom shown in Fig. 12 discussed in Sec. III.C.1, displays a monotonic profile over most of the computed scattering energies from the initial maximum at 0.5 eV. No features of resonant scattering is apparent in the total cross section, though this feature may be hidden by the large background contributions due to the presence of the computed 11.8 debye dipole moment. The SECP partial cross sections (solid lines) and the corresponding eigenphase sums (dashed lines) are reproduced in Fig. 15. The $^2B_2$ partial cross section exhibits the most likely candidate for resonance scattering although the SE and SECP eigenphase sums increase by less than π near 3.6 eV. Notably, the concomitant rise in the cross section at the midpoint of the rising phase sum is not evident due to the large background. The $^2A_2$ and $^2B_1$ partial cross sections, by contrast, indicate little evidence of resonant scattering, while the $^2A_1$ eigenphase sum shows a discontinuity near 5.2 eV that bears the features of a possible computational

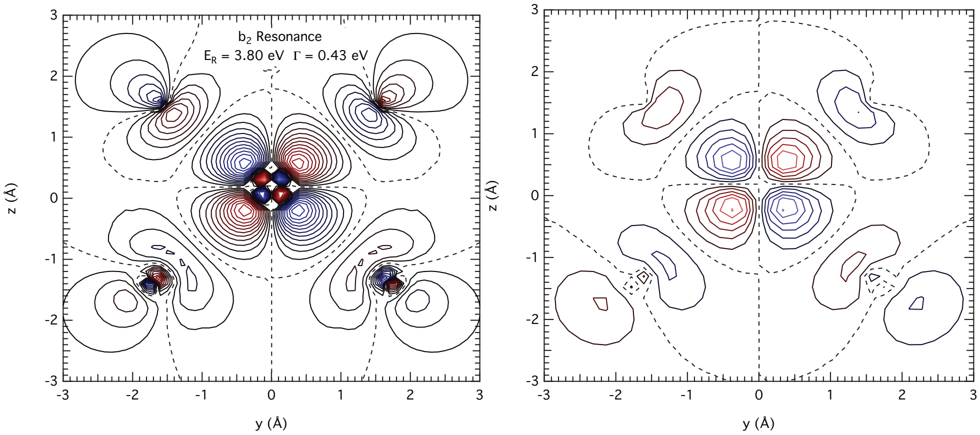

FIG. 16 Left-hand panel: Contour plot of the real part of the ASMECP $^2B_2$ resonance wave function of *cis*-diamminedichloroplatinum(II). Right-hand panel: Contour plot of the lowest-unoccupied molecular orbital (LUMO) of the mPW/D95(d,p)[SDD] calculation at the equilibrium geometry. The plots lie in the *yz* plane of the molecule in standard orientation, with each isocontour separated by 0.5 Å . Nodal surfaces are depicted as dashed lines.

artifact, as it does not present at this energy a concurrent increase in the cross section at this energy.

Resonant scattering features have been identified in each IR through the ASMECP method described previously, but we concentrate on those in the $^2B_2$ symmetry. To admit all possible resonances, we constrain the search over the real energy axis from 0.5 to 8.0 eV, while allowing the largest imaginary energy to be 8.44 eV. Among the twenty-four poles isolated in the search, we find one with complex coordinates (in eV) $(3.795, -0.216)$ that nearly matches the peak found in the SECP cross section. A contour plot of the real part of the resonant wave function, shown in Fig. 16, indicates that electron density is concentrated mostly on the Pt atom, with remaining density centered on each Cl atom. For comparison, the lowest-energy virtual orbital (in b_2 symmetry) from the PW DFT calculation is also presented. Interestingly, the $^2B_2$ resonance wave function we compute with the ASMECP operator shows similar nodal structure as that from the contour plot of the LUMO of CDDP computed at the B3LYP/LANL2DZ level which was shown by

TABLE 13 Complex eigenenergy of the CDDP ${}^{2}B_{2}$ resonance as a function of the rPtCl bond length (in Å) as obtained by the ASMECP method. Resonance energies E_R and widths Γ are in eV.

Bond length (Å)	E_R (eV)	Γ (eV)
2.0	5.476569	0.680460
2.1	4.954794	0.532590
2.2	4.391069	0.471288
2.3	3.855420	0.447028
2.4	3.340604	0.433306
2.5	2.757781	0.392654
2.6	2.233428	0.374642

Fig. 4 of Kopyra *et al.*, 2009. It is instructive to compare the ASMECP value of the CDDP resonance $E_R = 3.8$ eV, $\Gamma = 0.43$ eV, and the peak of the SECP ${}^{2}B_{2}$ partial cross section near $E = 3.6$ eV, to the proposed electron affinity of CDP being greater than 2.9 eV in Kopyra *et al.* (Kopyra *et al.*, 2009) in the light of the energy balance considerations. From their analysis, the cleavage of the two Pt-Cl bonds in the gaseous CDDP was estimated to be about 5.30 eV, while the concomitant formation of Cl_2 would result in an excess energy of 2.52 eV. We conjecture, from our computed resonant electron energy of about 3.6 eV, that the above excess energy could compensate for the residual threshold energy and subsequently cause the appearance of the $[Pt(NH_3)_2]^-$ signal at the threshold energy. The need to indicate a large value E_A for the CDP anion may therefore be not so compelling. It is certainly encouraging to see that our present calculations agree broadly with the various energy estimates and with the peak at zero energy seen by experiment.

We have performed an additional analysis of the dependence of the isolated ${}^{2}B_{2}$ resonance on the geometrical coordinates of CDDP in order to provide further insight into the elementary attachment mechanism driven by the resonant scattering. Specifically, we have determined the extent to which the spatial density of the resonant electron remains localized on the Pt atom when one introduces a symmetric (a_1) stretch of the rPtCl bonds.

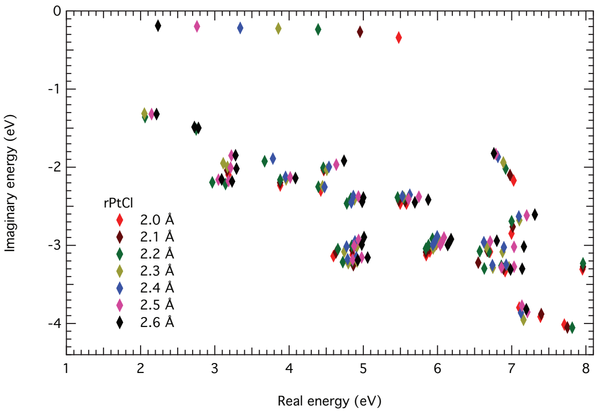

FIG. 17 Residue plot of the selected roots (complex zeros of the inverse *S*-matrix) of the Siegert eigenstates of the ASMECP potential for CDDP in b_2 symmetry. The real and complex energies are in eV.

A rigid structure scan was performed on the mPW/D95(d,p)[SDD] target (Frisch *et al.*, 2004) as the *r*PtCl bond coordinates were increased in twenty 0.1 Å symmetry-preserving increments from 2.0 Å to 4.0 Å , undertaking at each radial coordinate an ASMECP resonance search in b_2 symmetry. To account for the dispersion of the polarization interaction at increasing *r*PtCl bond separation, the CDDP FMP2 dipole polarizability was distributed among each heavy center through a partitioning scheme in which the experimental (NIST, 2012) isotropic polarizabilities of the Cl atom (14.73 au) and ammonia (14.21 au) were placed on each relevant atomic center while retaining the remaining FMP2 polarization contributions for the Pt atom alone (27.08 au). As in the previous resonance search at the equilibrium geometry, after limiting the search for poles with real energies less than 8.0 eV and complex energies less than 8.4 eV, we find a considerable number of poles for *r*PtCl bond lengths of less than $r = 2.7$ Å , as illustrated in Fig. 17. Clearly distinguished from the background poles, however, are a significant sequence of isolated poles near the real energy axis that we identify as CDDP scattering resonances. The resonance energies E_R and widths Γ in eV of the isolated b_2 poles are given in Table 13 at each bond coordinate for which they were found to exist. At increasing *r*PtCl bond lengths, both the energy of the resonance and its associated width decrease. Notably, isolated resonances were no longer found when the *r*PtCl bond length exceeded $r = 2.6$ Å , implying that the resonance

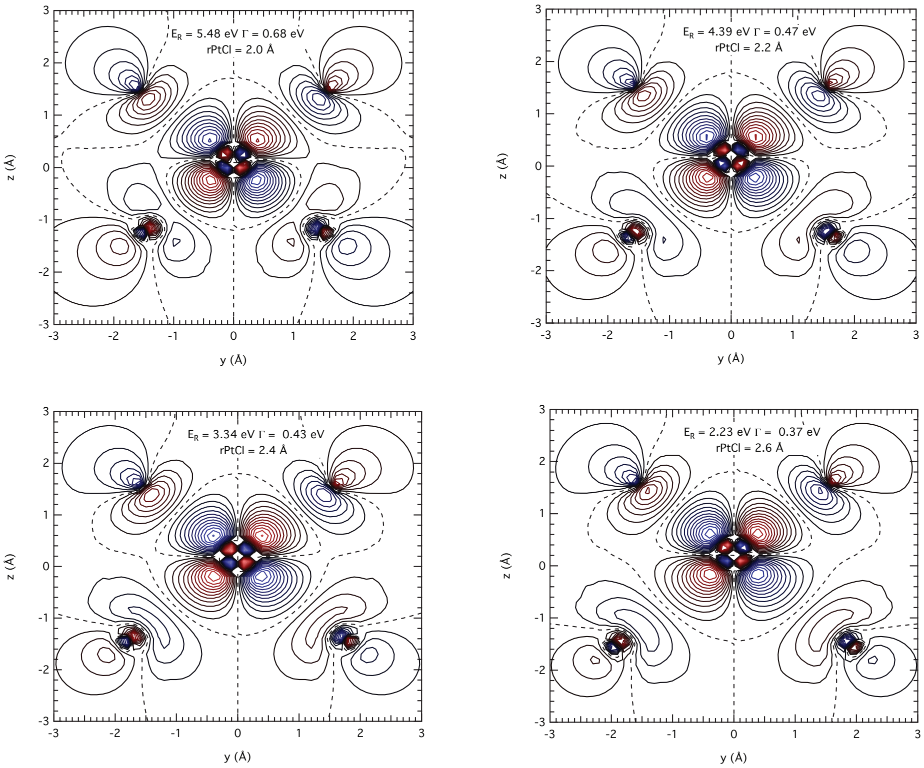

FIG. 18 Contour plots of the real part of the $^2B_2$ ASMECP resonance wave function with the associated resonance parameters E_R and Γ (in eV) given at selected *r*PtCl bond lengths. All plots lie in the *yz* plane, with the target shown in standard orientation. Each isocontour is separated 0.5 Å , with nodes given as dashed lines.

energy decreases to become that of an anionic bound states at the distances approaching PtCl bond dissociation. This finding is in accord with what was suggested by the experiment of Kopyra *et al.*, 2009 that surmised the formation of neutral Cl_2 molecules and the attachment of the stable anionic residue to the DNA moiety.

In Fig. 18 we display the contour plots of the real part of the $^2B_2$ resonance wave function at selected radial distances for which it is found to exist. As is evident, the excess density of the continuum electron remains well localized on the Pt atom at each increasing radial distance. In conjunction with the previous observation that no resonances are found beyond large values of the PtCl bonds, we conjecture that the excess electron density of the continuum electron is retained on the $[Pt(NH_3)_2]$ complex as a bound anion, and not on either of the departing Cl atoms which derive from the electron-induced dissociation of the CDDP complex.

D. Conclusions

We have obtained partial and total cross sections cross sections for CDDP and the Pt atom in a singlet electronic state using single determinant descriptions of both complex targets that incorporate relativistic contraction of the target orbitals through an all-electron basis set and through *ab initio* and model optical potentials that recover the primary continuum + target electron interactions of the scattering event. The calculations have employed a model-oriented approach in order to obtain a molecular description of the possible role of the target species in activation to DNA attachment within reasonable computational costs. We expect, however, that further refinements of various aspects of our modelling of the quantum dynamics might provide ways of increasing the reliability of our findings. Even at this preliminary level, however, we have already seen that our results yield fairly clear suggestions on the possible elementary mechanisms which preside over the electron-driven action of CDDP on DNA replication properties.

The current results, strengthened by the currently ongoing calculations on the Cl_2 species, nonetheless provide already a realistic overview to e^- scattering properties from gas-phase CDDP and the isolated Pt atom, which we can summarize as follows:

1. The SECP cross section for Pt atom in the ^1S state displays a monotonic decay from the threshold energies, with no prominent resonant scattering features present in any IR corresponding to the $l = 0, 1, 2$ atomic symmetries. This finding is in contrast to the results of Msezene and coworkers, who locate three well-characterized scattering resonances by their complex angular momentum method.

2. The SECP cross section for CDDP, which may be treated as the interaction of a free electron with the target orbitals of the Pt atom distorted by the anisotropic electron field induced by the ligand molecules, shows a largely isotropic decay behavior at higher collision energies. The CDDP cross section is an order of magnitude greater

than that of ^1S Pt atom. While no obvious scattering properties were observed in any of the partial cross sections, a resonant feature was seen in the $^2B_2$ eigenphase sum, the properties of which we have further characterized by using the ASMECP model potential.

3. To determine the possible spatial evolution of the $^2B_2$ resonance, we have carried out a systematic investigation of the resonance behaviour resulting from the symmetric stretch of the *r*PtCl bond coordinates. Our calculations discussed in the previous section show that the resonance is lowered in energy as the bond length is increased, in accord with results from a similar research conducted on the C-OH stretch of several amino acid species (Panosetti *et al.*, 2010), and it also exhibits an increased stability by having narrower width values as the bond length is stretched towards dissociation, a clear sign of the formation of a stable anionic fragment from the initial CDDP complex.

4. Contour plots of the resonance wave function indicate that the excess electron density remains centered on the Pt atom of CDDP at all bond lengths until dissociation, which here suggests the creation of the products $[\mathrm{Pt(NH_3)_2}]^- + 2\mathrm{Cl}$, with the electron density concentrated on the dechlorinated species.

In spite of the simplified, pseudo one-dimensional description of the rearrangement process after the primary electron attachment event, we have shown in this work that several elementary features of the quantum dynamics with electrons that were initially suggested by the experiments on the title molecule are indeed confirmed by our calculations, i.e. the formation of a stable $[\mathrm{Pt(NH_3)_2}]^-$ complex, the detachment of free chlorine atoms, and their possible stabilization as $\mathrm{Cl_2}$ molecules after fragmentation.

IV. APPLICATION OF THE MULTICHANNEL CONFIGURATION INTERACTION METHOD TO ELECTRON SCATTERING FROM CONSTITUENTS OF THE CIS-DIAMMINEDICHLOROPLATINUM(II) MOLECULE: MOLECULAR CHLORINE AND THE PLATINUM ATOM

A. Introduction

This study serves as a companion to the work on electron scattering and resonance phenomena of the inorganic molecular complex cis-diamminedichloroplatinum(II), $[\mathrm{Pt(NH_3)_2Cl_2}]$ (CDDP), better known under its clinical trial name cisplatin (Carey *et al.*, 2011). In the previous section (Sec. III) we discussed electron scattering cross sections from the CDDP molecule and the platinum transition metal center within the static-exchange approximation (Lane, 1980), accounting for dynamic electron correlation and the dipole polarizability through the use of an optical potential (Perdew and Zunger, 1981). The relativistic contraction of the core and inner valence shells of the target orbitals were realized through the use of scalar relativistic all-electron basis sets for the Pt, Cl, and N atoms (Noro *et al.*, 2012) to construct the single-determinant SCF wave function. As CDDP may be regarded as a coordinate complex in which the orbitals of the platinum atom are distorted in an electric field induced by the ligand atoms, we have also computed low-energy cross sections for the isolated Pt atom in the previous study. Because the electronic ground state of Pt is $(5d^9 6s)\ ^3D$, the computational model must account for the manifold of states that arise from the interaction of a continuum electron with the degenerate triplet ground state. Consequently, we constrained the electronic configuration of the platinum atom to an excited singlet state $(5d^{10})\ ^1S$ for ease of computation within the static-exchange approximation.

The intent of this section is twofold. We present a detailed study of the scattering phenomena of low-energy electrons with $\mathrm{Cl_2}$ in its $^1\Sigma_g^+$ ground state using multiconfigurational scattering methods, which may provide a more complete picture of the scattering process. Additionally, electron scattering cross sections with platinum atom will provide, to the best of our knowledge, the first *ab initio* results for this heavy transition metal center.

For this purpose we employ the multichannel configuration interaction method using the theory developed by Stratmann and Lucchese (Stratmann and Lucchese, 1995). The theoretical method is based on a close-coupling formalism, in which the target wave function consists of an expansion in configuration state functions (CSFs) of antisymmetrized product of the N-electron wave function and unbound electron channels. Naturally the target wave function must include all open channels within the range of collision energies of the continuum electron. Because the number of open channels becomes infinite past the target ionization energy, the close-coupling series must be truncated for the scattering calculation to remain computationally tractable. Usually, this involves limiting the expansion only to the most relevant electronic configurations as determined, for example, from a bound-state configuration interaction (CI) calculation. This unphysical cutoff introduces pathological features into the resulting scattering cross sections if energetically open channel configurations are neglected in the expansion (Burke and Mitchell, 1973).

In spite of the challenges inherent within the theory, multichannel calculations have the advantage of describing two-electron scattering and ionization effects in a theoretically sound manner, including target relaxation, dynamic correlation, and interchannel coupling. Asymptotic target orbital polarization resulting from the long-range interaction of the free electron is another important scattering effect (Winstead and McKoy, 1998). Unlike the two-electron processes amenable to CSF-based target expansions, polarization is an essentially perturbative interaction that is most effectively recovered through the use of optical potentials chosen to reproduce the effect of the dipole distortion (Padial and Norcross, 1984) or through augmenting the SCF or MCSCF wave function with a set of virtual polarizing orbitals optimized in a coupled perturbed Hartree-Fock scheme (Schneider and Collins, 1984). In the scattering theories making use of multiconfigurational targets, the second approach may be considered the more conceptually secure one (Rescigno *et al.*, 1995a).

The multiconfigurational complex Kohn variational method (McCurdy and Rescigno, 1989) was used in the study of Rescigno on electron scattering from molecular chlorine (Rescigno, 1994), which at the time had no published experimental electron scattering spectra and remains, to the best of our knowledge, the only computational investigation on this important molecule to date. The trial wave function included correlation through single-electron excitations into the lowest virtual orbital, relaxing the orthogonality condition by retaining penetration terms that correspond only to the dominant configuration of each scattering channel. At the SCF level, polarization interactions were included by a set of polarizing orbitals orthogonal to the valence shells. The correlated target wave functions were found to recover only a fraction of the total polarizability and yielded a cross section that overestimated the $^2\Sigma_g^+$ component at the lowest 0.5 eV to 3.5 eV scattering energies. The correlated plus polarized SCF trial wave function, in comparison, resulted in a total cross section that was found to be in relative agreement with electron transmission experiment above 1.0 eV conducted several years later by Gulley *et al.* (Gulley *et al.*, 1998a).

The multichannel scattering approach forms the basis of the advanced *R*-matrix methods that has been developed for atomic and molecular electron scattering by numerous researchers through the years (Berrington *et al.*, 1995; Burke *et al.*, 1971, 1977). The essential feature of all *R*-matrix based methods lies in the partition of the configuration space between an interaction region $r < a$ in which the $(N+1)$ target wave function is solved exactly, and an asymptotic region $r > a$ where exchange effects can be neglected and the scattering wave function can be solved using perturbation methods. The two solutions are joined at the matching radius a by the *R*-matrix, from which all scattering properties may be obtained. In most recent calculations on large Z transition metal targets making use of a close-coupled *R*-matrix method (Bostock *et al.*, 2010; Fursa *et al.*, 2009; Vilkas and Ishikawa, 2007; Zatsarinny and Bartschat, 2008), the inner valence and core orbitals are constructed from a Dirac SCF procedure, and a polarization potential is included to recover core-valence interactions between the ionic core and the valence electrons. The valence electrons are constructed by diagonalizing a semi-relativistic Breit-Pauli or fully relativistic Dirac-Fock Hamiltonian in the presence of the ionic core, thereby allowing the correct computational reproduction of the atomic fine structure. The resulting one-electron orbitals are used as target orbitals to perform CI calculations generating the target wave function. Within the inner region, the scattering equations are solved in a close-coupled expansion with a semi-relativistic Breit-Pauli or fully relativistic Dirac-Fock Hamiltonian in a basis composed of the antisymmetrized product of the target wave function and the scattering basis functions. The nature of performing close-coupled expansions using a Dirac-Fock Hamiltonian, however, limits treatment only to heavy atoms with one or two active electrons, as is apparent from the given references.

The intricate nature of the multiconfigurational scattering method necessitates discussion in a consistent manner. In Sec. IV.B, by way of background we present the formulas and terms of the static exchange plus polarization (SECP) theory and the MCCI method. In Secs. IV.C and IV.D we present the computational details of the Cl_2 and Pt target SCF and MCSCF wave functions and convergence criteria of the respective scattering calculations. After a comparison of the respective SECP and MCCI cross sections, we state areas of further investigation in Sec. IV.E.

B. Theory

The Schwinger multichannel electron scattering calculations were performed using the MCCI program suite of Lucchese and coworkers (Bandarage and Lucchese, 1993; Stratmann and Lucchese, 1995), which was developed for photoionization but is easily adapted to electron scattering. The SECP calculations were performed using the EPOLYSCAT code suite of Lucchese and collaborators (Gianturco *et al.*, 1994; Natalense and Lucchese, 1999). Both scattering codes make use of the Born-Oppenheimer approximation allowing the parametric dependence of the electronic wave function on the nuclear coordinates, and the fixed-nuclei approximation, which assumes that the nuclear coordinates remain stationary during the scattering event. Accordingly, neither method may account for electron attachment processes that result in vibrational excitation of the target. We briefly outline the two computational scattering methods employed in this report as follows.

1. *Static-exchange and polarization*

The three-dimensional wave functions of the bound and continuum electrons F are expanded in terms of symmetry-adapted spherical harmonics $X^{p\mu}_{lh}$

$$F^{p\mu}(\mathbf{r},\mathbf{R}) = \sum_{lh} r^{-1} f^{p\mu}_{lh}(r|R) X^{p\mu}_{lh}(\hat{r}), \tag{117}$$

where $p\mu$ label the μ^{th} component of the p^{th} irreducible representation of the point group of the target. The (lh) are the symmetry-adapted (lm)s defined from the expansion

$$X^{p\mu}_{lh}(\hat{r}) = \sum_{m} b^{p\mu}_{lmh} Y_{lm}(\hat{r}). \tag{118}$$

Once the functions have been expanded in terms of the spherical harmonics, inserting them into the nonrelativistic Schrödinger equation results in the close-coupled expressions

$$\begin{aligned} &\left[\frac{d^2}{dr^2} - \frac{l(l+1)}{r^2} + 2(E-\varepsilon_\alpha)\right] f^{p\mu\alpha}_{lh}(r) = \\ 2 &\sum_{l'h',p'\mu',\alpha'} \int dr'\, V^{p\mu\alpha p'\mu'\alpha'}_{lhl'h'}(r,r'|\mathbf{R}) f^{p'\mu'\alpha'}_{l'h'}(r'|\mathbf{R}), \end{aligned} \tag{119}$$

where E is the collision energy and ε_α the electron eigenvalue of the α^{th} scattering state. The kernel of the integral $V^{p\mu\alpha p'\mu'\alpha'}_{lhl'h'}$ therefore represents the interaction potential between the continuum electron and the target state. The form of the interaction potential may be simplified if the expansion over states α is limited to a single state only, such that $\alpha = \alpha' = 1$. If the target is described by a closed-shell SCF wave function, this truncation results in the static-exchange approximation. This approximation can be enhanced by the inclusion of a model optical potential (Perdew and Zunger, 1981) describing dynamical electron correlation, which is smoothly joined to the correct long-range dipole polarizability interaction through various switching functions that are described in Gianturco *et al.*, 1994 and Natalense and Lucchese, 1999.

2. *Multichannel configuration interaction*

In the multichannel configuration interaction method, both the N-electron initial and the $N+1$ electron + target states are constructed from configuration state functions whose coefficients are optimized in a configuration interaction calculation. The interaction of the electron with the initial state CSFs yields target states whose resulting electron configurations constitute unique scattering channels. The CI wave function of the target in the presence of a continuum electron is written as

$$\Psi_{\text{MCCI}} = \sum_{i=1}^{N_c} \Phi_i(\chi_i) = \sum_{i=1}^{N_c} \sum_{j=1}^{N_b} C_{ij} \psi_j(\chi_i) \tag{120}$$

where χ_i is the i^{th} channel scattering state, Φ_i the CI wave function of the ion in channel i, and N_c is the number of channels. Each spin-adapted $N+1$ electron CSF is denoted $\psi_j(\chi_i)$. The Schrödinger equation for the electronic motion is

$$H_N \Psi_{\text{MCCI}} = E \Psi_{\text{MCCI}}, \tag{121}$$

where the electronic Hamiltonian is given by

$$H_N = \sum_{i=1}^{N} f(i) + \sum_{ij}^{N} \frac{1}{r_{ij}} \tag{122}$$

and the one-electron operator $f(i)$ has the usual form

$$f(i) = -\frac{1}{2}\nabla_i^2 - \sum_{\alpha} \frac{Z_\alpha}{r_{i\alpha}}. \tag{123}$$

The scattering equations of Eq. 121 are reduced in a single center expansion (SCE) to a series of ordinary linear integro-differential equations that are solved using the Schwinger variational technique with Padé approximant corrections. This method yields the matrix Lippmann-Schwinger equation

$$\bar{\chi}_S = \bar{\chi}_S^{(0)} + \mathbf{G}\mathbf{V}_Q \bar{\chi}_s \tag{124}$$

where $\bar{\chi}_S$ and $\bar{\chi}_S^0$ are the vectors of the channel scattering states and the channel Bessel waves, $\mathbf{V}_Q$ the optical potential, and $\mathbf{G}$ the matrix of channel incoming phase Green functions. For multichannel scattering, the optical potential $\mathbf{V}_Q$ assumes the form of a Phillips-Kleinman pseudopotential (Lucchese *et al.*, 1982)

$$\mathbf{V}_Q = \mathbf{V} - \mathbf{LQ} - \mathbf{QL} + \mathbf{QLQ} \tag{125}$$

that explicitly enforces orthogonality between the continuum and target electrons among each unique channel. Except where otherwise noted, we employ penetration terms in the current study, relaxing the orthogonality conditions over only the most weakly occupied natural orbitals.

A compact variational scattering basis set in cartesian gaussian functions is implemented to enhance the convergence of the Padé approximant corrections. A harmonic potential well of the form

$$V' = \begin{cases} 0 & , r < r_0 \\ 2\alpha^2 (r - r_0)^2 & , r \geq r_0 \end{cases} \tag{126}$$

is appended to the target Hamiltonian to construct a model Hamiltonian that is diagonalized in the space of a large initial variational basis set. The eigenfunctions that are not doubly occupied in every CSF and with eigenvalues below a cutoff energy E_{cut} are reincorporated into the scattering calculation. Convergence of the cross section for both targets required initial variational basis functions with tighter exponents than those needed in Stratmann and Lucchese, 1995. For Cl_2, we used the model Hamiltonian parameters $\alpha = 0.3$ au^{-1}, $r_0 = 3$ au, and $E_{\text{cut}} = 3.0$ au. For Pt, stability required model Hamiltonian parameters $\alpha = 0.5$ au^{-1}, $r_0 = 2.5$ au, and $E_{\text{cut}} = 15.0$ au.

Hence, the solution method entails a multi-step approach. First, the target spatial orbitals ϕ are used to generate the ψ CSFs. The CI coefficients C_{ij} of Eq. 120 and the optical potential $\mathbf{V}$ including any pseudopotentials are then computed. Solutions of the scattering equations are numerically iterated until convergence of the cross sections σ is reached. From the converged T-matrix elements, we obtain the cross sections σ and eigenphase sums δ of physical interest.

C. Single-channel and multichannel electron scattering of Cl_2

To gauge the effectiveness of our methods on the molecular complex CDDP, we first compute integrated cross sections for the smaller but nonetheless nontrivial target chlorine Cl_2, for which computed (Rescigno, 1994) and experimental (Cooper *et al.*, 1999; Gulley *et al.*, 1998a; Makochekanwa *et al.*, 2003a) (quasi)elastic scattering cross sections are available. We compare scattering cross sections derived within the static-exchange approximation as in CDDP, and within the multichannel configuration interaction approximation as modified for electron scattering, which admits investigation of inherently multiconfigurational scattering properties taken into account in model fashion within the single-configuration static-exchange plus polarization approximation.

We briefly summarize the key features of the Cl_2 electron spectrum as provided in the comprehensive review of Christophorou and Olthoff (Christophorou and Olthoff, 1999). From the benchmark multireference doubles excitation CI (MRCID) calculations of Peyerimhoff and Buenker (Peyerimhoff and Buenker, 1981), two states of the neutral species are found with vertical excitation energies below 5 eV, including $^3\Pi_u$ (3.24 eV) and $^1\Pi_u$ (4.04 eV), and below 8 eV, including $^3\Pi_g$ (6.23 eV), $^1\Pi_g$ (6.86 eV), and $^3\Sigma_u^+$ (6.80 eV). The anion Cl_2^- has four measured electronic states (Kurepa and Belic, 1978): one bound $^2\Sigma_u^+$ state, with an average adiabatic electron affinity from the neutral of $E_A = 2.45$ eV, and dissociative states with electron attachment peaks $^2\Pi_g$ (2.5 eV), $^2\Pi_u$ (5.75 eV), and $^2\Sigma_g^+$ (9.7 eV). Most recent low-energy (< 10 eV) experimental electron scattering cross sections (Cooper *et al.*, 1999; Gulley *et al.*, 1998a; Makochekanwa *et al.*, 2003a) feature a minimum of 5 Å^2 near 0.4 eV and a peak of 30 Å^2 near 7 eV due to the mixing of a resonant $^2\Pi_u$ state at 5.5 eV with a Feshbach resonance at 7 eV. A weak feature near 2.5 eV is suspected to correspond to the energy of the anion $^2\Pi_g$ state (Gulley *et al.*, 1998a). It should be noted that a Ramsauer-Townsend minimum of ~ 2.1 Å at 0.75 eV has been identified in the total cross section of the ground state ($^2P_{3/2}$) Cl atom using a nonrelativistic *R*-matrix method in which dipole polarization was included through an expansion of pseudostates composed of polarized orbitals (Griffin *et al.*, 1995). Unfortunately, there are no experimental measurements to confirm this property.

1. Cl_2 *SECP computational details*

To obtain the SCF orbitals (Werner *et al.*, 2006), the ground state $(^1\Sigma_g^+)$ Cl_2 bond length was optimized at the full-core MP2 level (FMP2), using the DK3-VTZP basis set given in

Noro *et al.*, 2012 for the Cl atom augmented with $[1s, 1p, 1d, 1f]$ diffuse functions, which we denote aug-DKH3-VTZP, taking into account scalar relativistic corrections to the SCF energy through one-electron integrals computed with a third-order Douglas-Kroll-Hess Hamiltonian (Wolf *et al.*, 2002). This level of theory yielded FMP2 energies and bond lengths $E = -922.25400766$ au and $R = 1.9885$ Å , the latter differing by less than 0.01 Å from the experimental bond length of $E = 1.9879$ Å (Huber and Herzberg, 1979).

In the single-center expansion of the continuum orbital and the bound Cl_2 orbitals, partial waves were expanded to a maximum angular momentum of $l_{\mathrm{max}} = 80$. Truncation of the SCE resulted in Cl_2 orbitals normalized to better than the 0.993 of the Cl 1s $1\sigma_g$ and $1\sigma_u$ orbitals. We have treated polarization through the even distribution of the FMP2 isotropic polarizability $\bar{\alpha} = 30.73$ au on each Cl center. The computed isotropic polarizability compares well to an approximate experimental value of $\bar{\alpha} = 29.45$ au, *viz.*, twice the experimental dipole polarizability $\bar{\alpha} = 2 \times 2.180$ Å$^3 = 14.73$ au of the individual Cl atom (Miller and Bederson, 1978). The matching radius of the static polarizability to the model DFT correlation potential was $r_{\mathrm{match}} = 2.9397$ Å , with a maximum radial grid distance $r_{\mathrm{max}} = 11.5117$ Å .

2. Cl_2 SECP results

In Fig. 19, we present cross sections computed with the following varying levels of approximation for polarization interaction: the static-exchange level only (SE), the static-exchange plus polarization centered on the coordinate origin (SECP [centered]), and the static-exchange plus polarization distributed across each nuclear center (SECP [distributed]). These cross sections are compared to the "total electron scattering cross section" values listed in Table IX and the "total elastic electron scattering cross section" values listed in Table XI of Christophorou and Olthoff, 1999, which were constructed from a least-squares fit to available experimental data at the respective energy scales.

At the level of exact static-exchange, neglecting polarization yields a cross section displaying a local maximum near $E = 1$ eV. While the SE cross section does not resemble by any means either of the convolved experimental cross sections, this feature may be under-

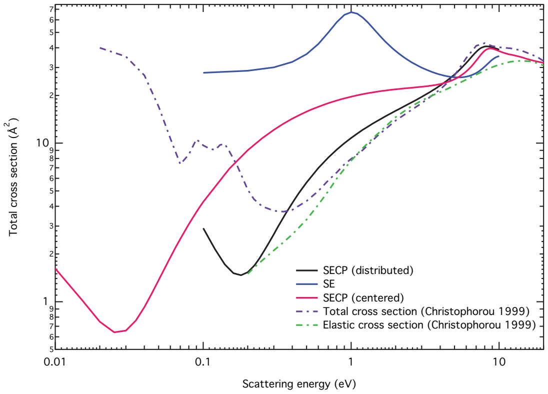

FIG. 19 Electron scattering cross sections of Cl_2 treating different levels of polarization. The cross sections are compared to the "elastic" and "total" cross section of Christophorou and Ohlmoff (Christophorou and Olthoff, 1999).

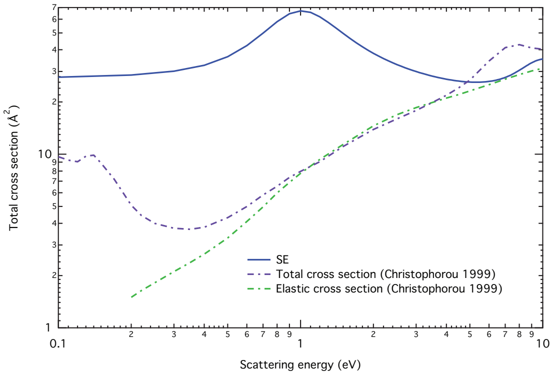

FIG. 20 Electron scattering cross section of Cl_2 at the level of exact static-exchange (SE). The cross section is compared to the "elastic" and "total" of Christophorou and Ohlmoff (Christophorou and Olthoff, 1999).

stood as the result of treating the $^2\Sigma_u^+$ bound state as a simple shape resonance within the static-exchange approximation (Rescigno, 1994). We illustrate this feature more clearly by presenting the SE partial wave cross sections in Fig. 21. The implications for the lack of an effective polarization interaction in the MCCI Cl_2 cross sections will be discussed later in this section.

In our initial SECP calculation, we introduced polarization into our single-configuration scattering method by placing the diagonal terms of the FMP2 static polarizability, $\alpha_{xx} =$ 24.602 au, $\alpha_{yy} = 24.602$ au, and $\alpha_{zz} = 41.502$ au, obtained from an earlier calculation

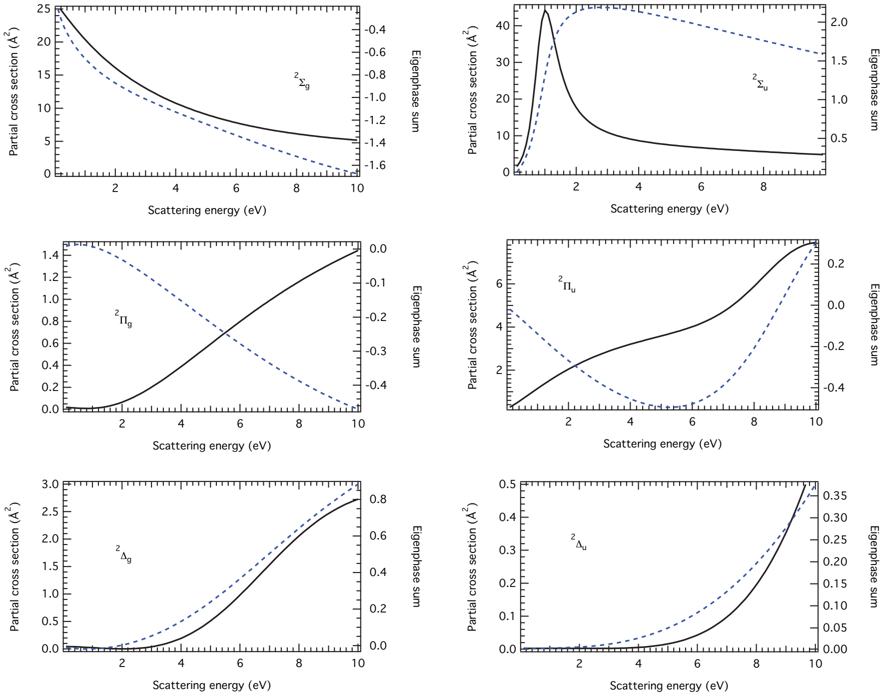

FIG. 21 Electron scattering partial cross sections (solid line) and eigenphase sums (dashed lines) of Cl_2 at the level of exact static-exchange (SE). Observe the 1 eV peak in the $^2\Sigma_u^+$ partial cross section at this level of theory.

using the relativistic polarized double zeta, 1st-order Douglas-Kroll-Hess Hamiltonian [DZP SARC-DKH] basis set of Pantazis *et al.* (Pantazis *et al.*, 2008), at the coordinate origin. In this case, centering the polarization at the coordinate origin results in a total cross section possessing several anomalous features as seen in Fig. 19: the SECP total cross section with polarization placed at the origin lacks the sharp minimum at 0.4 eV seen in the experimental data, instead being found at lower scattering energies of 0.05 eV. Furthermore, between scattering energies of 0.2 eV and 4 eV, the computed cross section displays a convex profile greater in magnitude than either of the convolved experimental curves at every scattering energy. The total cross section of Christophorou and Olthoff, 1999 displays a maximum of ~ 40 Å^2 at 7 eV, whereas the centered SECP calculation predicts the maximum to lie closer to 9 eV. The extent of the depth of the minimum seen in the fitted experimental total cross section of Christophorou and Olthoff is more prominent in the elastic rotational cross section than the total cross sections recorded in Cooper *et al.*,

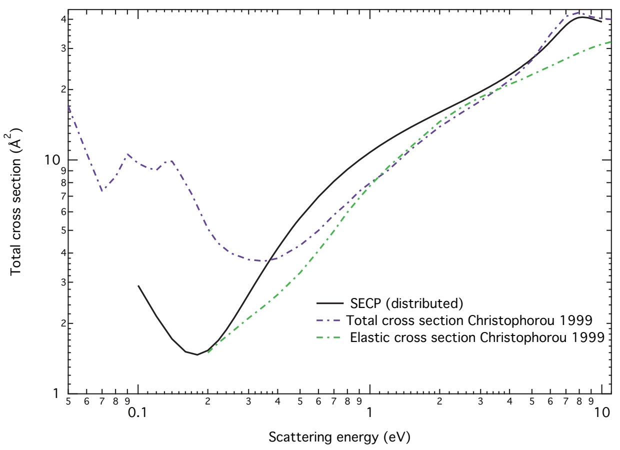

FIG. 22 The same as Fig. 20 for the distributed SECP calculation.

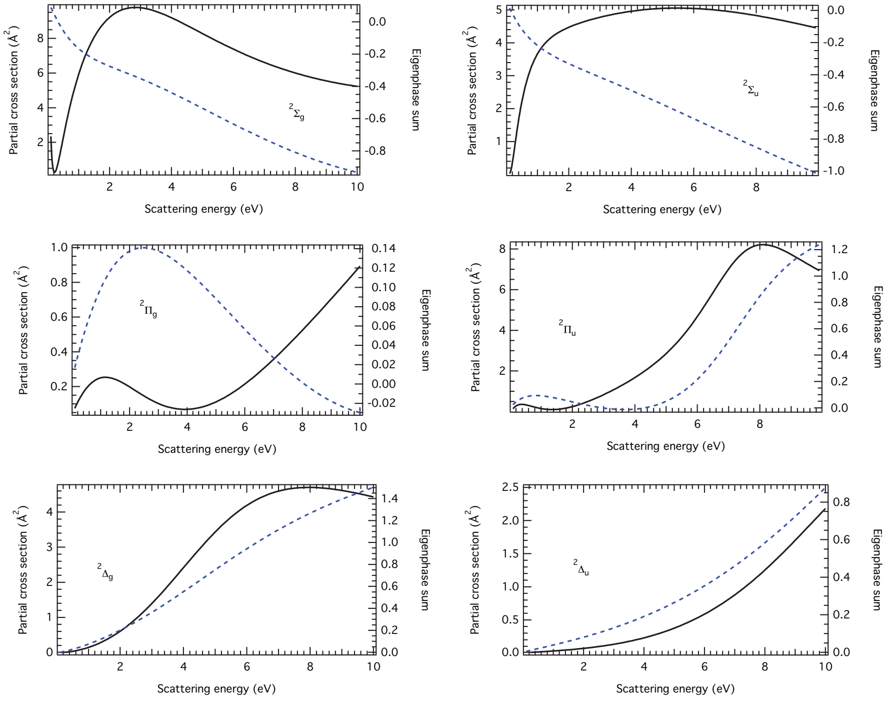

FIG. 23 The same as Fig. 21 for the distributed SECP calculation.

1999; Gulley *et al.*, 1998a; and Makochekanwa *et al.*, 2003a. These anomalous features are the consequence of centering the isotropic polarization potential of V_{CP} on the coordinate origin, *i.e.*, at the center of the chlorine bond, generating an unphysical isotropic polarization interaction resulting in an exaggerated cross section at low scattering energies.

The calculation that distributes the static FMP2 polarizability $\bar{\alpha}$ evenly across the nuclear centers finds substantial agreement with the convolved experimental data of Christophorou and Olthoff, 1999 at all scattering energies greater than 0.4 eV, reproducing both the increasing magnitude of scattering from the minimum and the local maximum seen in the convolved experimental data near 7 eV, as shown in detail in Fig. 22. The distributed SECP cross section, however, retains the convex cross section between 0.4 and 5 eV. This may be due to the truncation of the partial wave expansion to $l_{\text{max}} = 80$; with a greater number of partial waves this feature is expected to decrease upon increasing convergence of the single center expansion. Additionally, the distributed SECP cross section features an absolute minimum of 1.5 Å^2 at 0.2 eV, whereas the experimental cross section displays minor peaks attributed to resonance-enhanced vibrational excitation of the $^2\Sigma_u^+$ anion. The distributed SECP partial cross sections and eigenphase sums in the lowest $l \leq 2$ irreducible representations are presented in Fig. 23. The attractiveness of the interaction potential V_{CP} lowers the $^2\Sigma_u^+$ contribution of the total cross section to the level of bound states below electron energies of 1 eV. In addition, a Ramsauer-Townsend (RT) minimum in the $^2\Sigma_g^+$ partial cross section is observed near 0.2 eV.

To characterize the scattering resonances that may present in our one-electron calculation, we have also diagonalized an adiabatic hamiltonian termed ASMECP that is composed of the static interaction and an entirely local model exchange potential of Hara (Hara, 1967), in addition to the polarization potential V_{CP}. The resulting eigenfunctions are then extrapolated to large radial distance under the proper asymptotic scattering conditions to obtain the partial wave components of the S-matrix, the poles of which correspond to scattering resonances. In Table 14 we present the selected roots of the inverse of the S-matrix that correspond to the complex eigenenergies of the resonant states, neglecting all complex poles with an imaginary energy greater than $\Gamma/2 = 8.4$ eV. Notably, even after limitation of the search to poles near the real axis, we locate a greater number of poles in each state symmetry than have been observed experimentally. Scattering resonances may be distinguished from the manifold of computational background poles through technique described in Carey *et al.*, 2011 in which the resonance positions in each IR is computed at

TABLE 14 Selected roots (complex zeros of the inverse S-matrix) derived from the Siegert eigenstates of the ASMECP potential for electron scattering from ground-state Cl_2 in the equilibrium FMP2 geometry. Real energies E_{Re} and imaginary energies $E_{\mathrm{Im}} = \Gamma/2$ are in eV.

State	Root	E_{Re}	E_{Im}
$^2\Sigma_g^+$	1	1.011543	−1.629248
	2	2.427808	−2.681098
	3	2.640378	−2.483544
	4	4.131063	−3.467293
	5	4.734787	−3.321864
$^2\Sigma_u^+$	1	0.231584	−0.069985
	2	0.550130	−1.276671
	3	3.277497	−2.952186
	4	5.803969	−3.968231
$^2\Pi_g$	1	−0.449716	0.000000
	2	2.326532	−2.543658
$^2\Pi_u$	1	9.344371	−2.273116

each change of a specific reaction coordinate. Accordingly, both the real energy and the imaginary width of the scattering resonance should decrease as the coordinate is lengthened until it reaches the level of the bound states upon full separation.

The investigation of the resonance dynamics of Cl_2 proceeded as follows. We have solved the Schrödinger equation with ASMECP potential for Siegert eigenstates bearing the correct asymptotic scattering form in ten symmetric 0.1 Å increments of the chlorine bond from 1.5 Å to 2.5 Å . At each bond coordinate we constrained the search over the real energies of the inverse S-matrix from 0.1 eV to 8.0 eV for eigenstates in the $^2\Sigma_{g/u}^+$ and $^2\Pi_g$ symmetries and from 0.1 to 10.0 eV for eigenstates in the $^2\Pi_u$ symmetry. The search over the imaginary energy of the inverse S-matrix was limited to energies less than $\Gamma/2 = 8.4$ eV as that described for the resonance search in the equilibrium geometry.

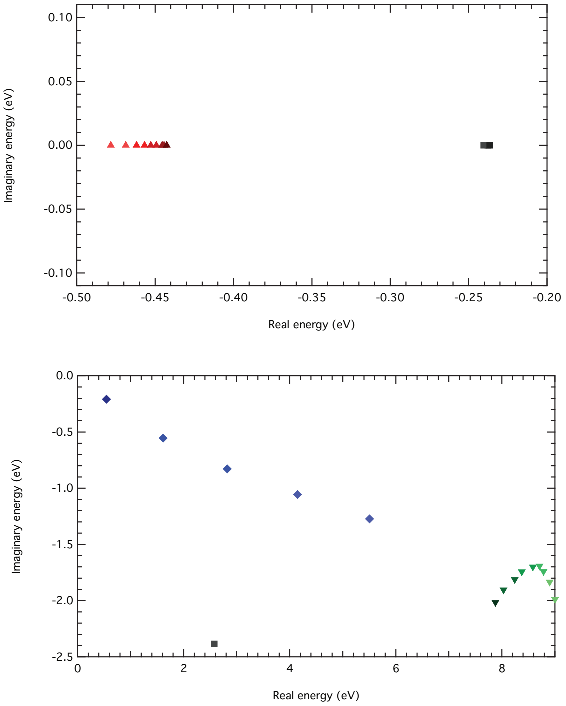

FIG. 24 Residue plot of complex poles of the *S*-matrix as a function of Cl_2 bond as determined from the Siegert eigenstates of the ASMECP potential. The real and imaginary energy grids are in eV. Squares: ${}^2\Sigma_g^+$; rhombus: ${}^2\Sigma_u^+$; up-triangles: ${}^2\Pi_g$; down-triangles: ${}^2\Pi_u$. The shaded intensity of each residue point is proportional to increased bond length.

Residue plots of selected complex poles of the *S*-matrix with complex coordinates near the real energy axis are shown in Fig. 24. We find that the ${}^2\Sigma_u^+$ resonance becomes lower in energy and narrower in width as the Cl_2 bond length is increased from 1.5 Å to 1.9 Å , vanishing altogether for bond lengths greater than 2.0 Å . The ${}^2\Sigma_g^+$ and ${}^2\Pi_g$ poles shown in the top panel of Fig. 24 are found on the real axis with negative energies, which is superficially indicative of a bound or virtual state. We may rule out the presence of bound states in these scattering symmetries, however, by the incorrect asymptotic form of the scattering wave function. The remaining poles are found in the ${}^2\Pi_u$ symmetry at real energies between 8.0 and 9.0 eV and imaginary width $\Gamma/2 = 2.0$ eV. These poles may correspond to the 5.5 eV ${}^2\Pi_u$ resonance seen in the experimental cross section of Gulley *et al.*, 1998a, but the clear trajectory of the residue with increasing bond length that is characteristic of resonant scattering in the particle-in-a-box approximation is not apparent.

The atomic vs. molecular dichotomy of the scattering resonances was observed in the $(5\sigma_u)^{-1}$ photoionization of CS_2 (Stratmann and Lucchese, 1992). In this study, resonance parameters were computed from the Breit-Wigner fits of the $5\sigma_u \rightarrow k\sigma_g$ and $5\sigma_u \rightarrow k\pi_g$ channel cross sections at the equilibrium C-S bond length and at a C-S bond length 10% larger. At the stretched bond coordinate, the real energy of the $5\sigma_u \rightarrow k\sigma_g$ resonance decreases, but the $5\sigma_u \rightarrow k\pi_g$ real energy remains unchanged, which suggests the latter is an atomic-type resonance.

3. Cl_2 MCCI computational details

We select target orbitals obtained from a complete active space self-consistent field (CASSCF) calculation performed on the electronic ground state ${}^1\Sigma_g^+$ of Cl_2 using the MOLPRO2006 program (Werner *et al.*, 2006). The resulting natural orbitals were then employed in the multireference configuration interaction (MRCI) method geometry optimization to obtain the wave function of the neutral state at an equilibrium geometry. In the CASSCF calculation, the active space is composed of all electrons in the inner and outer valence orbitals

$$(4\sigma_g)^2(4\sigma_u)^2(5\sigma_g)^2(2\pi_u)^4(2\pi_g)^4 \tag{127}$$

together with the lowest unoccupied $(5\sigma_u)^0$ orbital. The Cl 1s, 2s, and 2p core orbitals

$$(1\sigma_g)^2(1\sigma_u)^2(2\sigma_g)^2(2\sigma_u)^2(3\sigma_g)^2(3\sigma_u)^2(1\pi_u)^4(1\pi_g)^4, \tag{128}$$

were closed, *i.e.*, kept doubly occupied but optimized in all configurations, thereby resulting in a 14-electron 8-orbital (14,8) active space. In the numerical MRCI geometry optimization, the inactive orbitals of the CASSCF were correlated to the active electrons through closed-shell singles and doubles excitation configuration interaction (SDCI). The equilibrium energy and bond lengths resulting from the numerical geometry optimization at the MRCI level were $E = -922.24667832$ au and $R_0 = 2.0124$ Å , respectively.

To assess the quality of the various computational chemistry methods, we have also computed geometry optimizations of the anion ground state ${}^2\Sigma_u^+$ using analytic gradients obtained in the restricted full-core MP2 method (RFMP2), and numerical gradients of the MRCI method within the MOLPRO2006 code suite, retaining the aug-DK3-VTZP basis sets for each method. The multireference CI calculations were performed using natural orbitals obtained from the optimized CASSCF with a 14-electron 8-orbital active space. We find Cl_2^- RFMP2 energies $E = -922.34383499$ au and equilibrium bond length $R_e = 2.5666$ Å while the MRCI calculation yielded an anion energy $E = -922.31919293$ and a bond length $R_e = 2.5816$ Å . Consequently, our level of approximation results in adiabatic electron affinities (RFMP2) $E_A = 0.8982733 = 2.444$ eV and (MRCI) $E_A = 0.07251461 = 1.9732$ eV. The results of the current calculations may be compared to the more exhaustive multireference Raleigh-Schrödinger perturbation method (CASPT2) calculations of Leininger and Gadéa (Leininger and Gadea, 2000), who find a Cl_2 bond length of $R_e^{\mathrm{CASPT2}} = 1.991$ Å , a ground-state anion Cl_2^- bond length $R_e^{\mathrm{CASPT2}} = 2.562$ Å , and an adiabatic electron affinity $E_A^{\mathrm{CASPT2}} = 2.408$ eV.

The natural orbitals of Cl_2 at the MRCI optimized geometry were subsequently used to describe the target orbitals in the MCCI scattering calculations within the single-center expansion technique. The graphical unitary group configuration interaction procedure (GUGA CI) detailed in Stratmann and Lucchese, 1995 was used to generate CSFs of all target states below an excitation energy of 40 eV. In the numerical CI, electrons in the $1\sigma_g$ and $1\sigma_u$ orbitals corresponding to the atomic Cl 1s shells were kept frozen in all configurations. The maximum angular momentum in the SCE was $l_{\mathrm{max}} = 80$ and in the asymptotic region $l_{\mathrm{maxA}} = 40$. At this level of expansion all target orbitals were normalized better than the 0.993 normalization of the Cl 1s orbitals. The maximum angular momentum in the expansion of the T-matrix partial wave solutions was $l_{\mathrm{maxT}} = 12$. The orthogonality of the continuum wave function was enforced over all valence orbitals.

We have considered electron scattering with a wave function incorporating several neutral electronic states of the target with excitation energies below 10 eV as determined from the GUGA CI protocol in MCCI and list the absolute and relative excitation energies in Table 15. We observe that the GUGA CI ground state energy of -950.68323670 au is lower than either the FMP2 or MRCI energies at the respective optimized geometries because the SCE reduces the accuracy of the numerical CI.

TABLE 15 Absolute (in au) and relative (in eV) excited electronic state energies below 10 eV of Cl_2 as determined from the GUGA CI protocol compared to selected MRCID vertical excitation energies (in eV) and transitions calculated by Peyerimhoff and Buenker [Peyerimhoff and Buenker, 1981].

State and Excitation	GUGA CI energy (au)	GUGA CI excitation energy (eV)	Vertical E^{MRCI} (eV)
$X\ ^1\Sigma_g$	-950.68323670	0.0000	0.00
$1\ ^3\Pi_u\ \pi_g \rightarrow \sigma_u$	-950.50460446	4.8609	3.24
$1\ ^1\Pi_u\ \pi_g \rightarrow \sigma_u$	-950.47259524	5.7319	4.04
$1\ ^3\Pi_g\ \pi_u \rightarrow \sigma_u$	-950.39943912	7.7226	6.23
$1\ ^3\Sigma_u^+\ \sigma_g \rightarrow \sigma_u$	-950.39268972	7.9063	6.80
$1\ ^1\Pi_g\ \pi_u \rightarrow \sigma_u$	-950.38119365	8.2191	6.86
$2\ ^3\Pi_g\ \pi_u \rightarrow 4s$	-950.39943912	7.7226	6.23
$2\ ^1\Pi_g\ \pi_u \rightarrow 4s$	-950.39943912	7.7226	6.23
$2\ ^3\Pi_u\ \pi_u \rightarrow 4p\sigma$	-950.39943912	7.7226	6.23
$2\ ^1\Pi_u\ \pi_u \rightarrow 4p\sigma$	-950.39943912	7.7226	6.23
$1\ ^1\Sigma_u^+\ \pi_u \rightarrow 4p\pi$	-950.25699527	11.5987	8.35

4. Cl_2 MCCI results

We investigate the importance of the multichannel and interchannel effects through the coupling of the ground state and the low-energy ($\leq$ 10 eV) excited states of the neutral in predicting the low-energy electron scattering features observed in the total experimental Cl_2 cross sections. In Fig. 25 we present 1-state ($^1\Sigma_g^+$), 3-state ($^1\Sigma_g^+, ^{1/3}\Pi_g$), and 6-state ($^1\Sigma_g^+, ^{1/3}\Pi_u, ^{1/3}\Pi_g, ^3\Sigma_u^+$) integrated cross sections. The $^2\Sigma_{g/u}^+$, $^2\Pi_{g/u}$ and $^2\Delta_{g/u}$ partial cross sections for the 1-state, 3-state, and 6-state valence calculations are given in Fig. 26, in which each m of the target state symmetries constitutes a unique scattering channel. Only the summed $^1\Sigma_g^+$ state results are displayed for the multistate calculations.

We find that the 1-state ($^1\Sigma_g^+$) calculations replicate the multichannel Kohn variational results of Rescigno (Rescigno, 1994) and the static-exchange results displayed in Fig. 20,

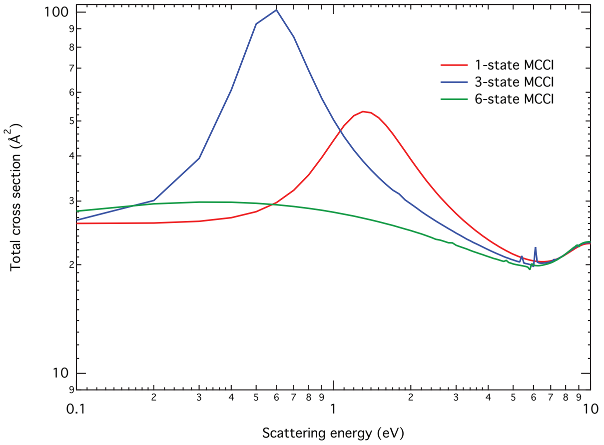

FIG. 25 One-state, three-state, and six-state multichannel electron scattering cross sections of Cl_2.

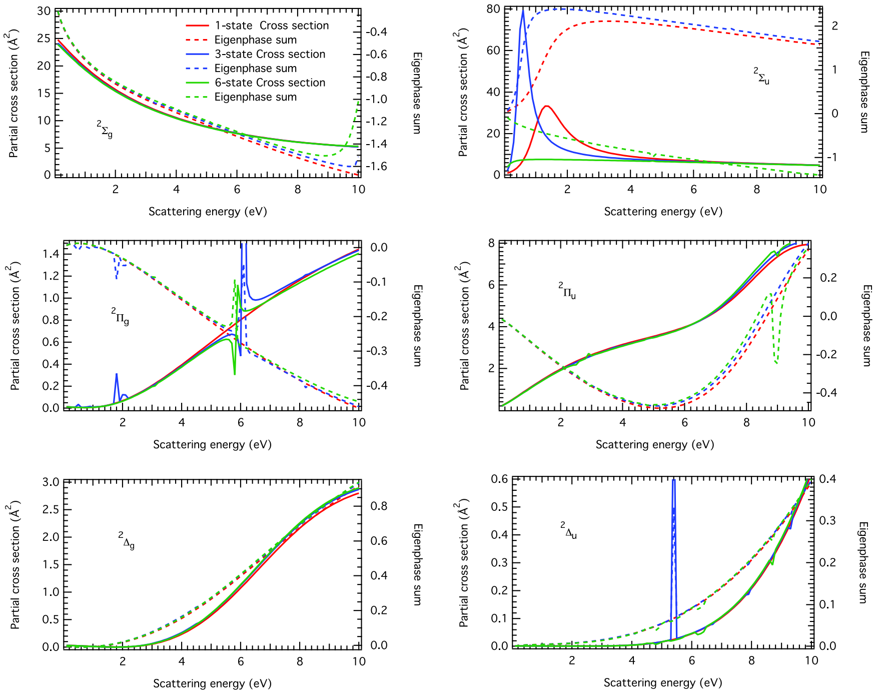

FIG. 26 One-state, three-state, and six-state multichannel electron scattering partial cross sections. of Cl_2.

that is, finding a resonance in the Σ_u^+ partial wave cross section due to treatment of Cl_2^- in this symmetry as an unbound anionic state as mentioned previously. Although several means of obtaining a set of well-contracted polarizing orbitals, orthogonal to the occupied orbitals, to incorporate isotropic polarization interactions in otherwise single-reference calculations are described in the literature (Rescigno *et al.*, 1995a), for the current calculations, we include an increasing number of states in the multichannel CI to admit contributions from all energetically allowed ($\leq$ 10 eV) open and closed channels. As seen in Fig. 25, the 6-state valence calculation results in a total cross section that is flat over most scattering energies between 0.1 eV and 10 eV; however, our total cross section is found at twice the magnitude ($\sim$ 20 Å^2) of the correlated-target cross section of Rescigno, 1994. As seen in Fig. 26, the position of the computational resonance in the $^2\Sigma_u^+$ partial cross section is lowered below threshold scattering energies in the 6-state valence calculations, while the remaining partial cross sections even at the 6-state valence level still retain the profiles and magnitudes of the partial cross sections neglecting correlation in Fig. 21. Additionally, as observed in Fig. 26, our 3-state and 6-state valence calculations possess several numerical artifacts particularly in the $^2\Pi_g$ and $^2\Delta_u$ anion symmetries, the consequence of neglecting the orthogonalization of the continuum orbital to the target $5\sigma_u^0$ virtual orbital, which has significant occupation in all non-ground state electronic configurations. We previously considered an alternative approach in which the orthogonality constraints were relaxed over all valence orbitals of Eq. 127, but abandoned this approach for simply increasing the target state expansion to include low-lying Rydberg transitions, leading to a "complete" expansion within the low-energy scattering range. To that end, we have generated partial cross sections in the dominant $^2\Sigma_g^+$ and $^2\Sigma_u^+$ IRs only for a 12-state calculation combining CSFs from $(X^1\Sigma_g^+, {}^{1/3}\Pi_u, {}^{1/3}\Pi_g, {}^3\Sigma_u^+)$ valence and $(2^{1/3}\Pi_g, 2^{1/3}\Pi_u, 1^1\Sigma_u, 1^1\Delta_u)$ Rydberg transitions (not shown), but find that they reproduce the cross sections and eigenphase sums of the smaller 6-state calculation Fig. 26 already discussed. Our converged 6-state MCCI calculations confirm earlier observations (Rescigno *et al.*, 1995a) that expansions in target eigenstates account poorly for the long-range polarization interaction, thus requiring the explicit inclusion of the dipole polarizability into the scattering calculation.

D. Single-channel and multichannel electron scattering of Pt

On account of the unfilled occupation of the 5*d* and 6*s* shells, the platinum atom possesses numerous electronic states even if only considering the states arising from occupation of the 5d and 6s shells alone. The lowest energy electronic states of Pt atom have the electron configuration $(5d^9 6s^1)$, namely the $^3D_3$ ground state and the ~ 0.1 eV $^1D_2$ state. The following state, $^3F_4$ at 0.1 eV, arises from the configuration $(5d^9 6s^2)$. The $(5d^{10})$ $^1S_0$ state is found 0.76 eV above the ground state (Hotop and Lineberger, 1973). The remaining states are produced from the $(5d^8 6s^2)$ configuration and are listed with excitation energy in Table 16. The populations of the states at thermal energies are $^3D_3$ 0.452, $^1D_2$ 0.197, $^3F_4$ 0.344, $^1S_0$ 0.13, and $^3D_2$ 0.005, whereas the higher energy states have negligible populations (Smirnov, 2004).

The bound anion Pt$^-$ has a ground state configuration $(5d^9 6s^2)$ $^2D_{5/2}$, with a recommended adiabatic electron affinity of $E_A = 2.13$ eV (Bilodeau *et al.*, 1999), and two excited states: a 1.21 eV $(5d^9 6s^2)$ $^2D_{3/2}$ state and a 1.28 eV $(5d^{10} 6s^1)$ $^2S_{1/2}$ anionic state that was predicted to exist by multiconfigurational Dirac-Fock structure calculations yet unobserved experimentally until quite recently (Andersson *et al.*, 2009). All remaining anion states are predicted to lie higher in energy than the ground state of the neutral species.

In analogy with Cl$_2$, we compare electron scattering from the neutral Pt atom within the SECP and MCCI approximations, taking into account the open-shell ground electronic state symmetry of the Pt atom within the multichannel calculation.

1. Pt SECP computational details

We obtain the SCF orbitals for the SECP calculation of the Pt atom in an Abelian D_{2h} symmetry, neglecting spin-orbit interactions. To assess the quality of the ^1S wave function that we will use in subsequent calculations, we compare SCF results for the single-configuration $^1S \rightarrow {}^1A_g$ state, and a five-fold degenerate ^3D ground state whose state symmetry is approximated with restricted open shell wave functions that span the relevant irreducible representations (IR) of the point group: ^3A_g, $^3B_{1g}$, $^3B_{2g}$, and $^3B_{3g}$. The SCF calculations were performed with the MOLPRO2006 code suite using the Pt DKH3-VTZP basis set augmented with $[1s1p1d1f]$ diffuse functions as given in Noro *et al.*, 2012 which we henceforth denote aug-DKH3-VTZP. We find FMP2 energies $E(^3D) = -18415.01479595$ au for all state symmetries, and a singlet state FMP2 energy $E(^1S) = -18415.00593488$

TABLE 16 Lowest-energy states arising from electron occupation of the $5d$ and $6s$ shells. Experimental values in cm^{-1} and eV are taken from the NIST database [Blaise *et al.*, 1992].

Configuration	Term	J	E (cm^{-1})	E (eV)
$5d^9 6s$	^3D	3	0.0	0.0
		2	6567.461	0.81
		1	10131.887	1.26
	^1D	2	775.892	0.10
$5d^8 6s^2$	^3F	4	823.678	0.10
		3	10116.729	1.25
		2	15501.845	1.92
$5d^{10}$	^1S	0	6140.180	0.76
$5d^8 6s^2$	^3P	2	13496.271	1.67
		0	16983.492	2.11
		1	18566.558	2.30
	^1G	4	21967.111	2.72
	^1D	2	26638.591	3.30

au, resulting in an FMP2 excitation energy $\Delta E = 0.00886107 = 0.24$ eV, which is substantially smaller than the SCF excitation energy of $\Delta E = 0.03496774 = 0.95$ eV. Likewise, after constructing the observed anion doublet state with restricted open shell wave functions, we find SCF and FMP2 energies for the ^2D states $E = -18414.53989017$ au and $E = -18415.08497409$ au and for the ^2S state $E = -18414.49960539$ au and $E = -18415.06400650$ au. The computed FMP2 adiabatic electron affinity $E_A(^3D \leftarrow {}^2D) = 0.07017814 = 1.91$ eV and transition energy $\Delta E(^3D \leftarrow {}^2S) = 0.04921055 = 1.34$ eV are in fair agreement with experiment, differing by only 10%; however, the respective SCF adiabatic electron affinity $E_A(^3D \leftarrow {}^2D) = 0.01571741 = 0.43$ eV and transition energy $\Delta E(^3D \leftarrow {}^2S) = -0.02456737 = -0.67$ eV are considerably poorer.

Clearly, the ^3D and ^2D ground states of the neutral and the anion species are not adequately described by a restricted open shell wave function if dynamic electron correlation is neglected. Consequently, we limit quantitative discussion of electron scattering properties of Pt computed within the SE approximation only to the ^1S excited state, leaving discussion of the ^3D state cross sections on the multichannel scattering results discussed in Sec. IV.D.5.

As mentioned previously, the orbitals of the atomic center are given in the Abelian D_{2h} point group from the SCF MOLPRO2006 output. However, for the current calculations, we consider the atom in an icosahedral symmetry since the irreducible representations of I_h uniquely span the lowest $l \leq 2$ atomic orbitals (Kettle and Smith, 1967), namely, $s \rightarrow a_g$, $p \rightarrow t_{1u}$, and $d \rightarrow h_g$. All higher order angular momenta, *e.g.* $f \rightarrow t_{2u} + g_u$, span multiple irreducible representations of the icosahedral point group and should yield degenerate electron scattering spectra. The atomic orbitals in this point group are given in Eqs. 129 and 130 are given as follows:

$$\begin{aligned}&(1a_g)^2(2a_g)^2(1t_{1u})^6(3a_g)^2(2t_{1u})^6(1h_g)^{10}(4a_g)^2(3t_{1u})^6(2h_g)^{10}\\&(5a_g)^2(t_{2u})^6(g_u)^8(4t_{1u})^6(3h_g)^{10} : {}^1A_g\end{aligned} \tag{129}$$

$$\begin{aligned}&(1a_g)^2(2a_g)^2(1t_{1u})^6(3a_g)^2(2t_{1u})^6(1h_g)^{10}(4a_g)^2(3t_{1u})^6(2h_g)^{10}\\&(5a_g)^2(t_{2u})^6(g_u)^8(4t_{1u})^6(3h_g)^9(6a_g)^1 : {}^3H_g :\end{aligned} \tag{130}$$

Accordingly, we compare SECP and SE electron scattering cross sections from Pt in the singlet state ^1A_g, but for ease of discussion we discuss the computed results with atomic symmetry. In the close-coupling expansion of the continuum orbital and the bound Pt orbitals, partial waves were expanded to a maximum angular momentum of $l_{\max} = 16$. In preliminary calculations on e^--Pt (Carey *et al.*, 2011), we found no significant difference in the computed cross sections when the orthogonality constraints of the scattering orbitals to the bound orbitals were relaxed with respect to either the outer valence $5d$ or inner valence $5d$, $4f$, and $5p$ shells. We recover the asymptotic polarization interaction through placement of the computed ^1S FMP2 isotropic dipole polarizability $\bar{\alpha} = 30.730518$ au on the Pt center. The matching radius of the dipole polarizability to the model DFT correlation potential in V_{CP} was $r_{\text{match}} = 2.939747$ Å , It should be noted that the non-relativistic DFT correlation potential we employ (Perdew and Zunger, 1981) has not been rigorously benchmarked for large Z targets for which relativistic interactions are presumed important. The relativistic correlation of a free electron within a dense homogeneous electron gas may be well approximated, however, by the augmentation of an otherwise nonrelativistic correlation density functional with expressions (Ramana and Rajagopal, 1981) generated within the relativistic random phase approximation (RRPA) (Engel *et al.*, 1995) if high accuracy is desirable.

2. *Pt SECP results*

To the best of our knowledge, the only electron scattering spectra available for the platinum atom are the computational studies of Msezane and collaborators (Felfli *et al.*, 2010; Msezane *et al.*, 2008), who have generated total cross sections and resonant scattering states for Pt and Au using a Regge pole method and a semiempirical Thomas-Fermi interaction potential. Msezane and collaborators find three resonances for Pt, with complex angular momentum L and energy $L = 1$ (0.14 eV), $L = 3$ (1.12 eV), and $L = 5$ (2.2 eV), the last corresponding to the Pt bound state. The computed total cross section of Msezane *et al.*, 2008 exhibits two peaks below 2.5 eV at the resonant energies superimposed upon a background decaying from a maximum ($\geq 1500 = 420$ Å^2) at threshold. This discussion extends that found in Carey *et al.*, 2011.

In Figs. 27 and 28, we present the Pt ^1S SE and SECP integrated and partial (^2S, ^2P, ^2D, and ^2F) cross sections for scattering below 10 eV. As stated in Carey *et al.*, 2011, with the exception of the lowest scattering energies in the s symmetry, relaxation of the orthogonality condition between the continuum and the target orbitals does not result in major differences in either the total or the partial SECP cross sections. Unlike the total cross section presented in Fig. 4 of Msezane *et al.*, 2008, both ^1S SE and SECP total cross sections display a monotonic decay at increasing scattering energies, with the ^2S partial cross section contributing the dominant intensity. The SE electron spectrum, however, exhibits a nearly power law distribution between the scattering energy and the cross section between

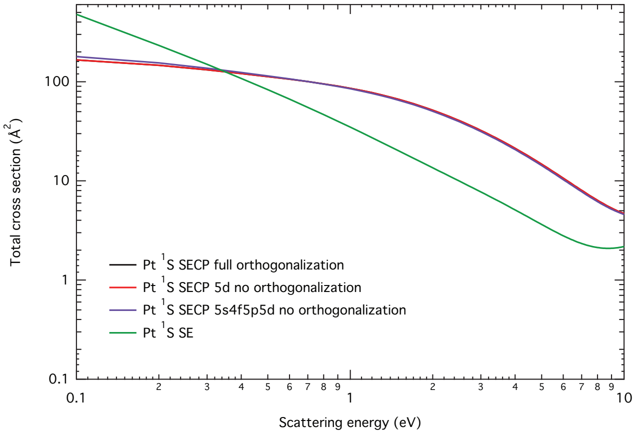

FIG. 27 Computed SE and SECP integrated cross sections for electron scattering from Pt atom in the ${}^1S$ state. Scattering energies are in eV and cross sections in Å^2.

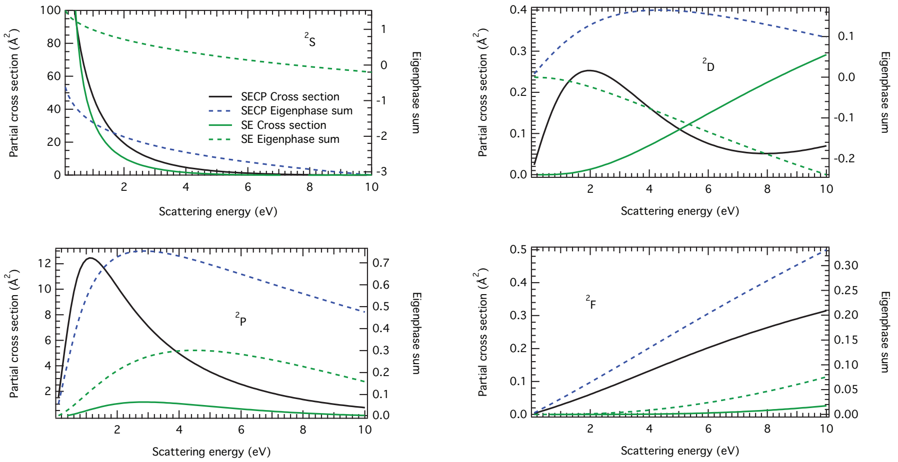

FIG. 28 Computed SE and SECP integrated partial cross sections (solid lines) and eigenphase sums (dashed lines) for electron scattering from Pt atom in the ${}^1S$ state. The continuum electron is orthogonalized to all bound orbitals in the SECP results. Scattering energies are in eV and cross sections in Å^2.

0.1 and 6 eV. Whereas the SECP total cross section is uniformly four times lower in magnitude than those given in Msezane *et al.* at scattering energies below 2.0 eV, the SE cross section is in good agreement with the Msezane *et al.*, 2008. The SECP ${}^2D$ and ${}^2F$ cross sections are small at all scattering energies, with cross sections below $\sigma = 0.5$ Å^2. The ${}^2P$ partial cross section, however, displays a maximum $\sigma = 12$ Å^2 near 1.0 eV electron energy, with the corresponding eigenphase sum rising to $\delta = \pi/4$ near 2.8 eV. Accordingly,

TABLE 17 Selected roots (complex zeros of the inverse S-matrix) of the Siegert eigenstates of the ASMECP potential for Pt atom in ^1S symmetry. Real and imaginary energies $\Gamma/2$ are in eV.

State	Root	E_{Re}	E_{Im}
^2P	1	0.892328	1.238679
	2	1.896298	1.912596
	3	3.327269	2.636854
	4	5.158943	3.380433
^2D	1	0.528934	1.107548
	2	1.518571	1.725821
	3	2.852494	2.391526
	4	4.540321	3.090286

we isolate the resonance parameters E_{Re} and $E_{\mathrm{Im}} = \Gamma/2$ from the Siegert eigenstates in ^2P and ^2D symmetry of the ASMECP potential as detailed previously and present the results in Table 17. The different levels of approximation do not shift appreciably the real or imaginary energies found in the search, which are significantly higher energy (short-lived) than those identified in the complex angular momentum analysis of Msezane *et al.*, 2008. The partial cross sections computed at the SE level, shown in Fig. 28, display a marked attenuation at all scattering energies for all but those in the ^2S scattering symmetry, with no other waves indicating evidence of resonant scattering.

3. *Convergence of the Pt MCSCF wave function*

For the MCCI calculations, we prepare the natural orbitals resulting from state-averaged CASSCF/aug-DKH3-VTZP calculations from several low-energy triplet, singlet, and anion doublet states of Pt, selecting a 10-electron, 6-orbital (10,6) active space comprised of the $5d$ and $6s$ orbitals. The remaining occupied orbitals were kept doubly-occupied but optimized to the active space in all CSFs. As a diagnostic procedure, we have performed a variety of state-averaged (10,6) CASSCF and (11,6) CASSCF calculations for a number of states of the atom and the anion, respectively, namely the ^3D and ^1S states of Pt, and the ^2D and ^2S states of Pt$^-$. In a more elaborate CASSCF calculation, we include the $5d^96s$ ^1D state and all singlet and triplet states of the neutral arising from the $5d^86s^2$ configuration (^3F, ^3P, ^1G and ^1D), thereby accounting for all possible states generated from occupation of the $5d$ and $6s$ shells.

In one set of CASSCF calculations, the singlet, triplet, and anion doublet states are state-averaged individually, which we shall denote 1S(S)-CAS, 1S(T)-CAS, and 2S(D)-CAS, respectively. In the other, all singlet and triplet states are state averaged together, which we denote SA-CAS, and compared to the 2S(D)-CAS anion doublet states. The transition energies of the numerical CI of the ^3D and ^1S 1S-CAS wave functions are compared to the fully state-averages SA-CAS wave function in the MCCI scattering calculations to be discussed later in this section.

We recover electron correlation energy from the zeroth-order CASSCF wave functions through two means: the multireference configuration interaction method (MRCI) performed on the natural orbitals of the CASSCF calculations, and the second-order Raleigh-Schrödinger perturbation method (RS2) on pseudocanonicalized orbitals from the CASSCF calculations, maintaining the same number of active electrons (10 for the atom, 11 for the anion) and orbitals (6) in each method. In one set of calculations, only electrons in the $5d$ and $6s$ active orbitals are correlated, which we denote ($5d6s$); in the other, $5s$, $5p$ and $4f$ orbitals are kept doubly occupied but correlated to the active orbitals through singles and doubles configuration interaction in the MRCI calculation and closed-shell second-order Møller-Plesset perturbation theory in the RS2 calculations. The more extensive correlation is abbreviated $[5s4f5p](5d6s)$. Electrons in the remaining occupied orbitals are uncorrelated to the active electrons. All calculations were performed using the MOLPRO2006 code suite.

A summary of the MCSCF, MRCI, and RS2 excitation energies (in eV) is compiled in Table 18. The absolute single-state and state-averaged ^3D energies (in au) are also given. The uncorrelated 1S-CAS MCSCF $^1S \rightarrow {}^3D$ transition energy agrees quite well with the experimental value given in Table 16, but greatly underestimates (~ 1.5 eV) the electron affinity E_A. The SA-CAS MCSCF calculation converges the ^1S energy 2.6 eV above the ^3D ground state, above all the remaining states. Perusing Table 18 further, we observe that the post-MCSCF calculations incorporating electron correlation from excitations among closed-shell $5s$, $4f$, and $5p$ orbitals substantially lowers the energy of the RS2 calculations yet contributes only small modifications to the MRCI results. The inclusion of the Davidson quadruples correction to the MRCI energy, labeled MRCI+Q, is seen to degrade the quality of the state-averaged transition energies through overcorrelation of the ^1S state.

Comparing the energies obtained from the $(5d6s)$ correlated active spaces, the $^1D \leftarrow {}^3D$ and $^3F \leftarrow {}^3D$ transitions appear too high in energy within the SA-CAS MRCI approximation (0.27 eV and 0.64 eV), yet are nearly isoenergetic to the ground state in the SA-CAS RS2 approximation (0.1 eV and 0.38 eV), as compared to their experimental values of ~ 0.1 eV in Table 16. The important 0.76 eV $^1S \leftarrow {}^3D$ transition, however, is better approximated by the SA-CAS MRCI value of 0.72 eV than the SA-CAS RS2 value of 0.23 eV. Both post-MCSCF correlated methods erroneously find the 2^1D state lower in energy than the ^1G state. Lastly, we note the comparatively poor values of the computed $(5d6s)$ and $[5s4f5p](5d6s)$ 1S-CAS MRCI electron affinities of 1.41 eV and 1.31 eV calculated without the Davidson quadrupoles correction, whereas the RS2 electron affinities of 1.73 eV and 1.81 eV lie within 20% of the measured electron affinity of $E_A = 2.13$ eV. The MCSCF dispersion, here defined to mean the difference between the 1S-CAS and SA-CAS ^3D energies, is found to be $\Delta E = -0.01326142$ au = -0.36 eV, or approximately the same order of magnitude as the $^1D \leftarrow {}^3D$ transition energy. If the quality of the target wave function is assessed through the zeroth-order and correlated transition energies, we conclude that no significant error is introduced in using the 1S-CAS ^3D and ^1S natural orbitals in preference to the fully state-averaged SA-CAS natural orbitals in the MCCI calculations.

4. *Pt MCCI computational details*

We have computed 1-state MCCI electron scattering cross sections for Pt atom in the ^1S state and the ^3D state. The MCCI program constructs all atomic orbitals in the finite

TABLE 18 State-averaged MCSCF and post-MCSCF transition energies (in eV) for low-energy excitations of Pt and Pt$^-$. The absolute computed energy (in au) of the ^3D state is given for reference.

	MCSCF		MRCI		MRCI+Q		RS2	
State/Transition	1S-CAS	SA-CAS	1S-CAS	SA-CAS	1S-CAS	SA-CAS	1S-CAS	SA-CAS
(5*d*6*s*)								
^3D (au)	−18414.52259887	−18414.50933745	−18414.75216755	−18414.75216589	−18414.76931244	−18414.77336582	−18414.78386672	−18414.77869311
$^1D \leftarrow {}^3D$		0.20055134		0.27026594		0.26699106		0.06466439
$^3F \leftarrow$		0.18386729		0.63513259		0.69209210		0.37925072
$^1S \leftarrow$	0.67735039	2.59085522	0.31586386	0.72189641	0.31168237	0.17289605	0.30213603	0.23167365
$^3P \leftarrow$		1.69986190		1.97404132		1.98859914		1.69473063
$^1G \leftarrow$		2.20806207		2.60035338		2.64350535		2.35222351
$^1D \leftarrow$		2.16494250		2.36463947		2.38824481		1.95946860
$^3D \leftarrow {}^2D$	0.41772084		1.40963624		1.74392692		1.73107389	
[5*s*4*f*5*p*](5*d*6*s*)								
^3D (au)			−18414.90609051	−18414.90526770	−18414.93897102	−18414.94360374	−18414.98488521	−18414.97592659
$^1D \leftarrow {}^3D$				0.25771946		0.26789589		−0.09886041
$^3F \leftarrow$				0.51428956		0.60727958		−0.01467838
$^1S \leftarrow$			0.45170293	0.97172563	0.45978259	0.37783281	0.49684374	0.51107356
$^3P \leftarrow$				1.82379533		1.85702739		1.28369607
$^1G \leftarrow$				2.39437469		2.45237495		1.89780414
$^1D \leftarrow$				2.18589343		2.19481512		1.66142947
$^3D \leftarrow {}^2D$			1.31455747		1.67641163		1.81109418	

$D_{\infty h}$ point group, a feature that introduces several complications in the interpretation of the resulting cross sections. The continuous atomic orbital symmetry spans the irreducible representations of the finite $D_{\infty h}$ point group with a formal $(2l+1)$ degeneracy for each value $|m|$ of the l atomic state; thus, for a given atomic state Λ, $S \rightarrow \Sigma$, $P \rightarrow \Pi + \Sigma$, $D \rightarrow \Delta + \Pi + \Sigma$, etc. For convenience, we refer to the largest allowed m in the identification of the ${}^1S \rightarrow {}^1\Sigma_g$ and ${}^3D \rightarrow {}^3\Delta_g$ target states.

To construct the CSFs needed for the MCCI calculations, we keep electrons in all non-active ($5d$, $6s$) orbitals doubly occupied. In preliminary calculations, increasing the active space to include the inner-valence $5s$, $4f$ and $5p$ shells did not enhance the convergence or lower the energies of the states resulting from the CI, an expected result given the well-known size inextensitivity of all forms of truncated configuration interaction. After construction of the CSFs, in the SCE of the target and continuum wave functions, the partial wave expansion was truncated to $l_{\text{max}} = 16$ as in the SECP calculations; however, the maximum l in the asymptotic scattering region was increased to $l_{\text{maxA}} = 16$. The maximum angular momentum in the partial wave expansion of the T-matrix solutions was $l_{\text{maxT}} = 8$. Orthogonality of the continuum orbital to the target orbitals was enforced over all occupied orbitals scattered from SA-CAS and 1S-CAS ${}^3\Delta_g$ wave functions and relaxed over the unoccupied $6s$ orbital for scattering from the SA-CAS and 1S-CAS ${}^1\Sigma_g$ target state. The absolute and transition energies of the target states constructed by the GUGA-CI from the state-averaged wave function SA-CAS are listed in Table 19.

As is evident in Table 19, the present state-averaged numerical CI fails utterly to provide even qualitatively accurate excitation energies for the relevant transitions among the $5d6s$ holes states. Most notably, the GUGA CI protocol for both 1S-CAS ${}^1S$ and ${}^3D$ wave functions, and the state-averaged SA-CAS wave function, determine ${}^1\Sigma_g$ to be the ground state in every calculation, while the ${}^3\Delta_g$ state is found approximately 20 eV higher in energy. With the exception of the ${}^1D \rightarrow {}^1\Delta_g$ state, all remaining states are 18 eV or higher above the ${}^3\Delta_g$ energy. When only the relevant 1S-CAS target states ${}^1S$ and ${}^3D$ are included in the numerical CI, a 6.1 eV energy difference is obtained, as given in Table 20, yet even here, the singlet state is computed to be lower in energy than the triplet state, a violation

TABLE 19 Absolute (in au) and relative (in eV) excited target state energies of Pt atom as determined from the GUGA CI method in MCCI comparing the single-state and state-averaged CASSCF natural orbitals. The dispersion energy (in eV) between the GUGA CI $^1S \rightarrow {}^1\Sigma_g$ and $^3D \rightarrow {}^3\Delta_g$ absolute energies is provided for reference.

	Absolute energy (au)				Transition energy (eV)				
	1S-CAS		SA-CAS		1S-CAS		SA-CAS		
State	^1S	^3D	^1S	^3D	^1S	^3D	^1S	^3D	Dispersion (eV)
$^3\Delta$	−14475.26117773	−14475.27332447	−14475.24982071	−14475.24982071	0.000	0.000	0.000	0.000	0.485
$^1\Delta$	−14475.22857852	−14475.24639314	−14475.22190158	−14475.22190158	0.887	0.732	0.760	0.760	8.455
$^3\Phi$	−14474.26016238	−14474.57434990	−14474.52333868	−14474.52333868	27.239	19.020	19.769	19.769	−8.159
$^1\Sigma_g$	−14476.24996467	−14475.95013004	−14475.95669254	−14475.95669254	−26.906	−18.417	−19.235	−19.235	0.331
$^3\Pi$	−14474.21225020	−14474.52439244	−14474.47220722	−14474.47220722	28.543	20.380	21.160	21.160	8.549
$^1\Gamma_g$	−14474.19189551	−14474.50261256	−14474.44951104	−14474.44951104	29.097	20.972	21.778	21.778	8.494
$^1\Delta_g$	−14474.22362402	−14474.53632618	−14474.48435814	−14474.48435814	28.233	20.055	20.829	20.829	8.509

TABLE 20 Absolute energy (in au) and difference energy (in eV) of single-state 1S-CAS ^1S and ^3D Pt as determined from the GUGA CI protocol.

State	CI Energy (au)
$^3\Delta$	-14474.80557725
$^1\Sigma_g$	-14475.03133452
ΔE (au)	0.22575727
ΔE (eV)	6.14

of Hund's rule. These results stem primarily from the lack of scalar relativistic corrections and post-MCSCF wave function correlation in the numerical CI. Clearly, no advantage is to be gained from utilization of a multistate expansion of the Pt target wave function within the MCCI calculation to recover target correlation, as was prescribed for Cl_2 and discussed in Sec. IV.C.4. Accordingly, we truncate the target state expansion to one state only for both ^1S and ^3D targets, thereby yielding MCCI scattering cross sections generated at the static-exchange level yet for multiconfigurational targets.

5. *Pt MCCI results*

Cross sections from each m_l state of the target yield unique scattering channels $\bar{m} = |m_l \pm m|$ for each m of the $(2l+1)$-degenerate continuum state, as discussed in the previous section. In the current calculations, we have not isolated the individual $\bar{m}$ contributions for each scattering state, so these partial cross sections contain a sum of all channels $\bar{m}$ consistent with the resultant anionic scattering symmetry.

In Fig. 29 the predominant components of the 1-state, 1-channel cross section of $^1S \rightarrow {}^1\Sigma_g$ is displayed. We observed no difference in the magnitudes or convergence features of the $^2\Sigma_g$ partial cross sections in which orthogonality of continuum orbital to the target 5*d* orbitals is enforced and relaxed (*i.e.*, no orthogonalization). When only one state comprises the target expansion wave function, the resulting cross section is fully equivalent to that computed at the level of the static exchange approximation, an expectation confirmed

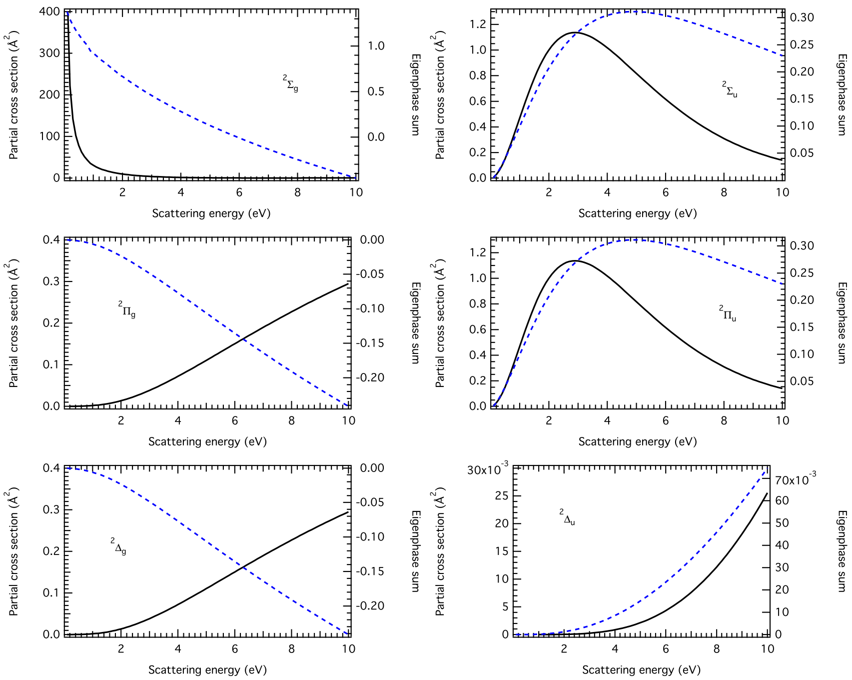

FIG. 29 Computed 1-state, 1-channel MCCI partial cross sections (solid lines) and eigenphase sums (dashed lines) for electron scattering from Pt atom in the $^1S \rightarrow {}^1\Sigma_g$ state. Scattering energies are in eV and cross sections in Å^2. The continuum electron is orthogonalized to the 5d orbitals.

in the $^1\Sigma_g$ electron spectrum. This stands as a crucial test of the reliability of the current method on the complex closed-shell target. As in the SE A_g partial cross section shown in Fig. 28, only the principal electron anionic state symmetry $^2\Sigma_g$ is found to yield a cross section with a magnitude $\sigma \geq 0.1$ Å^2. We find comparable magnitude amongst the ^2P and ^2D SE cross sections of Fig. 28 and the $^2P \rightarrow {}^2\Pi_u + {}^2\Sigma_u$ and $^2D \rightarrow {}^2\Delta_g + {}^2\Pi_g + {}^2\Sigma_g$ partial cross sections of the 1-state $^1\Sigma_g$ MCCI calculation. As in the SE calculation discussed in Sec. IV.D.2, the 1-state MCCI cross section predicts the predominance of s-wave scattering from the $5d^{10}$ ^1S Pt state.

In electron scattering from the open-shell targets, the coupling between the spin of the $s = 1/2$ continuum electron and m_s of the target allows anionic states of multiple spin angular momenta $\bar{m}_s = |m_s \pm 1/2|$ to formed. These states should be statistically weighted to admit the fullest comparison with experiment. In scattering from the $m_s = 1$ ^3D target,

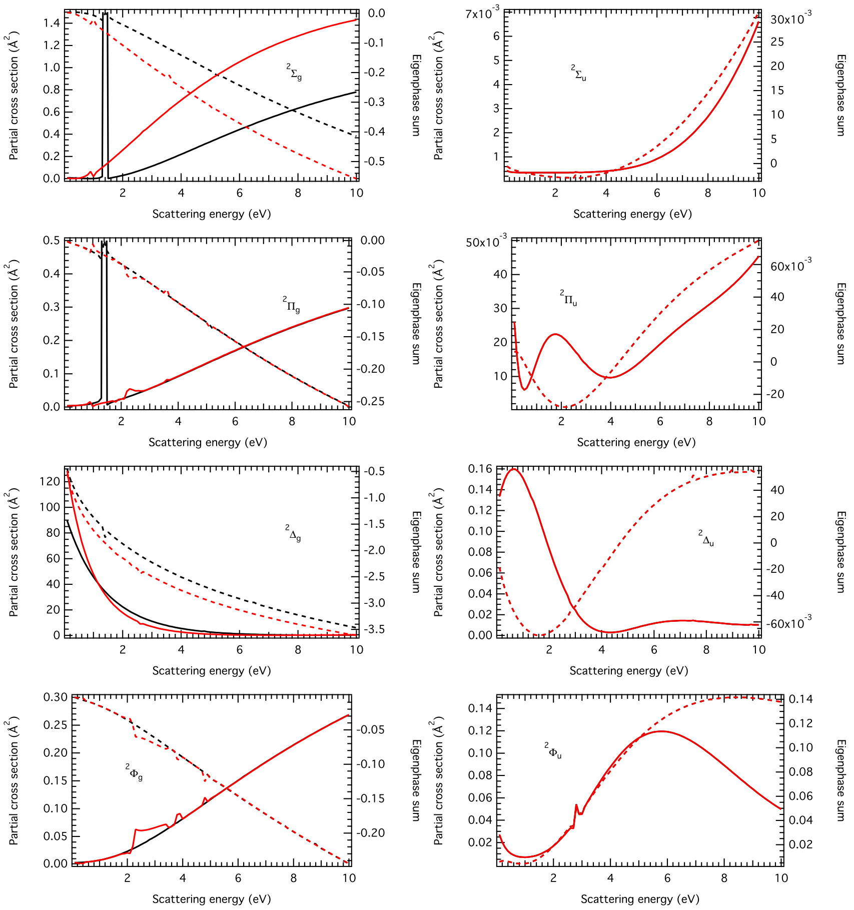

FIG. 30 Computed 1-state, 5-channel MCCI partial cross sections (solid lines) and eigenphase sums (dashed lines) for electron scattering from Pt atom in the $^3D \rightarrow {}^3\Delta_g$ state leading to doublet anion states. Only the $m_l = 2$ target component is presented. Black lines: the continuum electron is orthogonalized to both 5d and 6s orbitals. Red lines: the continuum orbital is not orthogonalized. Scattering energies are in eV and cross sections in Å^2.

we therefore must address both anion $\bar{m}_s = 1/2$ doublet and $\bar{m}_s = 3/2$ anion quartet cross sections that result from the coupling of the spin.

The MCCI 1-state, 5-channel partial cross section of electron scattering from $^3D \rightarrow {}^3\Delta_g$ Pt are presented in Figs. 30 (anion doublet states) and 31 (anion quartet states). In both figures, only the leading $m_l = 2$ target component is shown for clarity. Unlike scattering from the $^1S \rightarrow {}^1\Sigma_g$ target, the orthogonality constraints of the continuum electron are seen to result in cross sections of significantly different contour and levels of convergence. In

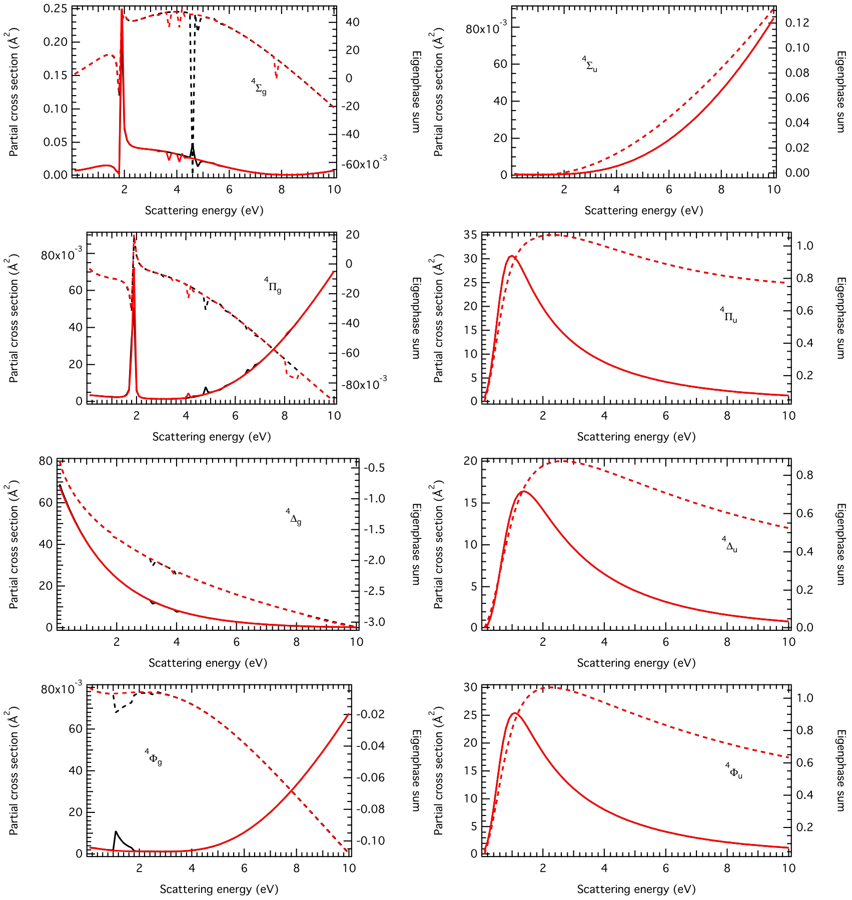

FIG. 31 Same as Fig. 30 leading to anion quartet states.

particular, in Fig. 30, the orthogonalized $^2\Delta_g$ partial cross section is lower in magnitude at threshold energies than the relaxed cross section, yet it still constitutes the greatest amplitude to the total scattering state. The orthogonalized $^2\Sigma_g$ and $^2\Pi_g$ partial cross sections display sharp pseudoresonances near 1.5 eV that are minimized but not eliminated in the relaxed partial cross sections. The remaining non-zero partial cross sections ($^2\Phi_g$, $^2\Delta_u$, and $^2\Phi_u$) are three orders of magnitude smaller than the $^2\Delta_g$ component over the scattering energy range. Although the symmetry of the scattering wave is not as evident as that of $^1S \rightarrow {}^1\Sigma_g$, we may characterize electron scattering from $^3D \rightarrow {}^3\Delta_g$ leading to the anion doublet states as also dominated by *s*-wave scattering albeit with a smaller magnitude.

As is apparent from Fig. 31, scattering leading to anion quartet states displays comparatively more complex dynamics. The 15-30 Å^2 peak in the $^4\Pi_u$, $^4\Delta_u$, and $^4\Phi_u$ partial cross sections may be considered the result of resonant p-wave attachment on the basis of the inversion symmetry and angular momentum coupling of the $m_l = 2$ target to a $l = 1$, $m = 0, \pm 1$ electron. The $^4\Sigma_g$ partial cross section bears a (pseudo) Fano resonance lineshape at 2.0 eV. Fano resonances are characterized by a cross section of the type (Rau, 2004)

$$\sigma = \sigma_a[(q+\varepsilon)^2/(1+\varepsilon^2)], \tag{131}$$

where σ_a is the background nonresonant cross section, $\varepsilon = 2(E - E_R)/\Gamma$ is the energy of the resonance, and q the so-called profile parameter. A fit of the $^4\Sigma_g$ eigenphase sum to the Fano profile as suggested by Eq. 5 of Rau, 2004 is not possible with the current data due to the mod π discontinuity at 1.8 eV. In any case, Fano resonance profiles constitutes a prominent feature of the autoionization resonances of the noble gases that have long been investigated theoretically (Armstrong *et al.*, 1975; Johnson *et al.*, 1980; Stener *et al.*, 1995),

E. Conclusion

We have adapted the multichannel configurational interaction code suite of Stratmann and Lucchese (Stratmann and Lucchese, 1995) for electron scattering and have computed preliminary cross sections for the constituent elements of the *cis*-diamminedichloroplatinum(II) molecule, namely Cl_2 and the platinum atom. Dynamic electron correlation is addressed through expansion of the target wave function in low-energy eigenstates. These cross sections are compared to available experiment and to SECP results. We summarize the major findings of the current study:

The essentially static-exchange 1-state 1-channel scattering calculation of Cl_2 possesses an artifactual scattering resonance in the $^2\Sigma_u^+$ symmetry that is eliminated upon expansion of the CI target wave function into the six lowest-energy states that arise from the valence-type excitations into the $(5\sigma_u)^0$ unoccupied orbital. This procedure recovers short-range correlation and removes the presence of the $^2\Sigma_u^+$ resonance. However, the long-range correlation due to the asymptotic dipole polarizability is not well reproduced in this approximation, which manifests itself as an isometric cross section between 0.1 and ~ 5 eV.

Cross sections for electron scattering from the isolated Pt atom were generated at the SECP level in the icosahedral point group for the ^1S state in the previous investigation of CDDP (Carey *et al.*, 2011). In the current study these results are augmented with those of SE and MCCI utilizing a $D_{\infty h}$ point group for both the ^1S and the degenerate ^3D ground state targets. Both static-exchange and MCCI ^1S calculations yield cross sections dominated by s-wave ($\Delta m = 0$) scattering. The inclusion of the dipole polarizability in the ^1S SECP cross section is seen to lower the magnitude at the lowest scattering energy by nearly a factor of 4. The 1-state 5-channel MCCI $^3D \rightarrow {}^3\Delta_g$ cross results are much more complex due to the spin and orbital angular momentum coupling between the continuum and the target electrons. In particular, while the doublet anion states are dominated by $\Delta m = 0$ scattering, the quartet anion states show large $\Delta m = 0$ and resonant $\Delta m = 1$ scattering contributions.

The multichannel scattering method as currently implemented requires additional modification to account for the dipole polarizability of a diatomic target in the presence of the scattered electron such as that detailed in Rescigno *et al.*, 1995a. However, extensive modification will be needed to address atomic scattering. For heavy targets, even neglecting the spin-orbit interaction that requires a fully relativistic scattering hamiltonian to generate (Zatsarinny and Bartschat, 2008), scalar relativistic corrections will be necessary to provide a qualitative account, for example, of the energy levels of the contracted orbitals and the correct ordering of the target states. These issues become imperative in the discussion on differential cross section (DCS), which are even more sensitive to the details of the computational method than the integrated cross sections detailed in the current study.

V. MOLECULAR AND RECOIL FRAME ANGULAR DISTRIBUTIONS OF THE C 1s AND Cl 2p PHOTOIONIZATION OF CHLOROMETHANE AND CHLOROETHANE

A. Introduction

Molecular frame photoelectron angular distributions (MFPADs), the differential cross sections of photoelectrons ejected from a oriented target, provide the maximal information about the spatial distribution of photoelectrons if the spin of the continuum electron is neglected (Yagishita *et al.*, 2005). The most general expression of these oriented angular distributions take the form of an expansion in spherical harmonics (Dill, 1976)

$$\frac{d\sigma}{d\Omega} = \sum_{LM} A_{LM} Y_{LM}\left(\hat{k}\right), \tag{132}$$

where $\hat{k}$ are the angles (θ_k, ϕ_k) measured from the molecular symmetry axis defined along the z axis and $L \leq 2l_{\max}$, where $l_{\max}$ is largest angular momentum of the continuum electron amplitude. When the electric vector of the light is parallel or perpendicular to the molecular axis, the expansion coefficients of Eq. 132 are given by (Dill *et al.*, 1976)

$$\begin{aligned} A_{LM} &= \pi\alpha h\nu(-1)^{\mu} \sum_{ll'} \left[(2l+1)(2l'+1)\right]^{1/2} \\ &\times i^{(l'-l)} \exp\left[i(\sigma_l - \sigma_{l'})\right] D_{l'\mu}^{(-)1s*} D_{l\mu}^{(-)1s} \\ &\times (l\mu, l'-\mu|L0)(K0|l0, l'0), \end{aligned} \tag{133}$$

which is a sum of the products of the transition amplitudes $D_{l\mu}$. Although theoretical MFPADs for small diatomic molecules such as N_2 and CO_2 have been known for some time (Dill *et al.*, 1976), experimental detection of the angular momentum of the photoelectron was not achieved until the application of angle-resolved coincidence techniques to photoelectron-photoion image detection (Golovin *et al.*, 1992; Shigemasa *et al.*, 1995). In this case, the coincidence experiment measures the recoil frame photoelectron angular distribution (RFPAD), in which an internal coordinate system is defined by the polarization or the electric vector of the light and the photofragment recoil axis. For nonlinear polyatomic molecules, the RFPAD coincides with the MFPAD only if several assumptions are made about the dynamics of the collision. In addition to the adiabatic approximation, the other vital approximation is the axial recoil approximation, first proposed by Zare (Zare, 1967), which assumes the lifetime of the dissociating state is shorter than the molecular rotational period, thereby allowing the recoil axis to be defined as coincident to the instantaneous direction of the dissociating bond.

Earlier experiments measured only the anisotropy of the photoelectron with respect to the propagation or electric vector component of the photocurrent. In this case, the experiment measures the photoelectron differential cross section averaged over all molecular orientations. The differential cross section are then given in terms of the total cross section σ and the photoelectron asymmetry parameter β_k through the relation (Wallace and Dill, 1978a)

$$\frac{d\sigma}{d\Omega} = \frac{\sigma}{4\pi}\left[1 + \beta_k P_2\left(\cos\theta\right)\right], \tag{134}$$

where $P_2(\cos\theta)$ is a Legendre polynomial. In fact, Eq. 134 constitutes the so-called *integrated target angular distribution* (ITAD), one of several partially integrated photoelectron differential cross sections (Wallace and Dill, 1978a). Another useful frame is the *integrated detector angular distribution* (IDAD), which takes an analogous form for cylindrically symmetric nonchiral targets

$$\frac{d\sigma}{d\Omega} = \frac{\sigma}{4\pi}\left[1 + \beta_n P_2\left(\cos\theta\right)\right]. \tag{135}$$

The distribution of Eq. 135 results from measuring the integrated photoelectron emission as a function of the orientation of the target relative to the orientation of the electric vector of the photocurrent. In particular, when β_n reaches a maximum $\beta_n = 2.0$, parallel transitions are dominant, whereas the minimum value $\beta_n = -1$ indicates the dominance of the perpendicular transition.

Valence MFPADs have been measured for a number of $\mathrm{CX}_n\mathrm{Y}_{4-n}$ systems, where X and Y represents any hydrogen or halide substituent. These include velocity imaging photoionization coincidence (VPICO) studies on the valence orbitals of the tetrahedral halides CF_4 and CCl_4 (Kinugawa *et al.*, 2002), VIPCO studies on the $\tilde{A}$ photoionization of CH_3F and CH_3Cl (Hikosaka *et al.*, 2001), and angle-resolved photoelectron photoion coincidence imaging (AR-PEPICOI) on the C_{3v} freon halide CF_3I (Downie and Powis, 1999a,b). Most of these studies (Downie and Powis, 1999a,b; Hikosaka *et al.*, 2001; Powis, 1997) employed the continuum multiscattering method (Dill and Dehmer, 1974) using a semiempirical $X\alpha$ local exchange functional to determine analytic photoionization cross sections and angular distributions. Earlier experiments that measured only the electron asymmetry parameter β_k include valence photoelectron spectroscopic studies on the chloromethanes (Keller *et al.*, 1983), the freon series CF_xCl_y (Potts *et al.*, 1985), the inner- and outer valence shell ionization of CH_3F and CH_3Cl (Novak *et al.*, 1986), and the outer valence ionization of CH_3Cl and CH_3I (Holland *et al.*, 2006). Valence methyl halide photoionization cross sections from Rydberg states have been generated by the multichannel quantum defect method (Mayor *et al.*, 2007). More thorough bibliographic reviews of the valence PES (von Niessen *et al.*, 1982) and electron energy loss spectra (EELS) (Hitchcock and Mancini, 1994) for a wide variety halide and freon gases may be found in the given references.

In this section we present computed cross sections and angular distributions of the core-level photoionization of chloromethane CH_3Cl and chloroethane C_2H_5Cl, using the frozen-core Hartree-Fock method (Lucchese *et al.*, 1982). Preliminary inner-shell photoelectron angular distributions for the direct photoionization of chloromethane

$$^1A_1 : \mathrm{CH_3Cl} + h\nu \rightarrow \mathrm{CH_3Cl^+} + e^- \tag{136}$$

leading to the primary dissociation of the CCl bond which we hereafter denote Reaction 1

$$\mathrm{CH_3Cl^+} \rightarrow \mathrm{CH_3^+} + \mathrm{Cl^+} + e^- \tag{137}$$

and a secondary reaction denoted Reaction 2 leading to dissociation of the CH bond

$$\mathrm{CH_3Cl^+} \rightarrow \mathrm{CH_2Cl^+} + \mathrm{H^+} + e^- \tag{138}$$

and two minor reactions leading to the products $H_3{}^+ + CCl^+$ and $CH_2{}^+ + HCl^+$, have been reported by Li *et al.* (Li *et al.*, 2007). Lucchese *et al.* (Lucchese *et al.*, 2009) have reported photoionization cross sections within the FCHF approximation. Both investigations have concentrated on the photoelectron differential cross sections resulting from the dissociation of the primary CCl bond of Reaction 1. In the present report, we shall briefly revisit the primary findings of the earlier calculations using tighter SCE convergence parameters than those of Lucchese *et al.*, 2009 and include more recent results for Reaction 2 leading to the dissociation of one of the symmetry-equivalent CH bonds.

The primary focus of the current study is the investigation of inner-shell photoionization of chloroethane. Not only is chloroethane a chemically relevant molecule particularly in its application as a topical anaesthetic (Buckley and Benfield, 1993; Fan and Leung, 2002), the second carbon atom affords the systematic investigation of the chemical shift of the methyl and methyl chloride C 1s photoionization cross sections (Abu-samha *et al.*, 2005). On account of it relative lack of abundance in the atmosphere, chloroethane has undergone comparatively little of the valence- or core-shell spectroscopic investigation noted for the methyl halides and freon gases. Early core-level X-ray photoelectron spectra (XPS) (Ohta and Kuroda, 1976; Perry and Jolly, 1974) found a very small difference ($\sim$ 1.0 eV) between the respective ionization potentials of the C 1s and Cl 2p shells of CH_3Cl and C_2H_5Cl. Hitchcock and Brion have measured the electron energy loss spectra measured for the Group VIII methyl halide series CH_3X (Hitchcock and Brion, 1978b) and the methyl chlorides CH_nCl_{4-n} and chloroethane (Hitchcock and Brion, 1978a) in the pre-ionization threshold region of the C 1s and Cl 2s and 2p spectrum, likewise found only small deviations in respective Rydberg excitations. Lindle *et al.* (Lindle *et al.*, 1991) recorded the Cl 1s and Cl 2s absorption features of CH_3Cl and the chlorofluoromethanes using X-ray emission spectroscopy. More recently, Fan and Leung (Fan and Leung, 2002) have reported generalized oscillator strengths df/dE, which are related to total cross sections σ by the Bethe-Born equation

$$\sigma\,(\mathrm{Mb}) = 109.75\frac{df}{dE}\left(\mathrm{eV}^{-1}\right), \tag{139}$$

of angle-resolved EELS of the valence and the C 1s and Cl 2p core shells of chloroethane. To the best of our knowledge, neither molecular-frame nor partially integrated angular distributions of valence and core shell photoionization are available for chloroethane. Consequently, we will compare our angular distributions with the AR-PEPICO C 1s Cl 2p

RFPADs of methyl chloride (Elkharrat, 2009; Li *et al.*, 2007). We also compare our C 1s σ and β_k parameters to the angle-resolved PES of ethane (Rennie *et al.*, 1999).

Chloroethane has a ground state electronic configuration, determined from core-level X-ray spectroscopy (Ohta and Kuroda, 1976) and HeI and Penning ionization electron spectroscopy (Imura *et al.*, 2001), in C_s symmetry,

$$\begin{aligned}&\underbrace{(1a')^2}_{\text{Cl 1s}}\underbrace{(2a')^2}_{\text{C 1s}}\underbrace{(3a')^2}_{\text{C 1s}}\underbrace{(4a')^2}_{\text{Cl 2s}}\underbrace{(5a')^2(6a')^2(1a'')^2}_{\text{Cl 2p}}\\ &\underbrace{(7a')^2(8a')^2(9a')^2(2a'')^2}_{\text{inner valence}}\\ &\underbrace{(10a')^2(11a')^2(3a'')^2(12a')^2(13a')^2(4a'')^2}_{\text{outer valence}}.\end{aligned} \tag{140}$$

We examine photoionization from the levels $(2a')^{-1}$, $(3a')^{-1}$, $(5a')^{-1}$, $(6a')^{-1}$, $(1a'')^{-1}$ in the reaction

$$A' : \mathrm{C_2H_5Cl} + h\nu \to \mathrm{C_2H_5^+} + e^- \tag{141}$$

leading to the primary dissociation of the CCl bond which we hereafter denote Reaction I

$$\mathrm{C_2H_5^+} \to \mathrm{C_2H_5^+} + \mathrm{Cl^+} + e^- \tag{142}$$

and a secondary reaction denoted Reaction II leading to the dissociation of the CC bond

$$\mathrm{C_2H_5^+} \to \mathrm{CH_2Cl^+} + \mathrm{CH_3^+} + e^- \tag{143}$$

to obtain random and fixed-orientation angular distributions of the photoelectron e^- with energies $E_k = 2.1$ eV and $E_k = 3.8$ eV above the Cl 2p ionization threshold and $E_k = 2.8$ eV above the respective C 1s thresholds. Other more complex fragmentation channels involve significant nuclear rearrangement of the ionized target before dissociation and cannot be adequately described by the current calculation methods.

To date, we are not aware of investigations on the core-level photodissociation dynamics of chloroethane in the gas phase. Photodissociation channels of $\mathrm{CH_3Cl}$ at the Cl 2p edge have been investigated by Thissen *et al.* (Thissen *et al.*, 1994), with valence absolute differential oscillator strengths of ion channels detected by Olney and coworkers (Olney *et al.*, 1996). Lago *et al.* have studied the valence and Cl 2p fragmentation of the related methyl halide chloroform, $CHCl_3$ (Lago *et al.*, 2004). A number of photoabsorption studies have investigated the dissociation properties of the alkyl halides at the valence level. Raymonda *et al.* have recorded the vacuum ultraviolet spectrum of the chloroalkanes from 50000 cm^{-1} (6.2 eV) to 90000 cm^{-1} (11.2 eV). Morgenthaler and Eyler (Morgenthaler and Eyler, 1979) investigated the unimolecular dissociation of $C_2H_5Cl^+$, finding only two major products above the first ionization energy. The dissociation limits of the methyl halides at 121.6 nm = 10.2 eV leading to production of radical species H + CH_3X have been investigated by Amaral *et al.* (Amaral *et al.*, 2001). Lin *et al.* (Lin *et al.*, 2002) investigated the dissociation limits of CH_3Cl leading to Cl + CH_3, H + CH_2Cl, and HCl + CH_2.

The outline of this paper is as follows. In Sec. V.B we present expressions for the nonlinear MFPAD and RFPAD and in Sec. V.G the computational details needed to generate the dipole transition elements for the photoionization cross section and asymmetry parameters discussed in Sec. V.H, whose computed Cl 2p and C 1s results compared to ethane (Rennie *et al.*, 1999) and chloromethane (Elkharrat, 2009). In Secs. V.I and V.J we present the angular distributions in the molecular frame and the recoil frame for Cl 2p photoionization 2.1 eV and 3.8 eV above threshold and C 1s photoionization at photoelectron energy 2.8 eV. We give a summary of the computed results in Sec. V.K.

B. Theory

1. *Functional form of the MFPADs*

We represent the neutral state Ψ_i as a converged Hartree-Fock determinant and the ionized target Ψ_f as the unrelaxed hole state resulting from the ionization. This constitutes the basis of the frozen-core Hartree-Fock (FCHF) approximation (Lucchese *et al.*, 1982). The three-dimensional scattering equations are decoupled by a single-center expansion (SCE) (Gianturco and Jain, 1986) of the bound and continuum electron wave functions, with the resulting one-dimensional radial scattering equations solved using the Schwinger variational method with Padé approximant corrections (Lucchese *et al.*, 1982). Details may be found in the given references. Photoionization dynamics in the close-coupling scheme are recovered from the dipole transition elements through the integral

$$I_{lm\mu}^{p_i\mu_i p_f\mu_f}(E) = \left\langle \Psi_i^{p_i\mu_i} \left| \hat{d}_\mu \right| \Psi_f^{p_f\mu_f} \phi_{lm}^{(-)} \right\rangle, \tag{144}$$

where $\Psi_i^{p_i\mu_i}$ is the initial (neutral) state with irreducible representation p_i and component μ_i, and $\Psi_f^{p_f\mu_f}$ the ionized target state with irreducible representation p_f and symmetry component μ_f. Because the neutral and ionized target possess an Abelian symmetry, $\mu_i = \mu_f = 1$. The continuum orbital of a given partial wave lm is represented by $\phi_{lm}^{(-)}$, and the dipole operator with spherical component μ is shown in Eq. 144 symbolically as $\hat{d}_\mu$. Among the equivalent gauge representations of the dipole operator d_μ, the so-called mixed gauge is perhaps the most useful, as it is known to satisfy the Thomas-Reiche-Kuhn sum rule

$$\sum_k f_k + \int \frac{df}{dE} dE = N \tag{145}$$

relating the oscillator strength, which is related to total photoionization cross section by Eq. 139, to the total number of electrons of the target N in the limit of a complete basis set description of the target orbitals. Since the experiment used linearly polarized light, we define $\mu_0 = 0$.

The details of the generation of the angular distributions have been given in Lucchese, 2004, so we will only provide an outline necessary to understand the current results. We define in the molecular frame photoelectron angular distributions (θ_k, ϕ_k) in terms of a coordinate system defined by the molecular axis and the direction of the polarization vector of the linearly polarized light with solid angle (θ_n, ϕ_n). In this notation, the photoelectron angular distributions in the molecular frame are stated, as follows:

$$I_{\mu_0}(\theta_k, \phi_k, \theta_n, \phi_n) = \frac{4\pi^2 E}{c g_{p_i}} \sum_{\mu_i, \mu_f} \left| T_{\mu_0}^{p_i\mu_i, p_f, \mu_f}(\theta_k, \phi_k, \theta_n, \phi_n) \right|^2, \tag{146}$$

where the transition amplitudes $T_{\mu_0}^{p_i\mu_i, p_f, \mu_f}$ are given by

$$T_{\mu_0}^{p_i\mu_i, p_f, \mu_f} = \sum_{lm\mu} I_{lm\mu}^{p_i\mu_i, p_f\mu_f}(E) Y_{lm}^*(\theta_k, \phi_k) D_{\mu,\mu_0}^1(R_n). \tag{147}$$

The set of rotations $R_n = (\alpha_n, \beta_n, \gamma_n)$ are the Euler angles in the z-y-z convention (Zare, 1988) that bring the molecular frame into the lab frame.

2. Functional form of the RFPADs

In a dissociative photoionization experiment satisfying the conditions of the axial recoil approximation, the photoelectron angular distribution can be measured with respect to a coordinate system defined by the recoil axis of the fragments and the polarization vector of the light, as mentioned in the Introduction. We define in the recoil frame the angle of the photoelectron momentum (θ'_k, ϕ'_k) and the momentum vector of the linearly polarized light as (θ'_n, ϕ'_n). The differential cross section in the recoil frame is obtained from a rotation through a set of Euler angles $R = (\alpha_R, \beta_R, \gamma_R)$ from the molecular frame into this recoil frame. The photoelectron angular distributions in the recoil frame are given thus:

$$\begin{aligned} I_{\mu_0,\alpha_R,\beta_R,\gamma_R} \quad \left(\theta'_k, \phi'_k, \theta'_n, \phi'_n\right) = \sum_{L'LN'N} H^{\mu_0,\alpha_R,\beta_R,\gamma_R}_{L'LN'N} \\ \times Y_{L'N'}\left(\theta'_k, \phi'_k\right) Y_{LN}\left(\theta'_n, \phi'_n\right)^*, \end{aligned} \tag{148}$$

where

$$\begin{aligned} H^{\mu_0,\alpha_R,\beta_R,\gamma_R}_{L'LN'N} = \sum_{JM'M} H^{\mu_0}_{L'LM'M} \left(\frac{2J+1}{2L'+1}\right) \left\langle JLPN|L'N'\right\rangle \\ \times \left\langle JLP'M|L'M'\right\rangle \left[D^J_{P',P}(\alpha_R, \beta_R, \gamma_R)\right]^*. \end{aligned} \tag{149}$$

The factors $H^{\mu_0}_{L'LM'M}$ contain a transformation of the dipole transition elements of Eq. 144 as

$$\begin{aligned} H^{\mu_0}_{L'LM'M} = \quad & \frac{4\pi^2 E}{c g_{p_i}} \sum_{\mu_f,\mu_i} \sum_{\substack{lm\mu \\ l'm'\mu'}} (-)^{M'-M+\mu-\mu_0} \\ & \times (I^{p_i\mu_i,p_f\mu_f}_{lm\mu})(I^{p_i\mu_i,p_f\mu_f}_{l'm'\mu})^* \\ & \times \left[\frac{(2l'+1)(2L'+1)}{2l+1)(2L+1)}\right]^{1/2} \left\langle L'l'M'-m'|l-m\right\rangle \\ & \times \left\langle L'l'00|l0\right\rangle \left\langle 11-\mu\mu'|L-M\right\rangle \\ & \times \left\langle 11\mu_0-\mu_0|L0\right\rangle. \end{aligned} \tag{150}$$

In a polyatomic coincidence experiment yielding two fragments, the absolute orientation of the molecule about the recoil axis is often not observable; consequently, the measured RFPAD results from the average of the MFPAD over the unobserved azimuthal angle γ_R

about the recoil axis. In this case, it can be shown (Lucchese, 2004) that the resulting photoelectron differential cross section takes the simple functional form, for linearly polarized light,

$$\begin{aligned} I_{\mu_0}\left(\theta_k', \phi_k', \theta_n', \phi_n'\right) &= F_{00}\left(\theta_k'\right) + F_{20}\left(\theta_k'\right) P_2^0\left(\cos\theta_n'\right) \\ &+ F_{21}\left(\theta_k'\right) P_2^1\left(\cos\theta_n'\right)\cos(\phi_k' - \phi_n') \\ &+ F_{22}\left(\theta_k'\right) P_0^2\left(\cos\theta_n'\right)\cos 2(\phi_k' - \phi_n') \end{aligned} \tag{151}$$

where the F_{LN} functions may be expressed in terms of a series expansion in associated Legendre polynomials

$$\begin{aligned} F_{LN}\left(\theta_k'\right) &= \frac{1}{2\pi(1+\delta_{N0})}\left[\frac{(2L+1)(L-N)!}{(L+N)!}\right]^{1/2} \\ &\times \sum_{L'}\left[\frac{(2L'+1)(L'-N)!}{(L'+N)!}\right]^{1/2} A_{L'NLN} P_{L'}^{N}\left(\cos\theta_k'\right). \end{aligned} \tag{152}$$

. The general expansion coefficients $A_{L'M'LM}$ are

$$\begin{aligned} A_{L'M'LM} = & \frac{4\pi^2}{cE}\sum_{lm\mu}\sum_{l'm'\mu'} I_{lm\mu} I^*_{l'm'\mu'}(-1)^{m+\mu}\left[\frac{(2l+1)(2l'+1)}{(2L+1)(2L'+1)}\right]^{1/2} \\ & \times \left\langle ll'00|L'0\right\rangle \left\langle ll', -mm'\right\rangle \langle 1100|L0\rangle \langle 11, \mu-\mu|LM\rangle . \end{aligned} \tag{153}$$

In addition to providing a closed-form expression of the photoelectron angular distribution at any orientation of recoil vector and light polarization, Eq. 151 also allows comparison between theory and experiment since it provides the maximal information to be obtained from experiment. Generally, the RFPADs given in the literature are discussed in terms of parallel and perpendicular transitions, in which the polarization vector of linearly polarized light is colinear with or perpendicular to the observed recoil axis averaged over all angles ϕ_n'. Parallel ($\theta_n' = 0°$) and perpendicular ($\theta_n' = 90°$) transitions in the recoil frame may be stated in terms of the F_{LN} functions according to the expressions

$$\begin{aligned} I_{\theta_n'=0^\circ}\left(\theta_k'\right) &= F_{00}\left(\theta_k'\right) + F_{00}\left(\theta_k'\right) \\ I_{\theta_n'=90^\circ}\left(\theta_k'\right) &= F_{00}\left(\theta_k'\right) - \frac{1}{2}F_{20}\left(\theta_k'\right) \end{aligned} \tag{154}$$

We have made use an alternative method of generating molecular or recoil frame distributions. The previously detailed method computes recoil frame angular distributions

TABLE 21 Chloromethane core ionization potentials (IP) in eV compared to experiment (Hitchcock and Brion, 1978b).

Molecular orbital	Symmetry	SCF Energy	Experiment
Cl 1s	$1a_1$	−2852.5909	−2828.7
C 1s	$2a_1$	−307.2461	−292.3
Cl 2s	$3a_1$	−287.1992	−277.2
Cl 2p	$4a_1$	−218.2697	−206.1[a]
	$1e$	−218.2189	

[a] Energy of Cl $2p_{3/2}$ electron. The Cl $2p_{1/2}$ electron is assumed 1.7 eV higher in energy.

from algebraic rotations of transition dipole elements generated at the default computational chemistry orientation. This method leads to complications when the desired bond does not correspond to a symmetry axis of the molecule. The method we employ for all subsequent photoionization calculations generates the transition dipole elements from a target geometry already initialized into the desired body frame. Specifically, the target geometrical coordinates are transformed from the Mulliken standard orientation of the point group (Mulliken, 1955) through a set of rotations $R_{\{x,y,z\}}$ and translations $T_{\{x,y,z\}}$ about the invariant x-, y-, or z-axis such that the desired molecular bond lies along, or is parallel to, the invariant $+z$-axis, which we define as the dissociation axis. This procedure has the advantage over rotations through the Euler angles R_n and R detailed previously and in Toffoli *et al.*, 2007 since the invariant axes and the molecular or recoil axis need not share a common point. Furthermore, this procedure allows a direct comparison with the ITAD β_k and β_n parameters recorded from experiment.

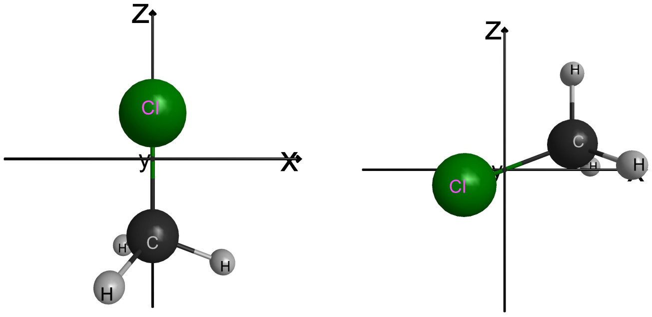

Reaction 1 Reaction 2

FIG. 32 Orientation of CH_3Cl within the Reaction 1 (left) and Reaction 2 (right) molecular frames.

C. CH_3Cl computational details

1. SCF parameters

The Hartree-Fock orbitals were obtained for chloromethane in C_{3v} symmetry, with molecular parameters derived from experimental values (Duncan *et al.*, 1973) and using the standard aug-cc-pVTZ basis set in the gaussian 03 code suite (Frisch *et al.*, 2004). The structural parameters in terms of internal coordinates are as follows: $r\mathrm{CCl} = 1.785$ Å , $r\mathrm{CH} = 1.090$ Å , $a\mathrm{HCCl} = 110.75^\circ$, and $a\mathrm{HCH} = 108.76^\circ$. We find a computed SCF energy of $E = -499.148279094$ au and a dipole moment of $\mu^{\mathrm{SCF}} = 2.10$ debye (D), and an isotropic polarizability of $\bar{\alpha}^{\mathrm{SCF}} = 39.74$ au. The computed dipole moment compares to an experimental dipole moment of $\mu^{\mathrm{Exp.}} = 1.87$ D from Nelson *et al.*, 1967. The SCF core orbital energies are compared to the C 1s and Cl 1s, 2s and $2\mathrm{p}_{3/2}$ ionization potentials obtained from the electron energy loss spectra of Hitchcock and Brion (Hitchcock and Brion, 1978b) in Table 21.

The standard orientation (Mulliken, 1955) of a molecule in the C_{3v} point group results in one of the $3\sigma_v$ symmetry elements coincident with the yz plane, which proved not to be the most convenient choice to compute the perpendicular transition PADs from the dipole matrix elements of Eq. 144. For calculation of the CH_3Cl dipole transition matrix elements $I_{lm\mu}^{p_i\mu_i p_f\mu_f}$, an initial rotation $R_z = -90^\circ$ was performed on the target geometry to

TABLE 22 The normalization of the core orbitals of CH_3Cl in the single-center expansion of the target orbitals in partial waves to a maximum angular momentum $l_{\max} = 60$.

Molecular orbital		Orbital normalization	
		Reaction 1	Reaction 2
Cl 1s	$1a_1$	0.99622664	0.99634578
C 1s	$2a_1$	0.99966716	0.99968493
Cl 2s	$3a_1$	0.99966972	0.99967902
Cl 2p	$4a_1$	0.99999834	0.99999833
	$1e$	0.99999292	0.99999292

effect a realignment of one σ_v onto the xz plane. No further rotations or translations were necessary to yield the relevant PADs for Reaction 1 (Eq. 137), while a second rotation $R_y = -110.75^\circ$ was performed to compute the PADs of Reaction 2 (Eq.138). To retain a high degree of normalization for the SCE of the Cl core orbitals, no translations of the target center of mass were considered. We present figures of CH_3Cl in the σ_{xz} plane in the Reaction 1 and Reaction 2 molecular frames in Fig. 32 (Bode and Gordon, 1998).

2. *CH_3Cl SCE parameters*

Dipole transition elements $I_{lm\mu}^{p_i\mu_i p_f\mu_f}(E)$ were computed using the EPOLYSCAT code suite of Lucchese and collaborators (Gianturco *et al.*, 1994; Natalense and Lucchese, 1999). For both conformations, partial waves up to $l_{\max} = 60$ were retained in the SCE of the continuum and target orbitals, and up to $2l_{\max}$ for the interaction potential. Consequently, the single-center expansion should be better converged than those found in Lucchese *et al.*, 2009, in which the partial wave expansion was truncated at $l_{\max} = 40$. The SCE with these parameters led to the well-converged target core orbitals, as observed in Table 22, with all inner and outer valence orbitals were normalized better than the Cl 1s normalization of 0.996. In a previous investigation on the RFPADs of Cl 2p ionization of CH_3Cl (Lucchese *et al.*, 2009), we computed core-level photoionization cross sections at

TABLE 23 Photoionization cross sections σ (in Mb) and asymmetry parameters of the electron, β_k, and ion fragment, β_N, computed within the length, mixed, and velocity gauges of the dipole operator. Results are presented for C 1s $(2a_1)^{-1}$ and Cl 2p $(4a_1)^{-1}$, $(1e)^{-1}$, and summed ionizations. The Cl 2p cross sections are obtained from the sum $\sigma_{4a_1}(E)+\sigma_{1e}(E)$ and electron and nuclear asymmetry parameters from the weighted average $\left(\beta_{\{k,N\}/4a_1}+2\beta_{\{k,N\}/1e}\right)/3$.

Molecular orbital	$h\nu$ (eV)	σ (Mb)			β_k			β_N	
		Length	Mixed	Velocity	Length	Mixed	Velocity	Length	Velocity
Reaction 1									
$2a_1$	294.60	0.9082	0.9436	0.9803	1.1801	1.1818	1.1835	−0.4338	−0.4251
	296.25	0.9596	0.9898	1.0210	1.1997	1.2009	1.2021	−0.4190	−0.4089
	297.90	0.9404	0.9619	0.9839	1.2900	1.2893	1.2885	−0.3450	−0.3355
$4a_1$	208.01	1.2039	1.2203	1.2370	0.2744	0.2724	0.2704	0.4092	0.3996
	209.66	1.2881	1.3059	1.3241	0.1481	0.1464	0.1447	0.4497	0.4385
	211.31	1.4018	1.4216	1.4417	0.0838	0.0829	0.0820	0.5122	0.5023
$1e$	208.01	3.0413	3.0513	3.0617	0.2085	0.2121	0.2156	−0.3871	−0.3882
	209.66	2.7376	2.7458	2.7542	0.3054	0.3098	0.3140	−0.3181	−0.3209
	211.31	2.5529	2.5606	2.5687	0.3986	0.4024	0.4061	−0.2430	−0.2472
Cl 2p	208.01	4.2452	4.2716	4.2987	0.2305	0.2322	0.2339	−0.1217	−0.1256
	209.66	4.0257	4.0517	4.0783	0.2530	0.2553	0.2576	−0.0622	−0.0678
	211.31	3.9547	3.9822	4.0104	0.2937	0.2959	0.2981	0.0087	0.0026
Reaction 2									
$2a_1$	294.60	0.9082	0.9436	0.9804	1.1801	1.1818	1.1835	0.1352	0.1325
	296.25	0.9596	0.9898	1.0211	1.1997	1.2009	1.2021	0.1306	0.1275
	297.90	0.9404	0.9619	0.9839	1.2900	1.2893	1.2885	0.1075	0.1046
$4a_1$	208.01	1.2039	1.2203	1.2370	0.2744	0.2724	0.2703	−0.1276	−0.1246
	209.66	1.2881	1.3059	1.3241	0.1481	0.1464	0.1447	−0.1402	−0.1367
	211.31	1.4018	1.4216	1.4417	0.0838	0.0829	0.0820	−0.1597	−0.1566
$1e$	208.01	3.0413	3.0513	3.0617	0.2085	0.2121	0.2156	0.1207	0.1210
	209.66	2.7376	2.7458	2.7542	0.3054	0.3097	0.3140	0.0992	0.0100
	211.31	2.5529	2.5606	2.5687	0.3986	0.4024	0.4061	0.0758	0.0771
Cl 2p	208.01	4.2452	4.2716	4.2987	0.2305	0.2322	0.2338	0.0379	0.0391
	209.66	4.0257	4.0517	4.0783	0.2530	0.2553	0.2576	0.0194	−0.0389
	211.31	3.9547	3.9822	4.0104	0.2937	0.2959	0.2981	−0.0027	−0.0008

the level of exact static-exchange (Lane, 1980). This was found to produce a satisfactory level of agreement with experiment and, accordingly, we have not included any model polarization terms in the current calculations.

D. Photoionization cross sections of chloromethane

In Table 23 we present the photoionization integrated cross sections σ and ITAD electron and ion asymmetry parameters β_k and β_N in the length, mixed, and velocity gauges of the dipole operator for C 1s $(2a_1)^{-1}$ and Cl 2p $(1a_1)^{-1}$ and $(1e)^{-1}$ ionization of chloromethane computed at photoelectron kinetic energies $E_k = 1.7$ eV, $E_k = 3.35$ eV, and $E_k = 5.0$ eV. To convert photoelectron energies to photon energies, we have assumed the experimental ionization potentials as stated in Elkharrat, 2009 of $E^{\mathrm{IP}} = 292.9$ eV for ionization of the $2a_1$ C 1s orbital, and $E^{\mathrm{IP}} = 206.3$ eV for both Cl 2p orbitals. The integrated cross sections

$$\sigma = \frac{4\pi^2}{3cE} \sum_{\mu} \sum_{lm} \left| I_{lm\mu} \right|^2 \tag{155}$$

for each conformation should be formally exact, independent of the immediate details of the orientation. Furthermore, the σ, β_k, and β_N parameters should be equal irrespective of the gauge of the dipole operator. These two requirements provide a test of the convergence of the transformation described in Sec. V.B.2. In this view, the values of σ computed for both reactions appear well converged, as inspected in Table 28. The electron asymmetry parameter β_k computed after the reorientation of the target likewise show only small differences between the Reaction 1 and Reaction 2 molecular frames, whereas the ion asymmetry parameter β_N, as expected, depends strongly on the initial coordinates of the target. To obtain photoionization parameters that may be directly compared to experiment, we perform a sum of the calculated $4a_1$ and $1e$ cross sections and a $(1:2)$ normalized average of the β_k and β_N asymmetry parameters at a given E. The current summed Cl 2p Reaction 1 asymmetry parameters $\beta_k = 0.26$ and $\beta_N = -0.07$ compare well to the $E = 3.5$ eV Cl $2p_{3/2}$ $\beta_k = 0.3$ and $\beta_N = -0.1$ asymmetry parameters measured for the $CH_3Cl \rightarrow CH_3{}^+ + Cl^+$ dissociation pathway of CH_3Cl (Elkharrat, 2009). Likewise, the Reaction 1 3.35 eV C 1s β_k and β_N values agree with the $E_k = 2.8$ eV experimental values $\beta_k = 1.0 \pm 0.1$ and $\beta_N = -0.25 \pm 0.1$ of Elkharrat, 2009.

E. Chloromethane MFPADs

1. Cl 2p

In Fig. 33 we display three-dimensional views (in Mb) of the Reaction 1 MFPADs for Cl 2p photoelectrons ejected from CH_3Cl with kinetic energy $E_k = 1.7$ eV, $E_k = 3.35$ eV,

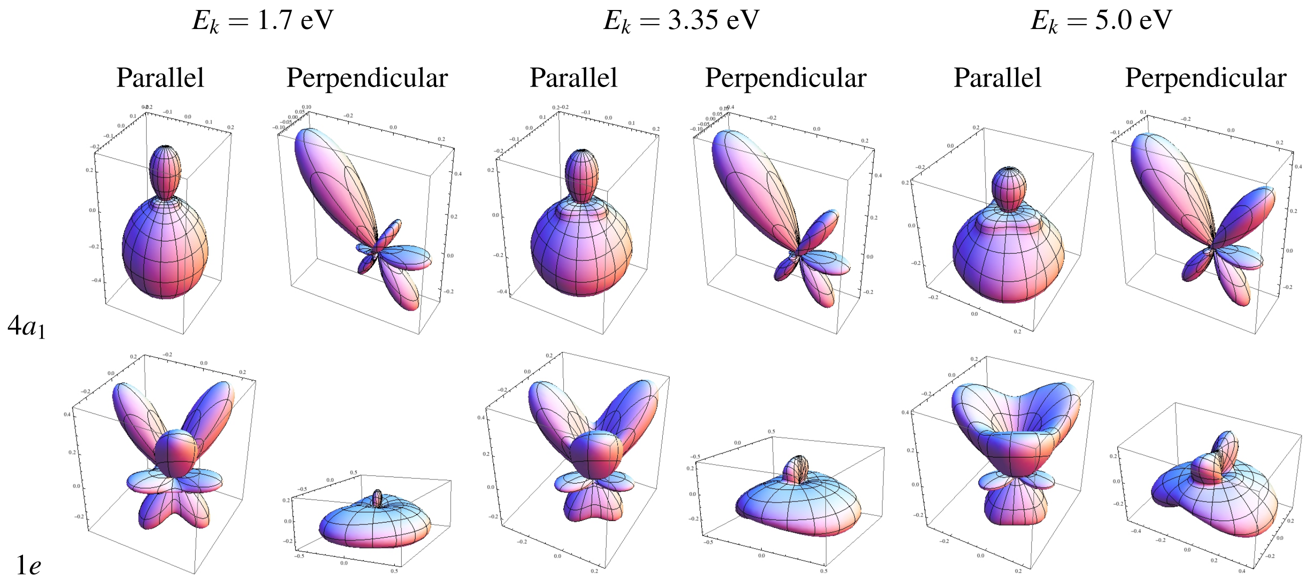

FIG. 33 Computed Reaction 1 MFPADs (in Mb) of $E_k = 1.7$ eV, $E_k = 3.35$ eV, and $E_k = 5.0$ eV photoelectrons ionized from the Cl 2p $4a_1$ (top row) and $1e$ (bottom row) orbitals of CH_3Cl. The distributions are given for light linearly polarized along the $+z$ axis yielding parallel transitions and $+x$ axis for perpendicular transitions. The CCl recoil axis in the molecular frame is coincident to $+z$ in all views.

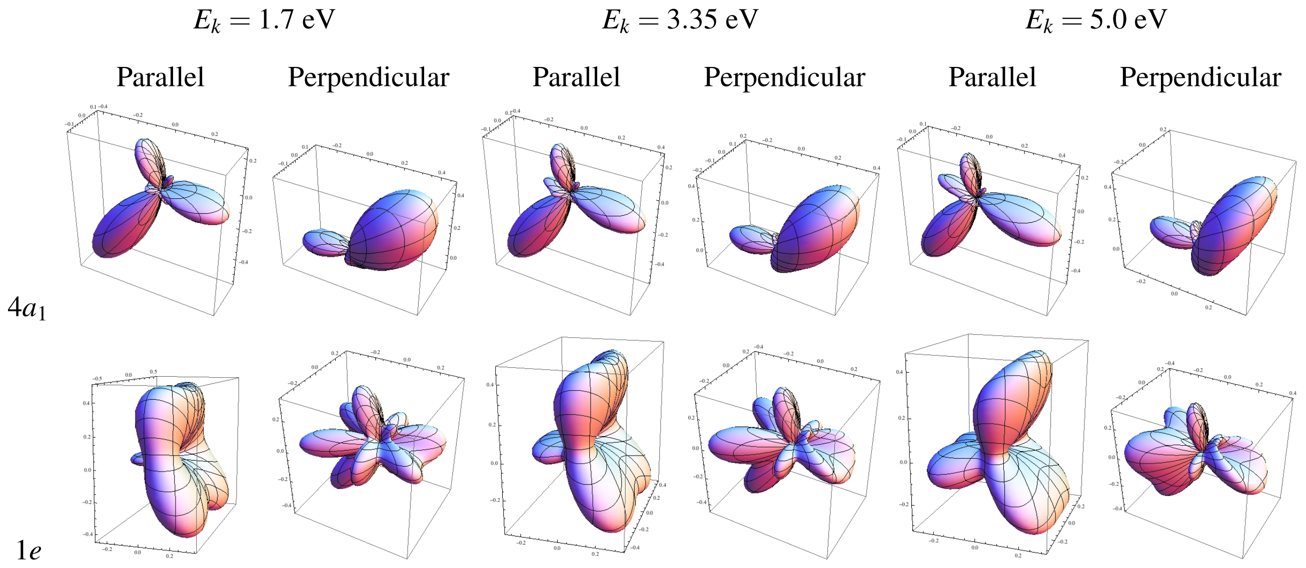

FIG. 34 Computed Reaction 2 MFPADs (in Mb) of $E_k = 1.7$ eV, $E_k = 3.35$ eV, and $E_k = 5.0$ eV photoelectrons ionized from the Cl 2p $4a_1$ (top row) and $1e$ (bottom row) orbitals of CH_3Cl. The distributions are given for light linearly polarized along the z axis yielding parallel transitions (left) and x axis for perpendicular transitions (right). The σ_{xz} CH recoil axis in the molecular frame is parallel to z in all views.

and $E_k = 5.0$ eV above ionization threshold, respectively. The corresponding Reaction 2 Cl 2p MFPADs are shown in Fig. 34. In standard orientation, while the $4a_1$ orbital is predominantly Cl $2p_z$ character, the $1e$ molecular orbital is a sum of the Cl 2p$_x$ and 2p$_y$ orbitals. After the rotation needed for the Reaction 1 molecular frame, in which the C_3 molecular axis is colinear with the invariant $+z$-axis, $4a_1$ transforms as $2p_z$ and $1e$ as $2p_x + 2p_y$, or as d_{xy} if considered as a single atomic orbital. The analysis after the rotations into the Reaction 2 molecular frame indicate that $4a_1$ transforms primarily as $2p_x$, whereas the $1e$ orbital has atomic symmetries $2p_z + 2p_y$, or as $3d_{yz}$. To a crude approximation, If the nodal structure of the MFPAD stems from the direct product of the angular momentum of the component of the polarization vector with the orbital symmetry from which the photoelectron was emitted (Lucchese, 2004), then we should expect all Cl 2p MFPADs to resemble the $3d$ or $4f$ orbitals of the appropriate nodal symmetry.

Inspection of the Cl 2p $4a_1$ Reaction 1 MFPADs of Fig. 33 reveals that ionization is dominated towards the CH_3 fragment when the photon polarization is coincident with the recoil axis, with the resulting MFPAD resembling a (distorted) d_{z^2} orbital. The corresponding σ_{xz} plane perpendicular transition MFPAD, however, reveals a strong anisotropy of the expected d_{xz} atomic orbital symmetry, with photoelectron intensity directed preferentially towards the $-xz$ quadrant. The Cl 2p $1e$ Reaction 1 MFPADs are strongly symmetric during parallel excitation, revealing a clear C_{3v} symmetry of the angular distribution. The perpendicular excitations, by contrast, are more isotropic, an expected result considering the Cl 2p $1e$ molecular orbital consists of degenerate p_x and p_y atomic orbitals resulting in a PAD comprising both d_{xz} and d_{yz} characteristics.

The Cl 2p Reaction 2 MFPADs leading to the ionization fragments $CH_2Cl^+ + H^+$, presented in Fig. 34, generally lack the clear nodal features of the Reaction 1 distributions, as the molecule possesses only the symmetry plane σ_{xz} when transformed into this recoil orientation. The parallel excitations from the $4a_1$ orbital reveals photoelectron density directed axially away from the Cl atom and the CH_3 fragment, whereas the perpendicular transitions show the same density directed axially towards the CH_3 fragment. The $1e$ parallel excitation PADs feature densities localized within the yz plane, otherwise losing

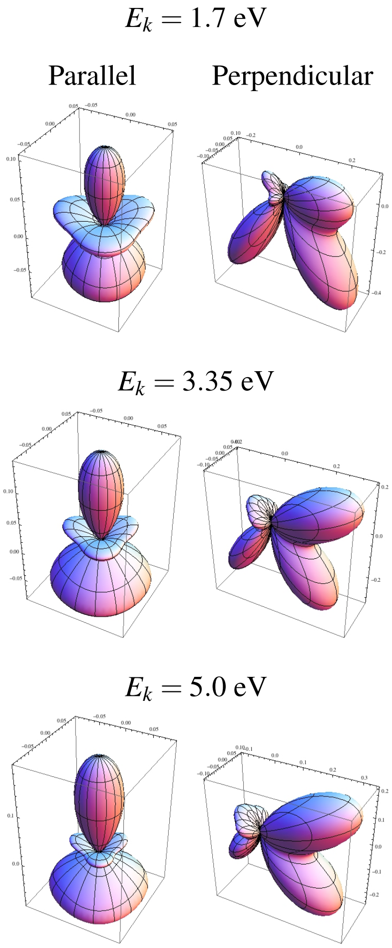

FIG. 35 Computed Reaction 1 MFPADs (in Mb) of $E_k = 1.7$ eV, $E_k = 3.35$ eV, and $E_k = 5.0$ eV photoelectrons ionized from the $2a_1$ orbital of CH_3Cl. The distributions are given for light linearly polarized along the z axis yielding parallel transitions and the x axis for perpendicular transitions. The CCl recoil axis in the molecular frame is coincident to z in all views.

most of the symmetry of the parent molecule. The $1e$ perpendicular transition PADs retain the clear C_3 axial symmetry of the parent molecule, with the C_3 axis colinear to the CCl bond in the transformed orientation (see Fig. 32).

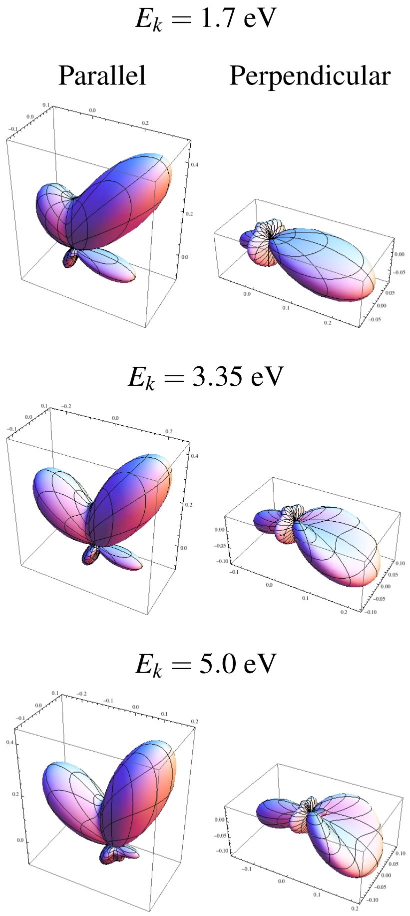

$E_k = 1.7$ eV

Parallel Perpendicular

$E_k = 3.35$ eV

$E_k = 5.0$ eV

FIG. 36 Computed Reaction 2 MFPADs (in Mb) of $E_k = 1.7$ eV, $E_k = 3.35$ eV, and $E_k = 5.0$ eV photoelectrons ionized from the $2a_1$ orbital of CH_3Cl. The distributions are given for light linearly polarized along the z axis yielding parallel transitions and the x axis for perpendicular transitions. The σ_{xz} CH recoil axis in the molecular frame is parallel to z in all views.

2. *C 1s*

Perhaps the most striking feature of the C 1s $2a_1$ MFPADs shown in Figs. 47 for the Reaction 1 channel and 48 for the Reaction 2 channel is the d-orbital scattering characteristics, an unexpected finding considering the expected p-orbital symmetry resulting from the convolution of the angular momenta of an s orbital with a $l = 1$ photon. The Reaction 1 parallel transition PADs, shown in Fig. 47, are directed axially along the CCl bond, with photoelectron density directed isotropically at increased photoelectron kinetic energies.

The perpendicular transition PADs possess a clear d_{xz} character strongly directed against the $+x$ photocurrent. The parallel transition Reaction 2 MFPADs, given in Fig. 48, show that photoelectron intensity is directed away from the CCl bond in the xz plane, while the in-plane perpendicular transitions coincident with the polarization vector, with intensity directed to the Cl atom of the CH_2Cl fragment increasing at higher photoelectron kinetic energies.

F. Chloromethane RFPADs

1. Cl 2p

Two-dimensional displays of Reaction 1 Cl 2p recoil-frame angular distributions are presented in Fig. 37. Two-dimensional views provide the advantages of both quantitative discussion of the differential cross section and allow the most direct comparison with experiment. We find that the parallel excitation $4a_1$ RFPADs (top row) display the axial symmetry of the respective MFPAD discussed in Sec. V.E, with photoelectron intensity strongly directed towards the CH_3 fragment. The perpendicular excitation RFPAD for ionization from this orbital is clearly observed to be much smaller in magnitude at all values E_k. The perpendicular $1e$ RFPAD is seen to dominate at lower photoelectron kinetic energies, with notable asymmetry to the CH_3 fragment. The summed Cl 2p RFPAD, shown in the bottom row, shows that both the parallel and perpendicular transitions become more isotropic, *i.e.* no preference for ejection towards either CH_3 or Cl fragment, with higher photoelectron kinetic energy. Furthermore, the Cl 2p cross section has nearly the same magnitude as that reported in Fig. 6 of Li *et al.*, 2007 and in Fig. 3 of Lucchese *et al.*, 2009 for a previous calculation using $l_{\max} = 40$, which implies that all dipole transition moments, and, consequently, all resulting cross sections, are well converged.

Reaction 2 Cl 2p RFPADs are shown in Fig. 38. We see that photoelectron intensity from the $1e$ orbital is on the order of four times the magnitude of that from ejection from $4a_1$ and comprises the majority of the PAD of the summed Cl 2p distribution at all photoelectron energies. Furthermore, the Reaction 2 PADs display an overall less nodal

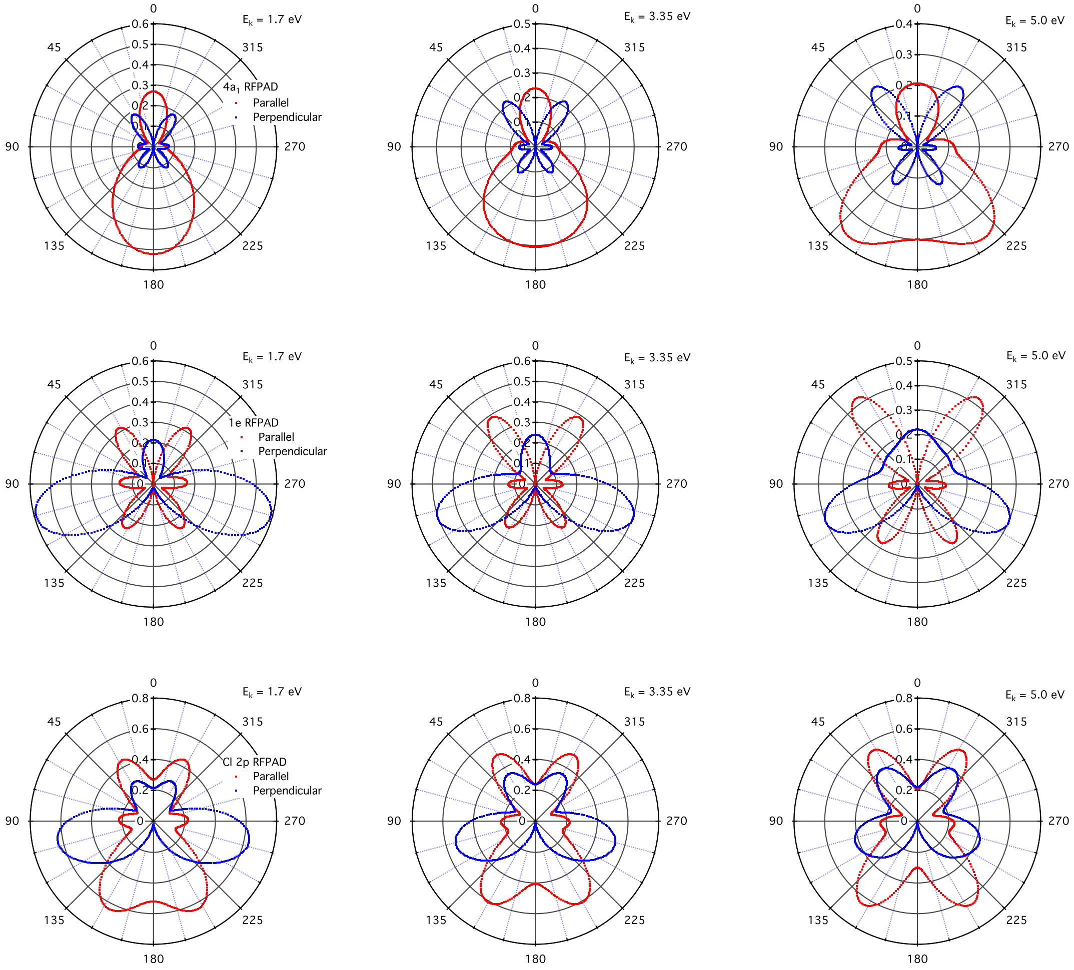

FIG. 37 Computed Reaction 1 RFPADs (in Mb str^{-1}) of $E_k = 1.7$ eV, $E_k = 3.35$ eV, and $E_k = 5.0$ eV photoelectrons ejected from the $4a_1$ (top row) and $1e$ (middle row) orbitals of CH_3Cl. The respective distributions are summed to yield the complete Cl 2p recoil frame angular distribution (bottom row). The distributions are given for linearly polarized light coincident with the recoil axis ($\theta'_n = 0°$) yielding parallel transitions (left) and perpendicular to the recoil axis ($\theta'_n = 90°$) for perpendicular transitions (right). The CCl axis is vertical in all views.

symmetry about the recoil axis than those of the Reaction 1 channel, which is expected given the asymmetric distribution of the target electron density about the CH recoil axis at the moment of fragmentation. Comparision of the computed Cl 2p RFPAD with preliminary experimental results for $E_k = 5.0$ eV photoelectrons emitted from the Cl $2p_{3/2}$

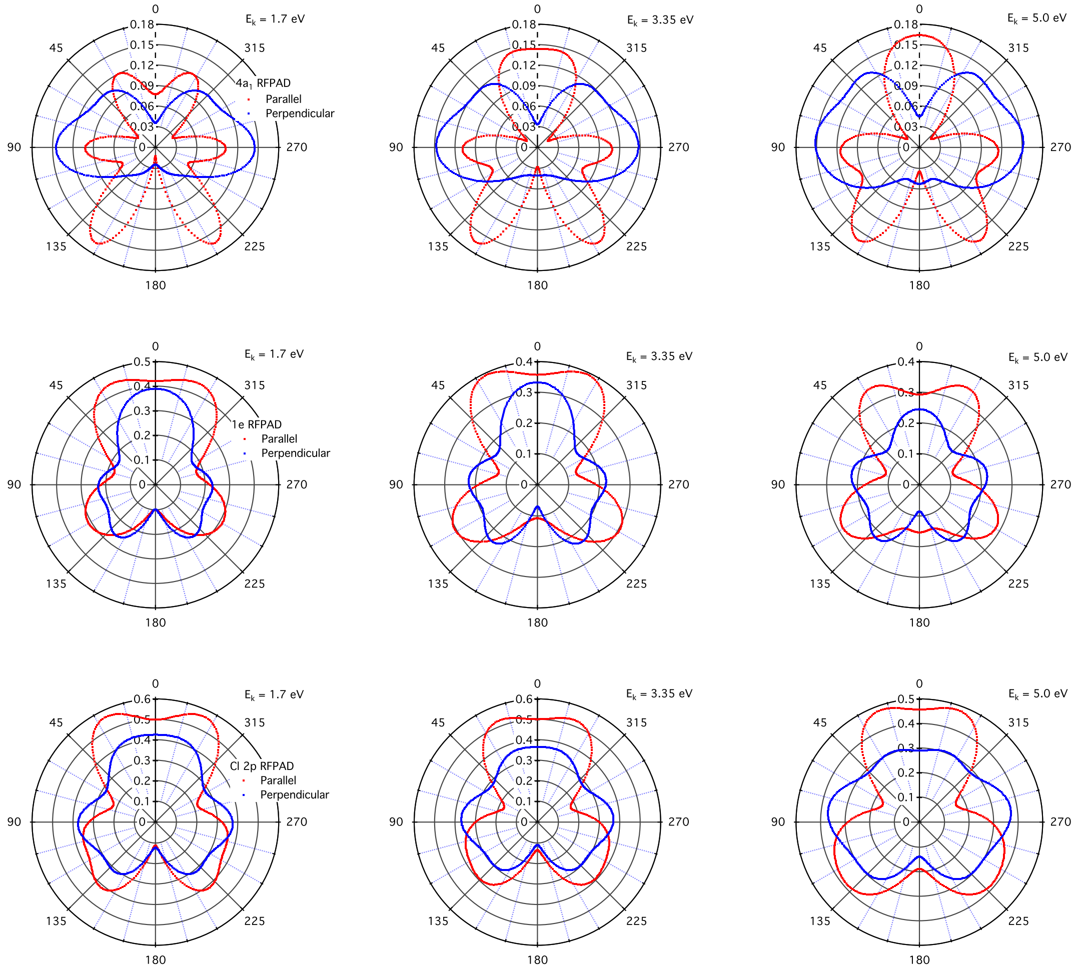

FIG. 38 Computed Reaction 2 RFPADs (in Mb str^{-1}) of $E_k = 1.7$ eV, $E_k = 3.35$ eV, and $E_k = 5.0$ eV photoelectrons ejected from the $4a_1$ (top row) and $1e$ (middle row) orbitals of CH_3Cl. The respective distributions are summed to yield the complete Cl 2p recoil frame angular distribution (bottom row). The distributions are given for linearly polarized light coincident with the recoil axis ($\theta_{n'} = 0°$) yielding parallel transitions (left) and perpendicular to the recoil axis ($\theta_{n'} = 90°$) for perpendicular transitions (right). The CH axis is vertical in all views.

orbital (Elkharrat, 2009) shows qualitative agreement with the perpendicular transition, but a discrepancy in the $90° - 270°$ profile of the parallel transition PAD.

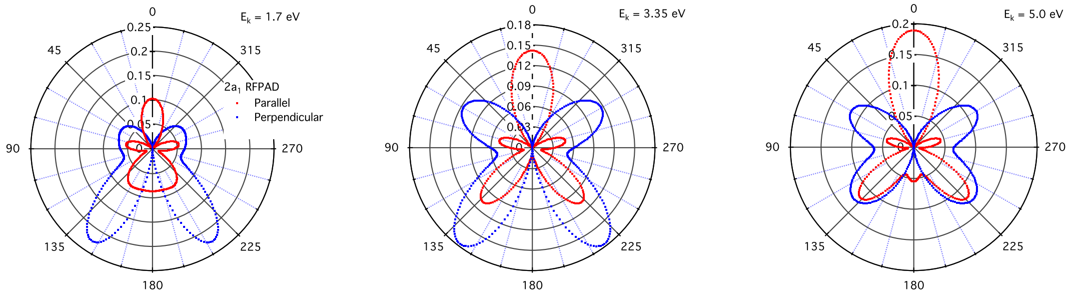

FIG. 39 Computed Reaction 1 RFPADs (in Mb str^{-1}) of $E_k = 1.7$ eV, $E_k = 3.35$ eV, and $E_k = 5.0$ eV photoelectrons ejected from the $2a_1$ orbital of CH_3Cl. The distributions are given for linearly polarized light coincident with the recoil axis ($\theta'_n = 0°$) yielding parallel transitions (left) and perpendicular to the recoil axis ($\theta'_n = 90°$) for perpendicular transitions (right). The CCl axis is vertical in all views.

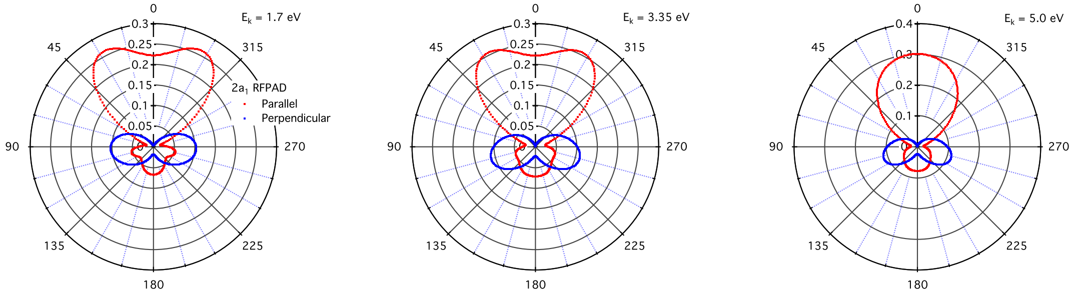

FIG. 40 Computed Reaction 2 RFPADs (in Mb str^{-1}) of $E_k = 1.7$ eV, $E_k = 3.35$ eV, and $E_k = 5.0$ eV photoelectrons ejected from the $2a_1$ orbital of CH_3Cl. The distributions are given for linearly polarized light coincident with the recoil axis ($\theta'_n = 0°$) yielding parallel transitions (left) and perpendicular to the recoil axis ($\theta'_n = 90°$) for perpendicular transitions (right). The CH axis is vertical in all views.

2. C 1s

In Fig. 39 the Reaction 1 C 1s RFPADs are presented. These distributions reveal strong agreement with experiment at $E_k = 2.8$ eV (Elkharrat, 2009) and show that the present methods are reliable particularly when the the recoil axis is coincident with a symmetry axis of the target. Photoelectron intensity is favored towards the CH_3 fragment in both

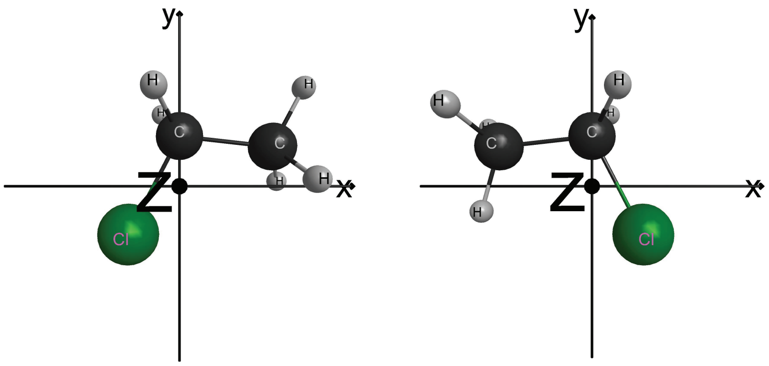

FIG. 41 The equilibrium geometry of C_2H_5Cl in staggered (left) and eclipsed (right) conformations.

TABLE 24 Structural parameters of C_2H_5Cl given in terms of internal coordinates. Bond lengths rXY are in Å and bond angles aXYZ in degrees

Geometry parameter	Value
rCCl	1.78882
rCC	1.50962
rCH	1.08622
aCCCl	111.0207
aCCH	111.8127

parallel and perpendicular distributions. By contrast, Reaction 2 C 1s RFPADs, shown in Fig. 40, indicate that parallel transitions are strongly favored over the p_x-wave perpendicular transitions, with photoelectron cross sections directed towards the H^+ fragment.

G. Computational details of chloroethane

1. SCF parameters

The Hartree-Fock orbitals were obtained for chloroethane constrained to C_s symmetry, with molecular parameters derived from scaled moments of inertia of Tam and coworkers (Tam *et al.*, 1991) and using the standard aug-cc-pVTZ basis set in the gaussian 03

TABLE 25 Chloroethane core ionization potentials (IP) in eV for the staggered and eclipsed conformers compared to experiment (Ohta and Kuroda, 1976).

Molecular orbital	Symmetry	Conformation		Experiment
		Staggered	Eclipsed	
Cl 1s	$1a'$	−2852.3626	−2952.3477	
C 1s	$2a'$	−307.2883	−307.2521	292.1
C 1s	$3a'$	−305.5824	−305.5176	291.1
C 2s	$4a'$	−286.9880	−286.9752	276.8
Cl 2p	$5a'$	−218.0569	−218.0433	206.0[a]
	$6a'$	−218.0085	−217.9952	
	$1a''$	−218.0079	−217.9943	

[a] Energy of Cl $2p_{3/2}$ electron. The Cl $2p_{1/2}$ electron is assumed 1.6 eV higher in energy.

code suite (Frisch *et al.*, 2004). The structural parameters in terms of internal coordinates are given in Table 24. A choice lay in the determination of the dihedral angle formed by the plane of the ClCCH nuclei, so we have generated SCF orbitals from two initial conformations, one in which the dihedral angle between the atoms comprising the C_s plane equals 90°, which we hereafter denoted the staggered conformer, and the other 0°, which we denote the eclipsed conformer. We find a computed SCF energy of the staggered isomer $E^{\text{stag}} = -538.200642034$ au, a dipole moment $\mu^{\text{SCF}} = 2.29$ D, and an isotropic polarizability of $\bar{\alpha}^{\text{SCF}} = 39.74$ au. The eclipsed conformer yields an SCF energy $E^{\text{eclip}} = -538.194146715$ au, a dipole moment $\mu = 2.27$ D, and an isotropic polarizability $\bar{\alpha} = 39.47$ au. These values compare to an experimental dipole moment of $\mu^{\text{Exp.}} = 2.05$ D from Nelson *et al.*, 1967 and a computed static polarizability $\bar{\alpha}^{\text{Exp.}} = 4.5$ Å$^3 = 30.40$ au from Zope *et al.*, 2008. The SCF interconversion energy of C_2H_5Cl was $\Delta E = 0.006495$ au = 0.18 eV, compared to the reference $\Delta E = 2.9$ kcal/mol = 0.13 eV interconversion energy of ethane. We present images of the equilibrium geometries of the staggered and eclipsed conformers in Fig. 41 (Bode and Gordon, 1998). The SCF core orbital energies

TABLE 26 Series of rotations (in degrees) about the invariant axis $R_{\{x,z\}}$ and translations (in Å) along the invariant x axis T_x needed to bring the reaction coordinate colinear with the z-axis.

Inertial axis	Molecular conformation			
	Reaction I		Reaction II	
	Staggered	Eclipsed	Staggered	Eclipsed
R_z	27.5	−27.5	96.5	−96.5
R_x	90.0	90.0	90.0	90.0
T_x	0.42	−0.42	0.42	−0.42

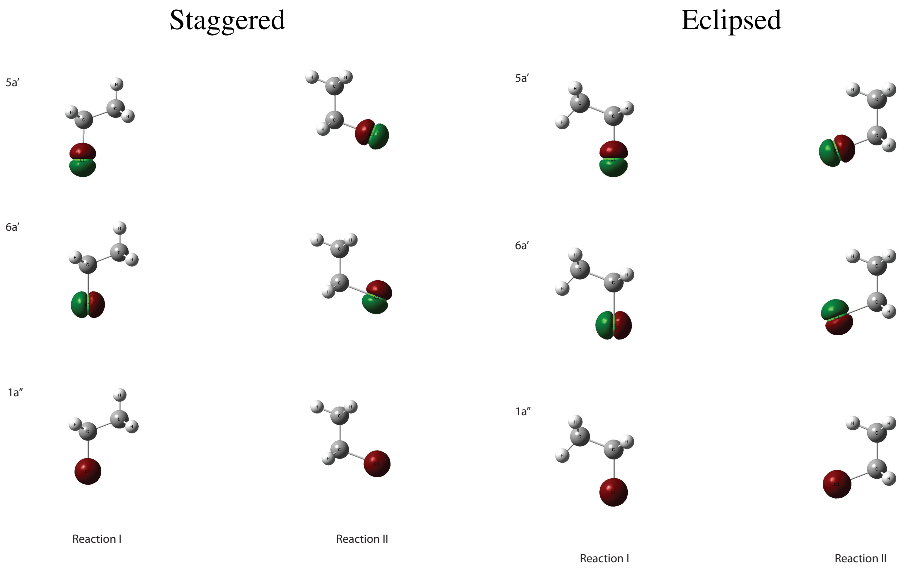

FIG. 42 The orientation of staggered and eclipsed conformation C_2H_5Cl within the Reaction I and Reaction II molecular frames. All images are displayed in the xz plane. The SCF $5a'$ (top row), $6a'$ (middle row), and $1a''$ (bottom row) Cl 2p orbitals after the rotation are also displayed.

are compared to the C 1s and Cl 2s and $2p_{3/2}$ ionization potentials obtained from the X-ray photoelectron spectra of Ohta and Kuroda (Ohta and Kuroda, 1976) in Table 25.

The orientation of the staggered and eclipsed conformations resulting from the GAUSSIAN03 calculation displayed in Fig. 41 likewise proved not to be the most convenient choice to compute the dynamical variables of Eq. 144. We have computed the dynamical

TABLE 27 The normalization of the core orbitals of C_2H_5Cl in the single-center expansion of the target orbitals in partial waves to a maximum angular momentum $l_{\max} = 60$.

Molecular orbital		Conformation			
		Reaction I		Reaction II	
		Staggered	Eclipsed	Staggered	Eclipsed
Cl 1s	$1a'$	0.98763932	0.98763930	0.98775649	0.98775647
C 1s	$2a'$	0.99987428	0.99987429	0.99987904	0.99987905
C 1s	$3a'$	0.99542482	0.99542504	0.99535991	0.99536012
Cl 2s	$4a'$	0.99884106	0.99884099	0.99885013	0.99885006
Cl 2p	$5a'$	0.99998896	0.99998895	0.99998896	0.99998895
	$6a'$	0.99995304	0.99995304	0.99995304	0.99995304
	$1a''$	0.99995303	0.99995303	0.99995303	0.99995303

variables of Eq. 144 from a target geometry that was rotated from the Mulliken standard orientation that defines σ of the C_s point group as coplanar to *xy* plane. The series of rotations and translations we have considered are listed in Table 26. Accordingly, the MFPADs of Eq. 146 to be discussed in Sec. V.I are generated from dynamical coefficients of the molecule already brought into the desired molecular frame, the RFPADs discussed in Sec. V.J resulting from the average about the azimuthal angle of the MFPADs with no subsequent rotations R. For reference, we present the views of the reoriented molecules in the *xz* plane with the active $5a'$, $6a'$, and $1a''$ Cl 2p orbitals in Fig. 42 as generated by the GAUSSVIEW utility (Dennington *et al.*, 2009).

2. *SCE parameters*

Dipole transition elements $I_{lm\mu}^{p_i\mu_i p_f\mu_f}(E)$ were computed using the EPOLYSCAT code suite of Lucchese and collaborators (Gianturco *et al.*, 1994; Natalense and Lucchese, 1999). For both conformations, partial waves up to $l_{\max} = 60$ were retained in the SCE of the continuum and target orbitals, and up to $2l_{\max}$ for the interaction potential. The SCE with these definitions led to the following target core orbital normalizations, shown in Table 27. All inner and outer valence orbitals were described with normalizations greater than 0.9998. In a previous investigation on the MFPADs of Cl 2p ionization of CH_3Cl (Lucchese *et al.*, 2009), we computed core-level photoionization cross sections at the level of exact static-exchange (Lane, 1980). This was found to produce a satisfactory level

TABLE 28 Photoionization cross sections σ (in Mb) and asymmetry parameters of the electron, β_k, and ion fragment, β_N, computed within the length, mixed, and velocity gauges of the dipole operator. Results are presented for Cl 2p photoionization from the staggered conformer.

Molecular orbital	$h\nu$ (eV)	σ (Mb)			β_k			β_N	
		Length	Mixed	Velocity	Length	Mixed	Velocity	Length	Velocity
				Reaction I					
$5a'$	208.8	1.1546	1.1756	1.1971	0.4041	0.4050	0.4060	0.6692	0.6535
	210.5	1.3421	1.3673	1.3931	0.3091	0.3113	0.3135	0.6278	0.6114
$6a'$	208.8	1.2471	1.2769	1.3076	0.2069	0.2129	0.2189	−0.4810	−0.4770
	210.5	1.2878	1.3183	1.3496	0.2566	0.2617	0.2669	−0.4126	−0.4089
$1a''$	208.8	1.2688	1.3001	1.3323	0.1094	0.1153	0.1213	−0.3112	−0.3083
	210.5	1.3389	1.3703	1.4024	0.2386	0.2438	0.2490	−0.2079	−0.2032
Cl 2p	208.8	3.6705	3.7526	3.8370	0.2401	0.2444	0.2487	−0.0041	−0.0044
	210.5	3.9688	4.0559	4.1451	0.2681	0.2725	0.2765	0.0024	−0.0002
				Reaction II					
$5a'$	208.8	1.1550	1.1760	1.1974	0.4037	0.4046	0.4055	−0.2954	−0.2920
	210.5	1.3423	1.3675	1.3933	0.3088	0.3110	0.3132	−0.2206	−0.2173
$6a'$	208.8	1.2470	1.2770	1.3077	0.2077	0.2137	0.2197	0.3410	0.3319
	210.5	1.2880	1.3185	1.3498	0.2571	0.2622	0.2674	0.2060	0.1979
$1a''$	208.8	1.2690	1.3004	1.3325	0.1096	0.1156	0.1215	0.0326	0.0383
	210.5	1.3391	1.3704	1.4026	0.2386	0.2438	0.2489	0.0538	0.0594
Cl 2p	208.8	3.6660	3.7534	3.8376	0.2403	0.2446	0.2489	0.0261	0.0261
	210.5	3.9694	4.0564	4.1457	0.2682	0.2726	0.2765	0.0131	0.0133

of agreement with experiment despite the fact that the neglect of relaxation of the ionized orbitals becomes problematic from excitations from the inner shell region (Lane, 1980). In the present work, in order to account for target relaxation and recover scattering dynamics beyond the SE approximation, we incorporate target static polarizability and correlation effects through the use of the density functional theory (DFT) expressions of Perdew and Zunger (Perdew and Zunger, 1981). The short-range correlation potential is smoothly joined to the nonzero terms of the SCF static polarizability tensor $\alpha_{\alpha\beta}$, centered on the coordinate origin, at the radial matching distance r_m, which was computed to be $r_m^{\text{stag}} = 2.5638$ Å and $r_m^{\text{eclip}} = 2.5896$ Å for the target oriented with the CCl reaction coordinate of Reaction I, and $r_m^{\text{stag}} = 2.5638$ Å and $r_m^{\text{eclip}} = 2.5692$ Å for target assuming a CC reaction coordinate of Reaction II.

TABLE 29 Photoionization cross section σ (in Mb) and asymmetry parameters of the electron, β_k, and ion fragment, β_N, computed within the length, mixed, and velocity gauges of the dipole operator. Results are presented for Cl 2p photoionization from the eclipsed conformer.

Molecular orbital	$h\nu$ (eV)	σ (Mb)			β_k			β_N	
		Length	Mixed	Velocity	Length	Mixed	Velocity	Length	Velocity
					Reaction I				
$5a'$	208.8	1.3769	1.4017	1.4271	0.3857	0.3869	0.3882	0.5945	0.5786
	210.5	1.3273	1.3517	1.3767	0.1241	0.1263	0.1286	0.6803	0.6654
$6a'$	208.8	1.3955	1.4288	1.4629	0.2439	0.2495	0.2550	−0.4987	−0.4946
	210.5	1.2664	1.2961	1.3265	0.3006	0.3054	0.3101	−0.4367	−0.4323
$1a''$	208.8	1.4508	1.4876	1.5253	0.0803	0.0855	0.0907	−0.1492	−0.1459
	210.5	1.3475	1.3793	1.4119	0.2591	0.2641	0.2692	−0.2423	−0.2384
Cl 2p	208.8	4.2232	4.3181	4.4153	0.2365	0.2406	0.2446	−0.0178	−0.0206
	210.5	3.9412	4.0271	4.1151	0.2279	0.2319	0.2360	0.0004	−0.0018
					Reaction II				
$5a'$	208.8	1.3776	1.4025	1.4279	0.3863	0.3876	0.3888	−0.4354	−0.4319
	210.5	1.3281	1.3526	1.3775	0.1247	0.1269	0.1292	−0.2435	−0.2393
$6a'$	208.8	1.3931	1.4265	1.4607	0.2446	0.2502	0.2559	0.2117	0.2026
	210.5	1.2690	1.2987	1.3292	0.3004	0.3051	0.3098	0.1286	0.1204
$1a''$	208.8	1.4437	1.4803	1.5179	0.0751	0.0804	0.0856	0.2822	0.2877
	210.5	1.3490	1.3808	1.4135	0.2558	0.2608	0.2659	0.0617	0.0671
Cl 2p	208.8	4.2144	4.3093	4.4065	0.2353	0.2394	0.2434	0.0196	0.0195
	210.5	3.9461	4.0321	4.1202	0.2270	0.2309	0.2350	−0.0177	−0.0173

H. Photoionization cross sections of chloroethane

In Tables 28 and 29 we present the photoionization cross sections σ and ITAD electron and ion asymmetry parameters β_k and β_N in the length, mixed, and velocity gauges of the dipole operator from the C 1s $(2a')^2(3a')^2$ and Cl 2p $(5a')^2(6a')^2(1a'')^2$ orbitals of chloroethane computed for photoelectron kinetic energies $E_k = 2.1$ eV and $E_k = 3.8$ eV. To convert photoelectron energies to photon energies, we have assumed the experimental ionization potentials, which were identical to those listed in Table 25 for ionization of the $2a'$ and $3a'$ C 1s orbitals, and $E^{\mathrm{IP}} = 206.7$ eV for all Cl 2p orbitals. The integrated cross sections σ for each conformation should be formally exact, independent of the immediate details of the orientation. Furthermore, the σ, β_k, and β_N parameters should be equal irrespective of the gauge of the dipole operator. These two requirements provide a test of the convergence of the current calculations. In this view, the values of σ computed for the staggered conformer appear well converged, as seen in Table 28. The electron asymmetry parameter β_k computed after the reorientation of the target likewise

TABLE 30 Photoionization cross sections σ (in Mb) and asymmetry parameters of the electron β_k and ion fragment β_N computed within the length, mixed, and velocity gauges of the dipole operator. Results are presented for the C 1s photoionization of the staggered and eclipsed conformers.

Molecular orbital	$h\nu$ (eV)	σ (Mb)			β_k			β_N	
		Length	Mixed	Velocity	Length	Mixed	Velocity	Length	Velocity
Staggered conformation									
Reaction I									
$2a'$	294.9	0.9770	1.0143	1.0531	0.9694	0.9662	0.9629	−0.3872	−0.3858
$3a'$	293.9	1.0091	1.0419	1.0758	1.2034	1.2021	1.2007	0.1444	0.1451
Reaction II									
$2a'$	294.9	0.9770	1.0143	1.0532	0.9689	0.9657	0.9625	−0.0134	−0.0091
$3a'$	293.9	1.0091	1.0418	1.0758	1.2036	1.2022	1.2008	−0.1778	−0.1704
Eclipsed conformation									
Reaction I									
$2a'$	294.9	0.8779	0.9107	0.9449	0.8413	0.8395	0.8377	−0.3988	−0.3978
$3a'$	293.9	0.8905	0.9187	0.9478	1.1241	1.1225	1.1210	0.0048	0.0092
Reaction II									
$2a'$	294.9	0.8780	0.9108	0.9450	0.8413	0.8395	0.8377	0.1198	0.1225
$3a'$	293.9	0.8906	0.9188	0.9480	1.1243	1.1228	1.1213	−0.0675	−0.0651

show only small differences between the Reaction I and Reaction II molecular frames, whereas the ion asymmetry parameter β_N depends strongly on the initial coordinates of the target. The cross sections σ listed in Table 29 show a greater disparity between the Reaction I and Reaction II results than the staggered conformer, particularly for scattering from the $5a'$ and $6a'$ levels. Notably, the photoionization cross sections for the eclipsed conformation in Table 29 are consistently greater in magnitude than those computed for the staggered conformation in Table 28. To obtain photoionization parameters that may be directly compared to experiment, we perform a sum of the calculated σ cross sections and an equal-weighted average of the β_k and β_N parameters. The computed Reaction I and II results may compared to the $E_k = 5.0$ eV Cl $2p_{3/2}$ $\beta_k = 0.3$ and $\beta_N = -0.1$ asymmetry parameters measured for the $CH_3Cl \rightarrow CH_3^+ + Cl^+$ dissociation pathway of CH_3Cl (Elkharrat, 2009), which implies that the dissociation in the partially integrated frames is best understood in terms of a fictive diatomic molecule $R-X$, comprised of a halide-like X fragment and an isotropic hydrocarbon distribution R.

In Table 30 we present length, mixed, and velocity gauge σ, β_k, and β_N parameters for the $(2a')^{-1}$ and $(3a')^{-1}$ C 1s ionization of chloroethane in both conformations. Cross sections were calculated at a single photoelectron kinetic energy $E_k = 2.8$ eV, which were converted to photon energies from the experimental vertical IPs given in Table 25, namely, a $2a'$ IP of $E^{\mathrm{IP}} = 292.1$ eV and $3a'$ IP of $E^{\mathrm{IP}} = 292.2$ eV. We observe that the reorientation of the molecule into a Reaction I or II molecular axis does not affect the magnitude of the photoionization cross sections with respect to the conformation geometry, in accord with the fact that σ, experimentally obtained from a Beer-Lambert relation, necessarily measures photoionization intensity over all orientations of the target as stated previously. The magnitude of the computed methyl-like $(3a')^{-1}$ ionization cross section σ and electron asymmetry parameters β_k for all gauges of the dipole operator are consistently larger than those of the halide-like $(2a')^{-1}$. Furthermore, the photoionization cross sections σ for the staggered conformation are on average 0.1 Mb larger than those of the eclipsed conformer. This is due to the higher SCF energy of the eclipsed conformer as discussed in Sec. V.G.1 and the energy dependence of the dipole transition elements of Eq. 144. Because photoionization cross sections and asymmetry parameters for C 1s shells of chloroethane are not available, we compare current results with the photoelectron $\beta_k = 1.0$ and fragment $\beta_N = -0.25$ asymmetry parameters of $E_k = 2.8$ eV photoelectrons ejected from the C 1s orbital of the primary dissociation channel of CH_3Cl (Elkharrat, 2009), and the $\sigma = 2.0$ Mb cross section and the $\beta_k = 0.7$ asymmetry parameter of $E_k = 2.2$ eV photoelectrons measured for C 1s ionization of the vibrational ground state of ethane (Rennie *et al.*, 1999). We find both computed halide-like $(2a')^{-1}$ and methyl-like $(3a')^{-1}$ C 1s β_k asymmetry parameters to be closer to those measured for CH_3Cl than C_2H_6, implying the dissociation of an $R-X$ dihalide as stated previously.

I. Chloroethane MFPADs

1. Cl 2p

In Figs. 43 and 44 we display three-dimensional views (in Mb) of the Reaction I MFPADs for Cl 2p photoelectrons ejected from staggered and eclipsed conformation C_2H_5Cl with kinetic energy $E_k = 2.1$ eV and $E_k = 3.8$ eV above ionization threshold, respectively.

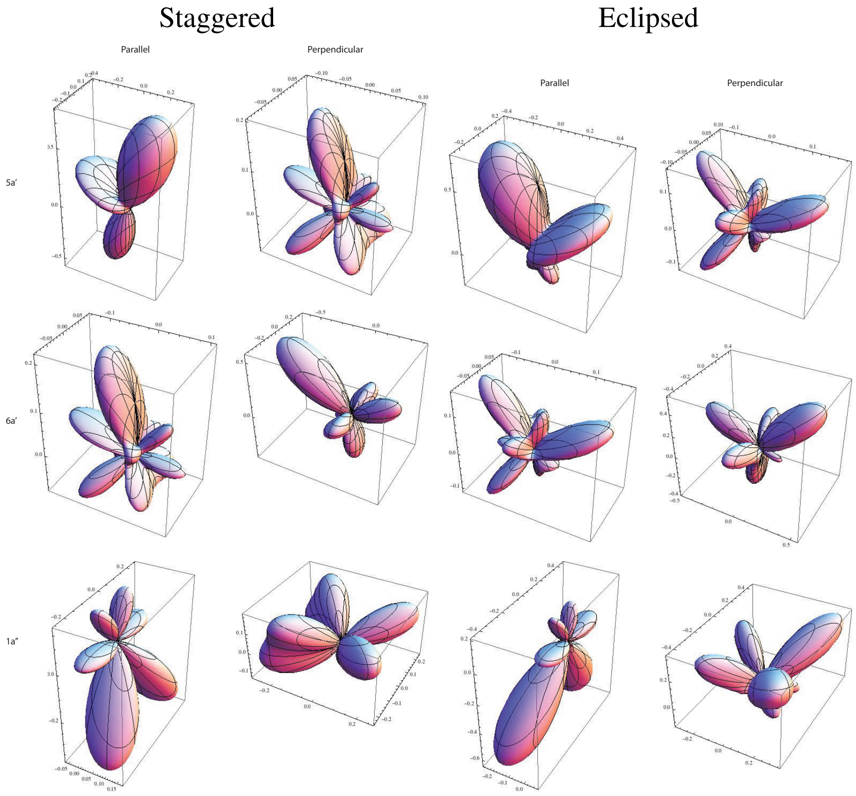

FIG. 43 Computed Reaction I MFPADs (in Mb) of $E_k = 2.1$ eV photoelectrons ionized from the $5a'$ (top row), $6a'$ (middle row), and $1a''$ (bottom row) orbitals of staggered and eclipsed conformation C_2H_5Cl. The distributions are given for light linearly polarized along the z axis yielding parallel transitions (left) and x axis for perpendicular transitions (right). The molecular axis is coincident to z in all views.

The corresponding Reaction II Cl 2p MFPADs are shown in Figs. 45 and 46. In standard orientation, while the $1a''$ orbital is predominantly Cl $2p_z$ character, the $5a'$ and $6a'$ molecular orbitals are a convolution of the Cl $2p_x$ and $2p_y$ orbitals, the $5a'$ orbital primarily Cl $2p_y$ and $6a'$ $2p_x$. After the rotations of both the staggered and eclipsed conformations needed to reorient the Reaction I molecular frame, in which the molecular axis is colinear with the invariant $+z$-axis, $5a'$ transforms as $2p_z$, $6a'$ as $2p_x$, and $1a''$ as $2p_y$. The analysis after the rotations into the Reaction II molecular frame indicate that $5a'$ transforms primarily as $2p_x$, $6a'$ as $2p_z$, and $1a''$ as $2p_y$. The electron density of the staggered and eclipsed

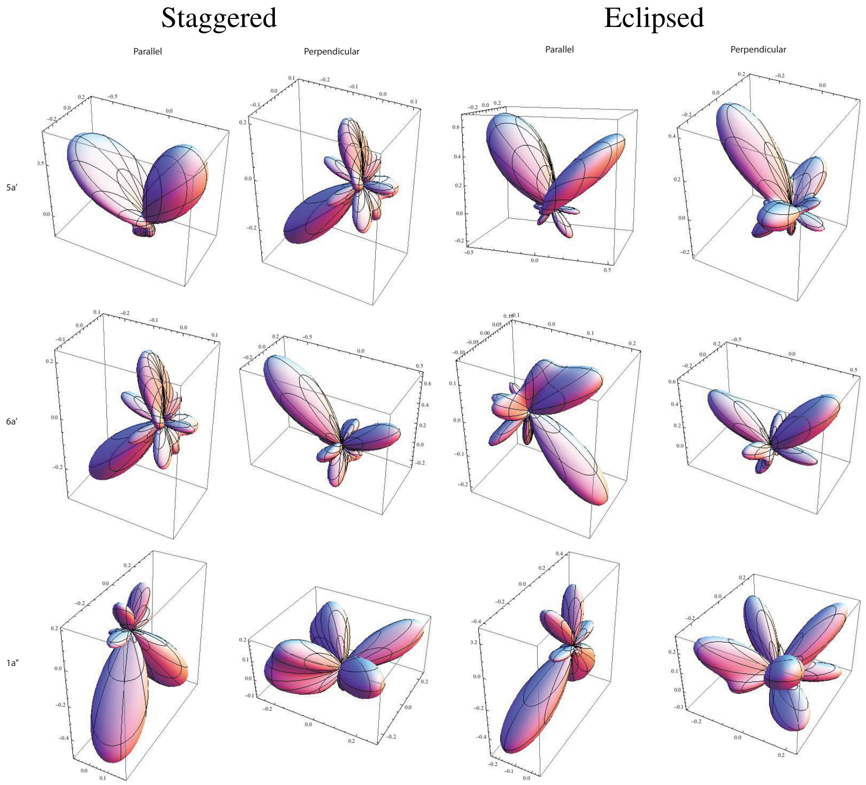

FIG. 44 Computed Reaction I MFPADs (in Mb) of $E_k = 3.8$ eV photoelectrons ionized from the $5a'$ (top row), $6a'$ (middle row), and $1a''$ (bottom row) orbitals of staggered and eclipsed conformation C_2H_5Cl. The distributions are given for light linearly polarized along the z axis yielding parallel transitions (left) and x axis for perpendicular transitions (right). The molecular axis is coincident with z in all views.

Cl 2p orbitals consequent to the rotations into the Reaction I and Reaction II molecular frames may be inspected in Fig. 42. If the nodal structure of the MFPAD stems from the direct product of the angular momentum of the component of the polarization vector with the orbital symmetry from which the photoelectron was emitted (Lucchese, 2004), then we should expect all Cl 2p MFPADs to resemble the $3d$ orbitals of the appropriate nodal symmetry.

Because the molecular axis is made colinear with z-axis in the procedure described in Sec. V.G, parallel transitions result from light polarized along $+z$ such that $(\theta_n = 0°, \phi_n = 0°)$, in the form of Eq 146. For a reaction coordinate consisting of the CCl bond (Reac-

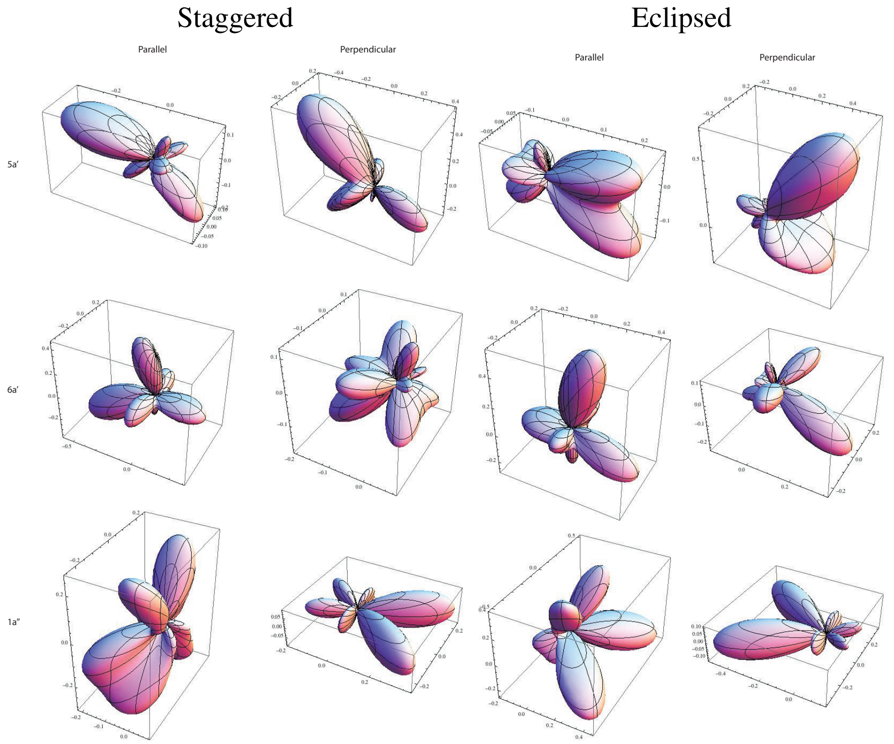

FIG. 45 Computed Reaction II MFPADs (in Mb) of $E_k = 2.1$ eV photoelectrons ionized from the $5a'$ (top row), $6a'$ (middle row), and $1a''$ (bottom row) orbitals of staggered and eclipsed conformation C_2H_5Cl. The distributions are given for light linearly polarized along the z axis yielding parallel transitions (left) and the x axis for perpendicular transitions (right). The molecular axis is coincident to z in all views.

tion I), the parallel transitions of both molecular conformations display outgoing waves strongly distorted from their expected nodal structure. The parallel transition angular distributions of $E_k = 2.1$ eV electrons ejected from the staggered stereoisomer, shown in the labeled subset of Fig. 43, are characteristic, with $(5a')^{-1}$ ionization resembling the expected d_{z^2} wave, the $(6a')^{-1}$ ionization displaying a nodal structure more complex than d_{xz}, and the MFPAD from the $1a''$ orbital containing an extra transition along $\pm y$ in addition to the symmetry-allowed d_{yz} wave structure. The perpendicular transitions, in which the light is polarized along $+x$ such that $(\theta_n = 90°, \phi_n = 0°)$, shown in the labeled panels of Fig. 43, are likewise notable: The perpendicular transition $(5a')^{-1}$ MFPAD for the

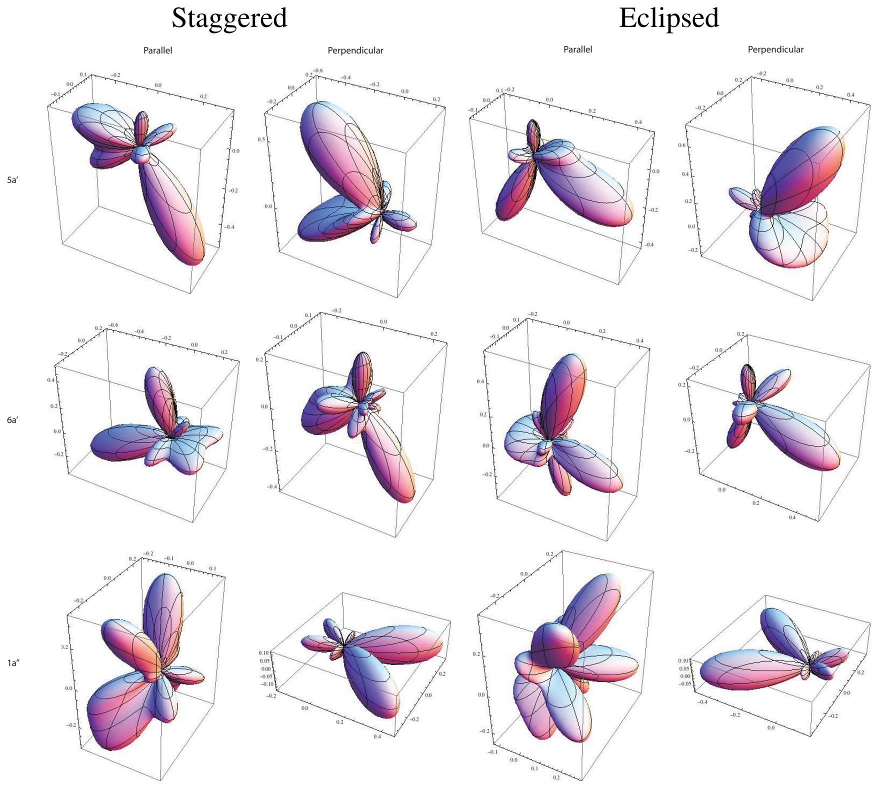

FIG. 46 Computed Reaction II MFPADs (in Mb) of $E_k = 3.8$ eV photoelectrons ionized from the $5a'$ (top row), $6a'$ (middle row), and $1a''$ (bottom row) orbitals of staggered and eclipsed conformation C_2H_5Cl. The distributions are given for light linearly polarized along the z axis yielding parallel transitions (left) and the x axis for perpendicular transitions (right). The molecular axis is coincident to z in all views.

staggered and eclipsed conformers display the same nodal structure as the parallel transition $(6a')^{-1}$ distributions. The perpendicular transition photoelectron distribution from $6a'$ displays a strong anisotropy from the predicted axial $\pm x$ intensity. Only the $(1a'')^{-1}$ distributions clearly reveal the dipole-allowed d_{xy} symmetry. At the higher photoelectron energy $E_k = 3.8$ eV, as seen in Fig. 44, the predictions break down further, particularly for the $(5a')^{-1}$ and $(6a')^{-1}$ ionizations. We again note the strong resemblance of the staggered conformation perpendicular $(5a')^{-1}$ MFPAD and parallel transition $(6a')^{-1}$ MFPAD, which, however, is not replicated in the respective transition of the eclipsed conformer. The $(5a')^{-1}$ and $(6a')^{-1}$ distributions for both conformers and both transitions are directed along $\pm x$, which photoelectron intensity directed away from the Cl atom in the direction of the $5a'$ and $6a'$ target electron density. With the exception of the $(1a'')^{-1}$ MFPADs, the angular distributions from the eclipsed conformer with a Reaction I coordinate, shown in the labeled panels of Figs. 43 and 44, are more strongly characterized as a product of the angular momenta of the linear polarization and the bound orbital. The $(5a')^{-1}$ and $(6a')^{-1}$ MFPADs at $E_k = 2.1$ eV (Fig. 43) show photoelectron propensity along both the xz and yz planes for both parallel and perpendicular transitions. At $E_k = 3.8$ eV (Figs. 44), the perpendicular transition $(5a')^{-1}$ and parallel $(6a')^{-1}$ MFPADs are scattered with the $6a'$ orbital electron density, the $(5a')^{-1}$ distribution directed towards the C_2H_5 fragment and the $(6a')^{-1}$ towards the Cl fragment.

The staggered conformation $(5a')^{-1}$ angular distribution of $E_k = 2.1$ eV Cl 2p electrons in the Reaction II molecular frame, shown in Fig. 45, has the greatest intensity directed along the CCl bond within both parallel and perpendicular transitions. The $(6a')^{-1}$ distributions are strongly directed along the $6a'$ electron density. At $E_k = 3.8$ eV (Fig. 46) this propensity in the parallel and perpendicular transitions of the $(5a')^{-1}$ and $(6a')^{-1}$ distributions becomes even more pronounced. The $(1a'')^{-1}$ MFPADs at both photoelectron kinetic energies show d_{yz} and d_{xy} parallel and perpendicular transitions, respectively, in accord with predictions based on the symmetry of the polarization and the photoelectron. The eclipsed conformation Reaction II $E_k = 2.1$ eV MFPADs, shown under the appropriate label in Fig. 45, reveal distributions more strongly distorted by the presence of the ionic target. A d_{xz} nodal structure is detectable for the parallel transition $(5a')^{-1}$ ionization, and a $+x$-directed d_{yz} and $-x$-directed d_{xy} structure for the parallel and perpendicular transitions of the $(1a'')^{-1}$ ionizations, respectively. At the higher $E_k = 3.8$ eV photoelectron energy (Fig. 46), the eclipsed conformation $(5a')^{-1}$ and $(6a')^{-1}$ MFPADs propagate towards $+x$ within the xz plane for both parallel and perpendicular transitions. It is interesting to note the degree of inequivalence between the MFPADs for the staggered and eclipsed conformations computed at the same photoelectron kinetic energy and for the same set of Cl 2p excitations.

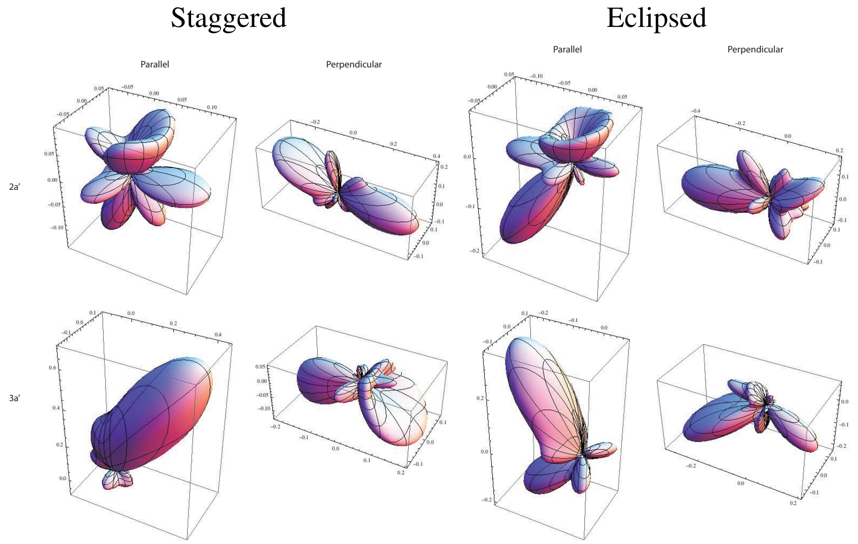

FIG. 47 Computed Reaction I MFPADs (in Mb) of $E_k = 2.8$ eV photoelectrons ionized from the $2a'$ (top row) and $3a'$ (bottom row) orbitals of staggered and eclipsed conformation C_2H_5Cl. The distributions are given for light linearly polarized along the z axis yielding parallel transitions and the x axis for perpendicular transitions. The molecular axis is coincident to z in all views

2. C 1s

Angular distributions were computed at a single photoelectron energy, $E_k = 2.8$ eV, for the $2a'$ and $3a'$ C 1s atoms of staggered and eclipsed conformations of C_2H_5Cl and are displayed in the Reaction I molecular frame in Fig. 47 and the Reaction II molecular frame in Fig. 48. Because of the atomic nature of these core orbitals, the $2a'$ and $3a'$ chloroethane orbitals may be understood simply as the C 1s orbitals of a halide-like CH_3Cl and methyl-like CH_4, respectively. Qualitative symmetry analysis predicts that parallel transitions should be directed along the molecular axis ($\pm z$) and perpendicular transitions perpendicular to the molecular axis ($\pm x$) within the symmetry plane, which is coextensive with the xz plane. Any degree of anisotropy from these results can reveal the detailed chemical environment of the C 1s atoms and the electron density of the resulting ionized fragments at the time of photon impact.

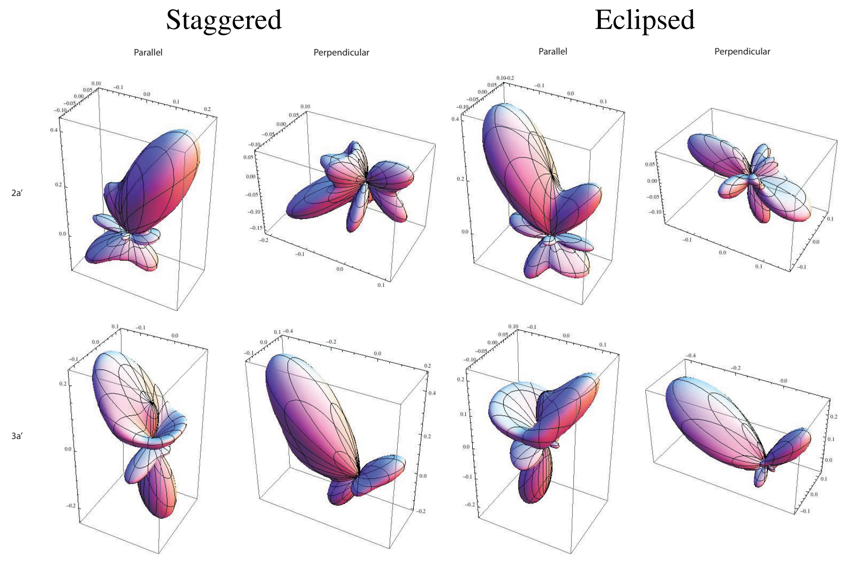

FIG. 48 Computed Reaction II MFPADs (in Mb) of $E_k = 2.8$ eV photoelectrons ionized from the $2a'$ (top row) and $3a'$ (bottom row) orbitals of staggered and eclipsed conformation C_2H_5Cl. The distributions are given for light linearly polarized along the z axis yielding parallel transitions and the x axis for perpendicular transitions. The molecular axis is coincident to z in all views.

The notable feature of the staggered and eclipsed Reaction I $(2a')^{-1}$ MFPADs, shown in Fig. 47, is the degree of intensity of the parallel transitions, with the absolute value of the differential cross sections of the eclipsed conformer twice that of the staggered conformer. Likewise, the staggered and eclipsed parallel transition Reaction I $(3a')^{-1}$ MFPADs, displayed in Fig. 47, are strikingly dissimilar, with photoelectron intensity directed along the CC bond of the C_2H_5 fragment for the staggered conformation, yet along the molecular plane more generally for the eclipsed conformer. In most other respects, the apparent asymmetry between the staggered and eclipsed forms of the perpendicular transitions of the $(2a')^{-1}$ ionization is merely a consequence of the target charge distribution after the rotations have been performed. In both instances the continuum electrons propagate towards the greater electron density of the C_2H_5 fragment. The Reaction II $(2a')^{-1}$ MFPADs for both conformers, shown in Fig. 48, may be understood in a similar view, with photoelectron intensity directed along the molecular axis towards the CH_3 fragment with linearly-propagated light, and the lesser-intensity perpendicular transitions directed axially with respect to the molecular axis. The staggered and eclipsed Reaction II $(3a')^{-1}$ MFPADs, shown in Fig. 48, are not nearly as asymmetric, sharing similar parallel and perpendicular distributions for both conformers.

J. Chloroethane RFPADs

1. Cl 2p

We must make a choice of an appropriate recoil axis relative the the molecular frame. We assume the validity of the axial recoil approximation, namely, that period of rotation is much less than the speed of collision, and therefore define the recoil axis to be equivalent to the selected molecular axes, which have been described in Sec. V.B.1. Since the recoil axis is derived as the average over the experimentally unobserved azimuthal angles ϕ_n about the molecular axis, the RFPADs we present in Figs. 49, 51, 53, and 55 may be understood as the average about the z-axis of the MFPADs described in Sec. V.B.1. We make use of the simplification of Eq. 154 and present two-dimensional RFPADs (in Mb str^{-1}) for linear and perpendicular transitions from the staggered and eclipsed conformers.

In Fig. 49 we show the Reaction I $(5a')^{-1}$, $(6a')^{-1}$ and $(1a'')^{-1}$ RFPADs for photoelectron energy $E_k = 2.1$ eV, comparing the staggered conformer distributions (in red) and the eclipsed conformer distribution (in blue). For parallel transitions $(\theta'_n = 0^\circ)$ from the $5a'$ and $6a'$ orbitals, the photoelectron density is directed away from the Cl fragment towards the C_2H_5 fragment, whereas the $(1a'')^{-1}$ distribution is directed away from the C_2H_5 fragment. The perpendicular transition $(\theta'_n = 90^\circ)$ of the $(5a')^{-1}$ ionization is well characterized as d_{xz}, while the $(6a')^{-1}$ and $(1a'')^{-1}$ perpendicular distributions are better understood as propagating towards the C_2H_5 fragment. The RFPADs from the eclipsed conformer display stronger photoelectron intensities and more sharply defined nodal profiles than the results from the staggered conformer. The Reaction I $(5a')^{-1}$ and $(6a')^{-1}$ RFPADs computed at $E_k = 3.8$ eV photoelectron energy, shown in Fig. 51 show slight differences from those computed at the lower energy, particularly with respect to the degree of intensity of the distribution along the recoil axis, between the staggered and eclipsed

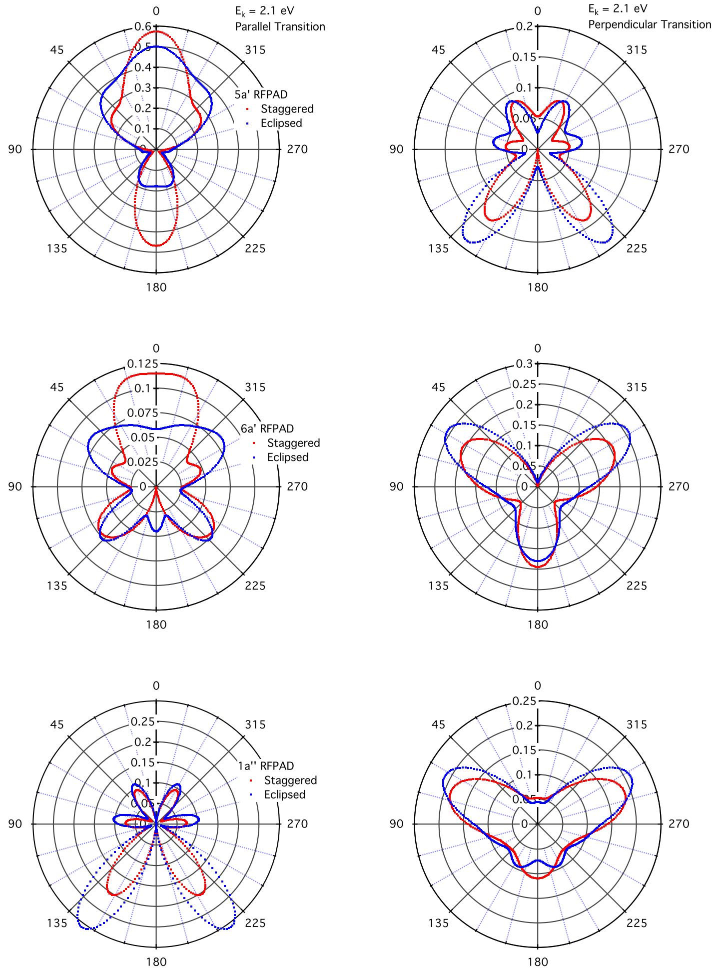

FIG. 49 Computed Reaction I RFPADs (in Mb str^{-1}) of $E_k = 2.1$ eV photoelectrons ionized from the $5a'$, $6a'$, and $1a''$ orbitals of staggered and eclipsed conformation C_2H_5Cl. The distributions are given for light linearly polarized along the recoil axis ($\theta_n' = 0°$) for parallel transitions (left) and at $\theta_n' = 90°$ to the recoil axis for perpendicular transitions (right).

conformers. We also remark on the small magnitude of the angular distributions predicted for the $(6a')^{-1}$ ionizations at both energies and conformations.

We display Reaction II RFPADs for $E_k = 2.1$ eV photoelectrons in Fig. 53. The $(5a')^{-1}$ RFPAD for the staggered and eclipsed conformers are similar, with attenuated parallel transitions and perpendicular transitions dominant at scattering angles near 90°. The parallel transition $(6a')^{-1}$ distributions are dominated by scattering towards the CH_3 fragment

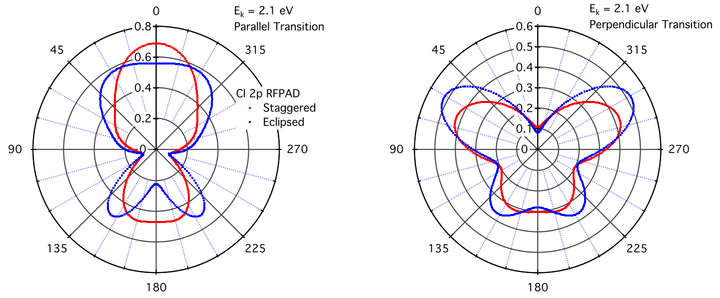

FIG. 50 Computed Reaction I RFPADs (in Mb str^{-1}) of $E_k = 2.1$ eV photoelectrons summed over all Cl 2p orbitals of staggered and eclipsed conformation C_2H_5Cl. The distributions are given for light linearly polarized along the recoil axis ($\theta_n' = 0°$) for parallel transitions (left) and at $\theta_n' = 90°$ to the recoil axis for perpendicular transitions (right).

and in fact comprise the largest Cl 2p component of scattering at this energy. The perpendicular transition $(6a')^{-1}$ RFPAD from the staggered conformer displays a d_{xz} wave characteristic that becomes more apparent in the eclipsed conformer at this energy. The parallel $(1a'')^{-1}$ RFPAD for the staggered conformer shows a greater intensity towards the CH_2Cl fragment than that seen in the eclipsed conformer. The most remarkable features of the $E_k = 3.8$ eV RFPADs, shown in Fig. 55, lie in the “opening up” of the angular distributions towards the CH_3 fragment, with both the (small) $(5a')^{-1}$ and $(6a')^{-1}$ RFPADs showing intensity greater intensity along the CC recoil axis defined at $\theta_n' = 0°$.

In experiment, the orbital angular momenta of the Cl 2p electrons are not observed, thus the measured RFPAD corresponds to a sum of all computed Cl 2p RFPADs. We accomplish this by an equal weight summation of the individual angular momentum components of the F_{LN} functions of Eq. 154. We present the Reaction I results in Figs. 50 and 52 and the Reaction II results in Figs. 54 and 56. We observe that ionization from one orbital component dominates the summed angular distribution particularly with respect to the parallel transitions. The summed Reaction I angular distributions at $E_k = 2.1$ and $E_k = 3.8$ eV show that angular distributions are directed towards the C_2H_5 fragment in both parallel and perpendicular transitions for C_2H_5Cl in both conformations. The eclipsed conformation, however, possesses an invagination at $E_k = 3.8$ eV along the recoil axis not seen in

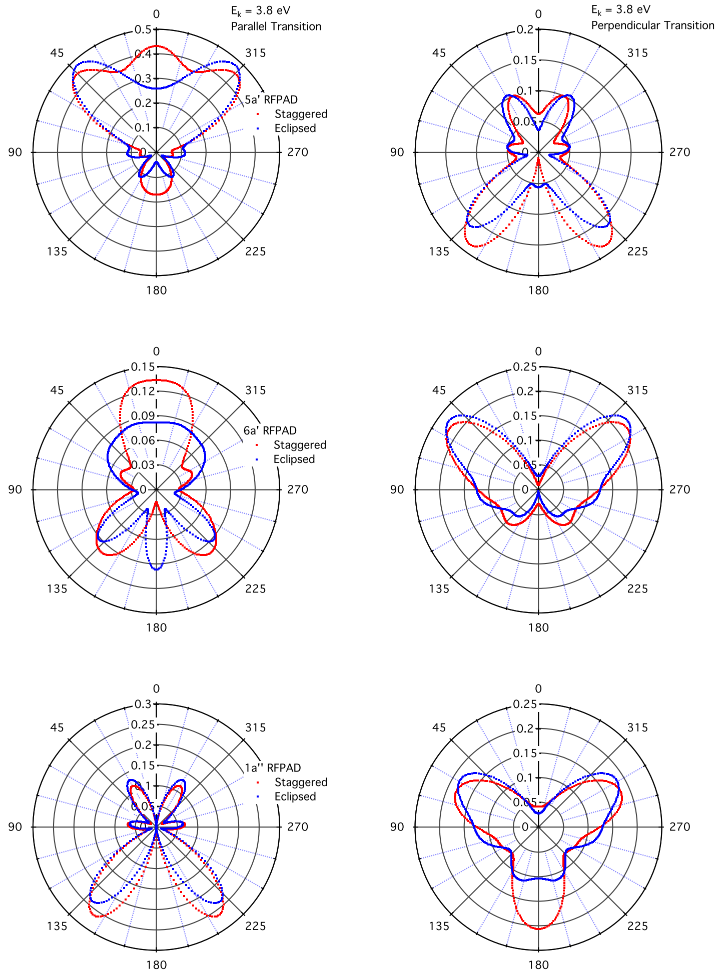

FIG. 51 The same as Fig. 49 for photoelectron kinetic energy $E_k = 3.8$ eV.

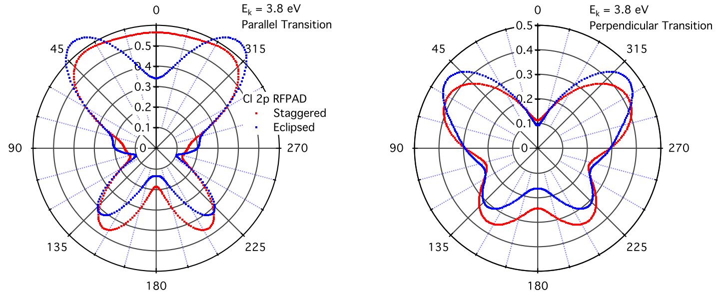

FIG. 52 The same as Fig. 50 for photoelectron kinetic energy $E_k = 3.8$ eV.

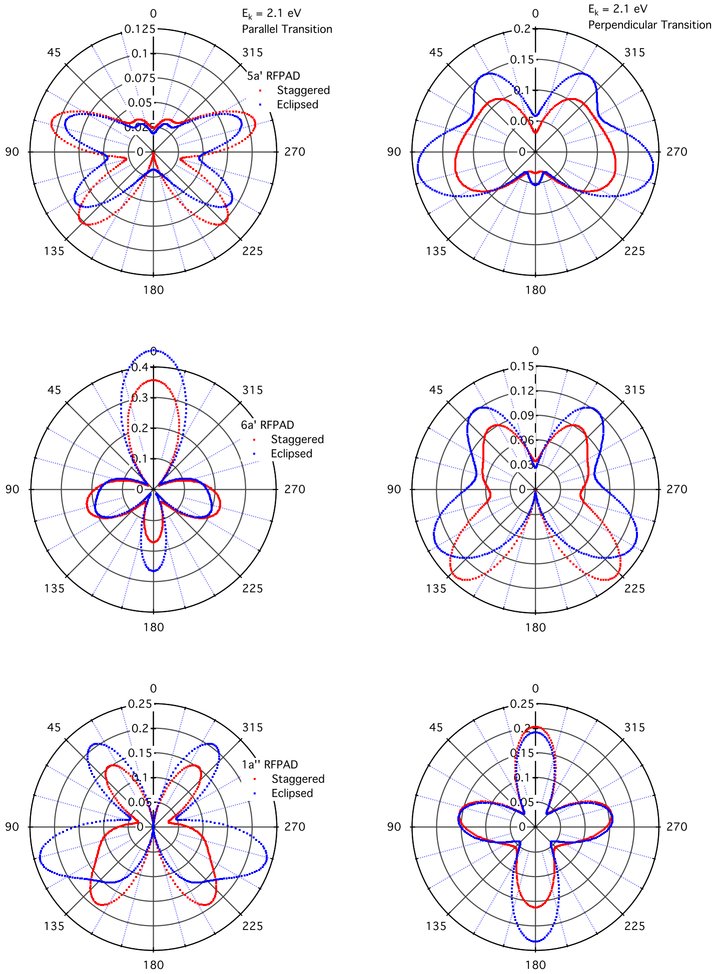

FIG. 53 Computed Reaction II RFPADs (in Mb str^{-1}) of $E_k = 2.1$ eV photoelectrons ionized from the $5a'$, $6a'$, and $1a''$ orbitals of staggered and eclipsed conformation C_2H_5Cl. The distributions are given for light linearly polarized along the recoil axis ($\theta_n' = 0°$) for parallel transitions (left) and at $\theta_n' = 90°$ to the recoil axis for perpendicular transitions (right).

the staggered conformation RFPAD at this energy. At both $E_k = 2.1$ eV and $E_k = 3.8$ eV the $(5a')^{-1}$ ionization cross section comprises the largest component of the summed parallel transition angular distributions. The composite Reaction II angular distributions (Figs. 54 and 56) show parallel transitions dominated by the CH_2Cl fragment and perpendicular transitions characterized by intensity distributed about the CC bond. For the Cl 2p Reaction II parallel distributions at both computed energies, the $(6a')^{-1}$ RFPADs provide

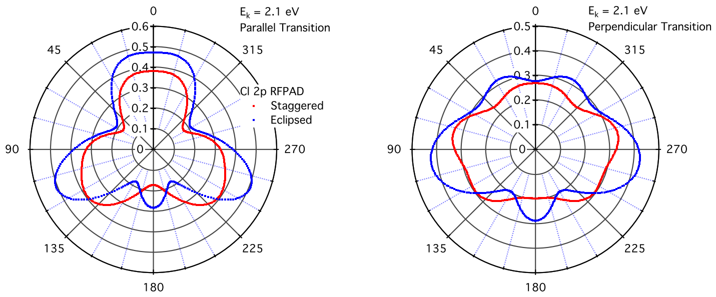

FIG. 54 Computed Reaction II RFPADs (in Mb str^{-1}) of $E_k = 2.1$ eV photoelectrons summed over all Cl 2p orbitals of staggered and eclipsed conformation C_2H_5Cl. The distributions are given for light linearly polarized along the recoil axis ($\theta'_n = 0°$) for parallel transitions (left) and at $\theta'_n = 90°$ to the recoil axis for perpendicular transitions (right).

the major component. The summed Reaction I Cl 2p RFPADs of the staggered conformer should be compared to the RFPADs of Cl 2p$_{3/2}$ $E_k = 4.3$ eV photoelectrons in the CCl dissociation of CH_3Cl reported by Li *et al.* in Li *et al.*, 2007 and Lucchese *et al.* in Lucchese *et al.*, 2009. In particular, the parallel and $(\theta'_n = 0°, \phi'_n = 180°)$ perpendicular $h\nu = 211$ eV Cl 2p RFPADs in Li *et al.*, 2007 have nearly the exact nodal profile as the eclipsed conformation averaged Cl 2p parallel and perpendicular RFPADs displayed in Fig. 54.

2. *C 1s*

The Reaction I $(2a')^{-1}$ and $(3a')^{-1}$ C 1s angular distributions for the staggered and eclipsed conformers, seen in Fig. 57, with the notable exception of the staggered conformer $3a'^{-1}$ distribution, are characterized by cross sections of low magnitude. The differential cross section for the parallel transition $(2a')^{-1}$ RFPAD and all (in-plane) perpendicular transition RFPADs reach an absolute value of only ~ 0.05 Mb. The dissimilarity between the staggered and eclipsed Reaction I RFPADs computed for the methyl $(3a')^{-1}$ C 1s photoionization has been previously noted in the discussion on the respective MFPADs in Sec. V.I.2. While the calculations predict a small, isotropic differential cross section for

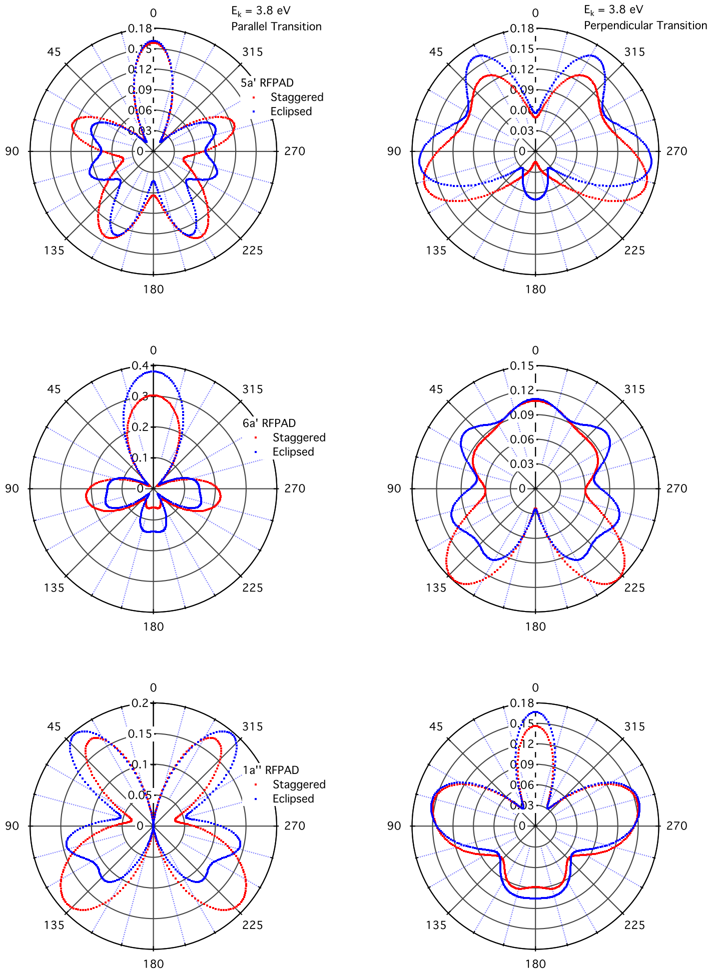

FIG. 55 The same as Fig. 53 for photoelectron kinetic energy $E_k = 3.8$ eV.

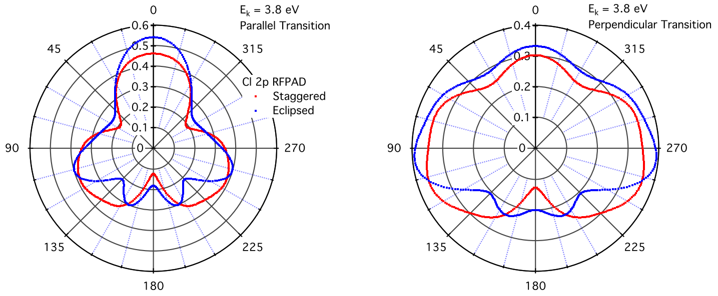

FIG. 56 The same as Fig. 54 for photoelectron kinetic energy $E_k = 3.8$ eV.

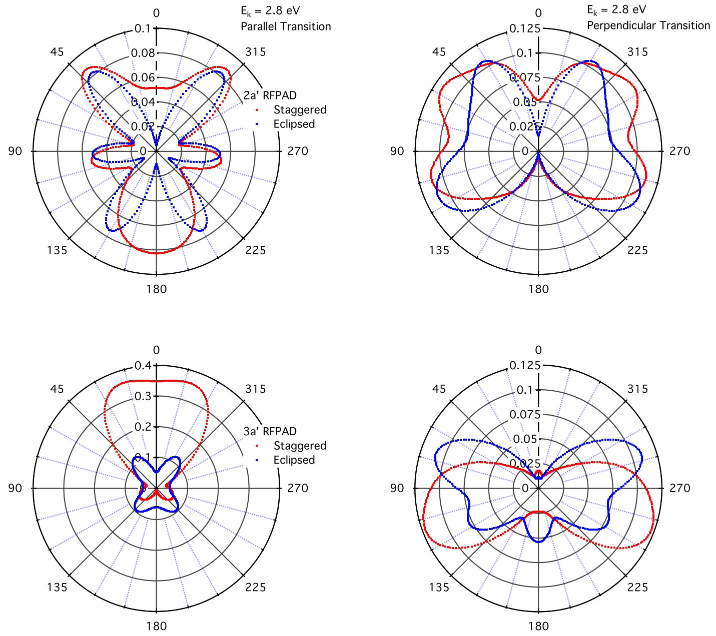

FIG. 57 Computed Reaction I RFPADs (in Mb str^{-1}) of $E_k = 2.8$ eV photoelectrons ionized from the $2a'$ and $3a'$ orbitals of staggered and eclipsed conformation C_2H_5Cl. The distributions are given for light linearly polarized along the recoil axis ($\theta_n' = 0°$) for parallel transitions (left) and at $\theta_n' = 90°$ to the recoil axis for perpendicular transitions (right).

the parallel transition in the eclipsed conformer, the angular distributions of the staggered conformer shows a strong propensity towards the C_2H_5 fragment.

The Reaction II $(3a')^{-1}$ RFPADs are presented in Fig. 58). Both staggered and eclipsed photoelectron distributions are ejected strongly along the recoil axis towards the CH_2Cl fragment in the parallel transition, whereas the perpendicular transitions favor photoelectrons propagating towards the CH_3 fragment. Furthermore, the $(2a')^{-1}$ and $(3a')^{-1}$ Reaction II angular distributions show an overall greater absolute magnitude than the C 1s distributions computed in the Reaction I recoil frame. The parallel transition distributions from the eclipsed conformer, however, are not as strongly axially oriented as those of the staggered conformer.

Both the computed Reaction II $(2a')^{-1}$ and $(3a')^{-1}$ C 1s RFPAD for the staggered conformer compare favorably to the measured C 1s $E_k = 2.8$ eV RFPAD of CCl bond

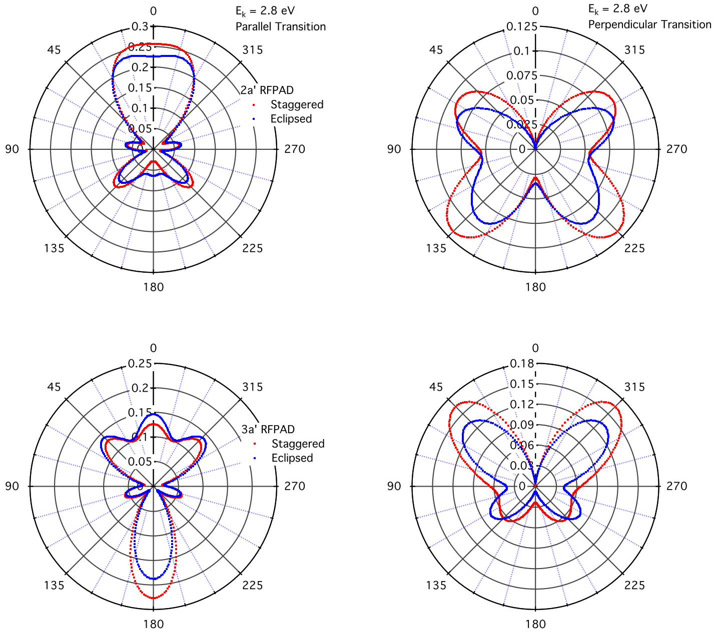

FIG. 58 Computed Reaction II RFPADs (in Mb str^{-1}) of $E_k = 2.8$ eV photoelectrons ionized from the $2a'$ and $3a'$ orbitals of staggered and eclipsed conformation C_2H_5Cl. The distributions are given for light linearly polarized along the recoil axis ($\theta'_n = 0°$) for parallel transitions (left) and at $\theta'_n = 90°$ to the recoil axis for perpendicular transitions (right).

dissociation of CH_3Cl (Elkharrat, 2009), yet the magnitude of the calculated $(2a')^{-1}$ C 1s C_2H_5Cl differential cross sections are considerably smaller than the $4a_1$ CH_3Cl RFPAD reported in Elkharrat, 2009. Recalling that Reaction 1 yields the fragments $CH_3CH_2^+ + Cl^+$ and Reaction II $CH_3^+ + CH_2Cl^+$, while the dissociation in Elkharrat, 2009 measured products $CH_3 + Cl^+$, we see that the nodal structure of the C 1s photoelectron angular distributions result more strongly from ejection of a methyl-like fragment than from the chemical environment of the carbon atom before the dissociation.

K. Conclusion

We have presented integrated photoionization cross sections and electron and ion asymmetry parameters for scattering from the Cl 2p orbitals of chloroethane at $E_k = 2.1$ eV and

$E_k = 3.8$ eV and the C 1s orbitals at $E_k = 2.8$ eV within the fixed nuclei and FCHF approximations, taking into account dynamic electron correlation in the latter with a DFT potential. The differential cross sections in the molecular frame were presented for inner-core ionization using linearly polarized light, with the CCl and CC bonds constituting the molecular axes for C_2H_5Cl and the CH bond for CH_3Cl. The outgoing angular distributions in the molecular frame were analyzed with qualitative symmetry arguments. The differential cross sections in the recoil frame were generated from a simple functional expression in terms of $F_{LN}(\theta'_k)$ functions (Lucchese, 2004) that contain all the dynamic information of the photoionization.

The computed $E_k = 3.8$ eV asymmetry parameters β_k and β_N of the staggered conformer were found to be in reasonable accord with the 5.0 eV Cl $2p_{3/2}$ photoelectrons ejected in the CCl dissociation pathway of CH_3Cl (Elkharrat, 2009). Only a slight change in magnitude between the photoionization cross sections from the halide-like $2a'$ and methyl-like $3a'$ C 1s orbitals were computed, a larger percent magnitude difference being noted between the σ and β parameters found for the staggered and eclipsed conformers.

The computed Cl 2p MFPADs, the first available for this target, may be more thoroughly understood in terms of the electron density of the ionized orbital in the molecular frame, as the $(5a')^{-1}$ and $(6a')^{-1}$ distributions display a convolution of parallel and in-plane perpendicular transitions that renders characterization in terms of symmetry arguments incomplete. A further rotation $R_{\{x',y',z'\}}$ that aligns the $5a'$ and $6a'$ orbitals with the invariant z or x axes may simplify the symmetry analysis. In the limit of the axial recoil approximation, the recoil frame distributions are an average over the unobserved azimuthal angle of the molecular frame distributions; consequently, the Cl 2p RFPADs reflect the average intensity of the computed MFPAD rotated about the invariant z axis. Furthermore, a equal weight average of the individual RFPADs was performed to obtain an angular distribution that may be directly compared with experiment. The averaged Cl 2p RFPADs show the greatest photoelectron intensity directed towards the C_2H_5 fragment in the CCl bond dissociation of Reaction I and the CH_2Cl fragment in the CC bond dissociation of Reaction II.

The $(2a')^{-1}$ and $(3a')^{-1}$ C 1s MFPADs show a great deal of dependence on the nature of the ionizing fragment, despite the fact that they have similar total cross sections σ and partially integrated distributions β_k. With the exception of the Reaction I $(3a')^{-1}$ MFPADs, the angular distributions for the staggered and eclipsed conformers show similar nodal properties. The Reaction I $(2a')^{-1}$ and, particularly, the Reaction II $(3a')^{-1}$ RFPADs may be compared with the C 1s CH_3Cl photoelectron distributions of Elkharrat, 2009. In this case, the computed C 1s angular distributions may provide more information than the experiment, since the measured C 1s cross sections are small and the observed differential cross section may involve a convolution of the angular distributions of the two inequivalent C 1s shells.

VI. MOLECULAR AND RECOIL FRAME ANGULAR DISTRIBUTIONS OF VALENCE PHOTOIONIZATION OF NITROMETHANE

A. Introduction

Nitromethane, the smallest nitro alkane, has long been considered as the prototype of an energetic, yet stable, molecule. Consequently, the ionization and fragmentation dynamics of nitromethane on photon and electron impact have been thoroughly investigated (Allam *et al.*, 1981; Asbrink *et al.*, 1981; Blais, 1983; Butler *et al.*, 1983; Chin *et al.*, 1992; Flicker *et al.*, 1979, 1980; Fujikawa *et al.*, 1974; Gilman *et al.*, 1983; Goebbert *et al.*, 2009; Guo *et al.*, 2009; Jiao *et al.*, 2003; Kandel, 1955; Katsumata *et al.*, 1982; Kilic *et al.*, 1997; Lao *et al.*, 1990; Lifshitz *et al.*, 1988; Mok *et al.*, 1991; Moss *et al.*, 1992; Nagakura, 1960; Napier and Norrish, 1967; Niwa *et al.*, 1981; Ogden *et al.*, 1983; Park *et al.*, 2001; Rabalais, 1972; Rockney and Grant, 1983; Schoen *et al.*, 1982; Wade *et al.*, 2006; Walker and Fluendy, 2001; Wodtke *et al.*, 1986; Yue *et al.*, 2007), yet many questions remain about the details of its interaction with light and the nature of its fragmentation.

The most recent electron impact (EI) ionization investigation of CH_3NO_2 up to 200 eV (Jiao *et al.*, 2003) yielded the parent ion $CH_3NO_2^+$ and CH_3NO^+, NO_2^+, NO^+, and CH_3^+ as the most abundant cations, with a maximum cross section at electron impact 60 eV. The NO^+ and CH_3NO^+ products stem from the following rearrangement reactions

$$CH_3NO_2^+ \rightarrow H_3CONO^+ \rightarrow NO^+ + CH_3NO \tag{156}$$

$$CH_3NO_2^+ \rightarrow H_2CN(O)OH^+ \rightarrow CH_2NO^+ + OH, \tag{157}$$

while the CH_3^+ and NO_2^+ fragments are generated from direct bond cleavage of the ion

$$CH_3NO_2^+ \rightarrow NO_2^+ + CH_3 \tag{158}$$

$$CH_3NO_2^+ \rightarrow CH_3^+ + NO_2. \tag{159}$$

The CH_3^+ ion has an internal kinetic energy of 1.0 eV, while the remaining fragments and the parent ion have little kinetic energy. These findings are in accord with the much earlier EI mass spectrum recorded by Kandel (Kandel, 1955), who found appearance potentials of 11.34 eV for the parent ion, 12.01 eV for NO^+, 12.47 eV for NO_2^+, and 13.58 eV for CH_3^+.

The valence photoelectron spectrum of CH_3NO_2 has been well-investigated (Asbrink *et al.*, 1981; Chin *et al.*, 1992; Fujikawa *et al.*, 1974; Katsumata *et al.*, 1982; Mok *et al.*, 1991; Niwa *et al.*, 1981; Rabalais, 1972), although a few discrepancies exist between the experimental and theoretical (Harris, 1973; Murdoch *et al.*, 1978; Murrell *et al.*, 1975) results, particularly among the ordering of the highest-energy valence orbitals. The vertical ionization potentials of the bands from ultraviolet photoelectron spectroscopy (UPS) are given in Table 31. At an equilibrium ground state geometry in staggered C_s symmetry, nitromethane has a Hartree-Fock inner- and outer-valence electron configuration (Arenas *et al.*, 2003, 2005)

$$\ldots(7a')^2(8a')^2(3a'')^2(4a'')^2(9a')^2(5a'')^2(10a')^2(6a''), \tag{160}$$

with molecular orbital assignments

$$\ldots\sigma_{\mathrm{NO}},\pi_{\mathrm{NO}},\sigma_{\mathrm{NO}},\sigma_{\mathrm{CH}},\sigma_{\mathrm{CH}},n\sigma_{\mathrm{O}},\sigma_{\mathrm{CN}},n\pi_{\mathrm{O}} \tag{161}$$

Because the electron density of the highest-occupied orbitals lies mostly with the NO_2 group, the valence orbitals of nitromethane have been customarily stated in terms of a fictive C_{2v} symmetry, which has been computed by several authors (Harris, 1973; Murrell *et al.*, 1975) as

$$\ldots(7a_1)^2(1b_1)^1(3b_2)^2(4b_2)^2(2b_1)^2(5b_2)^2(8a_1)^2(1a_2)^2. \tag{162}$$

The SCF and semiempirical calculations find the π $1a_2$ ($6a''$) orbital as the HOMO, and the $8a_1$ ($10a'$) and $5b_2$ ($5a''$) σ orbitals are nearly degenerate. This stands in contrast to the usual assignments found in UPS spectra (Katsumata *et al.*, 1982; Mok *et al.*, 1991; Rabalais, 1972) that find the π orbitals higher in energy than the unresolved oxygen $n\sigma$ peaks. It has been assumed (Chin *et al.*, 1992; Mok *et al.*, 1991) that the relaxation of the target orbitals upon ionization is neglected in the simple Kooopmans theorem picture of ionization spectra; however, Murrell *et al.* (Murrell *et al.*, 1975) contend that the arguments used to assign the peaks of the UPS spectra in Rabalais, 1972 are simply invalid.

The relative lack of structure in the optical spectra makes the identification of the excited states of the neutral and cation species resulting from the ionization of CH_3NO_2 difficult (Flicker *et al.*, 1980; Walker and Fluendy, 2001). Flicker *et al.* (Flicker *et al.*, 1980) have summarized the early findings of optical spectroscopy of the neutral target as follows: The UV spectrum yields a weak 4.5 eV peak assigned to a $n \rightarrow \pi^*$ transition, and a stronger 6.3 eV peak assigned to a $\pi \rightarrow \pi^*$ transition (Flicker *et al.*, 1980; Nagakura, 1960). The UV spectrum contains few features, with excitations between 4.06 and 4.6 eV attributed to CN stretching modes. The electron energy loss spectrum (EELS) measured by Flicker *et al.* (Flicker *et al.*, 1980) contains peaks at 3.8 eV due to transitions to a triplet $^3B_2 \leftarrow X^1A_1$ $(^3\pi^* \leftarrow \pi)$, a 4.45 eV peak to due a $1^1B_1 \leftarrow X^1A_1$ $(\pi^* \leftarrow \sigma)$ transition, and a 6.2 eV peak assigned to a $1^1B_2 \leftarrow X^1B_2$ $(\pi^* \leftarrow \pi)$ transition. In addition to these excitations, from a high resolution vacuum UV spectrum of the neutral, Walker and Fluendy (Walker and Fluendy, 2001) identify a 7.44 eV excitation from the HOMO a_2 π orbital (*contra* the assignments of Refs. Mok *et al.*, 1991 and Rabalais, 1972) to a 3s Rydberg orbital and a second 8.07 eV spectral feature to an excitation from HOMO-1 to a second 3s Rydberg state. In contrast to NO_2 (Au and Brion, 1997; Baltzer *et al.*, 1998; Brundle *et al.*, 1970; Eland and Karlsson, 1998; Morrison *et al.*, 1981; Shibuya *et al.*, 1997), the low energy electronic states and lifetimes of the neutral and cation species of nitromethane have not been well characterized by experiment. Goebbert *et al.* (Goebbert *et al.*, 2009) have tentatively assigned the few excited states of the neutral found by the various methods to date, including a triplet state a $^3A''$ at 3.8 eV and singlet states A $^1A''$ at 4.3 eV, B $^1A'$ at 4.5 eV, and C^1A'' about 6.2 eV above the electronic ground state.

Single and multiphoton experiments on nitromethane within the UV range leading to target dissociation are numerous (Blais, 1983; Butler *et al.*, 1983; Kilic *et al.*, 1997; Moss *et al.*, 1992; Nagata *et al.*, 1984; Wodtke *et al.*, 1986). A summary of the primary findings are provided by Guo *et al.* (Guo *et al.*, 2009). The primary dissociation reaction in the ultraviolet absorption spectrum at $h\nu = 270$ nm = 4.6 eV and at $h\nu = 198$ nm = 6.26 eV is the scission of the CN bond (Blais, 1983; Butler *et al.*, 1983; Moss *et al.*, 1992) to yield the radical fragments

$$CH_3NO_2 + h\nu \rightarrow CH_3 + NO_2 \tag{163}$$

that subsequently decay through two major channels

$$\text{(Major Channel) } NO_2\ (1^2B_2) \rightarrow NO + O \tag{164}$$

$$\text{(Minor Channel) } NO_2\ (2^2B_2) + h\nu\ (= 6.26\text{ eV}) \rightarrow NO + O. \tag{165}$$

The fragmentation of $CH_3NO_2^+$ must be found at energies greater than the first adiabatic IP of 11.08 eV. Accordingly, the dissociation of the CN bond of the nitromethane ion takes place at photon energies 11.97 eV and 12.35 eV (Kilic *et al.*, 1997; Ogden *et al.*, 1983)

$$CH_3NO_2^+ \rightarrow NO_2^+ + CH_3\ (\text{IP + 0.69 eV}) \tag{166}$$

$$\rightarrow CH_3^+ + NO_2\ (\text{IP + 1.07 eV}). \tag{167}$$

A competing reaction leading to production of NO^+ results from rearrangement of the nitromethane ion to a methyl nitrite ion (Ogden *et al.*, 1983). The unimolecular dissociation of $CH_3NO_2^+$ is regarded as vibrationally ergodic, with the kinetic energy distribution of the products stemming from the total energy of the system, and electronically excited states of the nitromethane ion dissociating to excited states of NO_2 (Ogden *et al.*, 1983).

Investigations of nitromethane to obtain the electron asymmetry parameter of photoelectrons ejected from a distribution of randomly oriented molecules (β_k) (Wallace and Dill, 1978b) are not as numerous as photoelectron spectra but have nonetheless been measured (Goebbert *et al.*, 2009; Katsumata *et al.*, 1982), primarily to determine the state of the HOMO. Measurements of the integrated photoionization cross section are likewise scarce, with only one very recent source (Xie *et al.*, 2011) recording the absolute photoionization cross section of gas-phase nitromethane and other small nitrogenous organic compounds from ionization threshold (10.8 eV) to 11.5 eV.

Photoelectron angular distributions measured within the molecular frame (MFPADs) reveal much of the detail of the amplitudes and phases of the continuum electron that is lost from randomly oriented molecules (Dill, 1976; Dill *et al.*, 1976). Although the expressions for the MFPAD have been known for decades, the experimental detection of the MFPAD, however, has become available only relatively recently (Shigemasa *et al.*, 1995). One common approach to obtain this observable lies in dissociative photoionization, in which the MFPAD may be measured through the angle-resolved photoelectron-photoion coincidence technique (Golovin *et al.*, 1992). Another means of identifying the MFPAD lies in measuring the photoelectron angular distributions in the lab frame following resonance-enhanced multiphoton ionization (REMPI) (Allendorf *et al.*, 1989; Leahy *et al.*, 1992, 1991; Reid *et al.*, 1992).

For linear diatomic and triatomic molecules, the molecular axis constitutes the sole recoil axis. In the case of polyatomic molecules, several assumptions must be made about the process, most notably that the recoil vector is aligned with the vector of the dissociating bond, and that the dissociation takes place within the rotational period of the target. These assumptions constitute the recoil axis approximation (Zare, 1967), which allows the angular distribution of the photoelectron to be measured with respect to an internal coordinate system defined by the polarization vector of (linear) light and the ion recoil axis. In a dissociative photoionization experiment of a nonlinear polyatomic yielding only two fragments, however, it is not possible to measure the orientation of the target over the unobserved azimuthal angle of the recoil vector, so only the angular distribution in the recoil frame (RFPAD) may be detected.

In the current report, we present a computational study to determine the MFPADs and RFPADs of the outer valence orbitals of nitromethane, CH_3NO_2, using the method we have implemented for single-photon ionization of NO_2 (Toffoli *et al.*, 2007), which has been found to yield qualitative results of the scattering process for nonlinear polyatomic molecules. We also present for completeness integrated photoionization cross sections and electron asymmetry parameters for photoelectrons of kinetic energy up to 20 eV above ionization threshold.

This study extends the preliminary calculations performed by the authors in collaboration with Vredenborg *et al.* (Vredenborg *et al.*, 2011) on the 400 nm multiphoton ionization of nitromethane. The experiment found an appearance energy of the CH_3^+ and NO_2^+ fragments at 12.6 eV and 12.1 eV, respectively, which result from a four-photon excitation energy of 12.4 eV. The measured RFPADs measured within 20° of the linear laser polarization indicate photoelectron density is directed along the CN axis preferentially towards the CH_3 moiety. However, because the NO_2^+ fragments were observed with a significant kinetic energy, Vredenborg *et al.* have proposed a five-photon process with excitation energy 15.5 eV. After canceling the contribution from photoelectron kinetic energy of 0.56 eV, they find a vertical ionization potential of 15.0 eV, which most nearly results from ionization of the $9a'$ orbital (see Table 31). Our computed RFPADs of the $9a'$ at 0.5 eV photoelectron kinetic energy did not reproduce their RFPADs (Vredenborg *et al.*, 2011). This disagreement was perhaps due to the fact that the calculations assume a single-photon dissociative ionization that does not account for the possible electronic and geometric excitations of the target resulting from the multiphoton excitation. The computed RFPADs of photoelectron kinetic energy 0.5 eV above the ionization threshold of the $10a'$ orbital, assuming linearly polarized light directed in parallel with a recoil vector defined by the CN axis, reproduces the features of their experimental RFPAD, although the calculation assumes contrasting experimental conditions.

B. Theory

1. *Functional form of the photoelectron angular distributions*

The MFPAD may be developed in terms of a coordinate system defined by the symmetry axis of the molecule at the time of photon impact and the orientation of the light field. The angles (θ_n, ϕ_n) define the polarization vector of linearly-polarized light, or the propagation vector of circularly-polarized light. The polarization vector is given an index μ_0 that equals +1 for left circularly polarized light, -1 for right circularly polarized light, and 0 for linearly polarized light. Since this study considers linearly polarized light, we set $\mu_0 = 0$. The direction of the photoelectron momentum is given by the angles (θ_k, ϕ_k) within the molecular frame. The set of rotations needed to bring the molecular frame into the lab frame is given in terms of the Euler angles $R_n = (\alpha_n, \beta_n, \gamma_n)$, employing the usual z-y-z rotation conventions (Zare, 1988). The differential cross section for photoionization in the molecular frame, for linearly polarized light, is thus given by the form

$$I_{\mu_0}\left(\theta_k,\phi_k,\theta_n,\phi_n\right)=\frac{4\pi^2E}{c}\left|T_{\mu_0}^{p_fp_i}\left(\theta_k,\phi_k,\theta_n,\phi_n\right)\right|^2, \tag{168}$$

where the transition amplitudes are given by

$$T_{\mu_0}^{p_fp_i}\left(\theta_k,\phi_k,\theta_n,\phi_n\right)=\sum_{lm\mu}I_{lm\mu}^{p_fp_i}(E)Y_{lm}^{*}\left(\theta_k,\phi_k\right)D_{\mu,\mu_0}^{1}(R_n) \tag{169}$$

In Eqs. 168 and 169, p_i and p_f label the irreducible representations of the initial state $\Psi_i^{p_i}$ of neutral molecule and target state $\Psi_f^{p_f}$ of the ionized molecule. The dipole transition elements $I_{lm\mu}^{p_fp_i}(E)$ are obtained from the integrals

$$I_{lm\mu}^{p_fp_i}(E)=\left\langle\Psi_i^{p_i}\left|\hat{\mu}\right|\Psi_f^{p_f}\psi_{lm}^{-}\right\rangle \tag{170}$$

where $\hat{\mu}$ is the dipole operator with spherical component μ and ψ_{lm}^{-} the lm-th partial wave component of the continuum electron. Details of the computation of $I_{lm\mu}^{p_fp_i}(E)$ may be found in Natalense and Lucchese, 1999.

In a dissociative photoionization of a nonlinear polyatomic molecule resulting in two fragments, it is possible only to measure the angular distribution of the photoelectron with respect to the photon momentum vector and the recoil vector. In the recoil frame of reference, the direction of the photoelectron are given by the angles (θ_k',ϕ_k') and the electric field of the polarization (θ_n',ϕ_n'). The photoelectron angular distributions obtained by a rotation $R=(\alpha_R,\beta_R,\gamma_R)$ from the molecular frame into the recoil frame are given by

$$\begin{aligned}&I_{\mu_0,\alpha_R,\beta_R,\gamma_R}^{\text{ion}}\left(\theta_k',\phi_k',\theta_n',\phi_n'\right)=\\&\sum_{LN,L'N'}H_{LN,L'N'}^{\mu_0,\alpha_R,\beta_R,\gamma_R}Y_{L'N'}\left(\theta_k',\phi_k'\right)Y_{LN}^{*}\left(\theta_n',\phi_n'\right),\end{aligned} \tag{171}$$

where

$$\begin{aligned}H_{LN,L'N'}^{\mu_0,\alpha_R,\beta_R,\gamma_R}&=\sum_{JMM'}H_{LM,L'M'}^{\mu_0}\left(\frac{2J+1}{2L'+1}\right)\left\langle JLPN|L'N'\right\rangle\\&\times\left\langle JLP'M|L'M'\right\rangle D_{P',P}^{J}(\alpha_R,\beta_R,\gamma_R)^{*}.\end{aligned} \tag{172}$$

The expansion coefficients $H^{\mu_0}_{LN,L'N'}$ are a unitary transformation of the dipole transition elements of Eq. 170, as follows:

$$\begin{aligned}H^{\mu_0}_{LM,L'M'} = {} & \frac{4\pi^2 E}{c} \sum_{lm\mu} (-)^{M'-M+\mu-\mu_0} I^{p_i,p_f}_{lm\mu} \\ & \times (I^{p_i,p_f}_{l'm'\mu'})^* \\ & \times \left[\frac{(2l'+1)(2L'+1)}{(2l+1)(2L+1)}\right]^{1/2} \left\langle L'l'M'-m'|l-m\right\rangle \\ & \times \left\langle L'l'00|l0\right\rangle \left\langle 11-\mu\mu'|L-M\right\rangle \left\langle 11\mu_0-\mu_0|L0\right\rangle\end{aligned} \tag{173}$$

The RFPAD may be obtained from the MFPAD of Eq. 168 by an average over the unobserved azimuthal angle γ about the recoil axis. The angular distribution after carrying out the average is

$$\begin{aligned}& I^{\text{ion}}_{\mu_0,\alpha_R,\beta_R}(\theta'_k,\phi'_k,\theta'_n,\phi'_n) \\ & \qquad = \sum_{LN,L'} H^{\mu_0,\alpha_R,\beta_R}_{LN,L'} Y_{L'N}(\theta'_k,\phi'_k) Y_{LN}(\theta'_n,\phi'_n)^*\end{aligned} \tag{174}$$

where the coefficients $H^{\mu_0,\alpha_R,\beta_R}_{LN,L'}$ are given by

$$\begin{aligned}H^{\mu_0,\alpha_R,\beta_R}_{LN,L'} = {} & \sum_{JMM'P} H^{\mu_0}_{LM,L'M'} \left[\frac{4\pi(2J+1)}{(2L'+1)^2}\right] \left\langle JL0N|L'N\right\rangle \\ & \times \left\langle JLPM|L'M'\right\rangle Y_{JP}(\alpha_R,\beta_R).\end{aligned} \tag{175}$$

The RFPAD given in Eq. 174 may be recast in an equivalent functional form for linearly polarized light as (Lucchese, 2004)

$$\begin{aligned}I^{\text{ion}}_{\mu_0}(\theta'_k,\phi'_k,\theta'_n,\phi'_n) = {} & F_{00}(\theta'_k) + F_{20}(\theta'_k) P^2_0(\cos\theta'_n) \\ & + F_{21}(\theta'_k) P^1_2(\cos\theta'_n)\cos(\phi'_k-\phi'_n) \\ & + F_{22}(\theta'_k) P^2_2(\cos\theta'_n)\cos 2(\phi'_k-\phi'_n)\end{aligned} \tag{176}$$

where the $F_{LN}(\theta'_k)$ functions can be expressed in terms of a series in spherical harmonics (Lucchese, 2004). The details of the formalism may be found in the given reference. The F_{LN} functions incorporate the complete dynamics of the scattering event and can be used to calculate the RFPAD for any given direction of the photoelectron and photon momentum in the recoil frame. They allow direct comparison with experiment since they represent the maximal information available within experiment.

As stated previously, the experimental apparatus does not observe the azimuthal dependence of the PAD about the recoil axis. Furthermore, experiments measuring the RFPAD often measure the fragmentation at specific angles of the photon momentum vector either parallel or perpendicular to the recoil axis. Averaging over the unobserved azimuthal angles $\phi'_k - \phi'_n$ of Eqn. 176 yields simple functional forms of the RFPAD

$$\begin{aligned} I^{\text{ion}}(\theta'_k, \theta'_n = 0^\circ) &= F_{00}(\theta'_k) + F_{20}(\theta'_k) \\ I^{\text{ion}}(\theta'_k, \theta'_n = 90^\circ) &= F_{00}(\theta'_k) - 0.5F_{20}(\theta'_k) \end{aligned} \tag{177}$$

that admit comparison with older published PADs. In Eq. 177, $(\theta'_n = 0^\circ)$ corresponds to a parallel transition (the light is coincident with the recoil axis) and $(\theta'_n = 90^\circ)$ to a perpendicular transition (the light is perpendicular to the recoil axis).

An alternative method we have considered for this report for the generation of MFPADs and RFPADs lies in generating the dipole transition elements $I^{p_f p_i}_{lm\mu}(E)$ from a target geometry already brought into the desired molecular frame. Specifically, we rotate and translate the molecule from its Mulliken standard orientation (Mulliken, 1955) generated in the computational chemistry program in a set of rotations $R_{\{x,y,z\}}$ and translations $T_{\{x,y,z\}}$ about an invariant coordinate axis into an orientation that aligns the desired bond along the positive z-axis, which we define as the molecular axis. This procedure has the advantage over rotations through the Euler angles R in that the lab frame and the body frame need not rotate about a common coordinate point. For this study, we have rotated CH_3NO_2 $R_x = 90^\circ$ with no subsequent translations, thereby aligning the CN bond with the z-axis and thereby fixing C_s along the xz-plane (see Fig. 59). No subsequent rotations about the Euler angles R_n or R were considered.

TABLE 31 Vertical ionization potentials of nitromethane comparing He (I) spectra and SCF results, as reproduced from Chin *et al.*, 1992

Band	UPS IP	HF/6-31G	
	IP (eV)	IP (eV)	MO Symmetry
1	11.26	13.60	$5a''$
		13.46	$10a'$
2	11.70	12.14	$6a''$
3	14.75	16.70	$9a'$
4	15.82	17.17	$4a''$
5	17.37	19.92	$3a''$
		20.53	$8a'$

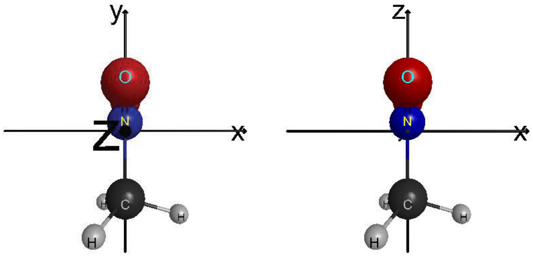

FIG. 59 The equilibrium geometry of CH_3NO_2 as produced in standard orientation (left) and after the rotation $R_{x=90^\circ}$ into the active frame (right).

2. *Computational details*

Calculations of the dipole transition elements $I_{lm\mu}^{p_f p_i}(E)$ of photoionization from the HOMO $(6'')^{-1}$, HOMO-1 $(10a')^{-1}$, HOMO-2 $(5a'')^{-1}$, HOMO-3 $(9a')$, and HOMO-4 $(4a'')^{-1}$ levels of ground-state nitromethane were calculated with the EPOLYSCAT code suite of Lucchese and collaborators (Gianturco *et al.*, 1994; Natalense and Lucchese, 1999). The transition dipole elements were obtained within the frozen-core Hartree-

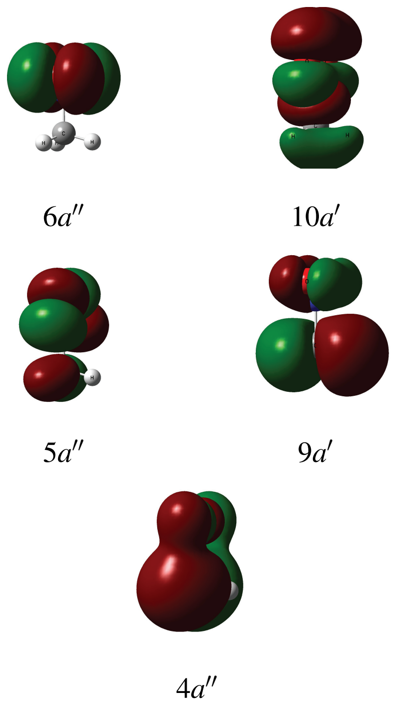

$6a''$ $10a'$

$5a''$ $9a'$

$4a''$

FIG. 60 The valence molecular orbitals of CH_3NO_2. The C_s plane is rotated 15° to allow better inspection of the nodal structure.

Fock (FCHF) approximation (Lucchese *et al.*, 1982) and the fixed-nuclei approximation (Gianturco and Jain, 1986). Briefly, the target and continuum orbitals are represented in a single-center expansion (SCE), recasting the three-dimensional nonrelativistic Schrödinger equation into a series of integro-differential radial equations that are solved using the Schwinger variational method with Padé approximant corrections (Lucchese *et al.*, 1986). The Hartree-Fock orbitals were obtained at an optimized equilibrium geometry with a standard aug-cc-pVTZ basis set available within the GAUSSIAN03 (Frisch *et al.*, 2004) code suite. The resulting SCF energy was $E^{\mathrm{SCF}} = -243.767849491$ au, with optimized geometric parameters r(CN)=1.4188 Å , r(NO)=1.18431 Å , in-plane r(CH)=1.07939 Å and out-of-plane r(CH)=1.07512 Å , and bond angle a(ONO)=125.64423° perpendicular to the molecular plane, which subsequent frequency analysis indicates is the potential minimum structure. In addition, the SCF dipole moment was $\mu = 3.9473$ D and isotropic static polarizability $\bar{\alpha} = 29.46$ au.

The standard orientation of CH_3NO_2, *viz.*, with the C_s plane defined as the *xy*-plane, proved not to be the most convenient to compute the dipole transition elements, so the geometry was rotated about the x-axis by 90° to align the CN bond coincident with the z-axis, as stated in Sec. VI.B.1. The resulting geometry is shown (Bode and Gordon, 1998) in Fig. 59, and the electron density of the valence orbitals in the molecular frame are illustrated (Dennington *et al.*, 2009) in Fig. 60. The target and continuum orbitals were expanded in the SCE to a maximum orbital angular momentum $l_{\text{max}} = 60$. This truncation leads to target orbitals normalized better than the 0.997 of the atomic O 1s orbitals $1a''$ and $1a'$. We recover dynamic electron correlation effects through the use of the density functional expressions of the Perdew and Zunger correlation potential (Perdew and Zunger, 1981), and long-range polarization by placing the non-zero terms of the computed polarizability tensor $\alpha_{\alpha\beta}$ at the center of mass as yielded from the optimization calculation. As mentioned in the Introduction, the ordering of the valence orbitals from SCF calculations do not coincide with the usual assignments of the ionization peaks revealed from photoelectron spectra; therefore, our calculations have assumed the experimental vertical ionization potentials listed in Table I of Mok *et al.*, 1991.

C. Photoionization cross sections

In Figs. 61 and 62 we present the partial photoionization cross sections σ (black) and electron asymmetry parameters β_k (blue) within the length (dashed line), velocity (dashed-dot line), and "mixed" (solid line) gauge representations of the dipole operator for ionization from the HOMO $(6a'')^{-1}$, HOMO-1 $(10a')^{-1}$, HOMO-2 $(5a'')^{-1}$, HOMO-3 $(9a')^{-1}$, and HOMO-4 $(4a'')^{-1}$ orbitals. As seen in Fig. 61 the $(6a'')^{-1}$, $(10a')^{-1}$, and $(5a'')^{-1}$ photoionization cross sections reach a maximum at photon energies near $h\nu = 18$ eV, with the corresponding $(6a'')^{-1}$ electron asymmetry parameters showing a maximum at $h\nu = 18$ eV, the $(10a')^{-1}$ asymmetry parameter at $h\nu = 15$ eV, and the $(5a'')^{-1}$ asymmetry parameter a local minimum also at $h\nu = 15$ eV. By contrast, the $(9a')^{-1}$ photoionization

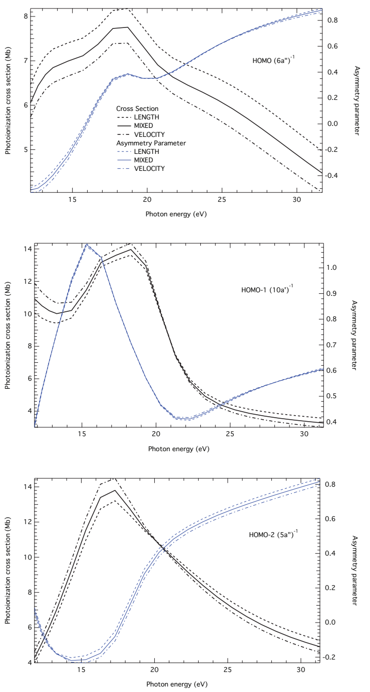

FIG. 61 Photoionization cross sections in Mb (in black) and electron asymmetry parameters (in blue) of CH_3NO_2 from the $6a''$, $10a'$, and $5a''$ orbitals.

cross section features only a monotonic decay with increasing photon energy, while the $(4a'')^{-1}$ cross section displays a local maximum at $h\nu = 24$ eV. The limitations of the theoretical treatment within the current calculations have been summarized in Toffoli *et al.*, 2004, particularly the lack of interchannel coupling and the use of the fixed-nuclei approximation in an excitation region in which vibrational excitation has been observed in the ionized CH_3 fragment (Jiao *et al.*, 2003).

Katsumata *et al.* (Katsumata *et al.*, 1982) reported HeI β_k values measured at two angles, $\theta = 90°$ and $\theta = 35°$, of $\beta_k = 0.21$ and a vertical ionization potential of $E^{\mathrm{IP}} = 11.28$ eV and $\beta_k = 0.34$ with a vertical ionization potential of $E^{\mathrm{IP}} = 11.69$ eV, and an unresolved feature with ionization energy at $E^{\mathrm{IP}} = 11.5$ eV. The NeI electron asymmetry parameters of Katsumata *et al.*, 1982 were $\beta_k = 0.08$ at $E^{\mathrm{IP}} = 11.28$, $\beta_k = 0.20$ and $E^{\mathrm{IP}} = 11.5$ eV, and $\beta_k = 0.14$ at $E^{\mathrm{IP}} = 11.69$ eV. The photoelectron kinetic energies were measured to be between $E_k = 9.5$ eV and $E_k = 9.9$ eV for the HeI values and $E_k = 5.1$ eV and $E_k = 5.6$

TABLE 32 Computed cross sections (in Mb) and asymmetry parameters in the length, mixed, and velocity gauges of photoelectrons with kinetic energies $E_k = 0.5$ eV, $E_k = 5.0$ eV, and $E_k = 10.0$ eV.

Orbital	Photon Energy (eV)	σ^{L} (Mb)	σ^{M} (Mb)	σ^{V} (Mb)	β^{L}	β^{M}	β^{V}
HOMO $(6a'')$ (IP 11.7 eV)	12.2	6.4691	6.0561	5.7370	−0.4925	−0.5107	−0.5298
	16.7	7.7642	7.3724	7.0446	0.1880	0.1748	0.1576
	21.7	7.0661	6.6369	6.2654	0.3985	0.4032	0.4044
HOMO-1 $(10a')$ (IP 11.3 eV)	11.8	10.0621	10.9316	11.8927	0.3794	0.3863	0.3926
	16.3	12.9198	13.1784	13.4851	1.0398	1.0411	1.0394
	21.3	7.4869	7.4266	7.3832	0.4104	0.4149	0.4191
HOMO-2 $(5a'')$ (IP 11.3 eV)	11.8	3.9975	4.2829	4.6429	0.0510	0.0709	0.0859
	16.3	12.7436	13.3959	14.1500	−0.1512	−0.1776	−0.2000
	21.3	10.0658	9.9240	9.8115	0.5030	0.4837	0.4639
HOMO-3 $(9a')$ (IP 14.7 eV)	15.2	16.1858	16.1322	16.1049	−0.2875	−0.2749	−0.2615
	19.7	10.9902	10.6534	10.3410	0.4828	0.4932	0.5029
	24.7	6.2447	5.9332	5.6483	0.7436	0.7476	0.7503
HOMO-4 $(4a'')$ (IP 15.7 eV)	16.2	15.5754	15.2244	14.8974	0.2369	0.2280	0.2183
	20.7	10.8285	10.3175	9.8484	0.3655	0.3654	0.3645
	25.7	8.5337	7.7834	7.1202	0.4018	0.4086	0.4139

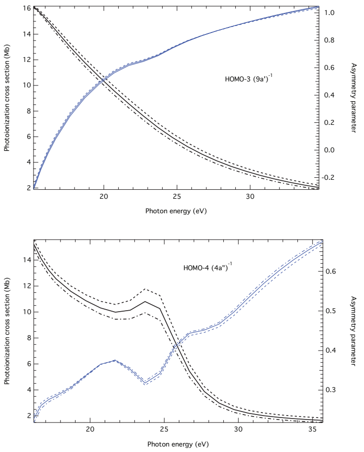

FIG. 62 Photoionization cross sections in Mb (in black) and electron asymmetry parameters (in blue) of CH_3NO_2 from the $9a'$ and $4a''$ orbitals.

eV for the NeI values. For quantitative comparison we present a table of the computed cross sections in Table 32 assuming the experimental values of the ionization potentials. The HOMO electron asymmetry parameters are of comparable magnitude to the He(I) and Ne(I) values, but HOMO-1 and HOMO-2 values are not in agreement. In particular, our computed HOMO-2 cross section reveals a strongly anisotropic asymmetry value of $\beta_k = 1.04$ at $h\nu = 16.3$ eV, or photoelectron kinetic energy $E_k = 5.0$ eV, that is absent in the unresolved HeI PES spectra of (Katsumata *et al.*, 1982).

The asymmetry parameters of photoelectrons associated with higher ionization potentials include $\beta_k = 0.55$ with a vertical ionization potential $E^{\mathrm{IP}} = 14.72$ eV and $\beta_k = 0.57$ with a vertical ionization potential of $E^{\mathrm{IP}} = 15.83$ eV. The kinetic energies of the photoelectrons were stated as $E_k = 6.5$ eV and $E_k = 5.4$ eV. As seen in Table 32, while the computed and experimental values of β_k for the $(9a')^{-1}$ $h\nu = 19.7$ eV ionization are qualitatively similar, the value of the computed asymmetry parameters of the $(4a'')^{-1}$ $h\nu = 20.7$ eV photoionization does not agree with the experimental value.

As the nitromethane photoabsorption spectrum is available only for a limited energy range (Xie *et al.*, 2011), we compare our result to the total photoabsorption curve of nitrobenzene of Cooper *et al.* (Cooper *et al.*, 2001), which displays a broad, relatively featureless spectrum with a large maximum cross section ($\sigma^{C_6H_5NO_2} = 190$ Mb) at photon energy near 18 eV. The broad maximum in the nitrobenzene photoabsorption spectrum has not not explained, but it will be reasonable to suppose that this photon energy corresponds to the scission of the $R-\mathrm{NO}_2$ bond. The structures in the nitrobenzene photoabsorption cross section between 10.2 eV and 13.8 eV involve valence-shell transitions into π^* orbitals and are not believed to be associated with transitions into Rydberg states. In the concomitant mass spectrometric study, the appearance energy of the fragment $\mathrm{C_6H_5^+ + NO_2}$ is found in Cooper *et al.*, 2001 at 11.3 eV, while the less abundant products $\mathrm{C_6H_5 + NO_2^+}$ were found at photon energies above 26 eV.

To identify possible resonant scattering features of the valence excitations at this photon energy, we have used the adiabatic static model exchange (ASMECP) method detailed in Lucchese and Gianturco, 1996 to search the complex energy plane for the poles of the S matrix, whose complex energies correspond to resonant states with energy E_R and lifetime Γ according to the relation

$$E = E_R - \frac{i}{2}\Gamma. \tag{178}$$

Resonance scattering calculations using the ASMECP model were considered for photoelectron kinetic energies 0.5 eV to 20 eV above threshold. To rule out the presence of background and spurious resonances, we have limited our search only for those poles lying relatively closely to the positive energy axis, *viz.*, with a lifetime of $\Gamma = 2.0$ eV. While the peaks in the HOMO, HOMO-1, and HOMO-2 photoionization cross sections appear to result from resonant scattering, such as that found in the FCHF $(1a_2)^{-1}$ photoionization cross section of $\mathrm{NO_2}$ computed by Toffoli *et al.* (Toffoli *et al.*, 2007), no poles were found within the energy spectrum with a lifetime less than $\Gamma = 10$ eV. The HOMO-3 cross section in Fig. 62 shows a monotonic decay from ionization threshold and consequently no possibility of resonant scattering. The HOMO-4 cross section in Fig. 62 shows a small feature at $h\nu = 25$ eV. A search from 0.5 eV above ionization threshold to 10 eV in the photon energy region encompassing this feature using the same criteria as the HOMO through HOMO-2 searches likewise proved unsuccessful.

Nitromethane readily attaches electrons both through covalent interactions and through interaction with its significant measured dipole moment of 3.46 D (Compton *et al.*, 1996), yet a low-energy electron scattering study of Lunt *et al* (Lunt *et al.*, 2001) found that the long-range dipole moment and rotationally inelastic transitions dominate the scattering cross section below 2.5 eV. The electron scattering spectrum of Lunt *et al,*, measured between 0.3 eV and 2.5 eV, extends into the energy region characteristic of resonant scattering for neutral nitromethane, one of which was computed at the multireference configuration interaction (MRCI) level to have a energy $E_R = 0.73$ eV and width $\Gamma = 0.25$ eV (Sommerfeld, 2002). While the electron scattering properties of cationic nitromethane are not yet available, we argue that resonant scattering properties may not be attainable at the FCHF static exchange plus polarization method considered for this report.

D. Recoil- and molecular-frame angular distributions

Molecular frame (MFPAD) and recoil frame (RFPAD) angular distributions were calculated for the primary CN bond dissociation channel of nitromethane (Kilic *et al.*, 1997; Ogden *et al.*, 1983) in the electronic ground state as given in Eq. 167. Molecular and recoil angular distributions were computed for photon energies 0.5 eV above ionization threshold of the HOMO $(6a'')$ through HOMO-4 $(4a'')$ orbitals. Recoil frame angular distributions were also computed 5.0 eV above the respective ionization. As mentioned in the Introduction, it is assumed that the total energy of the ion products and the photoelectrons is statistically related to the kinetic energy imparted by the photon and the neutral target (Ogden *et al.*, 1983). Because ionization is assumed to be rapid, and occurs before the dissociation (Kilic *et al.*, 1997), the state of the photoelectron may be identified by energetics from ionization of the relevant bound orbital of the neutral, as discussed in Vredenborg *et al.*, 2011. Unfortunately, neither experimental nor theoretical unimolecular dissociation channels relating the electronic states of $CH_3NO_2^+$ to the electronic states of NO_2 and the ionized products NO_2^+ and CH_3^+ have yet been published.

In Fig. 63 we present the computed RFPADs of 0.5 eV photoelectrons ejected from the the $(6a'')^{-1}$, $(10a')^{-1}$, and $(5a'')^{-1}$ orbitals of CH_3NO_2. The resulting photon energies, employing the UPS orbital assignments of Mok *et al.* in Mok *et al.*, 1991, are $h\nu = 11.8$ eV for the $(10a')^{-1}$ and $(5a'')^{-1}$ excitations and $h\nu = 12.2$ eV for the $(6a'')^{-1}$ excitation. The

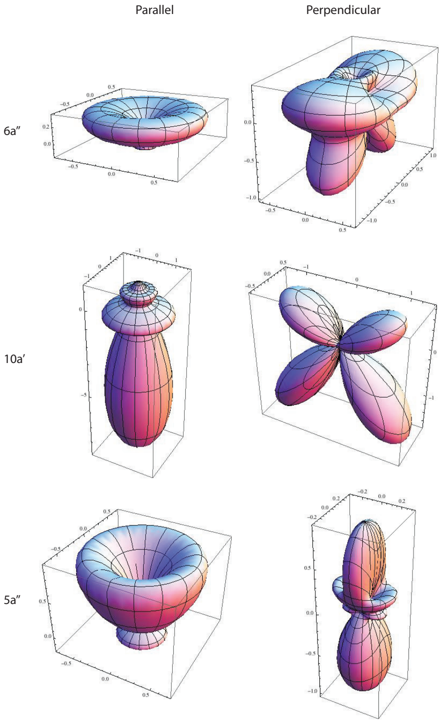

FIG. 63 Computed RFPADs for ionization of $E_k = 0.5$ eV photoelectrons from the $6a''$, $10a'$ and $5a''$ valence orbital of CH_3NO_2. The scale of the axes is given in Mb. The RFPADs are given for light linearly polarized 0° from the recoil axis yielding parallel transitions, and 90° for perpendicular transitions.

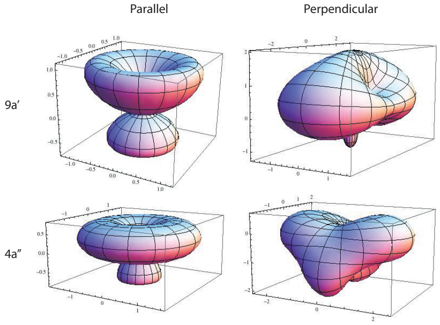

FIG. 64 Computed RFPADs for ionization of $E_k = 0.5$ eV photoelectrons from the $9a'$ and $4a''$ valence orbitals of CH_3NO_2. The scale of the axes is given in Mb. The RFPADs are given for light linearly polarized 0° from the recoil axis yielding parallel transitions, and 90° for perpendicular transitions.

recoil axis is defined along the z-axis, and angular distribution were computed according to Eq. 176, where ϕ_n' is set to $\phi_n' = 0°$, and $\theta_n' = 0°$ for parallel transitions and $\theta_n' = 90°$ for (in-plane) perpendicular transitions.

The RFPADs for parallel transitions from the $6a''$ and $5a''$ orbitals are comparatively small, and are dominated by photoelectron density propagated radially outwards from the NO_2 moiety. By contrast, the large parallel transition $(10a')^{-1}$ ionization is dominated by photoelectron density directed towards the CH_3 fragment. The perpendicular transitions from the three orbitals are notably distinct, and, for the $(6a'')^{-1}$ and $(5a'')^{-1}$ excitations, two to four times the magnitude of the parallel transitions. Photoelectrons are propagated from $6a''$ away from the nonbonding orbital density of the O atoms, d-wave scattering character in the $(10a')^{-1}$ ionization, and photoelectron emission directed along the CN bond from $5a''$. The computed 0.5 eV photoelectron β_k and fragment β_N asymmetry parameters for the HOMO, HOMO-1 and HOMO-2 excitations in the length gauge were $\beta_k = -0.49$, $\beta_N = -0.37$ for $(6a'')^{-1}$, $\beta_k = 0.34$ and $\beta_N = 0.76$ for $(10a')^{-1}$, and $\beta_k = 0.05$, $\beta_N = 0.25$ for $(5a'')^{-1}$.

In Fig. 64 we present the computed RFPADs for excitations from the $9a'$ and $4a''$ orbitals resulting in photoelectron kinetic energy of 0.5 eV. This results in photon energies of 15.2 eV and 16.2 eV, respectively. We consider both parallel and perpendicular transitions. The parallel transitions for these excitations resemble those computed for the $(5a'')^{-1}$ and $(6a'')^{-1}$ excitations, respectively, that is, electron distributions are directed radially from the O lone pair of the nitro group. Angular distributions resulting from perpendicular transitions, however, not are nearly as well-characterized as those from the higher energy orbitals, with both excitations featuring a nearly isotropic distribution directed towards the NO_2 moiety. The length gauge electron and fragment asymmetry parameters of the 0.5 eV HOMO-3 and HOMO-4 excitations were computed to be $\beta_k = 0.48$, $\beta_N = 0.17$ for the $(9a')^{-1}$ excitation and $\beta_k = 0.24$ and $\beta_N = -0.17$ for the $(4a'')^{-1}$ the excitation.

We have also computed RFPADs from the HOMO through HOMO-2 levels for photoelectron kinetic energy of $E_k = 5.0$ eV above ionization threshold. This results in photon energies of 16.7 eV for ionization from $(6a'')^{-1}$, and 16.3 eV for ionization from $(10a')^{-1}$

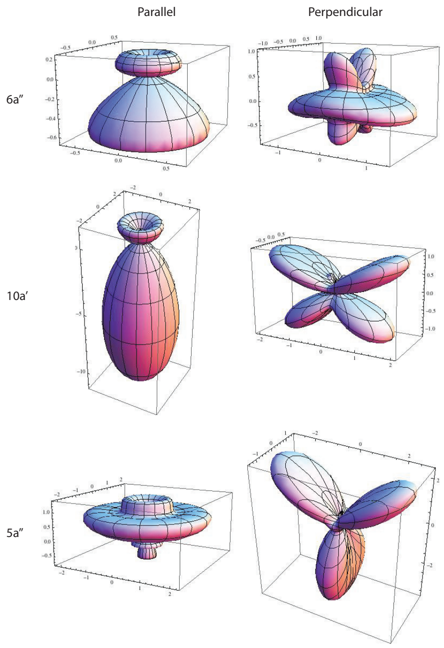

FIG. 65 Computed RFPADs for ionization of $E_k = 5.0$ eV photoelectrons from the $6a''$, $10a'$ and $5a''$ valence orbitals of CH_3NO_2. The scale of the axes is given in Mb. The RFPADs are given for light linearly polarized 0° from the recoil axis yielding parallel transitions, and 90° for perpendicular transitions.

and $(5a'')^{-1}$; consequently, these RFPADs have been computed for a photon energy approximately 1.0 eV above that measured for a 400 nm five-photon excitation in Vredenborg *et al.* (Vredenborg *et al.*, 2011) and closer to the photoelectron kinetic energies recorded by Katsumata *et al.* (Katsumata *et al.*, 1982) for ionization from the inner valence orbitals. The RFPADs are presented in Fig.65. We see that the prominent trend in all the computed RFPADs with parallel transitions is the “flattening” of the distributions, with photoelectrons ejected from the $6a''$ and $5a''$ orbitals propagated equatorially between the methyl and nitro groups. The parallel transition $(10a')^{-1}$ RFPAD becomes directed even more strongly towards the CH_3 group. The perpendicular transitions also display a tendency towards greater anisotropy of the photoelectron distributions at this energy, most notably for the $(5a'')^{-1}$ excitation, which no longer possesses an axially symmetric distribution at the N atom of the nitro group. The change is also noted in the computed length gauge

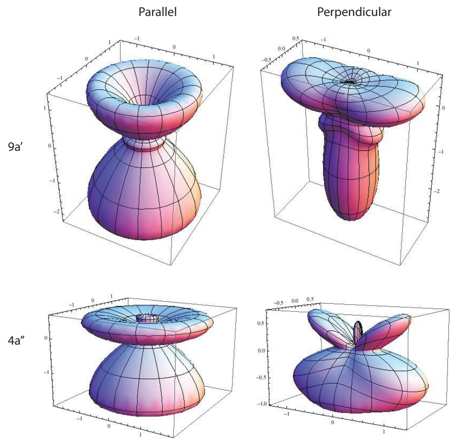

FIG. 66 Computed RFPADs for ionization of $E_k = 5.0$ eV photoelectrons from the $9a'$ and $5a''$ valence orbitals of CH_3NO_2. The scale of the axes is given in Mb. The RFPADs are given for light linearly polarized 0° from the recoil axis yielding parallel transitions, and 90° for perpendicular transitions.

asymmetry parameters, which are $\beta_k = 0.19$ and $\beta_N = -0.44$ for $(6a'')^{-1}$, $\beta_k = 0.10$ and $\beta_N = 0.5$ for $(10a')^{-1}$, and $\beta_k = -0.15$ and $\beta_N = 0.35$ for $(5a'')^{-1}$.

For reference we have also computed $(9a')^{-1}$ and $(4a'')^{-1}$ RFPADs for photoelectrons of kinetic energy $E_k = 5.0$, and present the results in Fig. 66. Converting the photoelectron energies to photon energies using the experimental ionization potentials given in Table 31, we find $(9a')^{-1}$ and $(4a'')^{-1}$ photon energies of $h\nu = 19.7$ eV and $h\nu = 20.7$ eV, respectively. The $(9a')^{-1}$ RFPADs become notably more intense at this energy, with both parallel and perpendicular transitions dominated by photoelectron propagation towards the CH_3 fragment. The parallel and perpendicular transitions of the $(4a'')^{-1}$ ionization retain the overall nodal shapes that characterized distributions from this orbital in the $E_k = 0.5$ eV photoelectron energy value. The computed length gauge electron and fragment beta parameters are stated as follows: $\beta_k = 0.48$ and $\beta_N = 0.17$ for the $(9a')^{-1}$ ionization and $\beta_k = 0.37$ and $\beta_N = 0.41$ for the $(4a'')^{-1}$ ionization.

The MFPADs are computed for photoionization resulting in ejection of a electron of kinetic energy 0.5 eV for light linearly polarized in the z and x directions, consequently resulting in parallel and perpendicular transitions, respectively. Making use of the C_{2v}

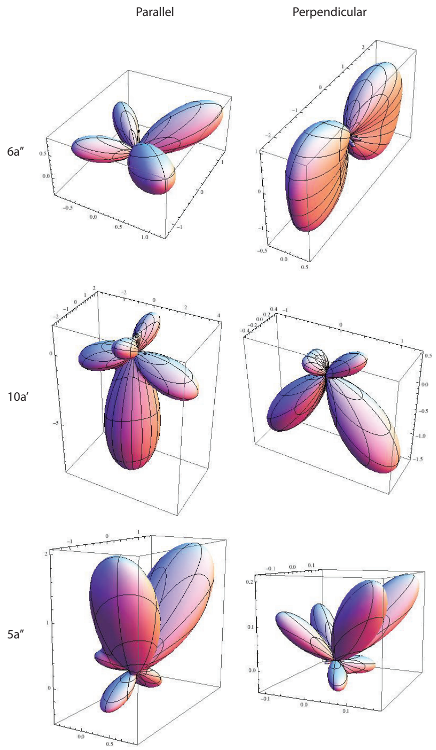

FIG. 67 Computed MFPADs for ionization of $E_k = 0.5$ eV photoelectrons from the $6a''$, $10a'$ and $5a''$ valence orbital of CH_3NO_2. The scale of the axes is given in Mb. The MFPADs are given for light linearly polarized in the z direction yielding parallel transitions, and the x direction for perpendicular transitions.

point group to describe spatial symmetry of the linear polarization vector and the molecular orbitals, and the fact that the photon imparts $\Delta l = \pm 1$ to the angular momentum of the photoelectron, we can make the following predictions about the nodal structure of the MFPAD. Because the CN bond is collinear with the z axis, linear transitions result from z-polarized light, which in C_{2v} transforms as a_1 and leave the irreducible representation (IR) of the excited electron unchanged, whereas perpendicular transition result from x-polarized light that transform according to b_1. In this view, the HOMO resembles a $3d_{xy}$ orbital; HOMO-1 a $3p_z$ orbital; HOMO-2 a $4f_{yz^2}$ orbital, or $3d_{yz}$ at the NO_2 group only to simplify the analysis; HOMO-3 a $3d_{xz}$ orbital; and HOMO-4 mostly $2p_y$, with $3p_y$ character at the O atoms of the NO_2 group. The angular momentum of the outgoing wave should

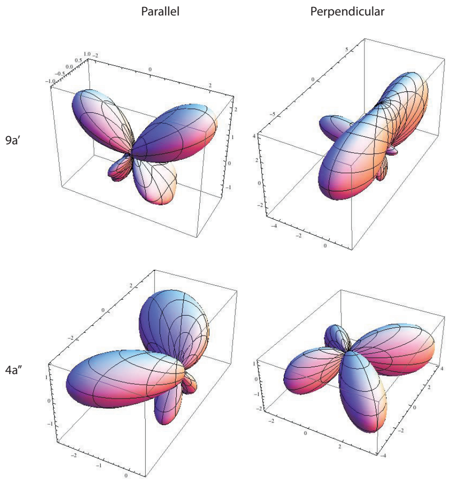

FIG. 68 Computed MFPADs for ionization of $E_k = 0.5$ eV photoelectrons from the $9a'$ and $4a''$ valence orbitals of CH_3NO_2. The scale of the axes is given in Mb. The MFPADs are given for light linearly polarized in the z direction yielding parallel transitions, and the x direction for perpendicular transitions.

simply be the direct product of the photon angular momentum and the angular momentum of the bound orbital from which it is ejected (Lucchese, 2004); thus, for z-polarized light, the outgoing continuum electron should have $4f_{xyz}$, $4d_{z^2}$, $4f_{yz^2}$, $4f_{xz^2}$, and $3d_{yz}$ nodal structures, respectively. For x-polarized light, the analysis yields $4f_{x^2y}$, $4d_{xz}$, $4f_{xyz}$, $4f_{x^2z}$, and $3d_{xy}$ nodal patterns of continuum orbitals.

In Fig. 67 we show the MFPADs computed for ionization from the HOMO through HOMO-2 orbitals with photoelectron kinetic energy $E_k = 0.5$ eV. For linear transitions ($\theta_n = 0^\circ, \phi_n = 0^\circ$), the nodal structure of the MFPAD for each excitation bears resemblance with the expected nodal structure, however, strongly influenced by the scattering from the molecular ion potential. The MFPAD of the $(6a'')^{-1}$ ionization possesses the expected f_{xyz} wave structure, but with its lower nodes, not visible within the figure, greatly attenuated, and strong propensity of ejection from the NO_2 π orbitals. The continuum electron from $10a'$ are ejected from the greater electron density present about the CH_3 group of the CN bond than the nitro group, but the MFPAD retains an overall d_{z^2} character. The outgoing waves of the $(5a'')^{-1}$ ionization are most strongly directed along the σ O orbital density in the *yz*-plane, which may be seen in Fig. 60. The MFPADs of 0.5 eV photoelectrons resulting from ionization from the HOMO-3 and HOMO-4 orbitals, shown in Fig. 68, indicate a less direct connection between the form of the bound orbital and the shape of the resulting MFPAD. However, we note that the MFPAD for $(9a')^{-1}$ given for the linear transition possesses a similar node within the *yz*-plane as the bound orbital, with the distribution preferentially propagating from the electron density of the NO_2 group. The similar propensity of ejection from the nitro group is seen in the $(4a'')^{-1}$ MFPAD, which also displays a nodal surface, in this instance, in the *xz*-plane, consistent with the prediction of a d_{yz} continuum wave structure.

The MFPADs resulting from perpendicular ($\theta_n = 90°, \phi_n = 0°$) transitions likewise show dipole-allowed results. The $(6a'')^{-1}$ MFPAD shows expected f_{x^2y} character, with prominent peaks in the $\pm y$ direction, similarly to the case for photoionization of the π $1a_2$ orbital of NO_2 (Toffoli *et al.*, 2007). The d_{xz} character of the $(10a'')^{-1}$ ionization is readily apparent, with photoelectron density propagated towards the methyl group. The complex scattering phenomena of the $(5a'')^{-1}$ MFPAD is noted in the fact that it possesses more nodes than its analysis as an f_{xyz} wave would suggest. In the case of $(9a')^{-1}$, the electron intensity lies along the *yz*-plane along the nitro group, with few of the features of a f_{x^2z} wave detected in the angular distribution. By contrast, the $(4a'')^{-1}$ MFPAD has a clear d_{xy} nodal pattern, with some anisotropy seen in the direction of $+x$.

E. Conclusion

We have computed integrated photoionization cross sections from threshold to 20 eV for the five highest-energy orbitals of CH_3NO_2 within the FCHF and the fixed-nuclei approximations. We find maxima in the photoionization cross sections near photon energy $h\nu = 18$ eV for the $(6a'')^{-1}$, $(10a')^{-1}$, and $(5a'')^{-1}$ ionizations, although these were shown by the ASMECP method (Lucchese and Gianturco, 1996) not to correspond to discrete one-electron resonant states. The $(9a')^{-1}$ ionization cross section featured a monotonic decay with increasing photon energy, while the $(10a'')^{-1}$ ionization shows a local maximum at $h\nu = 24$ eV. We have generated molecular frame and recoil frame photoelectron angular distributions of the photoelectrons ejected in the dissociation of the CN bond in terms of a simple expression involving $F_{LN}(\theta_e)$ functions, which contain the dynamics of the scattering process, within the axial recoil approximation. For ion recoil directions aligned parallel and perpendicular to the linear polarization axis, the intensity of the MF-PADs were observed to follow a simple product rule of the angular momentum the light polarization with that of the orbital from which the photoelectron was ejected. In particular, the parallel transition angular distributions from the $10a'$ orbital at photon energy $h\nu = 11.8$ eV displayed the greatest intensity along the CN bond of all the angular distributions calculated, and provides the best overall correspondence to the $\mathrm{CH}_3^+ + \mathrm{NO}_2^+$ $(9a')^{-1}$ RFPAD measured by Vredenborg *et al.* (Vredenborg *et al.*, 2011).

These calculations make use of the limiting assumptions of a single-photon ionization from a neutral, stationary target in its electronic ground state to discrete cation states well described by single electronic configuration by means of a dipole transition. In the case of a resonant-enhanced multiphoton excitation at a single frequency ω (the development follows that of Wang and McKoy, 1991),

$$AB + n\hbar\omega \to AB^* + \hbar\omega \to AB^+ + e^-, \tag{179}$$

an ion + photoelectron state $AB^+ + e^-$ stems from the absorption of a photon $\hbar\omega$ by a resonant state AB^* reached by n successive photon impacts of a neutral target AB. Labelling the neutral state $|0>$ with energy E_0, the resonant intermediate state $|i>$, with energy E_i and lifetime Γ_i, and the final ion + photoelectron state $|i>$, the differential cross section of multiphoton ionization may be given by

$$\frac{d\sigma}{d\Omega} \sim \left| \frac{\langle f|d_{\mu_0}|i\rangle \langle i|d_n|0\rangle}{E_i - E_0 - n\hbar\omega + i\Gamma_i} \right|^2, \tag{180}$$

where d_{μ_0} and d_n represent the dipole transition for linear light μ_0 and an effective dipole operator for the n-photon excitation, respectively. Preliminary derivations making use of an effective multiphoton dipole operator suggest that expressions for the RFPAD stated in terms of F_{LN} functions of the form Eq. 176 may be practicable. Progress in this area is ongoing.

In any case, such an analysis will be difficult to apply to the nitromethane molecule, since the lifetimes of the intermediate neutral states $|i>$ are not well characterized either by experiment or by theory, as mentioned in the Introduction. Furthermore, we are not aware of previous REMPI investigation of nitromethane. We must assume that in the multiphoton ionization experiment of nitromethane, as stated by Kilic *et al.* (Kilic *et al.*, 1997), ionization bypasses any intermediate valence or Rydberg states to proceed directly to a dissociative ionizing state. Despite this, we have no reason to suspect that a photoelectron ejected after n successive photon impacts can be understood as having been ejected from the bound orbital of the neutral species.

VII. POSITRON SCATTERING FROM C_{20}*

A. Introduction

Fullerenes are a class of closed polyhedral carbon clusters, C_n, characterized by a truncated icosahedral structure consisting of pentagonal and hexagonal faces among n carbon vertices (Kroto *et al.*, 1985). Consisting only of pentagonal faces, the smallest fullerene believed to exist is C_{20} (Kroto, 1987). Unlike the larger C_{60}, icosahedral C_{20} has an open-shell electronic structure, so the cage suffers Jahn-Teller distortion that leads to a lower symmetry equilibrium structure (Adams *et al.*, 1993; Parasuk and Almlof, 1991; Zhang *et al.*, 1992).

Theoretical investigation of the structure of C_{20} have mostly attempted to distinguish energy levels among several structural conformations, from fullerene "cage", corannulene "bowl", to rings and monocyclic chains (An *et al.*, 2005; Bylaska *et al.*, 1996; Cao, 2001; Chen and Thiel, 2003; Domene *et al.*, 1997; Greene and Beran, 2002; Grimme and Muck-Lichtenfeld, 2002; Grossman *et al.*, 1995; Handschuh *et al.*, 1995; Kroto *et al.*, 1985; Martin *et al.*, 1996; Parasuk and Almlof, 1991; Raghavachari *et al.*, 1993; Sawtarie *et al.*, 1994; Sokolova *et al.*, 2000; Taylor *et al.*, 1995; Zhang *et al.*, 2002). The results vary widely with the level of theory, as tabulated by Sokolova, *et al.* (Sokolova *et al.*, 2000). Although the cage has been calculated to be among the lowest in total energy, particularly among the density-functional theory (DFT) and post-Hartree Fock methods (Domene *et al.*, 1997; Parasuk and Almlof, 1991), due to the highly strained geometry of fullerene C_{20} caused by its violation of the "isolated pentagon rule" (Kroto, 1987), a few significant reports (von Helden *et al.*, 1993; Van Orden and Saykally, 1998) have cast doubt on its very existence.

Until fairly recently, the lack of experimental evidence of fullerene C_{20} has supported the conclusion that it does not exist as a stable structure (Grossman *et al.*, 1995). Additionally, experimental observation of C_{20} ions created by graphite vaporization shows

---

* Reproduced with permission from Ralph Carey, Robert R. Lucchese, and Franco A. Gianturco (2008), Phys. Rev. A **78**, 012706. Copyright 2008 American Physical Society.

monocyclic rings as the dominant structure (von Helden *et al.*, 1993). Subsequent DFT computations have confirmed that rings comprise the predominant products of graphite laser ablation (Lu *et al.*, 2003). Raman spectra of isolated C_{16}, C_{18}, and C_{20} clusters indicate that all three have the same type of geometry, which immediately rules out the corannulene bowl and fullerene cage as possible isomers (Ott *et al.*, 1998). Using Car-Parrinello molecular dynamics simulations, Brabec *et. al.* (Brabec *et al.*, 1992) have proposed that C_{20} rings form in preference to lower-energy cage and bowl isomers with increasing temperature.

On the other hand, the mass spectra of clusters evaporated from carbon nanotubes suggests the formation of cationic fullerene C_{20}^{+} and not chains or rings (Hata *et al.*, 1999). The question of the existence of gas-phase fullerene C_{20}, however, was not settled until Prinzbach and coworkers (Prinzbach *et al.*, 2000) pioneered its synthesis from dodecahedrane ($C_{20}H_{20}$). The photoelectron spectrum of the fullerene anion, C_{20}^{-}, shows an electron affinity of 2.25 eV and a vibrational progression of 730 cm^{-1}. Saito and Miyamoto (Saito and Miyamoto, 2001), in their hybrid time-dependent DFT calculation, found an electron affinity of 2.86 eV and an overall agreement with the experimental spectrum. At nearly the same time as the first synthesis of the gas-phase fullerene, the molecular solid dodecahedral *fullerite* C_{20} has been synthesized from Ar^{+} ion irradiation of high molecular weight polyethylene (Wang *et al.*, 2001). Iqbal et. al. (Iqbal *et al.*, 2003), under radically different conditions, have synthesized the solid from UV laser ablation of thin diamond-like carbon films. Considerable interest lies in the fullerite because of predictions that different phases may be either semiconductors or superconductors (Okada *et al.*, 2001).

Many of the properties of fullerene C_{20} beyond geometric optimization, reviewed in depth by Orden and Saykally (Van Orden and Saykally, 1998), and Lu and Chen (Lu and Chen, 2005), have been obtained only theoretically. These include computations of the polarizability of the series of fullerene clusters (Shanker and Applequist, 1994), with the C_{20} isomer constrained to the icosahedral (I_h) point group, the first ionization potential (Seifert *et al.*, 1996), and the vibrational spectrum (Galli *et al.*, 1998; Saito and Miyamoto, 2002). Therefore, in the case of electron, photon, and, particularly, the positron physics that forms the basis of this report, much of the discussion will compare results obtained here to the theoretically (Scuseria, 1991) and experimentally (Hedberg *et al.*, 1991) better-characterized fullerene C_{60}. We will very briefly state the relevant results.

In addition to having a low electron affinity near 2.7 eV (Wang *et al.*, 1991; Yang *et al.*, 1987), numerous electron attachment experiments have confirmed the existence of long-lived anionic metastable states in gas-phase C_{60} (Jaffke *et al.*, 1994; Lezius *et al.*, 1993; Matejcik *et al.*, 1995), during which almost no vibrational excitation takes place (Elhamidi *et al.*, 1997). Inelastic electron scattering cross sections of the gas-phase fullerene show many of the same features as the solid, with the band shifts due primarily to the collective vibrations of the latter (Keller and Coplan, 1992). The similarity of the valence photoelectron spectra of thin-film C_{60} to that of the gas phase has been noted as well (Lichtenberger *et al.*, 1991).

Photophysical processes of C_{60} have received less attention (Becker *et al.*, 2000). Berkowitz (Berkowitz, 1999) has constructed the absolute photoabsorption cross spectrum of C_{60} from the patchwork of available relative and absolute experiments. Becker and coworkers have performed a series of photoelectron angular distribution measurements over a range of photon energies (Korica *et al.*, 2005; Liebsch *et al.*, 1995; Xu *et al.*, 1996), noting not only similar photoelectron spectra of the gas phase to the solid phase (Benning *et al.*, 1991), but also the origin of the photoionization cross section oscillations of the highest occupied molecular orbitals (HOMO), specifically, quantum interference of the photoelectron wave functions from the nearly spherical target (Xu *et al.*, 1996). Subsequent theories using more elaborate representations of the fullerene target have verified this explanation (Decleva *et al.*, 2001; Hasegawa *et al.*, 1998).

Experiments on the simplest electron-molecule process, elastic scattering, have been performed only at high energy, in which the Born approximation is appropriate (Gerchikov *et al.*, 1998). To the best of our knowledge, the only results on low-energy electron scattering from gas-phase C_{60} are those of Tanaka, *at. al.* (Tanaka *et al.*, 1994), which report differential cross sections between 30 and 90 degrees at select energies.

Relevant experimental (Azuma *et al.*, 1991; Ito *et al.*, 2001; Ito and Suzuki, 1999; Jean *et al.*, 1992; Schaefer *et al.*, 1992) and theoretical (Ishibashi *et al.*, 1992; Puska and Nieminen, 1992) positron-fullerene studies are limited primarily to annihilation dynamics in fullerites. Most experiments have found a positron lifetime in solid C_{60} near 400 ps, greater than that of other carbon phases such as graphite, diamond or condensed-phase benzene (Puska and Nieminen, 1992; Schaefer *et al.*, 1992). Furthermore, due to pressure dependence of the lifetime, most researchers have concluded that positron density accumulates within the hexagonal interstices of the crystal lattice (Ito *et al.*, 2001), not the molecular fullerenes themselves. To date, no elastic positron scattering results from either fullerenes or fullerites have been published.

Theoretical studies of the photophysics of the fullerenes, including C_{20} through C_{60} and beyond, primarily made use of simplified models such as the spherical jellium model (Ivanov *et al.*, 2001; Rudel *et al.*, 2002; Yahana and Bertsch, 1994) to simulate the extensive carbon network. Amusia *et. al.* (Amusia *et al.*, 1998) have calculated photoionization cross sections using a spherical δ-function potential. Yu and collaborators (Xu *et al.*, 1996) used an even simpler spherical-well approximation of the C_{60} fullerene cage. On the other hand, Decleva and coworkers (Colavita *et al.*, 2001; Decleva *et al.*, 2001; Venuti *et al.*, 1999), in their study of the photoemission spectra of C_{60}, have avoided jellium approximations in favor of a single-center expansion of the fullerene orbitals computed under the local-density approximation (LDA) Hamiltonian; Saito and Miyamoto (Saito and Miyamoto, 2001) optimized neutral and anionic C_{20} at the BLYP/6-311G* level. Lima *et. al.* have computed the elastic electron scattering cross sections of C_{60}, in addition to several large hydrocarbons, with a Monte Carlo-adapted optical model (Ferreira *et al.*, 2006). To date, however, the highest-level electron and positron scattering calculations of fullerene targets have been those of Gianturco and collaborators (Gianturco *et al.*, 2002; Gianturco and Lucchese, 1999a,b, 2001; Gianturco *et al.*, 1999, 2003; Lucchese *et al.*, 1999) and, recently, Winstead and McKoy (Winstead and McKoy, 2006b), who applied the Schwinger multichannel method (SMC) to *ab initio* and semiempirical fullerene C_{60} models to obtain integral and differential elastic electron scattering cross sections.

Winstead and McKoy (Winstead and McKoy, 2006b) note that their computation at the level of exact exchange (SE) results in resonance energies that are uniformly too high. Accordingly, they shift their results down roughly 2-3 eV not only to align the lowest-energy resonances to the known anionic bound states of solid- and gas-phase C_{60}, but also to account for the correlation and polarization interactions neglected by the SE approximation. The energies and symmetries of their shifted resonances correspond approximately to those of Gianturco and collaborators (Gianturco *et al.*, 2002, 1999, 2003), whose calculations explicitly include correlation and polarization through one-electron model potentials. On the other hand, the energies of the bound states and lowest-energy resonances of C_{60}, as reported in Lucchese *et al.* (Rudel *et al.*, 2002), result in resonance and bound state energies consistently 0.6 eV above experiment. Similarly, in the valence photoemission of C_{60}, Becker and coworkers (Korica *et al.*, 2005) note the overall agreement between their experimental cross sections and those of Decleva *et al.* (Decleva *et al.*, 2001) and Gianturco and Lucchese (Gianturco and Lucchese, 2001) for the lowest-energy occupied orbitals, even as features in both theoretical cross sections suggest shape resonances not detected in experiment.

Clearly, one of the ongoing issues in molecular scattering theory lies in the accurate computation of bound and resonant energies, which relies on a rigorous description the electron- or positron-molecule interaction. In electron scattering, thorough *ab initio* procedures make use of multiconfigurational wave function descriptions of the target to account for electron correlation, and as recently noted (Winstead and McKoy, 2006a) even this computationally-expensive method fails to account for resonances due to core excitations unless the relevant configurations are explicitly included within the calculation. This difficulty lies at the heart of the present work, since the positron-molecule interaction is not as well understood the electron-molecule interaction and, particularly, no model has been provided to describe positron scattering resonances even while none have been identified conclusively in positron scattering studies from atoms or molecules to date.

In this report we consider partial and total integrated cross sections (ICS) for positron-C_{20} scattering. These cross sections, in conjunction with the plots of the eigenphase sums and the computed poles of the analytic S-matrix, provide evidence for the location of possible scattering resonances. Bound states will also be considered.

B. Theory

The theoretical basis for the present calculation is the same as that for cubane (Gianturco *et al.*, 2005) and fullerene C_{60} (Gianturco and Lucchese, 1999a). We will therefore present a very brief outline of the methods used.

The wave functions of the bound electrons of the target, $\phi_i^{p_i\mu_i}$, and of the impinging positron, $\psi^{p\mu}$ are written in terms of a single- center expansion (SCE) located at the center of mass of the target, under the assumptions of the Born-Oppenheimer and fixed-nuclei approximations:

$$\phi_i^{p_i\mu_i}(\mathbf{r}) = \frac{1}{r}\sum_{l,h} u_{ilh}^{p_i\mu_i}(r) X_{lh}^{p_i\mu_i}(\hat{r}), \tag{181}$$

$$\psi^{p\mu}(\mathbf{r}_\mathrm{p}) = \frac{1}{r_\mathrm{p}}\sum_{l,h} \psi_{lh}^{p\mu}(r_\mathrm{p}) X_{lh}^{p\mu}(\hat{r}_\mathrm{p}). \tag{182}$$

The label i refers to a specific orbital which belongs to the irreducible representation (IR) of the point group of the molecule. The index p refers to the relevant IR with μ indicating one of its components. The index h labels a specific angular basis function for a given partial wave l. The symmetry-adapted angular functions $X_{lh}^{p\mu}$ are defined in terms of the familiar spherical harmonics Y_{lm} by

$$X_{lh}^{p\mu}(\hat{r}) = \sum_m b_{lmh}^{p\mu} Y_{lm}(\hat{r}). \tag{183}$$

The details for the computation of the matrices $b_{lmh}^{p\mu}$ are found elsewhere (Gianturco and Jain, 1986). We note that for the Abelian systems under consideration the label μ may be dropped.

If the positron-molecule interaction can be expressed in a purely local form V_loc, then the SCE results in the reduction of the three-dimensional scattering Schrödinger equation to a set of coupled radial ordinary differential equations

$$\left[\frac{d^2}{dr_\mathrm{p}^2} - \frac{l(l+1)}{r_\mathrm{p}^2} + k^2\right] \psi_{lh}^{p}(r_\mathrm{p}) = 2\sum_{l'h'} \left[V_{\mathrm{loc},lh,l'h'}(r_\mathrm{p})\, \psi_{l'h'}^{p}(r_\mathrm{p})\right] \tag{184}$$

that are solvable using standard numerical techniques. The solutions yield rotationally summed, integral elastic cross sections for each IR. Elements of the K-matrix are obtained from fitting the solutions to the correct asymptotic form, namely (Gianturco *et al.*, 1995),

$$\lim_{r_\mathrm{p}\to\infty} \psi^{p}_{lh,l'h'} = \sin\left(kr_\mathrm{p} - \frac{1}{2}l\pi\right)\delta_{ll'}\delta_{hh'} + K^{p}_{ij}\cos\left(kr_\mathrm{p} - \frac{1}{2}l\pi\right) \tag{185}$$

which are related to the more-familiar S-matrix by

$$\mathbf{S} = \frac{\mathbf{I}+i\mathbf{K}}{\mathbf{I}-i\mathbf{K}}. \tag{186}$$

The local potential V_loc contains contributions from the dominant interactions between the positron and the molecular target,

$$V_\mathrm{loc}\left(\mathbf{r}_\mathrm{p}\right) = V_\mathrm{st}\left(\mathbf{r}_\mathrm{p}\right) + V_\mathrm{pcp}\left(\mathbf{r}_\mathrm{p}\right), \tag{187}$$

where V_st is the electrostatic potential between the positron and the molecular nuclei and electrons, while V_pcp combines the short-range correlation potential V_corr and long-range polarization potential V_pol.

C. The positron model

The correlation-polarization potential V_pcp consists of the sum

$$V_\mathrm{pcp} = V_\mathrm{corr} + V_\mathrm{pol}. \tag{188}$$

The asymptotic polarization potential V_pol simply equals the lowest-order truncation of its second-order perturbation theory expansion

$$V_\mathrm{pol} = -\sum_{l=1}^{\infty} \frac{\alpha_l}{2r_\mathrm{p}^{2l+2}}. \tag{189}$$

To model the dominant short-range correlation interaction between the positron and the electrons of the target, we have used a DFT model, derived by Arponen and Pajanne (Arponen and Pajanne, 1975), that assumes the positron is an isolated charged impurity interacting with an electron gas. Boronski and Nieminen (Boroński and Nieminen, 1986) found the values of the correlation energy ε^{e-p} over all ranges of the electron density parameter r_s which satisfies the relationship $\frac{4}{3}\pi r_s^3\rho\left(\mathbf{r}\right)=1$. That relationship between V_{corr} and ε^{e-p} is given by

$$V_{\mathrm{corr}}\left(\mathbf{r}_{\mathrm{p}}\right)=\frac{d}{d\rho}\left[\rho\left(\mathbf{r}_{\mathrm{p}}\right)\varepsilon^{e-p}\rho\left(\mathbf{r}_{\mathrm{p}}\right)\right], \tag{190}$$

where ρ denotes the undistorted electron density of the target. The full potential V_{pcp} consists of the piecewise-defined function matched at a distance r_{p}^{c},

$$V_{\mathrm{pcp}}(\mathbf{r}_{\mathrm{p}})=\begin{cases}V_{\mathrm{corr}}^{\mathrm{DFT}}(\mathbf{r}_{\mathrm{p}}), & r_{\mathrm{p}}\leq r_{\mathrm{p}}^{c}\\ V_{\mathrm{pol}}(\mathbf{r}_{\mathrm{p}}), & r_{\mathrm{p}}>r_{\mathrm{p}}^{c},\end{cases} \tag{191}$$

the physical veracity of which is discussed in Lucchese, *et al.* (Lucchese *et al.*, 2001).

D. Results and discussion

As mentioned in the Introduction, neutral fullerene C_{20} is not a regular dodecahedron of symmetry I_h because of the Jahn-Teller distortion resulting from the degenerate electronic states arising from the partially-filled molecular orbitals of its ground state (Parasuk and Almlof, 1991). In the majority of geometry optimizations the fullerene is found to belong to the low-symmetry point groups C_i or C_2, although occasionally higher-order point groups such as C_{2h} and D_{2h} have been obtained (Lu and Chen, 2005). The recent work of Chen *et al.* (Chen *et al.*, 2004) has demonstrated that the geometries of fullerenes in most non-dihedral point groups are nearly isoenergetic. Nevertheless, the C_i and C_2 isomers were chosen because they represent the lowest-symmetry ground states consistent with the principles of Jahn-Teller distortion.

The ground state electronic configuration of C_{20} was optimized with the GAUSSIAN03 (Frisch *et al.*, 2004) at the B3LYP/D95* level of theory for isomers of both point groups. With 120 bound electrons, the C_i isomer has an SCF energy of -761.5279 au, average bond length of 1.45 Å and molecular radius of 2.04 Å; the C_2 isomer has an SCF energy of -761.5298 au, and average bond length of 1.45 Å and a molecular radius of 2.04 Å. Calculated isotropic polarizabilities of 171.56 and 171.55 au^3 for the respective C_i and C_2

isomers will be important in the discussion of the nature of the positron-target interaction potential

The convergence parameters of the SCE are as follows. For fullerenes of both point groups, the maximum orbital angular momentum for the expansion of the wave functions of the molecular orbitals and of the incident positron is limited to $l_{\text{max}} = 40$. The summation over the optical and nuclear potentials is set to $2l_{\text{max}}$. The matching of the correlation, V_{corr} and polarization, V_{pol}, potentials of V_{pcp} is done by explicitly placing a “polarizability center”, $1/20^{\text{th}}$ the total isotropic polarizability, on each carbon nucleus. This results in a minor difference of 8.5780 au^3 and 8.5775 au^3 per carbon nucleus of the C_i and C_2 fullerene isomers and imparts a non-spherical model of the full V_{pcp} of Equation 11. The analytic matching radii r_{p}^{c} were, for the respective C_i and C_2 isomers, 5.6726 au or 2.95 Å and 5.9780 au or 3.11 Å.

1. *Features of the adiabatic potentials*

In addition to the symmetry-adapted angular basis set X_{lh}^{p}, angular eigenfunctions obtained from diagonalizing the angular Hamiltonian at each radial distance r provide an alternative expansion basis set for the SCE. These distance-dependent, angular eigenstates Z_k^p, denoted adiabatic angular basis functions, are linear combinations of the previous angular basis set X_{lh}^{p}:

$$Z_k^p\left(\mathbf{r}_{\text{p}}\right) = \sum_{lh} X_{lh}^{p} C_{lh,k}\left(r_{\text{p}}\right). \tag{192}$$

The expansion coefficients $C_{lh,k}$ are given by the matrix equation

$$\sum_{l'h'} V_{\text{loc},lh,l'h',k}\left(r_{\text{p}}\right) C_{l'h',k}\left(r_{\text{p}}\right) = C_{lh,k}\left(r_{\text{p}}\right) V_k\left(r_{\text{p}}\right). \tag{193}$$

The eigenvalues V_k form the adiabatic potentials for each IR comprising the relevant point group of the target for each index value k, representing an “angular channel” (l,h), over the range of the positron-molecule distance. It can be shown (Lucchese and Gianturco, 1996) that solving the appropriate scattering equations using these adiabatic potentials can yield the same results for systems with purely local potentials given by the SCE method outlined

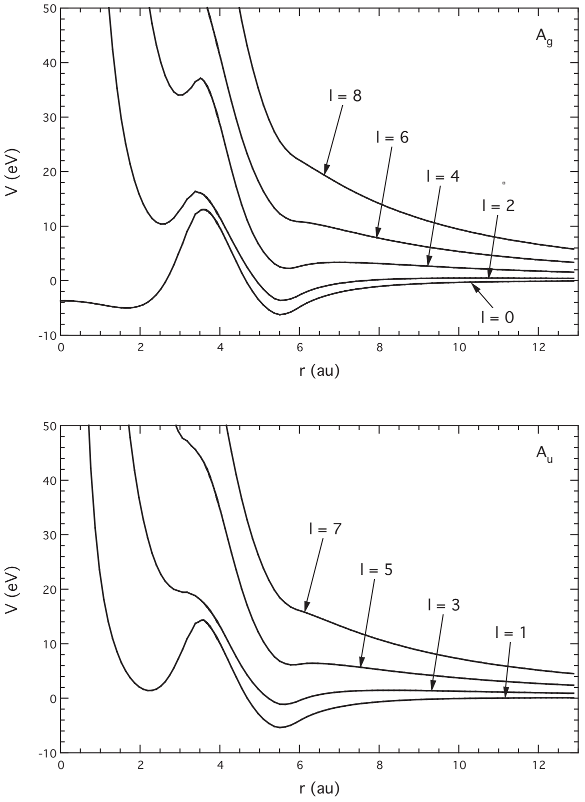

FIG. 69 Computed adiabatic potentials for C_i structural isomer

previously. One of the advantages of using these potentials is that a single potential often is found responsible for the appearance of a given resonance. These potentials, therefore, allow the dominant features of the positron-molecule interaction to be seen qualitatively at a glance.

As shown in Figures 69 and 70, only the $l = 0$ radial potentials of the symmetric IRs A_g in the C_i and A in the C_2 point groups possess an attractive region within the framework of the carbon cage, which is located approximately 3.5 au away from the center of mass at $r = 0$. This potential barrier at the cage boundary is the result of the unique spatial features of C_{20} as computed by V_{tot}, where the repulsive Coulombic potential and the attractive V_{pcp} meet. However, all adiabatic potentials with $l \leq 3$ possess fairly substantial attractive wells, ranging from 3 eV to 8 eV just outside the cage. We should note that the exohedral positron-C_i fullerene potential wells are about 1.5 eV shallower than cor-

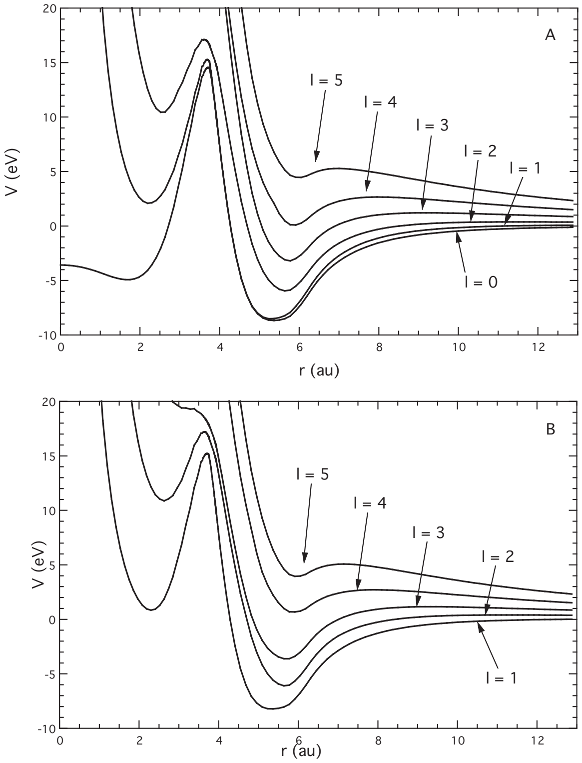

FIG. 70 Computed adiabatic potentials for C_2 structural isomer

responding wells formed by the C_2 cage, thereby indicating a more repulsive interaction between the positron and the C_i isomer.

2. *Features of the integrated cross sections*

Unlike the positron cross section for C_{60}, which increases to some large finite value as the collision energy vanishes (Gianturco and Lucchese, 1999a), the ICS for both isomers, as shown in Fig. 71, display strong near-threshold peaks, with a gradual, but not monotonic, decay at higher scattering energies. Comparing the present positron ICS to the electron total cross sections computed previously (Gianturco *et al.*, 2002), the collision energies of the most prominent peak of both isomers is shifted to lower energy by about 2 eV. This is due to the stronger nature of the V_{pcp} potential at low collision energies, in contrast

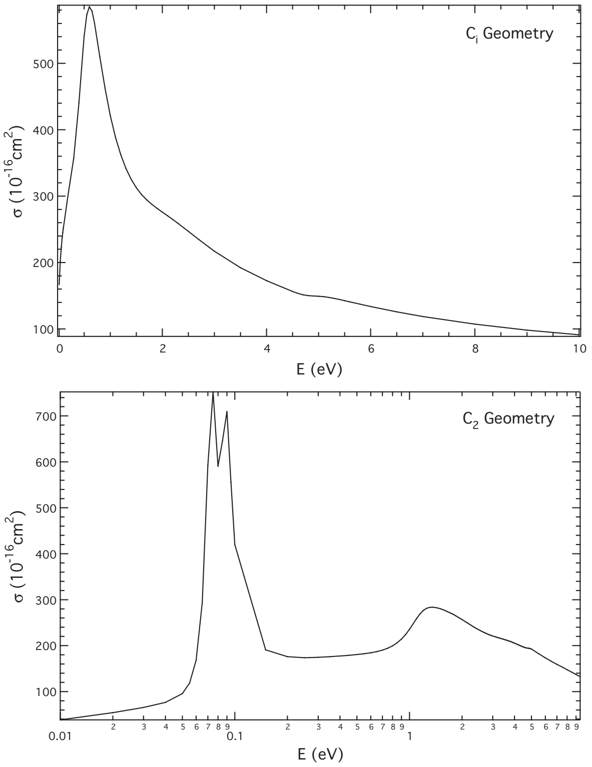

FIG. 71 Total positron scattering cross sections for C_{20} cage of C_i (upper panel) and C_2 (lower panel) geometries

to the model electron correlation-polarization and exchange potentials discussed at length in Gianturco *et al.*, 2003 and Gianturco and Lucchese, 1999b. However, at higher scattering energies, the positron ICSs display fewer of the structural features present in electron scattering cross sections from the respective systems. This, too, is due to the Coulombic nuclear repulsion, which dominates the weakly-attractive long-range polarization interaction.

Partial cross sections were computed for each IR comprising the total point group of the fullerene cage, namely A_g and A_u for the C_i isomer, shown in Fig. 72, and A and B for the C_2 isomer, in Fig. 73. In C_i, the symmetric IR contributes nearly two-thirds of the total scattering cross section peak seen just under 1 eV. Furthermore, the broader peak around 5 eV is due exclusively to the A_g IR. The C_2 total cross section, displayed in the lower panel of Fig. 71, is plotted against the logarithm of the positron impact energy to better resolve

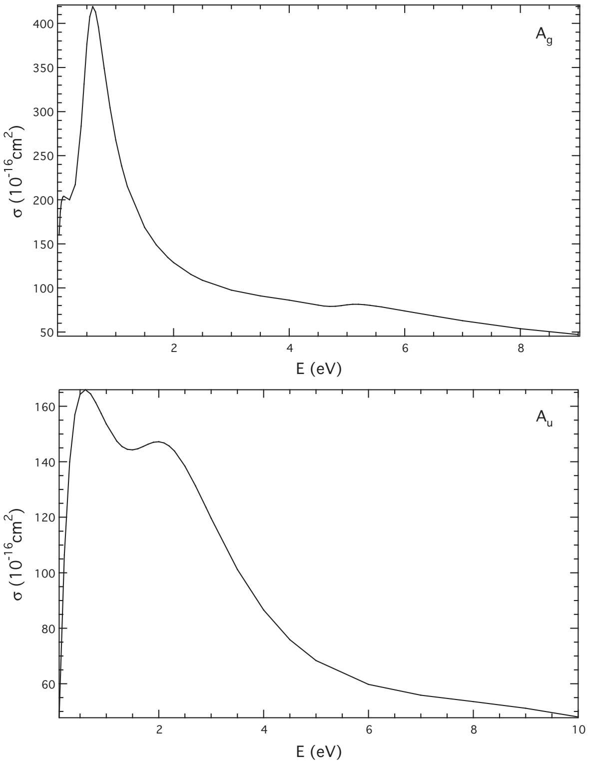

FIG. 72 Computed A_g (upper panel) and A_u (lower panel) partial cross sections for C_i cage geometry

/

the sharp, narrow double peaks at 0.1 eV. Similar to the C_i isomer, these sharp peaks are due to the symmetric IR (upper panel of Fig. 73) since the B partial cross section (Fig. 73, lower panel) rises to less than 160 Å^2 at its maximum. Other noted features of the C_2 total cross section include the broad peak seen near 1.3 eV and the comparatively small peak at 5 eV, both found in the A IR.

3. *Resonance properties*

In resonant scattering, each isolated resonance of energy E_R, possessing a width Γ inversely proportional to its lifetime, is due to a pole at a complex energy $E = E_R - \frac{i}{2}\Gamma$ of the S-matrix (Taylor, 1972). The matrix elements of **S** are obtained from solutions of

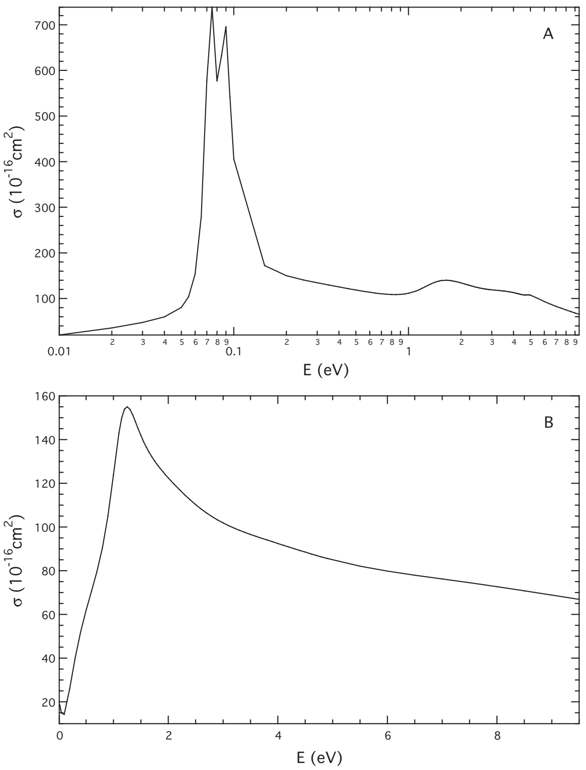

FIG. 73 Computed *A* (upper panel) and *B* (lower panel) partial cross sections for C_2 cage geometry

Equation 184 with the asymptotic form

$$\lim_{r_\mathrm{p}\to\infty} \psi_{lh,l'h'}\left(r_\mathrm{p}\right) = h_l^-(kr_\mathrm{p})\delta_{ll'}\delta_{hh'} - S_{lh,l'h'}h_l^+(kr_\mathrm{p}) \tag{194}$$

where $h^\pm$ are spherical Hankel functions. Resonances occur at energies for which det $\mathbf{S}^{-1} = 0$. In general the task of locating complex zeros of a complex-valued function is not trivial; a full account of the methodology to find the roots of the inverse *S*-matrix may be found in Stratmann and Lucchese (Stratmann and Lucchese, 1992).

Although this procedure finds numerous poles for all IRs for both isomers– twenty-seven poles for the *A* and twenty-five for the *B* IRs for the C_2 isomeric cage alone with real parts of the energy between 0 and 14 eV– only those poles whose widths Γ that are small enough such that corresponding poles in the *S*-matrix lay reasonably close to the positive real axis were investigated further. In this case, somewhat arbitrarily, we have considered states with widths less than about 2 eV, which correspond to lifetimes τ of about 0.01 ps,

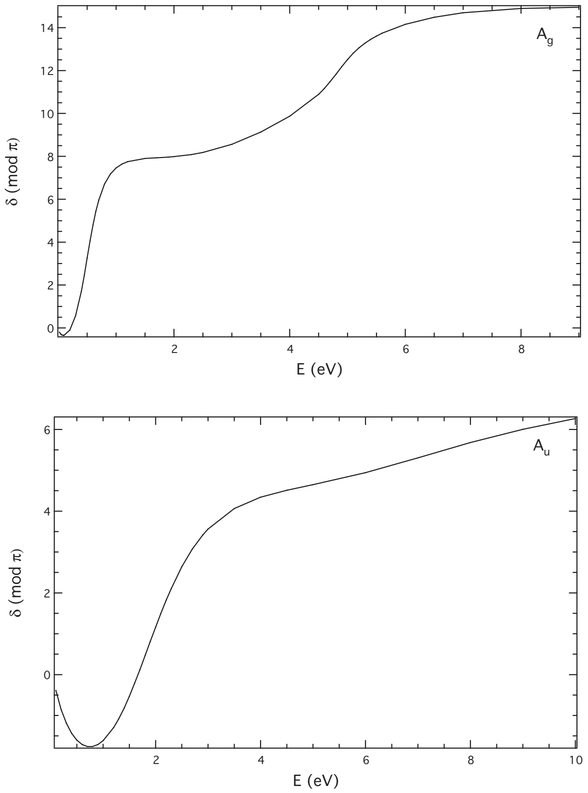

FIG. 74 Eigenphase sums for A_g (upper panel) and A_u (lower panel) IRs of C_i geometry

according to the relation $\tau \sim \frac{\hbar}{\Gamma}$. Tables 33 and 34 lists the energies, widths, and dominant asymptotic partial waves of the "physical" S-matrix poles of the C_i and C_2 isomeric cages, respectively.

In addition to the quantitative search of the assorted roots of the inverse S-matrix, resonances were also located by inspection of the eigenphase sums, shown in Figures 74 and 75. Ideally, the phase shift rises by π wherever the scattering energy moves across an isolated resonance, the position of which is determined at the energy for which $\delta_{\text{res}} = \frac{1}{2}\pi$ $(\text{mod } \pi)$. Overlapping resonances induce a rapid rise by several π over the slowly-rising background through a narrow energy region. Although no empirical fitting procedure such as the Breit-Wigner formula was used to extract resonance properties from the phase sums directly, when analyzed in conjunction with the analytic search of poles of the S-matrix, the eigenphase plots provide greater information on the positions of the energies of scat-

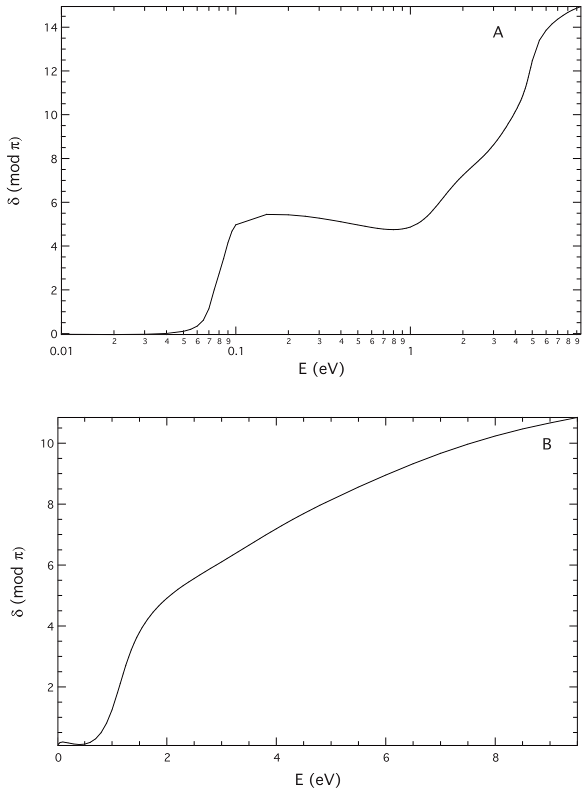

FIG. 75 Eigenphase sums for the *A* (upper panel) and *B* (lower panel) IRs for C_2

FIG. 76 Three-dimensional representations of the resonant orbitals localized within the C_i *left* and C_2 *right* cages

tering resonances, particularly weak or broad ones, than that allowed from inspection of the integrated cross sections alone.

Shape resonances in electron scattering occur when electrons are trapped behind the potential barrier formed by the strongly-attractive electron-molecule static potential and

TABLE 33 Resonant states of e^{+} + C_{20} in C_i geometry. Resonance energies E_R and widths Γ are in eV

Cage Geometry	IR	E_R	Γ	Partial Wave
C_i	A_g	0.49	0.43	*d*
		0.49	0.43	*d*
		0.51	0.43	*d*
		0.51	0.44	*d*
		0.52	0.42	*d*
		4.80	0.83	*s*
	A_u	1.39	2.16	*f*
		1.47	2.31	*f*
		1.48	2.32	*f*
		1.50	2.32	*f*
		1.51	1.96	*f*
		1.60	2.04	*f*
		1.60	2.04	*f*

the centrifugal barrier associated with the angular momentum of the incoming electron. By contrast, the strongly repulsive interaction between the positron and the nuclei of the molecular target, combined with the centrifugal barrier, limits a similar angular momentum mechanisms in positron resonances to low angular momentum states. For example, in electron scattering from C_{20}, resonant states with angular momentum including $l = 8$ were found (Gianturco *et al.*, 2003) However, fullerene C_{20}, like C_{60}, has a large computed polarizability relative to its volume (Gueorguiev *et al.*, 2004) and an absence of nuclear potential within the cage itself, thus leading to resonances trapped, as such, by the $l = 0$ potential barrier. In addition, as suggested by the adiabatic potentials presented earlier in

TABLE 34 Resonant states of e^+ + C_{20} in C_2 geometry. Resonance energies E_R and widths Γ are in eV

Cage Geometry	IR	E_R	Γ	Partial Wave
C_2	A	0.06	0.01	d
		0.07	0.01	d
		1.26	0.84	d
		1.33	1.47	f
		4.80	0.92	s
	B	0.04	2.03	p, d, f
		1.07	0.70	d, f
		1.11	0.50	f
		1.39	1.77	f

TABLE 35 Bound states of e^++C_{20} in C_i symmetry. Bound state energies E_B are in eV

Cage Geometry	IR	E_B	Partial Wave
C_i	A_g	-0.78	s
	A_u	-0.25	p
		-0.23	p
		-0.23	p

Figs. 69 and 70, positrons trapped by angular momentum barriers may appear for states $l \neq 0$ at low collision energies.

For the C_i isomer, the A_g eigenphase sum, displayed in the lower panel of Fig. 74, rises strongly near the scattering energy of 0.5 eV, and more slowly at 4.7 eV. The energies of

TABLE 36 Bound states of e^{+}+C_{20} in C_2 symmetry. Bound state energies E_B are in eV

Cage Geometry	IR	E_B	Partial Wave
C_2	A	-2.10	s
		-0.37	d
	B	-1.90	p,d
		-1.84	p,d
		-0.47	p,d,f
		-0.22	p,d,f

these features in the eigenphase sums correspond well to the six narrow-width poles of the S-matrix found for this system, as listed in Table 33. Five poles were found in the region of the rising phase shift between 490 and 520 meV. These are in general long-lived $l = 2$ scattering resonances that lie outside the carbon cage. However, the remaining pole, located at $E_R = 4.80$ eV, $\Gamma = 0.83$ eV, did yield an *encaged* s-wave positron resonance, the significance of which will be discussed below.

By contrast, the eigenphase sum of the antisymmetric A_u IR, seen in the lower panel of Fig. 74, is *decreasing* between 0 and 700 meV, a phenomenon that is in keeping with the presence of an entirely repulsive potential (Taylor, 1972). The analytic search of poles for this IR found seven short-lived $l = 3$ resonances with energies between 1.39 and 1.50 eV and are listed in Table 33. In this case, the correlation between these seven poles and the eigenphase sum, which rises by only π over a falling background, is less explicit.

For the C_2 isomer, the A eigenphase sum, shown in the upper panel of Fig. 75, rises sharply, by 2π within a 0.3 eV scattering energy range. It rises again, less steeply, between 1 and 2 eV, and further still between 4 and 5 eV. Four poles of the S-matrix, reported in Table 34, have real parts of their energies lying within the ranges of the features of the eigenphase shifts. Two poles with very low resonance energies, $E_R = 60$ meV and $E_R = 70$

meV, are long-lived d-wave resonances. Another pole, with energy $E_R = 1.26$ eV, is a high orbital angular momentum f-wave resonance. The remaining resonance, at $E_R = 4.8$ eV, $\Gamma = 0.92$ eV, is an *encaged* s-wave resonance very close in energy, but somewhat broader in width, to that found for the A_g IR of the C_i isomer.

The eigenphase sum of the B IR in Fig. 75 shows a single narrow rise by approximately 4π for scattering energies near 1 eV. The B IR yields four S-matrix poles with energies lying within this region, as listed in Table 34. Two long-lived resonances, one at $E_R = 1.07$ eV and the other at $E_R = 1.11$ eV, have dominant f-wave components. One of the two shorter lifetime resonances has a very low resonant energy of $E_R = 40$ meV and is predominantly of p-wave nature, while the other is a higher-energy ($E_R = 1.39$) $l = 3$ state.

The most remarkable feature of broad resonances in electron scattering is the possibility of the metastable electron tunneling through a lower angular-momentum potential barrier. This "leaking out" from a dominant higher partial wave through lower partial waves consequently leads to short lifetimes (Gianturco *et al.*, 2003). Such a mechanism does not appear responsible for the short-lived resonances found here. The B resonance wave at $E_R = 1.07$ eV, in Table 34, contains both an $l = 2$ and $l = 3$ partial wave that does not appreciably reduce its lifetime as compared to the single-channel $l = 3$ resonance at $E_R = 1.11$ eV. By contrast, the lowest-energy B resonance of 40 meV contains three competing channels, the lowest of which, $l = 1$, allows very rapid escape of the positron as reflected in its broad resonance width of 2.02 eV.

Computed three-dimensional wave functions of the s-wave resonances of both isomers in Fig. 76 clearly indicate that the majority of their probability amplitudes exist within the cavity of the fullerene cages. Although the lifetimes of these resonances are fairly short (approximately 0.07 ps for widths around 900 meV), the energies are not high enough to cause the dissolution of the carbon network. How this relates to the positron dynamics of fullerene C_{20} remains unclear. Experimental results do not support the hypothesis that positron density localizes within C_{60} fullerenes, as stated in the Introduction; therefore, it is even less likely that positron density should be found within the smaller C_{20} cage.

However, among C_{60} fullerites, positron annihilation may occur within the cavity if heavy alkali atoms are doped within the hexagonal interstices of the molecular crystal (Ito *et al.*, 2001; Lou *et al.*, 1992). Thus, positron localization within the fullerene cage is certainly *possible* if not *favored*, particularly for fullerenes in the gas phase. Indeed, assuming that the $l = 0$ adiabatic potentials of both isomers may be crudely represented as a square well of width $r = 1$ au and height $V = 15$ eV at the cage boundary, and neglecting processes such as virtual positronium formation (Schrader and Moxom, 2001) not modeled in the present SCE, then the probability of the positron of resonance energy $E = 4.8$ eV tunneling through the repulsive cage barrier is a considerable 10%. This result assumes the lifetime of the computed resonance is less than the annihilation lifetime of positrons in C_{20}, for which no result, theoretical or experimental, to date has been published.

So-called "endohedral" A_g resonances are also seen in the C_{60} calculations of both Winstead and McKoy (Winstead and McKoy, 2006b) and Gianturco and Lucchese (Gianturco and Lucchese, 1999b). The SMC at the level of exact static-exchange found an endohedral resonance lying at $E_R = 3.2$ eV, $\Gamma = 0.89$ eV, while the SCE found the equivalent resonance at $E_R = 2.76$ eV, $\Gamma = 0.52$ eV. Gianturco and Lucchese argue that this resonance results from the dynamic coupling of the $l = 0$ to the $l = 10$ partial waves, while Winstead and McKoy state that the A_g resonance corresponds to an anomalous ("non-σ, non-π") anion identified in the condensed molecular photoemission spectrum. Similarly, in their study on positron scattering from C_{60}, making use of a comparative electron correlation potential, Gianturco and Lucchese (Gianturco and Lucchese, 1999a) found an encaged A_g positron resonance at 3.24 eV and a width of less than 0.01 eV; similar calculation using the positron correlation potential in the present report finds the A_g resonance lowered in energy to yield a positronic bound state, i.e. the formation of C_{60}^{+} by positron impact. Interestingly, investigation of the electron scattering resonance on the C_2 isomer of C_{20} (Gianturco *et al.*, 2003) yielded no resonant wave functions with significant probability density trapped within the cage.

At this point in the discussion, we should mention that our search of all physically meaningful poles of the S-matrix yielded a number of bound states as well, and are listed by IR, energy, dominant partial wave in Tables 35 and 36. The location along the negative real axis of the complex energy plane and the requirement that the wave function decay at asymptotic radial distances distinguish these bound states from resonant states discussed previously.

The C_i isomer possesses four bound states as listed in Table 35, among which, the lowest in energy is an s-wave A_g bound state of -780 meV, while the remaining three are higher-energy A_u p-wave states between -250 and -220 meV. The probability maxima of all of these bound states lie near 6 au, outside the fullerene network. The C_2 fullerene cage has a larger array of bound states, listed in Table 36, that are not as well characterized by partial wave as those of the C_i isomer. While the A IR has two bound states, an s-wave state at -2.11 eV and a d-wave state at -370 meV, the B IR has four bound states consisting of multiple partial waves. Two bound states with energies near -1.8 eV have p- and d-wave components, while those at energies -460 and -230 meV each have predominant p- and d-, and minor f-wave, components.

The depth of the adiabatic potential wells $l \leq 3$, shown in Figures 69 and 70, at the junction of the asymptotic and correlation-polarization potentials of V_{loc} allow for the formation of these bound states, since no bound states arise with significant probability densities inside either isomeric cage. The majority of bound states have probability maxima near 6 au; that is, only slightly removed from the matching radii r_{p}^{c} of Equation 11.

The large number of bound and resonant positron states found in the present work suggest that fullerene C_{20}, in both symmetries, easily supports weak positron attachment, even under the assumption of the fixed-nuclei approximation that the nuclear geometry remains constant during the scattering event. This suggestion must be qualified by the fact that cation formation through positron attachment has been conclusively demonstrated only theoretically, and at that merely for atoms (Mitroy *et al.*, 2002). But the fact that all bound states, and all but one resonance each for the two C_{20} isomers, are located outside the cage, corroborates the result of positron annihilation experiments on C_{60} and C_{70} surveyed in the Introduction that positron density accumulates mostly outside the fullerene network.

E. Conclusion

We have reported the results of low-energy positron scattering from C_{20} using a DFT potential to model the interaction of a positron with a multielectron target. The motivation for this work lies not only in the identification of possible scattering resonances and bound states, but also in the question whether positrons may be localized within the fullerene network.

Model adiabatic potentials show that the interaction between the positron and the molecule becomes strongly repulsive for all partial waves $l > 0$, with attractive regions for $l \leq 3$ located outside the cage. The depth of these wells support a small number of bound states for positrons of low, and resonances at higher, angular momenta. These results are sensitive not only to the adiabatic and fixed-nuclei approximations of the SCE, but also to the nature of the assumed interaction potential V_{loc}, a function dependent on a correlation model that treats the positron as an isolated positive point charge and neglects positronium formation. Both assumptions enhance the attractive positron-molecule interaction, thereby increasing the depth of the adiabatic potentials and the number of any metastable states.

The conclusions obtained from this qualitative analysis of the model potentials agree with those obtained from computed integrated partial cross sections, eigenphase sums, and analytic search of physical roots of the inverse S-matrix. The partial ICS and eigenphase sums show evidence of several scattering resonances for both low symmetry isomers. However, the probability maxima of the resonance radial wave functions indicate that the majority of these resonances, and all of the bound states, lie outside the framework of the carbon cage. In general, at least in elastic scattering, no energetic advantage exists for positrons to localize within the fullerene cavity.

VIII. CONCLUSIONS

Due to increases both in computing technology and in developments in molecular structure theory, photoionization and electron scattering calculations can now accomodate more complex molecular targets. Specifically, we have computed electron scattering cross sections from the biologically relevant targets pyridine and pyrimidine and the inorganic antitumour complex *cis*-diamminedichloroplatinum within the static-exchange approximation (Lane, 1980), including an optical potential that corrects for asympototic polarization and short-range dynamic electron correlation (Perdew and Zunger, 1981). Photoionization spectra for CH_3R, where $R = \{Cl, CH_2Cl, NO_2\}$, were computed within the frozen-core Hartree-Fock approximation (Lucchese, 2002), and photoelectron angular distributions derived using equations adapted from linear molecules (Lucchese, 2004). Lastly, we have computed positron cross sections for the fullerene C_{20}, approximating the vital positron-electron density interaction with a model DFT potential (Boroński and Nieminen, 1986).

Pyridine and pyrimidine, both isoelectronic with the parent hydrocarbon benzene, are found to possess a number of scattering resonances whose energies and scattering phenomena may be understood as the perturbation by the nitrogen atom of the well-investigated benzene π^* e_{2u} 1.1 eV resonance and the 4.0 eV b_{2g} resonance (Nenner and Schulz, 1975). Higher-energy σ^* resonances in pyridine and pyrimidine may correspond to the e_{1u} resonance in benzene at 8.5 eV (Allan, 1989), although we suspect that this benzene resonance may have multiconfigurational characteristics not taken into account in the SE calculations.

We have undertaken a project to compute the electron scattering properties of *cis*-diamminedichloroplatinum, which remains the largest target we have considered to date. While the low-energy (0.5 eV to 10 eV) scattering cross sections remain in progress, we have completed a search through each scattering symmetry (in C_{2v}) for bound states with resonance energies less than $\Gamma/2 = 8.4$ eV.

In addition to the major complex, we have also treated electron scattering from the substituents chlorine ($^1\Sigma_g^+$) and the platinum atom (^1S, ^3D) in both the SE approximation and in multichannel CI approximation (Stratmann and Lucchese, 1995), which was implemented for this purpose. The multichannel CI results for Cl_2 are in accord with the SE results neglecting polarization and correlation (Rescigno, 1994); this is seen to degrade the quality of the computed cross sections below a scattering energy of 4 eV where correlation effects are needed to reproduce the scattering cross section seen in experiment. The Pt atomic cross sections, the first we have computed for a transition metal, show a monotonic decay from low scattering energies, in contrast to the computed results of Msezane *et al.* (Msezane *et al.*, 2008), which features narrow peaks at the energies corresponding to shape resonances.

We have also computed integrated and differential inner-shell C 1s and Cl 2p photoionization cross sections for chloromethane and chloroethane, neglecting (in the former) and incorporating (in the latter) correlation effects through an optical DFT potential. We have calculated molecular- and recoil-frame angular distributions leading to various ionic channels that are shown to correspond well to those obtained from photoion-photoelectron coincidence experiments (Elkharrat, 2009). We have also computed angular distributions for ionization from the outer valence shells of nitromethane, one of which, $(10a')^{-1}$, is shown to relate to the measured RFPAD of the dissociating CN bond although it does not match the energy or the state symmetry of the suspected ionizing orbital in experiment (Vredenborg *et al.*, 2011).

The positron scattering study from C_{20} includes on of several scattering studies performed for this small fullerene cage (Gianturco *et al.*, 2002, 2003). Although positrons have not been indicated to form scattering resonances (Surko *et al.*, 2005), we have identified a number of scattering resonances for this target on account of the strongly interactive nature of the polarization. In particular, one resonance is shown to possess positron density within the network of carbon atoms, in conjunction to the non-π non-σ T_{1u} electron scattering resonance found in calculations on the better investigated fullerene C_{60} (Gianturco and Lucchese, 1999b; Winstead and McKoy, 2006b).

REFERENCES

Abu-samha, M., K. Borve, L. Saethre, and T. Thomas (2005), Phys. Rev. Lett. **95** (10), 103002.

Adamo, C., and V. Barone (1998), J. Chem. Phys. **108** (2), 664.

Adams, G., O. Sankey, J. Page, and M. O'Keeffe (1993), Chem. Phys. **176** (1), 61.

Allam, S., M. Migahed, and A. Khodary (1981), Int. J. Mass Spectrom. Ion Processes **39** (1), 117.

Allan, M. (1989), J. Electron Spectrosc. Relat. Phenom. **48** (3-4), 219.

Allan, M. (2007), J. Phys. B At. Mol. Opt. Phys. **40** (17), 3531.

Allendorf, S., D. Leahy, D. Jacobs, and R. Zare (1989), J. Chem. Phys. **91** (4), 2216.

Amaral, G., K. Xu, and J. Zhang (2001), J. Phys. Chem. A **105** (7), 1115.

Amusia, M., A. Baltenkov, and B. Krakov (1998), Phys. Lett. A **243** (1-2), 99.

An, W., Y. Gao, S. Bulusu, and X. Zeng (2005), J. Chem. Phys. **122** (20), 204109.

Andersson, P., A. O. Lindahl, D. Hanstorp, and D. J. Pegg (2009), Phys. Rev. A **79** (2), 022502.

Andrae, D., U. Haussermann, M. Dolg, H. Stoll, and H. Preuss (1990), Theor. Chim. Acta **77** (2), 123.

Arenas, J., J. Otero, D. Pelaez, and J. Soto (2003), J. Chem. Phys. **119** (15), 7814.

Arenas, J., J. Otero, D. Pelaez, and J. Soto (2005), J. Chem. Phys. **122** (8), 084324.

Armstrong, L., B. Beers, and S. Feneuille (1975), Phys. Rev. A **12** (5), 1903.

Arponen, J., and E. Pajanne (1975), Ann. Phys. **91** (2), 450.

Asbrink, L., A. Svensson, W. von Niessen, and G. Bieri (1981), J. Electron Spectrosc. Relat. Phenom. **24** (3), 293.

Au, J., and C. Brion (1997), Chem. Phys. **218** (1-2), 109.

Azuma, T., H. Saito, Y. Yamazaki, K. Komaki, Y. Nagashima, H. Watanabe, T. Hyodo, H. Kataura, and N. Kobayashi (1991), J. Phys. Soc. Jpn. **60** (9), 2812.

Baltzer, P., L. Karlsson, B. Wannberg, D. Holland, M. MacDonald, M. Hayes, and J. Eland (1998), Chem. Phys. **237** (3), 451.

Bandarage, G., and R. R. Lucchese (1993), Phys. Rev. A **47**, 1989.

Basden, B., and R. R. Lucchese (1988), Phys. Rev. A **37**, 89.

Baym, G. (1973), *Lectures on Quantum Mechanics* (Westview Press, Boulder, Colorado).

Becke, A. (1993a), J. Chem. Phys. **98** (7), 5648.

Becke, A. (1993b), J. Chem. Phys. **98** (2), 1372.

Becker, U., O. Gessner, and A. Rudel (2000), J. Electron Spectrosc. Relat. Phenom. **108** (1-3), 189.

Benning, P., D. Poirier, N. Troullier, J. Martins, J. Weaver, R. Haufler, L. Chibante, and R. Smalley (1991), Phys. Rev. B **44** (4), 1962.

Berkowitz, J. (1999), J. Chem. Phys. **111** (4), 1446.

Berrington, K. A., W. B. Eissner, and P. H. Norrington (1995), Comp. Phys. Comm. **92** (2-3), 290.

Bettega, M., C. Winstead, and V. McKoy (2000), J. Chem. Phys. **112** (20), 8806.

Bilodeau, R. C., M. Scheer, H. K. Haugen, and R. L. Brooks (1999), Phys. Rev. A **61**, 012505.

Blackman, G., R. Brown, and F. Burden (1970), J. Mol. Spectrosc. **35** (3), 444.

Blais, N. (1983), J. Chem. Phys. **79** (4), 1723.

Blaise, J., J. Vergés, J.-F. Wyart, and R. Engleman (1992), J. Res. Natl. Inst. Stand. Tech. **97** (1), 213.

Bode, B., and M. Gordon (1998), J. Mol. Graphics Mod. **16** (3), 133+.

Boese, A., and J. Martin (2004), J. Phys. Chem. A **108** (15), 3085.

Bostock, C. J., D. V. Fursa, and I. Bray (2010), Phys. Rev. A **82** (2), 022713.

Bouchiha, D., J. Gorfinkiel, L. Caron, and L. Sanche (2006), J. Phys. B At. Mol. Opt. Phys. **39** (4), 975.

Boudaiffa, B., P. Cloutier, D. Hunting, M. Huels, and L. Sanche (2000), Science **287** (5458), 1658.

Brabec, C., E. Anderson, B. Davidson, S. Kajihara, Q. Zhang, J. Bernholc, and D. Tomanek (1992), Phys. Rev. B **46** (11), 7326.

Brundle, C., D. Neumann, W. Price, D. Evans, A. Potts, and D. Streets (1970), J. Chem. Phys. **53** (2), 705.

Buckley, M., and P. Benfield (1993), Drugs **46** (1), 126.

Burke, P., and K. Berrington (1993), *Atomic and Molecular Processes: an R-Matrix Approach* (Institute of Physics Pub., Bristol).

Burke, P. G., A. Hibbert, and W. D. Robb (1971), J. Phys. B. At. Mol. Phys. **4** (2), 153.

Burke, P. G., I. Mackey, and I. Shimamura (1977), J. Phys. B. At. Mol. Phys. **10** (12), 2497.

Burke, P. G., and J. F. B. Mitchell (1973), J. Phys. B At. Mol. Phys. **6** (2), 320.

Burrow, P. (2005), J. Chem. Phys. **122** (8), 087105.

Burrow, P., J. Michejda, D. Lun, J. Sullivan, R. McEachran, D. Newman, and S. Buckman (1998), J. Phys. B At. Mol. Opt. Phys. **31** (24), L1009.

Butler, L., D. Krajnovich, Y. Lee, G. Ondrey, and R. Bersohn (1983), J. Chem. Phys. **79** (4), 1708.

Bylaska, E., P. Taylor, R. Kawai, and J. Weare (1996), J. Phys. Chem. **100** (17), 6966.

Calaminici, P., K. Jug, A. Koster, V. Ingamells, and M. Papadopoulos (2000), J. Chem. Phys. **112** (14), 6301.

Cao, X. Z. (2001), Chin. Phys. Lett. **18**, 1060,.

Carey, R., R. R. Lucchese, and F. A. Gianturco (2011), “Electron Scattering from *cis*-Diamminedichloroplatinum(II),” to be submitted.

Carpenter, J., and F. Weinhold (1988), Theochem J. Mol. Struct. **46**, 41.

Chang, R., and T. Furtak (1982), *Surface Enhanced Raman Scattering* (Plenum Press, New York).

Chen, D., and G. Gallup (1990), J. Chem. Phys. **93** (12), 8893.

Chen, P., and R. Holroyd (1996), J. Phys. Chem. **100** (11), 4491.

Chen, Z., T. Heine, H. Jiao, A. Hirsch, W. Thiel, and P. Schleyer (2004), Chem.-Eur. J. **10** (4), 963.

Chen, Z., and W. Thiel (2003), Chem. Phys. Lett. **367** (1-2), 15.

Chin, W., C. Mok, H. Huang, S. Masuda, S. Kato, and Y. Harada (1992), J. Electron Spectrosc. Relat. Phenom. **60** (2), 101.

Cho, H., R. Gulley, K. Sunohara, M. Kitajima, L. Uhlmann, H. Tanaka, and S. Buckman (2001), J. Phys. B At. Mol. Opt. Phys. **34** (6), 1019.

Christophorou, L., and J. Olthoff (1999), J. Phys. Chem. Ref. Data **28** (1), 131.

Christophorou, L. G., and J. K. Olthoff (2004), *Fundamental Electron Interactions with Plasma Processing Gases* (Kluwer Academic/Plenum Publishers, New York).

Chupka, W., B. J, and D. Gutman (1971), J. Chem. Phys. **55** (6), 2724.

Colavita, P., G. De Alti, G. Fronzoni, M. Stener, and P. Decleva (2001), Phys. Chem. Chem. Phys. **3** (20), 4481.

Colyer, C. J., V. Vizcaino, J. P. Sullivan, M. J. Brunger, and S. J. Buckman (2007), New J. Phys. **9**, 41.

Compton, R., H. Carman, C. Desfrancois, H. Abdoul-Carime, J. Schermann, J. Hendricks, S. Lyapustina, and K. Bowen (1996), J. Chem. Phys. **105** (9), 3472.

Cooper, G., J. Sanabia, J. Moore, J. Olthoff, and L. Christophorou (1999), J. Chem. Phys. **110** (1), 682.

Cooper, L., L. Shpinkova, E. Rennie, D. Holland, and D. Shaw (2001), Int. J. Mass Spectrom. **207** (3), 223.

Dampc, M., A. R. Milosavljevic, I. Linert, B. P. Marinkovic, and M. Zubek (2007), Phys. Rev. A **75** (4), 042710.

De Oliveira, E. M., M. A. P. Lima, M. H. F. Bettega, S. d. Sanchez, R. F. da Costa, and M. T. d. N. Varella (2010), J. Chem. Phys. **132** (20), 204301.

Decleva, P., S. Furlan, G. Fronzoni, and M. Stener (2001), Chem. Phys. Lett. **348** (5-6), 363.

Dedieu, A. (2000), Chem. Rev. **100** (2), 543.

Dennington, R., T. Keith, and J. Millam (2009), “GaussView Version 5,” Semichem Inc. Shawnee Mission KS.

Desfrancois, C., H. Abdoul-Carime, N. Khelifa, and J. Schermann (1994), Phys. Rev. Lett. **73** (18), 2436.

Dill, D. (1976), J. Chem. Phys. **65** (3), 1130.

Dill, D., and J. Dehmer (1974), J. Chem. Phys. **61** (2), 692.

Dill, D., J. Siegel, and J. Dehmer (1976), J. Chem. Phys. **65** (8), 3158.

Domene, M., P. Fowler, D. Mitchell, G. Seifert, and F. Zerbetto (1997), J. Phys. Chem. A **101** (44), 8339.

Dora, A., J. Tennyson, L. Bryjko, and T. van Mourik (2009), J. Chem. Phys. **130** (16), 164307.

Douglas, M., and N. Kroll (1974), Ann. Phys. **82** (1), 89.

Downie, P., and I. Powis (1999a), J. Chem. Phys. **111** (10), 4535.

Downie, P., and I. Powis (1999b), Phys. Rev. Lett. **82** (14), 2864.

Duncan, J., D. McKean, P. Mallinson, and R. McCulloch (1973), J. Mol. Spectrosc. **46** (2), 232.

Eland, J., and L. Karlsson (1998), Chem. Phys. **237** (1-2), 139.

Elhamidi, O., J. Pommier, and R. Abouaf (1997), J. Phys. B At. Mol. Opt. Phys. **30** (20), 4633.

Elkharrat, C. (2009), Ph.D. thesis (Université Paris-Sud).

Engel, E., S. Keller, A. F. Bonetti, H. Müller, and R. M. Dreizler (1995), Phys. Rev. A **52**, 2750.

Fan, X., and K. Leung (2002), J. Electron Spectrosc. Relat. Phenom. **123** (2-3), 287.

Felfli, Z., A. R. Eure, A. Z. Msezane, and D. Sokolovski (2010), Nucl. Instrum. Methods Phys. Res. Sect. B Beam Interact. Mater. Atoms **268** (9), 1370.

Fernholt, L., and C. Romming (1978), Acta Chem. Scand. A **32** (3), 271.

Ferreira, L., A. Lopes, M. Lima, and M. Bettega (2006), J. Phys. B At. Mol. Opt. Phys. **39** (5), 1045.

Flicker, W., O. Mosher, and A. Kuppermann (1979), Chem. Phys. Lett. **60** (3), 518.

Flicker, W., O. Mosher, and A. Kuppermann (1980), J. Chem. Phys. **72** (4), 2788.

Fortunelli, A. (1999), Theochem J. Mol. Struct. **493**, 233.

Frisch, M. J., G. W. Trucks, H. B. Schlegel, G. E. Scuseria, M. A. Robb, J. R. Cheeseman, J. A. Montgomery, Jr., T. Vreven, K. N. Kudin, J. C. Burant, J. M. Millam, S. S. Iyengar, J. Tomasi, V. Barone, B. Mennucci, M. Cossi, G. Scalmani, N. Rega, G. A. Petersson, H. Nakatsuji, M. Hada, M. Ehara, K. Toyota, R. Fukuda, J. Hasegawa,

M. Ishida, T. Nakajima, Y. Honda, O. Kitao, H. Nakai, M. Klene, X. Li, J. E. Knox, H. P. Hratchian, J. B. Cross, V. Bakken, C. Adamo, J. Jaramillo, R. Gomperts, R. E. Stratmann, O. Yazyev, A. J. Austin, R. Cammi, C. Pomelli, J. W. Ochterski, P. Y. Ayala, K. Morokuma, G. A. Voth, P. Salvador, J. J. Dannenberg, V. G. Zakrzewski, S. Dapprich, A. D. Daniels, M. C. Strain, O. Farkas, D. K. Malick, A. D. Rabuck, K. Raghavachari, J. B. Foresman, J. V. Ortiz, Q. Cui, A. G. Baboul, S. Clifford, J. Cioslowski, B. B. Stefanov, G. Liu, A. Liashenko, P. Piskorz, I. Komaromi, R. L. Martin, D. J. Fox, T. Keith, M. A. Al-Laham, C. Y. Peng, A. Nanayakkara, M. Challacombe, P. M. W. Gill, B. Johnson, W. Chen, M. W. Wong, C. Gonzalez, and J. A. Pople (2004), "Gaussian 03, Revision C.02," Gaussian, Inc., Wallingford, CT, 2004.

Fujikawa, T., T. Ohta, and H. Kuroda (1974), Chem. Phys. Lett. **28** (3), 433.

Fulscher, M., K. Andersson, and B. Roos (1992), J. Phys. Chem. **96** (23), 9204.

Fursa, D., I. Bray, and G. Lister (2003), J. Phys. B At. Mol. Opt. Phys. **36** (21), 4255.

Fursa, D. V., C. J. Bostock, and I. Bray (2009), Phys. Rev. A **80** (2), 022717.

Galli, G., F. Gygi, and J. Golaz (1998), Phys. Rev. B **57** (3), 1860.

Garrett, W. (1971), Phys. Rev. A **3** (3), 961.

Gerchikov, L., P. Efimov, V. Mikoushkin, and A. Solov'yov (1998), Phys. Rev. Lett. **81** (13), 2707.

Giaccone, G. (2000), Drugs **59** (Suppl. 4), 9.

Gianturco, F., and A. Jain (1986), Phys. Rep. Rev. Sec. Phys. Lett. **143** (6), 347.

Gianturco, F., A. Jain, and L. Pantano (1987), J. Phys. B At. Mol. Opt. Phys. **20** (3), 571.

Gianturco, F., G. Kashenock, R. Lucchese, and N. Sanna (2002), J. Chem. Phys. **116** (7), 2811.

Gianturco, F., and R. Lucchese (1998), J. Chem. Phys. **108** (15), 6144.

Gianturco, F., and R. Lucchese (1999a), Phys. Rev. A **60** (6), 4567.

Gianturco, F., and R. Lucchese (1999b), J. Chem. Phys. **111** (15), 6769.

Gianturco, F., and R. Lucchese (2000), J. Chem. Phys. **113** (22), 10044.

Gianturco, F., and R. Lucchese (2001), Phys. Rev. A **64** (3), 032706.

Gianturco, F., and R. Lucchese (2004), J. Chem. Phys. **120** (16), 7446.

Gianturco, F., R. Lucchese, and N. Sanna (1994), J. Chem. Phys. **100** (9), 6464.

Gianturco, F., R. Lucchese, and N. Sanna (1999), J. Phys. B At. Mol. Opt. Phys. **32** (9), 2181.

Gianturco, F., R. Lucchese, and N. Sanna (2003), J. Chem. Phys. **118** (9), 4013.

Gianturco, F., S. Meloni, P. Paioletti, R. Lucchese, and N. Sanna (1998), J. Chem. Phys. **108** (10), 4002.

Gianturco, F., P. Nichols, T. Gibson, and R. Lucchese (2005), Phys. Rev. A **72** (3), 032724.

Gianturco, F., D. Thompson, and A. Jain (1995), in *Computational Methods for Electron-Molecule Collisions*, edited by W. Huo and F. Gianturco, pp. 75–118.

Gianturco, F. A., F. Sebastianelli, R. R. Lucchese, I. Baccarelli, and N. Sanna (2008), J. Chem. Phys. **128** (17), 174302.

Gianturco, F. A., F. Sebastianelli, R. R. Lucchese, I. Baccarelli, and N. Sanna (2009), J. Chem. Phys. **131** (24), 249901.

Gilman, J., T. Hsieh, and G. Meisels (1983), J. Chem. Phys. **78** (3), 1174.

Goebbert, D. J., K. Pichugin, and A. Sanov (2009), J. Chem. Phys. **131** (16), 164308.

Golovin, A., N. Cherepkov, and V. Kuznetsov (1992), Z. Phys. D Atoms Mol. Clusters **24** (4), 371.

Greene, K., and K. Beran (2002), J. Comput. Chem. **23** (9), 938.

Griffin, D. C., M. S. Pindzola, T. W. Gorczyca, and N. R. Badnell (1995), Phys. Rev. A **51**, 2265.

Grimme, S., and C. Muck-Lichtenfeld (2002), ChemPhysChem **3** (2), 207+.

Grossman, J., L. Mitas, and K. Raghavachari (1995), Phys. Rev. Lett. **75** (21), 3870.

Gueorguiev, G., J. Pacheco, and D. Tomanek (2004), Phys. Rev. Lett. **92** (21), 215501.

Gulley, R., and S. Buckman (1999), J. Phys. B At. Mol. Opt. Phys. **32** (14), L405.

Gulley, R., T. Field, W. Steer, N. Mason, S. Lunt, J. Ziesel, and D. Field (1998a), J. Phys. B At. Mol. Opt. Phys. **31** (13), 2971.

Gulley, R., S. Lunt, J. Ziesel, and D. Field (1998b), J. Phys. B At. Mol. Opt. Phys. **31** (12), 2735.

Guo, Y. Q., A. Bhattacharya, and E. R. Bernstein (2009), J. Phys. Chem. A **113** (1), 85.

Han, S., J. Kim, J. Song, and S. Kim (1998), J. Chem. Phys. **109** (22), 9656.

Han, S., J. Song, J. Kim, H. Oh, and S. Kim (1999), J. Chem. Phys. **111** (9), 4041.

Handschuh, H., G. Gantefor, B. Kessler, P. Bechthold, and W. Eberhardt (1995), Phys. Rev. Lett. **74** (7), 1095.

Hara, S. (1967), J. Phys. Soc. Jpn. **22** (3), 710.

Harris, L. (1973), J. Chem. Phys. **58** (12), 5615.

Hasegawa, S., T. Miyamae, K. Yakushi, K. Inokuchi, K. Seki, and N. Ueno (1998), Phys. Rev. B **58** (8), 4927.

Hata, K., M. Ariff, K. Tohji, and Y. Saito (1999), Chem. Phys. Lett. **308** (3-4), 343.

Hay, P., and W. Wadt (1985), J. Chem. Phys. **82** (1), 270.

Hedberg, K., L. Hedberg, D. Bethune, C. Brown, H. Dorn, R. Johnson, and M. Devries (1991), Science **254** (5030), 410.

von Helden, G., M. Hsu, N. Gotts, P. Kemper, and M. Bowers (1993), Chem. Phys. Lett. **204** (1-2), 15.

Hendricks, J., S. Lyapustina, H. de Clercq, and K. Bowen (1998), J. Chem. Phys. **108** (1), 8.

Hikosaka, Y., J. Eland, T. Watson, and I. Powis (2001), J. Chem. Phys. **115** (10), 4593.

Hitchcock, A., and C. Brion (1978a), J. Electron Spectrosc. Relat. Phenom. **14** (6), 417.

Hitchcock, A., and C. Brion (1978b), J. Electron Spectrosc. Relat. Phenom. **13** (3), 193.

Hitchcock, A., and D. Mancini (1994), J. Electron Spectrosc. Relat. Phenom. **67** (1), 1.

Hoffmann, R. (1964), J. Chem. Phys. **40** (9), 2745.

Holland, D. M. P., I. Powis, G. Ohrwall, L. Karlsson, and W. von Niessen (2006), Chem. Phys. **326** (2-3), 535.

Hotop, H., and W. Lineberger (1973), J. Chem. Phys. **58** (6), 2379.

Howe, H., P. Wingo, M. Thun, L. Ries, H. Rosenberg, E. Feigal, and B. Edwards (2001), J. Natl. Cancer Inst. **93** (11), 824.

Huber, K. P., and G. Herzberg (1979), *Molecular Spectra and Molecular Structure of Diatomic Molecules* (Van Nostrand Reinhold, New York).

Huebner, R. H., R. N. Compton, and H. C. Schweinler (1968), Chem. Phys. Lett. **2** (6), 407.

Huels, M. A., B. Boudaffa, P. Cloutier, D. Hunting, and L. Sanche (2003), J. Am. Chem. Soc. **125** (15), 4467.

Huo, W. M. (1995a), in *Computational Methods for Electron-Molecule Collisions* (Plenum Press) pp. *v–vii*.

Huo, W. M. (1995b), in *Computational Methods for Electron-Molecule Collisions* (Plenum Press) pp. 327–355.

Imura, K., N. Kishimoto, and K. Ohno (2001), J. Phys. Chem. A **105** (26), 6378.

Innes, K., I. Ross, and W. Moomaw (1988), J. Mol. Spectrosc. **132** (2), 492.

Iqbal, Z., Y. Zhang, H. Grebel, S. Vijayalakshmi, A. Lahamer, G. Benedek, M. Bernasconi, J. Cariboni, I. Spagnolatti, R. Sharma, F. Owens, M. Kozlov, K. Rao, and M. Muhammed (2003), Eur. Phys. J. B **31** (4), 509.

Ishibashi, S., N. Terada, M. Tokumoto, N. Kinoshita, and H. Ihara (1992), J. Phys. Condes. Matter **4** (11), L169.

Itikawa, Y., and N. Mason (2005), J. Phys. Chem. Ref. Data **34** (1), 1.

Ito, Y., Y. Iwasa, N. Tuan, and S. Moriyama (2001), J. Chem. Phys. **115** (10), 4787.

Ito, Y., and T. Suzuki (1999), Phys. Rev. B **60** (23), 15636.

Ivanov, V., G. Kashenock, R. Polozkov, and A. Solov'yov (2001), J. Phys. B At. Mol. Opt. Phys. **34** (21), L669.

Jaffke, T., E. Illenberger, M. Lezius, S. Matejcik, D. Smith, and T. Mark (1994), Chem. Phys. Lett. **226** (1-2), 213.

Jamieson, E., and S. Lippard (1999), Chem. Rev. **99** (9), 2467.

Jean, Y., X. Lu, Y. Lou, A. Bharathi, C. Sundar, Y. Lyu, P. Hor, and C. Chu (1992), Phys. Rev. B **45** (20), 12126.

Jiao, C., C. DeJoseph, and A. Garscadden (2003), J. Phys. Chem. A **107** (42), 9040.

Johnson, W., K. Cheng, K. Huang, and M. Ledourneuf (1980), Phys. Rev. A **22** (3), 989.

Judson, I., and L. Kelland (2000), Drugs **59** (Suppl. 4), 29.

Jung, Y., and S. J. Lippard (2007), Chem. Rev. **107** (5), 1387.

Kandel, R. (1955), J. Chem. Phys. **23** (1), 84.

Katsumata, S., H. Shiromaru, K. Mitani, S. Iwata, and K. Kimura (1982), Chem. Phys. **69** (3), 423.

Kelland, L. (2000), Drugs **59** (Suppl. 4), 1.

Keller, J., and M. Coplan (1992), Chem. Phys. Lett. **193** (1-3), 89.

Keller, P., J. Taylor, T. Carlson, and F. Grimm (1983), Chem. Phys. **79** (2), 269.

Kettle, S., and A. Smith (1967), J. Chem. Soc. A (4), 688.

Khakoo, M. A., J. Muse, K. Ralphs, R. F. da Costa, M. H. F. Bettega, and M. A. P. Lima (2010), Phys. Rev. A **81** (6), 062716.

Kilic, H., K. Ledingham, C. Kosmidis, T. McCanny, R. Singhal, S. Wang, D. Smith, A. Langley, and W. Shaikh (1997), J. Phys. Chem. A **101** (5), 817.

Kimura, M., C. Makochekanwa, and O. Sueoka (2004), J. Phys. B At. Mol. Opt. Phys. **37** (7), 1461.

Kimura, M., O. Sueoka, A. Hamada, and Y. Itikawa (2007), "A comparative study of electron-and positron-polyatomic molecule scattering," in *Advances in Chemical Physics* (Wiley) pp. 537–622.

Kinugawa, T., Y. Hikosaka, A. Hodgekins, and J. Eland (2002), J. Mass Spectrom. **37** (8), 854.

Klonover, A., and U. Kaldor (1977), Chem. Phys. Lett. **51** (2), 321.

Klonover, A., and U. Kaldor (1978), J. Phys. B At. Mol. Phys. **11** (9), 1623.

Koga, T., H. Tatewaki, and T. Shimazaki (2000), Chem. Phys. Lett. **328** (4-6), 473.

Kopyra, J., C. Koenig-Lehmann, I. Bald, and E. Illenberger (2009), Angew. Chem. Int. Edit. **48** (42), 7904.

Korica, S., D. Rolles, A. Reinkoster, B. Langer, J. Viefhaus, S. Cvejanovic, and U. Becker (2005), Phys. Rev. A **71** (1), 013203.

Kroto, H. (1987), Nature **329** (6139), 529.

Kroto, H., J. Heath, S. O'Brien, R. Curl, and R. Smalley (1985), Nature **318** (6042), 162.

Kurepa, M., and D. Belic (1978), J. Phys. B At. Mol. Opt. Phys. **11** (21), 3719.

Lago, A., A. Santos, and G. de Souza (2004), J. Chem. Phys. **120** (20), 9547.

Lane, N. (1980), Rev. Mod. Phys. **52** (1), 29.

Lao, K., E. Jensen, P. Kash, and L. Butler (1990), J. Chem. Phys. **93** (6), 3958.

Leahy, D., K. Reid, H. Park, and R. Zare (1992), J. Chem. Phys. **97** (7), 4948.

Leahy, D., K. Reid, and R. Zare (1991), J. Chem. Phys. **95** (3), 1757.

Lebwohl, D., and R. Canetta (1998), Eur. J. Cancer **34** (10), 1522.

Lee, C., W. Yang, and R. G. Parr (1988), Phys. Rev. B **37**, 785.

Leininger, T., and F. Gadea (2000), J. Phys. B At. Mol. Opt. Phys. **33** (4), 735.

Lengsfield, B. H., and T. N. Rescigno (1991), Phys. Rev. A **44**, 2913.

Leroy, R., and R. Bernstein (1971), J. Mol. Spectrosc. **37** (1), 109.

Levesque, P., M. Michaud, and L. Sanche (2005), J. Chem. Phys. **122** (9), 094701.

Lezius, M., P. Scheier, and T. Mark (1993), Chem. Phys. Lett. **203** (2-3), 232.

Li, W. B., J. C. Houver, A. Haouas, F. Catoire, C. Elkharrat, R. Guillemin, L. Journel, R. Montuoro, R. R. Lucchese, M. Simon, and D. Dowek (2007), J. Electron Spectrosc. Relat. Phenom. **156**, 30.

Li, X., L. Sanche, and M. D. Sevilla (2002), J. Phys. Chem. A **106** (46), 11248.

Li, X., M. Sevilla, and L. Sanche (2003), J. Am. Chem. Soc. **125** (29), 8916.

Lichtenberger, D., K. Nebesny, C. Ray, D. Huffman, and L. Lamb (1991), Chem. Phys. Lett. **176** (2), 203.

Liebsch, T., O. Plotzke, F. Heiser, U. Hergenhahn, O. Hemmers, R. Wehlitz, J. Viefhaus, B. Langer, S. Whitfield, and U. Becker (1995), Phys. Rev. A **52** (1), 457.

Lifshitz, C., M. Rejwan, I. Levin, and T. Peres (1988), Int. J. Mass Spectrom. Ion Processes **84** (3), 271.

Lin, J., Y. Chen, Y. Lee, Y. Lee, and X. Yang (2002), Chem. Phys. Lett. **361** (5-6), 374.

Lindle, D. W., P. L. Cowan, T. Jach, R. E. LaVilla, R. D. Deslattes, and R. C. C. Perera (1991), Phys. Rev. A **43** (5), 2353.

Lou, Y., X. Lu, G. Dai, W. Ching, Y. Xu, M. Huang, P. Tseng, Y. Jean, R. Meng, P. Hor, and C. Chu (1992), Phys. Rev. B **46** (4), 2644.

Lu, J., S. Re, Y. Choe, S. Nagase, Y. Zhou, R. Han, L. Peng, X. Zhang, and X. Zhao (2003), Phys. Rev. B **67** (12), 125415.

Lu, X., and Z. Chen (2005), Chem. Rev. **105** (10), 3643.

Lucchese, R. (2004), J. Electron Spectrosc. Relat. Phenom. **141** (2-3, Sp. Iss. SI), 201.

Lucchese, R., and F. Gianturco (1996), Int. Rev. Phys. Chem. **15** (2), 429.

Lucchese, R., F. Gianturco, P. Nichols, and T. Gibson (2001), in *New Directions in Antimatter Chemistry and Physics*, edited by C. Surko and F. Gianturco, pp. 475–492.

Lucchese, R., F. Gianturco, and N. Sanna (1999), Chem. Phys. Lett. **305** (5-6), 413.

Lucchese, R., G. Raseev, and V. McKoy (1982), Phys. Rev. A **25** (5), 2572.

Lucchese, R., K. Takatsuka, and V. McKoy (1986), Phys. Rep. Rev. Sec. Phys. Lett. **131** (3), 147.

Lucchese, R. R. (2002), "Molecular Photoionization," in *Encyclopedia of Computational Chemistry* (John Wiley & Sons, Ltd).

Lucchese, R. R., R. Carey, C. Elkharrat, J. C. Houver, and D. Dowek (2009), J. Phys. Conf. Ser. **141**, 12009.

Lunt, S., D. Field, J. Ziesel, N. Jones, and R. Gulley (2001), Int. J. Mass Spectrom. **205** (1-3, Sp. Iss. SI), 197.

Makochekanwa, C., H. Kawate, O. Sueoka, and M. Kimura (2003a), J. Phys. B At. Mol. Opt. Phys. **36** (9), 1673.

Makochekanwa, C., O. Sueoka, and M. Kimura (2003b), Phys. Rev. A **68** (3), 032707.

Martin, J., J. El Yazal, and J. Francois (1996), Chem. Phys. Lett. **248** (5-6), 345.

Matejcik, S., T. Mark, P. Spanel, D. Smith, T. Jaffke, and E. Illenberger (1995), J. Chem. Phys. **102** (6), 2516.

Mathur, D., and J. Hasted (1976), Chem. Phys. **16** (3), 347.

Mayor, E., A. M. Velasco, and I. Martin (2007), Chem. Phys. Lett. **441** (4-6), 347.

McCurdy, C. W., and T. N. Rescigno (1989), Phys. Rev. A **39**, 4487.

Milburn, G., and M. Truter (1966), J. Chem. Soc. A (11), 1609.

Miller, T. M., and B. Bederson (1978) (Academic Press) pp. 1 – 55.

Mitroy, J., M. Bromley, and G. Ryzhikh (2002), J. Phys. B At. Mol. Opt. Phys. **35** (13), R81.

Mok, C., W. Chin, and H. Huang (1991), J. Electron Spectrosc. Relat. Phenom. **57** (2), 213.

Morgenthaler, L., and J. Eyler (1979), J. Chem. Phys. **71** (3), 1486.

Morrison, R., B. Rockney, and E. Grant (1981), J. Chem. Phys. **75** (6), 2643.

Moss, D., K. Trentelman, and P. Houston (1992), J. Chem. Phys. **96** (1), 237.

Mozejko, P., G. Kasperski, C. Szmytkowski, G. Karwasz, R. Brusa, and A. Zecca (1996), Chem. Phys. Lett. **257** (3-4), 309.

Mozejko, P., E. Ptasinska-Denga, A. Domaracka, and C. Szmytkowski (2006), Phys. Rev. A **74** (1), 012708.

Msezane, A. Z., Z. Felfli, and D. Sokolovski (2008), J. Phys. B At. Mol. Opt. Phys. **41** (10), 105201.

Mulliken, R. (1955), J. Chem. Phys. **23** (11), 1997.

Murdoch, J., A. Streitwieser, and S. Gabriel (1978), J. Am. Chem. Soc. **100** (20), 6338.

Murrell, J., B. Vidal, and M. Guest (1975), J. Chem. Soc., Faraday Trans. 2 **71**, 1577.

Nagakura, S. (1960), Mol. Phys. **3** (2), 152.

Nagata, T., M. Suzuki, K. Suzuki, T. Kondow, and K. Kuchitsu (1984), Chem. Phys. **88** (1), 163.

Napier, I., and R. Norrish (1967), Proc. R. Soc. A **299** (1458), 317.

Natalense, A., and R. Lucchese (1999), J. Chem. Phys. **111** (12), 5344.

Nelson, R. D., D. R. Lide, and A. A. Maryott (1967), *Selected values of electric dipole moments for molecules in the gas phase* (U.S. Dept. of Commerce, National Bureau of Standards, Washington, D.C.).

Nenner, I., and G. Schulz (1975), J. Chem. Phys. **62** (5), 1747.

Newton, R. G. (1982), *Scattering Theory of Waves and Particles* (Springer Verlag, New York).

Boroński, E., and R. M. Nieminen (1986), Phys. Rev. B **34**, 3820.

von Niessen, W., L. Asbrink, and G. Bieri (1982), J. Electron Spectrosc. Relat. Phenom. **26** (2), 173.

NIST, (2012), “Computational Chemistry Comparison and Benchmark Database,” see http://cccbdb.nist.gov/.

Niwa, Y., S. Tajima, and T. Tsuchiya (1981), Int. J. Mass Spectrom. Ion Processes **40** (3), 287.

Noro, T., M. Sekiya, and T. Koga (1997), Theor. Chem. Acc. **98** (1), 25.

Noro, T., M. Sekiya, and T. Koga (2003), Theor. Chem. Acc. **109** (2), 85.

Noro, T., M. Sekiya, Y. Osanai, E. Miyoshi, T. Koga, and H. Tatewaki (2012), “Segmented Gaussian Basis Sets,” see http://setani.sci.hokudai.ac.jp/sapporo/.

Novak, I., J. Benson, and A. Potts (1986), J. Electron Spectrosc. Relat. Phenom. **41** (3-4), 225.

Ogden, I., N. Shaw, C. Danby, and I. Powis (1983), Int. J. Mass Spectrom. Ion Processes **54** (1-2), 41.

Ohta, T., and H. Kuroda (1976), Bull. Chem. Soc. Jpn. **49** (11), 2939.

Okada, S., Y. Miyamoto, and M. Saito (2001), Phys. Rev. B **64** (24), 245405.

Olney, T., G. Cooper, W. Chan, G. Burton, C. Brion, and K. Tan (1996), Chem. Phys. **205** (3), 421.

Osanai, Y., T. Noro, E. Miyoshi, M. Sekiya, and T. Koga (2004), J. Chem. Phys. **120** (14), 6408.

Ott, A., G. Rechtsteiner, C. Felix, O. Hampe, M. Jarrold, R. Van Duyne, and K. Raghavachari (1998), J. Chem. Phys. **109** (22), 9652.

Padial, N., and D. Norcross (1984), Phys. Rev. A **29** (4), 1742.

Palmer, M., I. Walker, M. Guest, and A. Hopkirk (1990), Chem. Phys. **147** (1), 19.

Panosetti, C., I. Baccarelli, F. Sebastianelli, and F. A. Gianturco (2010), Eur. Phys. J. D **60**, 21.

Pantazis, D. A., X.-Y. Chen, C. R. Landis, and F. Neese (2008), J. Chem. Theory Comput. **4** (6), 908.

Parasuk, V., and J. Almlof (1991), Chem. Phys. Lett. **184** (1-3), 187.

Park, M., K. Jung, H. Upadhyaya, and H. Volpp (2001), Chem. Phys. **270** (1), 133.

Perdew, J., J. Chevary, S. Vosko, K. Jackson, M. Pederson, D. Singh, and C. Fiolhais (1992), Phys. Rev. B **46** (11), 6671.

Perdew, J., and Y. Wang (1992), Phys. Rev. B **45** (23), 13244.

Perdew, J., and A. Zunger (1981), Phys. Rev. B **23** (10), 5048.

Perry, W., and W. Jolly (1974), Inorg. Chem. **13** (5), 1211.

Peyerimhoff, S. D., and R. J. Buenker (1981), Chem. Phys. **57** (3), 279.

Pisanias, M., L. Christophorou, J. Carter, and D. McCorkle (1973), J. Chem. Phys. **58** (5), 2110.

Potts, A., I. Novak, F. Quinn, G. Marr, B. Dobson, I. Hillier, and J. West (1985), J. Phys. B At. Mol. Opt. Phys. **18** (15), 3177.

Powis, I. (1997), J. Chem. Phys. **106** (12), 5013.

Prinzbach, H., A. Weller, P. Landenberger, F. Wahl, J. Worth, L. Scott, M. Gelmont, D. Olevano, and B. von Issendorff (2000), Nature **407** (6800), 60.

Puska, M., and R. Nieminen (1992), J. Phys. Condes. Matter **4** (10), L149.

Rabalais, J. (1972), J. Chem. Phys. **57** (2), 960.

Raghavachari, K., D. Strout, G. Odom, G. Scuseria, J. Pople, B. Johnson, and P. Gill (1993), Chem. Phys. Lett. **214** (3-4), 357.

Ramana, M. V., and A. K. Rajagopal (1981), Phys. Rev. A **24**, 1689.

Rau, A. R. P. (2004), Phys. Scr. **69** (1), C10.

Reid, K., D. Leahy, and R. Zare (1992), Phys. Rev. Lett. **68** (24), 3527.

Rennie, E. E., H. M. Köppe, B. Kempgens, U. Hergenhahn, A. Kivimäki, K. Maier, M. Neeb, A. Rüdel, and A. M. Bradshaw (1999), J. Phys. B At. Mol. Opt. Phys. **32** (11), 2691.

Rescigno, T. (1994), Phys. Rev. A **50** (2), 1382.

Rescigno, T., and B. Lengsfield (1992), Z. Phys. D Atoms Mol. Clusters **24** (2), 117.

Rescigno, T., and B. Schneider (1992), Phys. Rev. A **45** (5), 2894.

Rescigno, T. N., B. H. Lengsfield, and C. W. McCurdy (1995a), in *Modern Electronic Structure Theory, Part 1* (World Scientific) pp. 501–588.

Rescigno, T. N., C. W. McCurdy, A. E. Orel, and B. H. Lengsfield (1995b), in *Computational Methods for Electron-Molecule Collisions* (Plenum Press) pp. 1–44.

Rockney, B., and E. Grant (1983), J. Chem. Phys. **79** (2), 708.

Rosenberg, B., L. Vancamp, and T. Krigas (1965), Nature **205** (4972), 698.

Rosenberg, B., L. Vancamp, J. Trosko, and V. Mansour (1969), Nature **222** (5191), 385.

Rudel, A., R. Hentges, U. Becker, H. Chakraborty, M. Madjet, and J. Rost (2002), Phys. Rev. Lett. **89** (12), 125503.

Saito, M., and Y. Miyamoto (2001), Phys. Rev. Lett. **87** (3), 035503.

Saito, M., and Y. Miyamoto (2002), Phys. Rev. B **65** (16), 165434.

Sanche, L. (2005), Eur. Phys. J. D **35** (2), 367.

Sanna, N., and F. Gianturco (1998), Comput. Phys. Commun. **114** (1-3), 142.

Sawtarie, M., M. Menon, and K. Subbaswamy (1994), Phys. Rev. B **49** (11), 7739.

Schaefer, H., M. Forster, R. Wurschum, W. Kratschmer, and D. Huffman (1992), Phys. Rev. B **45** (20), 12164.

Schneider, B. I., and L. A. Collins (1984), Phys. Rev. A **30**, 95.

Schoen, P., M. Marrone, J. Schnur, and L. Goldberg (1982), Chem. Phys. Lett. **90** (4), 272.

Schrader, D., and J. Moxom (2001), in *New Directions in Antimatter Chemistry and Physics*, edited by C. Surko and F. Gianturco, pp. 263–290.

Schreiber, M., M. R. J. Silva, S. P. A. Sauer, and W. Thiel (2008), J. Chem. Phys. **128** (13), 134110.

Schulz, G. (1973a), Rev. Mod. Phys. **45** (3), 378.

Schulz, G. (1973b), Rev. Mod. Phys. **45** (3), 423.

Scuseria, G. (1991), Chem. Phys. Lett. **176** (5), 423.

Seifert, G., K. Vietze, and R. Schmidt (1996), J. Phys. B At. Mol. Opt. Phys. **29** (21), 5183.

Sekiya, M., T. Noro, T. Koga, and H. Matsuyama (1998), Theochem J. Mol. Struct. **451** (1-2, SI), 51.

Sevilla, M., B. Besler, and A. Colson (1994), J. Phys. Chem. **98** (8), 2215.

Sevilla, M., R. Failor, and G. Zorman (1974), J. Phys. Chem. **78** (7), 696.

Shanker, B., and J. Applequist (1994), J. Phys. Chem. **98** (26), 6486.

Sheehy, J., T. Gil, C. Winstead, R. Farren, and P. Langhoff (1989), J. Chem. Phys. **91** (3), 1796.

Shibuya, K., S. Suzuki, T. Imamura, and I. Koyano (1997), J. Phys. Chem. A **101** (4), 685.

Shigemasa, E., J. Adachi, M. Oura, and A. Yagishita (1995), Phys. Rev. Lett. **74** (3), 359.

Smirnov, Y. (2004), Opt. Spectrosc. **96**, 319, 10.1134/1.1690022.

Sokolova, S., A. Luchow, and J. Anderson (2000), Chem. Phys. Lett. **323** (3-4), 229.

Sommerfeld, T. (2002), Phys. Chem. Chem. Phys. **4** (12), 2511.

Sorensen, G., L. Mahler, and N. Rastrup-Andersen (1974), J. Mol. Struct. **20** (1), 119.

Stener, M., P. Decleva, and A. Lisini (1995), J. Phys. B At. Mol. Opt. Phys. **28** (23), 4973.

Stratmann, R., and R. Lucchese (1992), J. Chem. Phys. **97** (9), 6384.

Stratmann, R. E., and R. R. Lucchese (1995), J. Chem. Phys. **102** (21), 8493.

Sueoka, O. (1988), J. Phys. B At. Mol. Opt. Phys. **21** (20), L631.

Surko, C., G. Gribakin, and S. Buckman (2005), J. Phys. B At. Mol. Opt. Phys. **38** (6), R57.

Suzuki, Y.-I., and T. Suzuki (2008), J. Phys. Chem. A **112** (3), 402.

Szybalski, W. (1974), Cancer Chemoth. Rep. **58** (4), 539.

Takatsuka, K., and V. McKoy (1984), Phys. Rev. A **30**, 1734.

Tam, H., J. Choe, and M. Harmony (1991), J. Phys. Chem. **95** (23), 9267.

Tanaka, H., L. Boesten, K. Onda, and O. Ohashi (1994), J. Phys. Soc. Jpn. **63** (2), 485.

Taylor, J. R. (1972), *Scattering Theory: The Quantum Theory of Nonrelativistic Collisions* (Wiley, New York).

Taylor, P., E. Bylaska, J. Weare, and R. Kawai (1995), Chem. Phys. Lett. **235** (5-6), 558.

Tennyson, J. (2010), Phys. Rep. **491** (2-3), 29.

Thirring, W. (2002), *Quantum Mathematical Physics: Atoms, Molecules and Large Systems*, Physics and Astronomy Online Library (Springer, Berlin).

Thissen, R., M. Simon, and M. Hubin-Franskin (1994), J. Chem. Phys. **101** (9), 7548.

Thoss, M., and W. Domcke (1998), J. Chem. Phys. **109** (16), 6577.

Tixier, S., G. Cooper, R. Feng, and C. Brion (2002), J. Electron Spectrosc. Relat. Phenom. **123** (2-3), 185.

Toffoli, D., R. R. Lucchese, M. Lebech, J. C. Houver, and D. Dowek (2007), J. Chem. Phys. **126** (5), 054307.

Toffoli, D., M. Simpson, and R. Lucchese (2004), Phys. Rev. A **69** (6), 062712.

Tolstikhin, O., V. Ostrovsky, and H. Nakamura (1997), Phys. Rev. Lett. **79** (11), 2026.

Tolstikhin, O., V. Ostrovsky, and H. Nakamura (1998), Phys. Rev. A **58** (3), 2077.

Tonzani, S., and C. Greene (2006a), J. Chem. Phys. **124** (5), 054312.

Tonzani, S., and C. H. Greene (2006b), J. Chem. Phys. **125** (9), 094504.

Tosic, S. D., M. S. Rabasovic, D. Sevic, V. Pejcev, D. M. Filipovic, L. Sharma, A. N. Tripathi, R. Srivastava, and B. P. Marinkovic (2008), Phys. Rev. A **77** (1), 012725.

Trevisan, C. S., A. E. Orel, and T. N. Rescigno (2006), J. Phys. B At. Mol. Opt. Phys. **39** (12), L255.

Van Orden, A., and R. Saykally (1998), Chem. Rev. **98** (6), 2313.

Venuti, M., M. Stener, G. De Alti, and P. Decleva (1999), J. Chem. Phys. **111** (10), 4589.

Vilkas, M. J., and Y. Ishikawa (2007), Phys. Rev. A **75**, 062508.

Vredenborg, A., C. S. Lehmann, D. Irimia, W. G. Roeterdink, and M. H. M. Janssen (2011), Chem. Phys. Chem. , n/a.

Wade, E., K. Reak, S. Li, S. Clegg, P. Zou, and D. Osborn (2006), J. Phys. Chem. A **110** (13), 4405.

Walker, I., and M. Fluendy (2001), Int. J. Mass Spectrom. **205** (1-3, Sp. Iss. SI), 171.

Walker, I., M. Palmer, and A. Hopkirk (1990), Chem. Phys. **141** (2-3), 365.

Wallace, S., and D. Dill (1978a), Phys. Rev. B **17** (4), 1692.

Wallace, S., and D. Dill (1978b), Phys. Rev. B **17** (4), 1692.

Wang, C.-R., J. Nguyen, and Q.-B. Lu (2009), J. Am. Chem. Soc. **131** (32), 11320.

Wang, K., and V. McKoy (1991), J. Chem. Phys. **95** (7), 4977.

Wang, L., J. Conceicao, C. Jin, and R. Smalley (1991), Chem. Phys. Lett. **182** (1), 5.

Wang, Z., X. Ke, Z. Zhu, F. Zhu, M. Ruan, H. Chen, R. Huang, and L. Zheng (2001), Phys. Lett. A **280** (5-6), 351.

Werner, H.-J., P. J. Knowles, G. Knizia, F. R. Manby, M. Schütz, *et al.* (2006), "Molpro, version 2006.1, a package of ab initio programs," See http://www.molpro.net.

Whelan, C., and N. Mason (2005), *Electron Scattering: from Atoms, Molecules, Nuclei, and Bulk Matter*, Physics of atoms and molecules (Kluwer Academic/Plenum Publishers).

Wijesundera, W., I. Grant, and P. Norrington (1992), J. Phys. B At. Mol. Opt. Phys. **25** (9), 2143.

Winstead, C., and V. McKoy (1998), Phys. Rev. A **57**, 3589.

Winstead, C., and V. McKoy (2006a), Phys. Rev. Lett. **98**, 113201.

Winstead, C., and V. McKoy (2006b), Phys. Rev. A **73** (1), 012711.

Winstead, C., and V. McKoy (2006c), J. Chem. Phys. **125** (24), 244302.

Winstead, C., and V. Mckoy (2006), J. Chem. Phys. **125** (7), 074302.

Winstead, C., and V. McKoy (2007a), Phys. Rev. A **76** (1), 012712.

Winstead, C., and V. McKoy (2007b), Phys. Rev. Lett. **98** (11), 113201.

Winstead, C., and V. McKoy (2008), J. Chem. Phys. **129** (7), 077101.

Winstead, C., V. McKoy, and M. Bettega (2005), Phys. Rev. A **72** (4), 042721.

Winstead, C., V. McKoy, and S. d. Sanchez (2007), J. Chem. Phys. **127** (8), 085105.

Wodtke, A., E. Hintsa, and Y. Lee (1986), J. Chem. Phys. **84** (2), 1044.

Wolf, A., M. Reiher, and B. Hess (2002), J. Chem. Phys. **117** (20), 9215.

Wysokinski, R., and D. Michalska (2001), J. Comput. Chem. **22** (9), 901.

Xie, M., Z. Zhou, Z. Wang, D. Chen, and F. Qi (2011), Int. J. Mass Spectrom. **In Press, Corrected Proof**, n/a.

Xu, Y., M. Tan, and U. Becker (1996), Phys. Rev. Lett. **76** (19), 3538.

Yagishita, A., K. Hosaka, and J. Adachi (2005), J. Electron Spectrosc. Relat. Phenom. **142** (3), 295.

Yahana, K., and G. Bertsch (1994), J. Chem. Phys. **100** (8), 5580.

Yang, S., C. Pettiette, J. Conceicao, O. Cheshnovsky, and R. Smalley (1987), Chem. Phys. Lett. **139** (3-4), 233.

Yue, X.-F., J.-I. Sun, Q. Wei, H.-M. Yin, and K.-L. Han (2007), Chin. J. Chem. Phys. **20** (4), 401.

Zamenhof, S., R. DeGiovanni, and S. Greer (1958), Nature **181** (4612), 827.

Zare, R. (1967), J. Chem. Phys. **47** (1), 204.

Zare, R. N. (1988), *Angular Momentum* (John Wiley & Sons, Inc., New York).

Zatsarinny, O., and K. Bartschat (2008), Phys. Rev. A **77** (6), 062701.

Zatsarinny, O., and K. Bartschat (2009), Phys. Rev. A **79** (4, Part A), 042713.

Zecca, A., L. Chiari, G. Garcia, F. Blanco, E. Trainotti, and M. J. Brunger (2010), J. Phys. B At. Mol. Opt. Phys. **43** (21), 215204.

Zecca, A., C. Perazzolli, and M. Brunger (2005), J. Phys. B At. Mol. Opt. Phys. **38** (13), 2079.

Zhang, B., C. Wang, K. Ho, C. Xu, and C. Chan (1992), J. Chem. Phys. **97** (7), 5007.

Zhang, C., X. Xu, and Q. Zhang (2002), Chem. Phys. Lett. **364** (3-4), 213.

Zhang, Y., Z. Guo, and X. You (2001), J. Am. Chem. Soc. **123** (38), 9378.

Zheng, Y., D. J. Hunting, P. Ayotte, and L. Sanche (2008), Phys. Rev. Lett. **100** (19), 198101.

Zope, R. R., T. Baruah, M. R. Pederson, and B. I. Dunlap (2008), Int. J. Quantum Chem. **108** (2), 307.

VITA

Name: Ralph J. Carey

Address: Department of Chemistry
Texas A&M University
P. O. Box 30012
College Station, TX 77842-3012

Email Address: rcarey@mail.chem.tamu.edu

Education: B.S., Chemistry
Louisiana State University, Baton Rouge, 2003